Non-invasive Dissection of the Human Visual System

by

Daniela Petrova

A dissertation submitted to the graduate faculty

in partial fulfilment of the requirements for the degree of

Doctor of Philosophy

University College London

London, U.K.

2011

Declaration

I, Daniela Petrova, confirm that the work presented in this thesis is my own. Where information has been derived from other sources, I confirm that this has been indicated in the thesis.

Signature: .....…….

Abstract

A flickering stimulus can appear brighter or of different colour than a steady stimulus of the same spectral composition and equal time-averaged intensity. The change in appearance is consistent with the distortion product of a nonlinearity in the human visual system. This nonlinearity is used for non-invasive dissection of the human visual system into pre-nonlinearity and post-nonlinearity linear stages, which affect the amplitude of the sinusoidal signals that they process.

A five-channel Maxwellian system was used to generate cosine-windowed, amplitude-modulated, sinusoidally-flickering stimuli. The subjects adjusted the maximum modulation of the signal in order to set the threshold for the perception of flicker and colour or brightness change. The pre-nonlinearity filter was tested by varying the carrier frequency between 5 Hz and 60 Hz and the post-nonlinearity filter was measured by varying the amplitude-modulation frequency between 0.25 Hz and 5 Hz. The L- and M-cone pathways are separately measured by using a new combination of the silent-cone-substitution technique and the sandwich model. The distortion product at the output of the nonlinearity is measured by using a new matching method for measuring the colour and brightness changes.

The results suggest that the pre-nonlinearity filter is band-pass and shows substantial adaptation with light intensity that can explain most of the adaptation in the visual pathways. The post-nonlinearity filter is low-pass and shows little or no adaptation with light intensity. The input-output function of the nonlinearity can be described as an expansive, quadratic function that rapidly saturates at high input levels.

The function of the pre-nonlinearity stage is correlated with retinal physiology. Therefore, the method developed in this study has applications in testing retinal function and separate stages of the cone pathways.

Contents

Acknowledgements

I would like to thank my supervisor, Professor Andrew Stockman, for his patience and supervision from the very beginning of my time at the Institute of Ophthalmology. The advice I have received from him will last me a lifetime.

I am very grateful to Dr. Bruce Henning for his rigorous approach and meticulous style. Many thanks also go to Dr. Caterina Ripamonti. Her talent for describing complicated concepts, her approachable demeanour and her style of teaching have been very helpful throughout.

I would also like to acknowledge the administrative support from Nick Burt and Anne-Marie Preston at the Institute of Ophthalmology. Their timely and efficient responses to queries have been greatly appreciated from the beginning to the end.

I have been fortunate to be able to work with a great team of people throughout my studies and I look forward to continuing my collaboration with them throughout my professional career.

This project would not have been possible without the funding and scholarship awarded by the Biotechnology and Biological Sciences Research Council (BBSRC).

List of Figures

List of Equations

List of Tables

List of abbreviations

CFF	Critical Fusion Frequency for flicker
CFFD	Critical Fusion Frequency for Distortion in the form of a change in appearance at f_{am}
TCSF	Temporal Contrast Sensitivity Function
f_c	Carrier frequency
f_{am}	Amplitude-modulation frequency
IMIDOC	Input-Modulation vs. Input-DC vs. Output-Contrast-at-f_{am} 3D graph
IMOAC	Input-Modulation vs. Output-Appearance-Change-at-f_{am} curve
IMOC	Input-Modulation vs. Output-Contrast-at-f_{am} curve
LGN	Lateral Geniculate Nucleus

Glossary

Amplitude-modulation: involves changing the amplitude of a 'carrier' signal by multiplying it with a 'modulator' signal.

Broca-Sulzer effect: the increase in brightness of light flashes with durations 50-100 ms compared to flickes of shorter and longer durations given the same chromaticity and peak intensity.

Brücke-Bartley effect: the change in the apparent brightness of a flickering light compared to a steady light of the same chromaticity and time-averaged intensity.

Bezold-Brücke hue shift: the shift in the apparent hue of a visual stimulus towards invariant hues with increasing light intensity.

Contrast-at-f_{am}: the ratio of the f_{am}:DC amplitudes at the output of a nonlinearity.

Input-modulation: the modulation of a signal at the input to a nonlinearity.

Sandwich model. The serial sequence of an early linear filter, a nonlinearity and a late linear filter in signal-processing.

1 Introduction

Non-invasive dissection of the human visual system is potentially of great importance for better understanding neural processing and visual function. The ability to dissect a system allows the study of individual stages of that system, particularly serial (sequential) ones. The possibility to carry out such a study in a non-invasive way extends its applications to a wide range of *in vivo* conditions. However, currently there is no widely used diagnostic or experimental technique that allows the non-invasive dissection of the visual pathways for processing colour and brightness information in response to temporally-varying stimuli.

This chapter outlines the context of the present study in four main sections. The first section describes the main behavioural findings related to the human visual system and their correlation to physiological data. The second section evaluates linear and nonlinear systems' analysis that is essential for the non-invasive investigation of separate stages of the visual system. The third section analyses the visual phenomenon that will allow the dissection of the visual system in this study. Finally, the fourth section describes the main aims and objectives that will be addressed in later chapters.

1.1 The human visual system

Psychophysical models generally explain all or part of the visual perception in terms of the activity of chromatic and achromatic pathways (Guth, Massof & Benzschawel, 1980; Hurvich & Jameson, 1957; Ingling & Tsou, 1977; King-Smith & Carden, 1976). A version of such a model is the three-stage zone model established by Müller (Müller, 1930) and later extended (De Valois & De Valois, 1993; Guth, 1991; Judd, 1949; Stockman & Brainard, 2009).

The first stage of the three-stage model is related to the photoreceptor level, which involves the S-, M- and L-cones at photopic light levels. The individual normalised spectral sensitivities of the three cone types are shown in Figure 1.1, according to measurements at the cornea by Stockman and Sharpe (2000b).

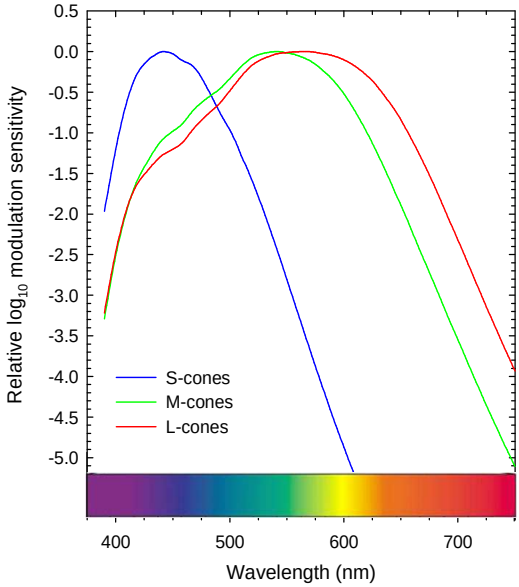

Figure 1.1. Corneally-measured, normalised spectral sensitivities for the L-cones (peaking at 566 nm), M-cones (peaking at 541 nm) and S-cones (peaking at 441 nm) at the central 2° of the visual field (data from Stockman & Sharpe, 2000b).

The second stage of the zone model is considered to reflect the post-receptoral luminance (achromatic) mechanism (receiving L- and M-cone inputs i.e. L+M) and the two cone-opponent mechanisms (receiving L-M and S-(M+L) cone inputs, where + and – indicate additive and opposing cone inputs, respectively), which contribute to two chromatic pathways. Detection and discrimination experiments indicate that substantial spatial coding and adaptation occurs at the cone-opponent stage (Boynton, 1979; De Lange, 1958a; Eisner & MacLeod, 1980; Guth, Alexander, Chumbly, Gillman & Patterson, 1968; Luther, 1927; Pokorny, Moreland & Smith, 1975; Schrödinger, 1925; Walls, 1955).

Whereas the second stage contains cone-opponent channels that can account for chromatic discrimination (e.g. Eisner & MacLeod, 1981; Guth, 1991), the third stage of the zone model combines the outputs of these channels to give four colour-opponent mechanisms to account for colour appearance (Hurvich & Jameson, 1955; Hurvich & Jameson, 1957). Following early perceptual observations (Hering, 1878), quantitative data for colour-opponency was provided by Hurvich & JamesonHurvich & Jameson (Hurvich & Jameson, 1957) who used hue-cancellation paradigms to isolate four unique hue precepts (red, green, blue and red).

It is important to note that the conventional notation of the cone-opponent mechanisms (L-M and S-(L+M)) and the luminance mechanism (L+M) as well as the colour-opponent mechanisms is greatly simplified. For instance, there are small, opponent M- and L-cone inputs (Ebenezer, Michaelides, Jenkins, Audo, Webster, Cheetham, Stockman, Maher, Ainsworth, Yates, Bradshaw, Holder, Moore & Hardcastle, 2005; Stockman & Plummer, 2005a; Stockman & Plummer, 2005b; Stockman, Plummer & Montag, 2005) and inverted S-cone inputs to the luminance pathway (Cole, Hine & McIlhagga, 1993; Lee & Stromeyer, 1989; MacLeod, Stockman, Johnson & Vivian, 1987) as well as S-cone inputs to the L-M pathway (Mullen & Kingdom, 1996). A further simplification of the three-stage model is that it assumes linearity within individual pathways despite evidence for visual nonlinearities (see Sections 1.2 and 1.3).

The results from psychophysical studies can be related to the results from physiological studies. For instance, the psychophysically measured cone spectral sensitivities at the level of the cornea (Figure 1.1, data from Stockman Stockman & Sharpe, 2000a) are analogous to the cone photopigment spectral sensitivities measured at the retina level when corrected for lens and macula absorptions (e.g. Schnapf, Kraft & Baylor, 1987). (At the corneal level the S-

cone spectral sensitivity peaks at a longer wavelength than at the retinal level, 441 nm instead of 420 nm, due to short-wavelength absorption by the lens and macula.)

Each cone has a univariant output that conveys a single quantity dependent only on the number of photons absorbed i.e. the principle of univariance as described by Rushton (1972). The photon count can be varied by both the spectral characteristics and the intensity of a light. Thus, in the presence of a single cone type, gradations between light and dark (i.e. relative light energy) cannot be distinguished from changes in wavelength.

The second-stage luminance mechanism and the two cone-opponent mechanisms can be related to the phasic and tonic ganglion cells also known as magnocellular and parvocellular ganglion cells, respectively, (Lee, Martin & Valberg, 1988) while their connections can be related to the magnocellular and parvocellular layers in the lateral geniculate nucleus (LGN), respectively (Derrington, Krauskopf & Lennie, 1984). The L-M and S-(L+M) cone-opponent mechanisms were initially related to a large and small population of parvocellular neurons, respectively (Derrington et al., 1984), with approximately orthogonal response in the isoluminant plane of the cardinal axis (Krauskopf, Williams & Heeley, 1982). Subsequent work showed that the smaller parvocellular population can be more precisely identified as the koniocellular population in the LGN (Casagrande & Kaas, 1994; Hendry & Yoshioka, 1994). Apart from the differences in response in the isoluminant plane, further differences between the information carried by the koniocellular pathway vs. the parvocellular pathway include low spatial resolution vs. high spatial resolution (Derrington & Lennie, 1984; Livingstone & Hubel, 1987; Wiesel & Hubel, 1966). These differences between the koniocellular and the parvocellular pathways are also in agreement with psychophysical data showing differences in spatial contrast sensitivity between the S-(L+M) and the L-M chromatic pathways (Cavonius & Estévez, 1975; Green, 1968; Hess, Mullen & Zrenner, 1989; Kelly, 1974).

Both the L- and M-cones provide L+M inputs to ON (i.e., depolarising in response to light) and OFF (i.e., hyperpolarising in response to light) diffuse bipolar cells, which synapse onto magnocellular retinal ganglion cells (RGCs) that show centre-surround behaviour (either ON-centre and OFF-surround or OFF-centre and ON-surround). Magnocellular cells do not contribute to wavelength discrimination and contribute little to low spatial-frequency resolution but they have high contrast sensitivity and high temporal resolution. Increment thresholds for magnocellular RGCs (De Monasterio, 1978; De Monasterio & Gouras, 1975) were found to be very similar to the human photopic contrast sensitivity function (De Lange, 1952; Kelly, 1971a). For instance, the minimization of magnocellular RGC responses in electrophysiology closely corresponds to the heterochromatic flicker null in psychophysics (Lee et al., 1988; Stromeyer & Lee, 1987). Magnocellular RGCs synapse on to magnocellular neurons in the LGN, which retain the band-pass characteristics as the magnocellular RGCs for both temporal and spatial frequencies (Derrington & Lennie, 1984; Lee, Pokorny, Smith, Martin & Valberg, 1990; Purpura, Tranchina, Kaplan & Shapley, 1990). Ganglion cells in the magnocellular pathway are highly sensitive to small luminance variations, and show a rapidly saturating contrast response function to luminance, but they are approximately tenfold less sensitive to chromatic stimuli than ganglion cells in the parvocellular pathway (Derrington & Lennie, 1984; Kaplan & Shapley, 1986; Lee et al., 1990; Lennie, 1984);.

Parvocellular cells in the parvocellular pathway have chromatic discrimination and high spatial resolution but low contrast sensitivity properties. The parvocellular cells shows centre-surround behaviour where one cone type mediates the centre and another cone type or mixture of cones mediate the surround of both ON and OFF cells (Lee et al., 1990; Reid & Shapley, 1992). Consequently, there are four subtypes of parvocellular ganglion cells: +L-M, -L+M, +M-L, -M+L. Increment thresholds for parvocellular RGCs were found to be similar

to the chromatic (equiluminant) contrast sensitivity function (Lee, Martin & Valberg, 1989b; Lee, Martin & Valberg, 1989c; Livingstone & Hubel, 1987). Parvocellular cells show high contrast sensitivity to equiluminant stimuli that can be characterized by a slightly decelerating response function with increasing chromatic contrast. However, parvocellular RGCs are relatively insensitive to luminance stimuli (with approximately tenfold lower contrast response than magnocellular RGCs) and they give an almost linear response with increasing luminance contrast (Derrington et al., 1984; Lee et al., 1990). The parvocellular ganglion cells have a lower overall contrast gain than the magnocellular ganglion cells: when stimulus contrast is expressed in cone modulation units, the parvocellular ganglion cells' response to chromatic modulation remains approximately twofold less sensitive than the magnocellular ganglion cells' response to luminance modulation (Wesner, Pokorny, Shevell & Smith, 1991).

The parvocellular ganglion cells provide inputs to the parvocellular pathway, which multiplexes (i.e. carries both) opponent and non-opponent information (Kelly, 1983; Merigan & Eskin, 1986; Schiller, Logothetis & Charles, 1990). Parvocellular neurones have low-pass frequency responses to both temporal and spatial sinusoidal stimuli modulated in chromaticity (i.e. equiluminant) and band-pass responses to stimuli modulated in luminance. No other pathway except the parvocellular provides the sampling density that is necessary to support low-temporal and high-spatial frequency resolution observed in psychophysical experiments (Kaiser, Lee, Martin & Valberg, 1990; Kaplan, Lee & Shapley, 1990; Lennie & D'Zmura, 1988; Livingstone & Hubel, 1987). The presence of multiplexing suggests the existence of centres higher up in the visual system (cortical) that can separate (i.e. demultiplex) luminance and chromatic signals. Some studies of the early visual cortex have not revealed the physiological basis for demultiplexing (Lennie, Krauskopf & Sclar, 1990)

while others have revealed partial decoding, i.e. extraction only of the luminance information (Billock, 1995), which suggests that the location may be even higher in the visual system and/or that different information is carried by different subpopulations of cells as suggested by the large number of specialised bipolar and ganglion cell types (Boycott & Wässle, 1991).

Considering that both magnocellular and parvocellular pathways respond to changes in luminance, there are at least two distinct luminance pathways as explored in several papers by Ingling et al (Ingling & Martinez-Uriegas, 1983; Ingling & Martinez-Uriegas, 1985; Ingling & Martinez, 1983; Ingling & Tsou, 1988; Lennie, Pokorny & Smith, 1993). Since magnocellular ganglion cell inputs to the magnocellular pathways and parvocellular ganglion cell inputs to the parvocellular pathway differ in their spatial and temporal characteristics, it is possible to delineate their luminance mechanisms as $(L+M)_M$ and $(L+M)_P$ respectively, with the former having high temporal frequency sensitivity and the latter having high spatial frequency sensitivity at low and high frequencies (Gouras & Zrenner, 1979; Ingling, Grigsby & Long, 1992; Ingling, Barley & Ghani, 1996; Ingling & Martinez-Uriegas, 1985; Ingling & Tsou, 1988; Martinez-Uriegas, 1985). While the $(L+M)_M$ mechanism is likely to carry just luminance information and to signal luminance perception, the $(L+M)_P$ mechanism is likely to carry both chromatic and luminance information and to signal brightness perception. This is supported by some studies that show brightness and chromatic information are encoded by the same cells (Derrington et al., 1984; Kelly, 1983; Lennie, 1984) and others that show the brightness pathway receives luminance and chromatic information (Kaiser & Comerford, 1975), possibly carried by double-duty P cells (P-cell multiplexing).

1.2 Systems' analysis

The visual system can be analysed in terms of linear and nonlinear stages (Section 1.2.1). If a nonlinearity is present in a component pathway then that pathway may be analysed using the sandwich method (Section 1.2.2). Several models have emerged that try to explain the temporal contrast sensitivity function using mainly linear but also some nonlinear stages (Section 1.2.3).

1.2.1 Linear and nonlinear systems

Although sinusoidal waveforms are simple waveforms that contain a single frequency component (the fundamental) they were harder to generate prior to the studies done by De Lange (1952) than non-sinusoidal rectangular waveforms, which can be produced by beam interruption and contain higher harmonics of the fundamental frequency. Ives showed, for the first time, that high-frequency flicker thresholds for certain waveforms can be predicted from thresholds for their underlying frequency components (Ives, 1922). Later, De Lange (1952) showed that for many waveforms the temporal contrast sensitivity function (TCSF), or flicker thresholds, could be predicted from the sine-wave thresholds.

Waveforms can be analysed by (and synthesized from) their sinusoidal components. The analysis of input waveforms in terms of their sinusoidal components (i.e. Fourier analysis) is essential in theoretical prediction. Forsyth (1860) concluded that the eye's response can be adequately described by Fourier analysis of the stimulus over a large range of stimulus conditions.

A temporal sine wave ($c(t)$) can be defined by four parameters: frequency (ω), phase (φ), modulation (m) and mean intensity for light stimuli (k) as in Equation 1.1:

$$c(t) = m\sin(\omega t + \varphi) + k \ , \qquad \text{Equation 1.1}$$

where ω is the angular frequency in radians s^{-1}, which can also be specified as frequency in Hz (f) as in Equation 1.2,

$$f = \frac{\omega}{2\pi}. \qquad \text{Equation 1.2}$$

The phase, φ, can be specified either in radians (φ_r) or in degrees (φ_d), as in Equation 1.3,

$$\varphi_d = \frac{360\varphi_r}{2\pi}. \qquad \text{Equation 1.3}$$

The modulation, m, (also known as Raleigh or Michelson contrast for a uniform field) is calculated as a fraction of the mean, according to Equation 1.4,

$$m = \frac{I_{max} - I_{min}}{I_{max} + I_{min}}, \qquad \text{Equation 1.4}$$

where I_{max} and I_{min} are the maximum and minimum values of the sinusoid, respectively.

The simplest model that can be made for flicker TCSF responses is shown in Figure 1.2, where *f(t)* represents a stimulus waveform at the input to some linear stage of the visual system and *h(t)* represents the corresponding waveform at the output of some linear stage of the visual system. A linear stage can only scale (change the amplitude) and delay (change the phase) of a signal that passes through it but it cannot introduce new components (e.g. other frequencies). A stage is defined as *linear* if it has the two mathematical properties: *homogeneity* (where a stimulus *f(t)* scaled in intensity by a factor of α evokes a response α times greater than *h(t)*) and *superposition* (or *additivity*, where the response to the sum of two stimuli, $h(f_1(t) + f_2(t))$, is equal to the sum of the responses to the two individual stimuli, $h(f_1(t)) + h(f_2(t))$. When superposition holds then the output of a given stage from a system, in response to a known input, can be calculated using the transfer function, $G(\omega)$, or its inverse Fourier transform i.e. the impulse response of the given stage.

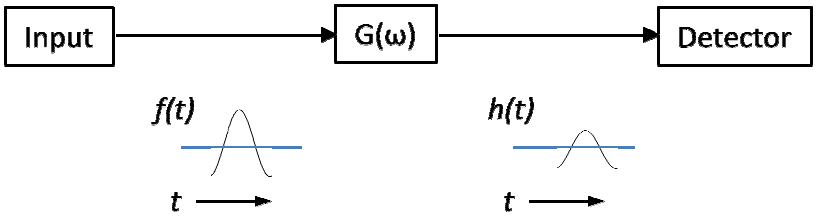

Figure 1.2. Schematic representation of the simplest linear model for flicker sensitivity; *f(t)* is the stimulus waveform, *G(ω)* is the transfer function and *h(t)* is the output waveform.

The transfer function of the linear model in Figure 1.3, which can be derived from the linear integro-differential equation of the system, depends on the absolute amplitude response (|*A*| or modulus of) and the phase response ( ) of the model, Equation 1.5,

. Equation 1.5

Most systems obey the principle of linear superposition over small input ranges that are still sufficiently wide to be useful for analysis, which is why linear models are widely used. Flicker responses in particular have been extensively studied using linear system analysis (e.g. Hess & Snowden, 1992; Kelly, 1969; Kelly, 1971b; Levinson, 1966; Mandler & Makous, 1984; Rashbass, 1976; Tyler & Hamer, 1990; Veringa, 1970). However, no real system obeys linear superposition under all possible conditions.

A temporal signal with a given frequency spectrum passing through a nonlinearity will have its frequency spectrum changed by the nonlinearity so that new frequency components are produced (called distortion products) at harmonics of the original frequencies and at combinations (sums and differences) of the original frequencies (Bedrosian & Rice, 1971). A static nonlinearity, as the one assumed to be subject of this study (Section 1.3), is one whose input-output relation depends on the instantaneous value of the input (*S*), and not on the past history of *S* as it would be the case for a dynamic nonlinearity.

1.2.2 The sandwich model

The sandwich model is a simple model for a sequential nonlinear system that can be described by a linear-nonlinear-linear sequence of stages. Successive linear stages in the same pathway cannot be measured independently unless there is an intervening nonlinearity because they would give an output indistinguishable from a single linear stage. Thus the presence of a nonlinearity can separate two linear stages (i.e. the pre-nonlinearity stage that is relatively early in the visual system and the post-nonlinearity stage that is relatively late in the visual system) and can allow their separate measurement, which may not otherwise be possible.

The sandwich model has been used to analyze the nonlinear interactions between stimuli of two or more sinusoidal frequencies or interactions within white noise for the study of spatial vision (Burton, 1973; MacLeod, Williams & Makous, 1992; Williams, 1985), temporal vision (Burns, Elsner & Kreitz, 1992; MacLeod & He, 1993; Stockman, MacLeod & DePriest, 1991), colour vision (Chang, Burns & Kreitz, 1993; Stockman & MacLeod, 1986; Stockman, MacLeod & Lebrun, 1993) and brightness enhancement (Krauskopf, Wu & Farell, 1996).

The sandwich model will be applied in this study to allow non-invasive dissection of an early, pre-nonlinearity stage from a late, post-nonlinearity stage when an identifiable nonlinearity is present in a visual pathway. The identifiable nonlinear distortion is in the form of a colour change (see Section 1.3.1 for details) at long wavelengths (from red towards yellow) and shorter wavelengths (from green or blue towards desaturated yellow) or brightness change at middle wavelengths (see Section 1.3.2 for details), as shown in Figure 1.3. If the pathway that determines temporal contrast sensitivity is linear then no slow colour

or brightness change would be perceived at the amplitude-modulation frequency (f_{am}, 0.5 Hz in Figure 1.3) and all temporal changes would be perceived at the physical frequencies of the stimulus (i.e., at the carrier frequency, f_c , its lower sideband, $f_c – f_{am}$, and its higher sideband $f_c + f_{am}$, i.e. 10 Hz, 9.5 Hz and 10.5 Hz in Figure 1.3, respectively).

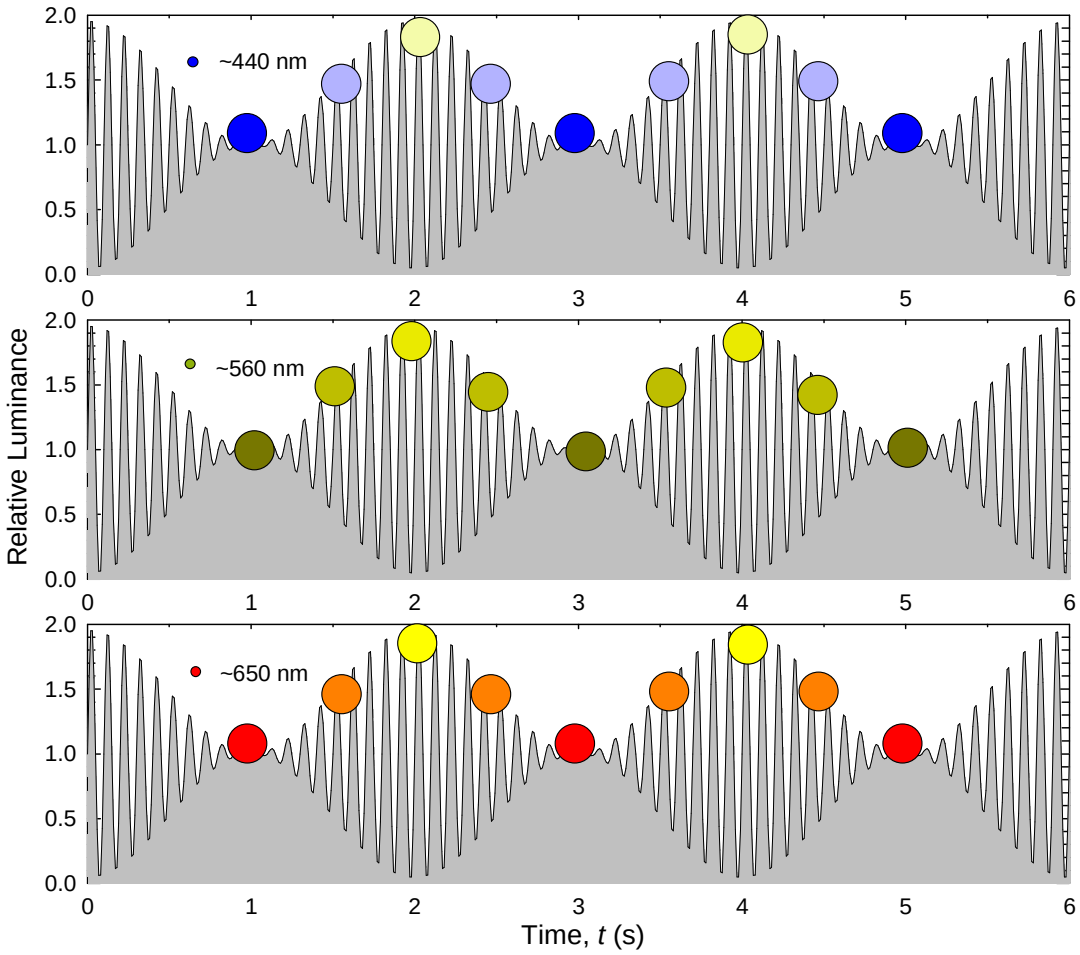

Figure 1.3. Approximate simulated colour changes in appearance around 440 nm for S-cone-isolating stimuli (using an L- and M-cone saturating background) from blue to yellow (top panel) and around 650 nm from red to yellow (bottom panel) as well as brightness changes around 560 nm (middle panel) of 100% amplitude-modulated flickering stimuli (f_c=10, f_{am}=0.5 Hz). The changes in colour and brightness become more apparent as the modulation of the light increases.

The Talbot-Plateau law states that a flickering light at a frequency above the critical flicker fusion frequency (CFF, i.e. at which a flickering light appears steady) should appear indistinguishable from a steady light of the same time-averaged intensity and chromaticity

(Plateau, 1835; Talbot, 1834). Therefore, if the Talbot-Plateau holds, the changes in colour and brightness illustrated in Figure 1.3 should only be apparent at carrier frequencies below the CFF. Considering that the early stages of the visual system can follow flicker at rates substantially above the CFF (Brindley, 1962; Stockman et al., 1993) then the Talbot-Plateau law implies that, at least for flicker above the CFF, the early (pre-nonlinearity) visual stages must be operating in an approximately linear range above CFF. However, at least for the S-cone pathway, nonlinearity has been demonstrated to exist at frequencies above CFF (Stockman & Plummer, 1998).

1.2.3 Temporal contrast sensitivity models

Kelly noted that at high photopic levels, when the flicker sensitivity is plotted on log-log coordinates it has a maximum slope of about -2 at high frequencies (Kelly, 1961c). Later studies modelled the loss of flicker sensitivity at high frequencies as a cascade of leaky integrators (e.g. Sperling & Sondhi, 1968; Watson & Robson, 1981).

A resistor-capacitor (RC) circuit is the commonest example of a leaky integrator. Rather than perfectly integrating a signal over time like causal integrators, many physical devices integrate part of the input signal while leaking the other part in a rate proportional to the amount accumulated (where the constant of proportionality is $1/\tau$). In the RC circuit, the capacitor's voltage would be the integral of the current if it acted as a causal integrator (Equation 1.6) but, generally, a capacitor leaks some electrons and thus acts as a leaky integrator (Equation 1.7). As $\alpha \rightarrow 0$ in Equation 1.7, the leaky integrator tends to act as a causal integrator.

$$y(t) = \int_{-\infty}^{t} x(\tau) d\tau \ , \qquad \text{Equation 1.6}$$

$$y(t) = \int_{0}^{\infty} x(t-\tau) e^{-\alpha\tau} d\tau \ . \qquad \text{Equation 1.7}$$

This leakage of the signal makes the RC circuit act as a low-pass filter (i.e. an exponential filter). If *n* identical RCs are cascaded and their response is plotted on log-log coordinates, then the response of this circuit is flat at low frequencies (below a frequency of $(2\pi\tau)^{-1}$ the amplitude approaches an asymptote of τ^n) and it falls off with an asymptotic slope of *n* at high frequencies (above a frequency of $(2\pi\tau)^{-1}$ the amplitude approaches an asymptote of $(2\pi\omega)^{-n}$). By varying *n* in integer steps, cascades of leaky integrators can be used to describe a low-pass filter with any integer high-frequency slope. A wide range of band-pass filters can also be described by combining a low-pass and a high-pass filter. (In physiology, for instance, the high-pass filter can be described by an inhibitory stage with low-pass filter characteristics.)

Fuortes & Hodgkin (1964) noted that the impulse response of *Limulus* receptors was very similar to the impulse response of a linear filter, which led them to model the receptors' response as an n-stage low-pass filter. Subsequently, similar but more elaborate models were proposed (e.g. Matin, 1968; Sperling & Sondhi, 1968). The predicted amplitude-sensitivity vs. temporal frequency functions by the Sperling & Sondhi (1968) model share a common high-frequency envelope similar to the de Lange functions (De Lange, 1958a; De Lange, 1958b) and consistent with high frequency linearity. The Sperling & Sondhi model incorporates a cascade of four components: nonlinear feedback (2 RC stages), nonlinear delayed feedforward (1 RC stage), linear low-pass filter (6 stages) and detector (obeys constant criterion).

In comparison, Kelly's model of high-frequency temporal sensitivity (and of linearity at high frequencies) is based on a diffusion process (Kelly, 1969; Kelly & Wilson, 1978). Unlike the leaky-integrator model in which the high-frequency data asymptote to fall with a constant slope on a log-log scale, the diffusion-process model can account for high-frequency data the slope of which continuously increases on a log-log plot. Kelly accounts for the low-

frequency characteristics by an inhibitory feedback loop whose parameters depend on the light adaptation level and spatial configuration (Kelly, 1971a; Kelly, 1971b).

Roufs (1974) noted that Kelly's model was not enough to account for the greater low-frequency attenuation of certain pulse and pulse-pair thresholds compared to those for flicker. He proposed that the TCSF is the envelope of two underlying functions: one band-pass and one low-pass. This model supports earlier evidence for "transient" and "sustained" channels (Kulikowski & Tolhurst, 1973).

Kelly (1972) argued that n-stage models, including cascaded RC circuits, could not account for the high frequency linearity in TCSF measurements because the TCSF gradient at high frequencies increased with increasing frequency (i.e. the TCSF plot curved downwards) rather than tending to a constant gradient. However, Watson (1986) showed that this linearity applied over a relatively very small range, if at all, of the TCSF measurements. In addition, he supported the evidence provided by Roufs (1972) that following appropriate horizontal and vertical displacements on log-log coordinates for small targets, the TCSFs overlap, especially at high frequencies, in a manner consistent with n-stage models. Watson's model had three stages: a linear filter, a probability summation stage over time, and asymmetric thresholds for increments and decrements. (Stockman, Langendörfer, Smithson & Sharpe, 2006), who measured flicker sensitivities and flicker delays, found failures of high-frequency linearity at all levels. To explain their data, they invoked an n-stage filter model with sensitivity scaling, which is, in fact, consistent with molecular models of light adaptation in the photoreceptor.

The models based on a cascade of leaky integrators (e.g. Sperling & Sondhi, 1968; Watson & Robson, 1981) assume that there is a single channel that is being modeled. These models also do not incorporate a source of variability; e.g. a stage accounting for the noise in

the channel. In the present study the pre-nonlinearity and post-nonlinearity stages are modeled as a cascade of leaky integrators (Chapter 7) separated by a static nonlinearity.

1.3 The dissection tool

As discussed in the previous section, a distortion product of a nonlinearity, such as a colour change, can be used to derive information about the pre-nonlinearity and post-nonlinearity stages. In this section, two examples of distortion products are given: colour changes (Section 1.3.1) and brightness changes (Section 1.3.2) for temporally-varying or intensity-varying stimuli. The examples given in the two sections are useful because they suggest that nonlinearities might exist both in the chromatic and in the achromatic pathways and consequently they might provide information about the early and the late stages of these two separate pathways. The changes in the temporal contrast sensitivity of these pathways with adaptation will also be considered as well as their possible relationship to the early and late stages within the pathways.

1.3.1 Colour changes

If the spectral composition of a light is kept constant but its intensity is varied then most lights would appear to change colour. This phenomenon, originally investigated by Bezold (von Bezold, 1873) and Brücke (Brücke, 1878), has become more commonly known as the Bezold-Brücke effect and extensively investigated (e.g. Bimler & Paramei, 2005; Jacobs & Wascher, 1967; Nagy, 1980; Pridmore, 1999; Savoie, 1973).

Peirce was probably the first to attempt to explain colour changes with intensity (Peirce, 1877). According to him, the light detecting mechanisms, which were later attributed to the photoreceptors (Walraven, 1961), are subject to a compressive nonlinearity where the response of the most active mechanism is compressed more than the response of the least

active mechanism. The difference in compression between the mechanisms results in a change of the response ratio between mechanisms and therefore a change in the perception of colour.

Purdy measured the hue change with intensity (i.e. the Bezold-Brücke effect) by varying the wavelength of a steady reference field to match the hue of a steady target field that was 10 times brighter (Purdy, 1931). At the higher intensity, wavelengths above about 510 nm tended to appear more yellow. Purdy documented that the invariant hues for the Bezold-Brücke effect, where no hue change is seen with increasing intensity, are around 475 nm, 507 nm and 575 nm. Similar invariant hues were later confirmed by Wildt and Bouman (1968).

Hurvich & JamesonHurvich & Jameson (1957) attempted to explain the changes in appearance observed in the Bezold-Brücke effect in terms of different rates of response increase with increasing intensity between different third stage, colour-opponent mechanisms, where the achromatic mechanism has the highest rate of response increase and the red-green mechanism has the lowest rate. Although the relative rate of response increase from the red-green mechanism through the blue-yellow mechanism and to the achromatic mechanism is similar to the relative increase in contrast sensitivity from the parvocellular neurones through the koniocellular and to the magnocellular neurones (discussed in Section 1.1), the ganglion cells' response at the LGN level cannot account for colour-opponency. In addition, according to Hurvich & JamesonHurvich & Jameson's theory, the unique hues (where the colour-opponent mechanisms are balanced) should not undergo any change in appearance i.e. they should coincide with the invariant hues (Hurvich & Jameson, 1957). However, the wavelengths corresponding to the unique hues (Hurvich & Jameson, 1955) do not coincide exactly with the invariant wavelengths in the Bezold-Brücke effect (Purdy, 1931). For instance, no invariant wavelength has been found to correspond to unique red. In

addition, Hurvich & JamesonHurvich & Jameson do not consider the possible contribution of nonlinearities to the differences between their colour-opponent mechanisms: although each of the colour-opponent mechanisms is linear according to their theory, the interaction between the mechanisms and their combined output can be nonlinear.

Walraven (1961; Walraven, 1962) supported Peirce's theory (Peirce, 1877) and explained the Bezold-Brücke effect as a result of differences in response compression (i.e. compressive nonlinearities) between the photoreceptors, with the most active photoreceptor for a particular wavelength having the most compressed response. For instance, with increasing intensity of a red light the L-cone response would be compressed much more than the M-cone response, so that the cone responses will tend to be similar to wavelengths closer to those where the two cone types have equal sensitivity, near 560 nm. Consequently, colour changes will tend towards yellow at long wavelengths and high intensities.

Flickering lights have been reported to undergo hue changes that are largely similar in appearance to those of the Bezold-Brücke effect (Ball, 1964; Bartley & Nelson, 1960; Bleck & Craig, 1965; Stewart, 1887) as well as desaturation (Ball, 1964; Ball & Bartley, 1966; Bartley & Nelson, 1960; Jameson & Hurvich, 1955). Hue changes evoked by flickering lights have been found to vary with wavelength (Ball, 1964; Nilsson & Nelson, 1971; van der Horst & Muis, 1969), luminance (Nilsson & Nelson, 1971; van der Horst & Muis, 1969; Wildt & Bouman, 1968), temporal frequency (van der Horst & Muis, 1969) and modulation (Stockman, 1993; Stockman & Plummer, 1998).

Generally in the above studies on change in appearance of flickering lights, yellow-green (around 560 nm) and blue-green targets (around 490 nm) are reported to be relatively invariant while red and green undergo considerable hue shift towards yellow, and blue undergoes considerable desaturation and some colour change towards yellow. A few studies

report contradictory results where red targets shift their appearance towards deeper red instead of yellow (Bleck & Craig, 1965), where blue targets shift their appearance towards violet instead of desaturating (Ball, 1964) or where the hue change of flickering lights is substantially different from the hue changes in the Bezold-Brücke effect (Nilsson & Nelson, 1971). Such contradictions can be attributed to colour induction between the flickering target and the matching stimulus as well as due to speckle or segmentation in the appearance of the target into sections undergoing slightly different hue shifts, which affects the results of untrained subjects in particular (Nilsson & Nelson, 1971). Interestingly, changes in colour produced by both changes in intensity and changes in flicker frequency are subject to very similar 'invariant' wavelengths (around 480 nm, 500 nm and 580 nm) where the hue does not change (Ayama, Nakatsue & Kaiser, 1987; Nagy, 1979).

More recent studies of colour change produced by flickering lights have used amplitude-modulated flickering waveforms to measure the colour change of red lights towards yellow (Stockman, 1993) and of blue lights towards pale (desaturated) yellow (Stockman & Plummer, 1998), and analyse it in terms of a new frequency component produced by the underlying nonlinearity. Stockman & Plummer (Stockman & Plummer, 1998) stimulated the S-cone pathway (using an amplitude-modulated flickering 440-nm target superimposed on an intense, steady 620-nm background) and measured the temporal-attenuation characteristics of the pre-nonlinearity and estimated the post-nonlinearity stages in the pathway that produced colour change at peak modulation (from blue to yellow). They concluded that the nonlinearity causing the colour change for S-cone stimuli was a 'hard' saturating nonlinearity (i.e. linear at low modulations and limited by a response ceiling at high modulations) rather than a smooth compressive nonlinearity as suggested by Peirce (1877). However, their results supported earlier theories (Peirce, 1877; Walraven, 1961; Walraven, 1962) that the

nonlinearity was located within the retina prior to the combination of signals from the three cone types and, consequently, that the pre-nonlinearity stage reflected the temporal attenuation of single cones.

Stockman & Plummer's results also revealed that the pre-nonlinearity and post-nonlinearity S-cone pathway stages could be described by a band-pass and low-pass filter, respectively (Stockman & Plummer, 1998). They demonstrated that colour changes due to nonlinearities in the early S-cone pathway can still be perceived above the critical fusion frequency (CFF). In addition, when the S-cone-stimulating flicker was cancelled with an M- and L-cone-stimulating flickering light, a distortion product was still visible in the form of a colour change from blue to yellow, which showed the nonlinearity is early and before the combination of cone signals. Both of these results show a failure of the Talbot-Plateau law for amplitude-modulated S-cone stimuli. This is consistent with the failure of the Talbot-Plateau law and Bloch's law (which states that the threshold is a product of the duration and intensity of stimuli at short duration and low intensity (Bloch, 1985)) demonstrated in an earlier study for flickering stimuli around 10 cycles per second (Ball & Bartley, 1965). The fact that the distortion product was visible at much higher frequencies than the flicker indicated that the nonlinearity is comparatively early in the S-cone pathway and that it is subject to less transmission losses than flicker sensitivity.

The existing research on colour changes, covered in the above paragraphs, suggests that colour changes are produced by an early compressive nonlinearity. However, there is still debate about whether the nonlinearity is smooth (Kelly, 1981; Walraven, van Hout & Leebeek, 1966) or rapidly saturating as shown to be the case for S-cone stimuli (Stockman & Plummer, 1998). Figure 1.4 shows a schematic version of the sandwich model for a compressive nonlinearity hypothesised to underlie colour changes of amplitude-modulated

flickering lights changing in appearance from green or blue to pale yellow and from red to yellow. The top row in Figure 1.4 shows the stage of the visual system, the second row shows one cycle of the temporal signal at the end of each preceding stage, the third row shows the approximate appearance of the 440-nm and 650-nm lights at three points in the signal, and the fourth row shows the frequency components in the signal.

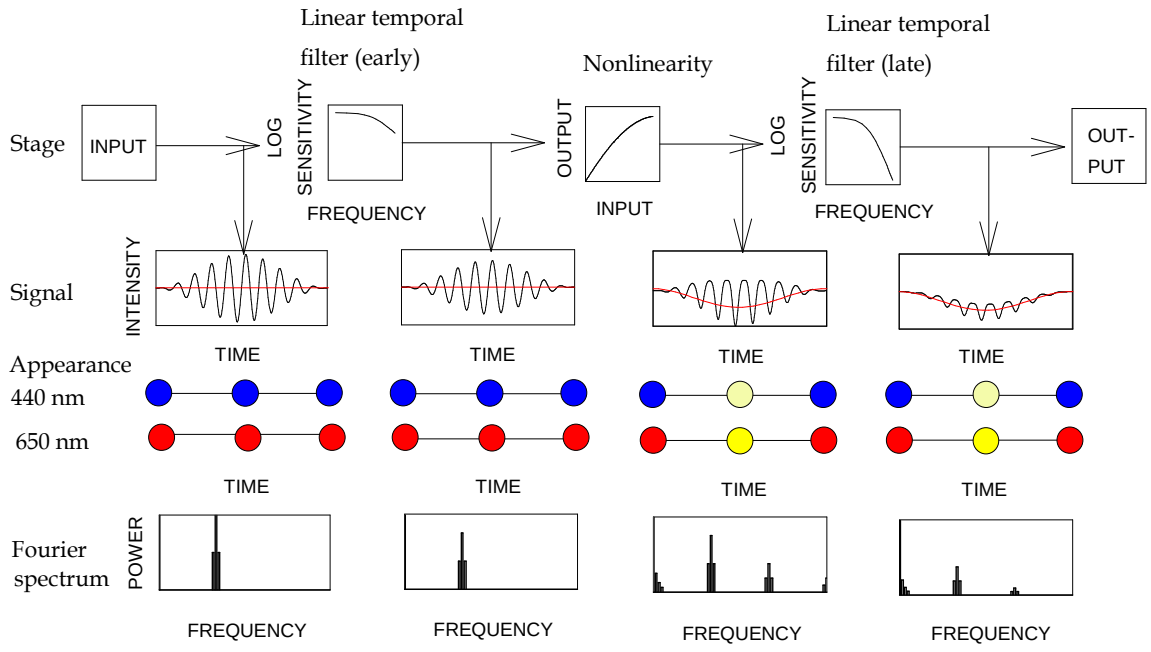

Figure 1.4. An example of a compressive nonlinearity separating two linear filters (top row), the relative signal produced at the end of each stage (second row), the approximate colour changes produced by the nonlinearity for S-cone stimuli with target at 440 nm and background at 620 nm, and for L- and M-cone stimuli with target at 650 nm (coloured circles). The frequency components of each signal are shown in the bottom row. The mean of the carrier frequency is shown as a red line.

1.3.2 Brightness changes

In addition to the studies on colour changes, extensive research has been carried out on sub-fusional brightness changes, where the brightness of a flickering light appears higher (enhanced) than the brightness of a steady light of equal chromaticity and intensity (e.g., Ball & Bartley, 1966; Bartley, 1938; Bartley, 1939; Bartley, 1951b; Bleck & Craig, 1965; Brewster, 1838; Brücke, 1848; Nelson & Bartley, 1961; Nilsson, 1972; van der Horst & Muis, 1969).

Sub-fusional brightness enhancement is also often referred to as the Brücke-Bartley effect. The effect has typically been studied with square waves produced with black and white disks (Brücke, 1848; Brücke, 1878) or with episcotisters where a sector of a disk was removed so that when the disk was rotated in front of a light source it allowed periodic variation in the flashes of light (Bartley, 1938; Bartley, 1939). The Brücke-Bartley effect is related to the Broca-Sulzer effect (Broca & Sulzer, 1902; Broca & Sulzer, 1904). In the Broca-Sulzer effect, a stimulus of duration around 50 ms at high intensities and around 100 ms at low intensities (i.e. duration equivalent to the increment period of a 10 Hz and 5 Hz square wave, respectively) appears brighter than a stimulus of either shorter or longer durations (Figure 1.5).

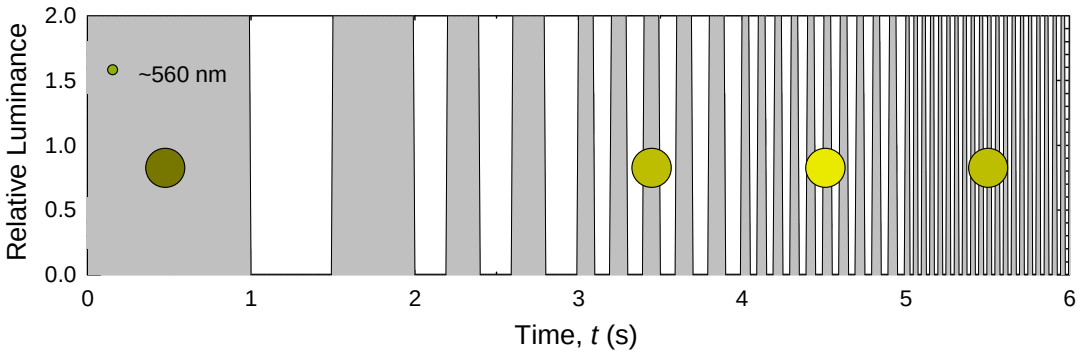

Figure 1.5. Approximate brightness changes for a 560-nm light of various pulse durations (shown in grey), which are shown to change every second (1000 ms, 250 ms, 100 ms, 50 ms and 25 ms).

In the Broca-Sulzer effect, the brightness-enhancement sensitivity curve as a function of flash duration has a similar shape to the firing rate of ganglion cells as a function of time following a flash stimulus, which was consequently thought to be the physiological basis for the brightness enhancement (Le Grand, 1968). However, when the frequency of action potentials is measured for similar stimulus duration times to those for which brightness enhancement is measured, the curve is very different to the brightness enhancement curve, which means that the firing rate of ganglion cells action is not directly related to the Broca-Sulzer effect (Wasserman & Kong, 1974).

Brightness enhancement is dependent on flicker frequency (Bartley & Nelson, 1960; Bartley, Nelson & Ranney, 1961; Nelson & Bartley, 1961; Piéron, 1929), mean radiance (Bartley, 1951a; Bartley, 1951b; van der Horst & Muis, 1969), target size (Rabelo & Grossner, 1961) and waveform (Bartley, 1959; Bartley & Nelson, 1960; Bartley, Paczevitz & Valsi, 1957; Nelson & Bartley, 1961). Using various conditions, the wavelength of peak brightness enhancements has been found to vary from short wavelengths (Broca & Sulzer, 1903), to middle wavelengths around 500 nm (Ball, 1964; Ball & Bartley, 1966) and wavelengths close to those of the unique hues (Wasserman, 1966) . However, in these earlier

studies, tests of spectral variation were limited by the use of broadband filters at wide and irregular intervals.

Subsequent studies (Walters & Harwerth, 1978) have found that sensitivity to brightness enhancement (for 10 Hz and 25 Hz rectangular-wave flickering stimuli) varies with wavelength in approximately the same way as the standard luminosity function. This variation with luminosity is also supported by recent studies that report peak brightness enhancement occurs around 560 nm (Wu, Burns, Reeves & Elsner, 1996).

Wu et al. (1996) used a 560-nm light whose temporal waveform alternated between a cycle of amplitude-modulated flicker and a cycle of cosine with equal frequency to the amplitude-modulation frequency. They changed the amplitude of the cosine until its appearance matched the brightness enhancement of the amplitude-modulated cycle at various modulations. Based on their matching data they modelled the nonlinearity causing brightness enhancement of the amplitude-modulated stimulus as an expansive nonlinearity. They also varied the carrier frequency of the amplitude-modulated stimulus to estimate the pre-nonlinearity temporal filter response. They found that the pre-nonlinearity filter was broad-band and had a broader and shallower slope at high frequencies than the overall flicker sensitivity curve. They related the early temporal filter from their results to the early spatial filter found in earlier work where a retinal nonlinearity fed by single cones leads to brightness enhancement (MacLeod et al., 1992). The nonlinearities succeeding these early temporal and spatial filters may also be related to the nonlinearity found in spatial contrast perception (Benton & Johnston, 1999).

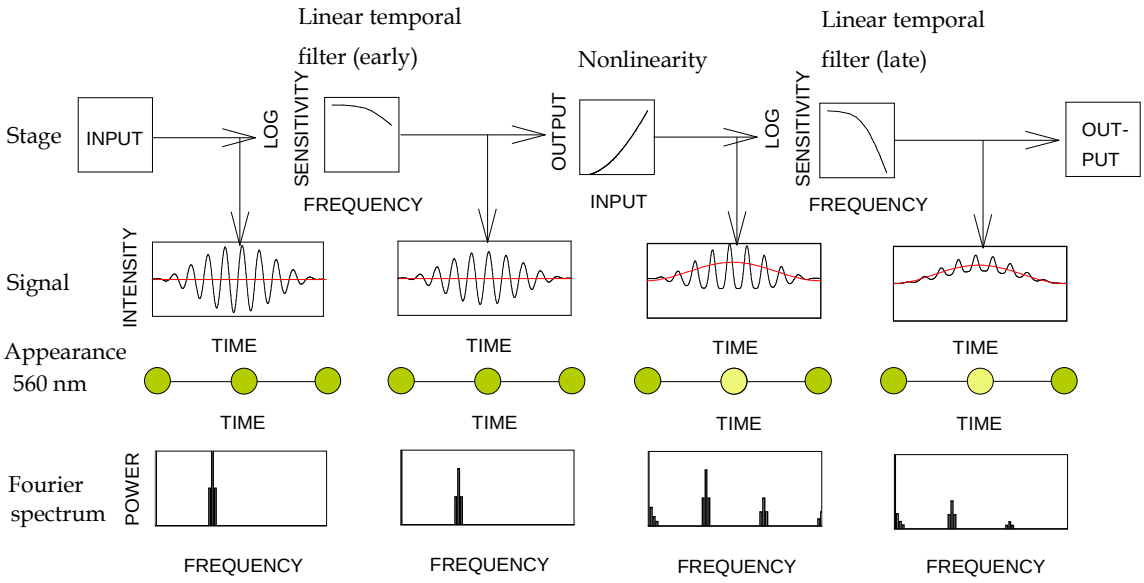

Figure 1.6. An example of an expansive nonlinearity separating two linear filters (top row), the relative signal produced at the end of each stage (second row), the brightness change produced by the nonlinearity for a light around 560 nm (coloured circles), and the frequency components of each signal (bottom row). The mean of the carrier frequency is shown as a red line.

An early nonlinearity, fed by single cones is thought to produce brightness enhancement (Wu et al., 1996) as well as colour changes (see literature in Section 1.3.1). Considering that the brightness pathway receives cone-opponent information in addition to luminance information (Guth & Lodge, 1973; Ikeda, Yaguchi, Yoshimatsu & Ohmi, 1982; Ingling & Tsou, 1977), it is possible that the nonlinearity underlying brightness change is due to nonlinear cone-opponent inputs from single cones that also lead to colour change carried by the chromatic pathways. However, if this is the case then the nonlinearity would be the same for both pathways and it would not be possible to describe the nonlinearity underlying colour changes as compressive (Figure 1.4) and the nonlinearity underlying brightness changes as expansive (Figure 1.6).

The literature reviewed in the above paragraphs suggests that the nonlinearities underlying colour change (Section 1.3.1) and brightness change (Section 1.3.2) of flickering stimuli are compressive and expansive, respectively. Explanations of colour and brightness

change are very different despite certain similarities in the periodicities and intensities at which they occur. For instance, Peirce's (1877) and Walraven's (1961) explanations that the colour change is due to the saturation of the most active cone type do not explain brightness enhancement. In addition, explanations that could underlie brightness enhancement fail to explain colour change, e.g. ON and OFF cell asymmetries (Chander & Chichilnisky, 2001) and response times of ganglion cells (Le Grand, 1968), because they do not explain the changes in the cone ratios consistent with the colour change. However, the nonlinearities producing colour and brightness of flickering light also share similar characteristics (e.g. they are located early in the visual pathway and are likely to receive inputs from single cones) that suggest they may be related.

The relationship between duration and frequency (when duration increases frequency decreases), and the relationship of intensity to absolute amplitude and modulation further suggest that the nonlinearities reported to underlie the Bezold-Brücke effect (colour change of lights with increasing intensity), the colour change of flickering lights, the Brücke-Bartley effect (brightness enhancement of flickering lights) and the Broca-Sulzer effect (brightness enhancement at 50-100 ms increment durations) may be closely related to one another.

Several questions remain unanswered about the visual pathways containing the nonlinearities that produce colour and brightness changes e.g.: what is the relationship between the nonlinearity producing brightness enhancement and the nonlinearity producing colour change; what are the temporal attenuation characteristics of the early and late linear temporal stages of the various L- and M-cone pathways carrying information about brightness and colour changes; how are these early and late stages as well as the intervening nonlinearities affected by changes in light intensity; and what are the relative L- and M-cone

contributions to the nonlinearity. The aims and objectives of the present study are structured to help solve these questions.

1.4 Aims and objectives

The aim of this study is to extend existing non-invasive techniques to dissect the visual system into early (pre-nonlinearity) and late (post-nonlinearity) stages. The focus will be on the temporal contrast sensitivity of pathways that carry brightness (or luminance) and colour information. The L- and M-cones will also be separately stimulated. There are six main objectives in the present study. The first objective is to extend existing methods (Chapter 2) and to develop new experimental procedures (Chapters 3-6) for measuring separate stages of the L- and M-cone pathways carrying temporal contrast sensitivity information. The next objective is to measure and compare the early stage with the overall temporal contrast sensitivity functions for flicker (TCSF, Chapter 3). The third objective is to measure the changes in amplitude produced by the stages after the pre-nonlinearity stage (i.e. to measure the output of the post-nonlinearity stage relative to the output of the pre-nonlinearity stage). The subsequent objective is to measure the change in appearance of a light that is induced by the nonlinearity and to determine the output of the nonlinearity i.e. the input to the post-nonlinearity stage (Chapter 5). The penultimate objective is to estimate the attenuation by the late stage (Chapter 6). The final objective is to model the early and late stages as well as the input-output function of the nonlinearity and to develop existing models of human temporal contrast sensitivity (Chapter 7). Figure 1.7 summarises the stages of the L- and M-cone pathways for temporal contrast sensitivity that will be subject of Chapters 3-6.

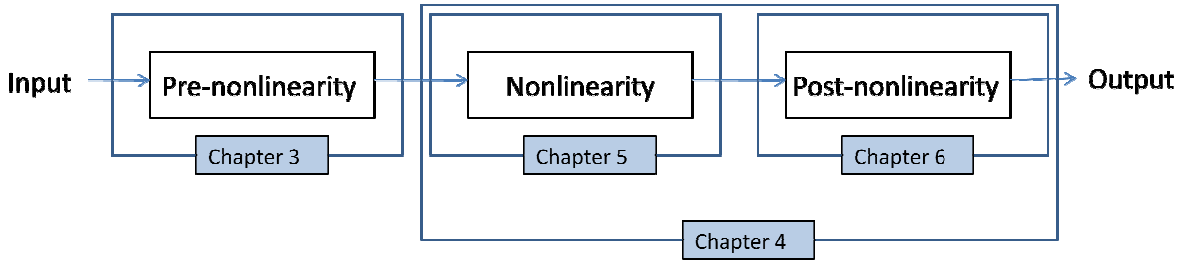

Figure 1.7. Schematic diagram showing the distinction between the attenuation characteristics of: the pre-nonlinearity stage (measured in Chapter 3), the stages after the pre-nonlinearity stage (measured in Chapter 4), the nonlinearity (measured in Chapter 5) and the post-nonlinearity stage (estimated in Chapter 6).

2 Methodology

In previous work, a nonlinearity causing a colour change of amplitude-modulated S-cone stimuli was used to separate the pre- and post-nonlinearity stages of the S-cone pathway (Stockman & Plummer, 1998) using the sandwich model (Section 1.2). The present study extends the method used to separate the pre- and post-nonlinearity stages of the S-cone pathway and provides suitable techniques for measuring the pre- and post-nonlinearity stages of the L- and M-cone brightness pathway (Petrova, 2010; Petrova, Henning & Stockman, 2010b) and colour pathway (Petrova et al., 2010b).

Section 2.1 will provide a description of the basic method that has been applied for the study of the S-cone pathway and that will also be applied in this study of the L- and M-cone pathways. Section 2.2 will describe some of the new procedures that have to be employed to study the L- and M-cone brightness and colour pathways.

2.1 Basic method

The apparatus and the calibration procedures were the same for all experiments of the present study.

2.1.1 Apparatus

A five-channel Maxwellian-view optical system was used (for a detailed review of such systems, see Westheimer, 1966). The infrared (IR) and ultraviolet (UV) radiation from the light source were minimised by glass absorbing filters (Schott). Interference filters (Ealing and Oriel) with 10 nm bandwidth were used to select the wavelengths of the visual stimuli. The interference filters were positioned perpendicular to the incident light in parts of the collimated pathway (Figure 2.1, in which L1 and L3 are collimating lenses, and L2 and L4

are focusing lenses). The radiances of the channels were attenuated as necessary with a 3 $\log_{10}$ variable neutral density wedge (VNDW) and neutral density filters (Inconel). Undesirable back reflections from the neutral density filters were minimised by giving them a ±30° tilt relative to the vertical plane. All the filters were calibrated within the apparatus.

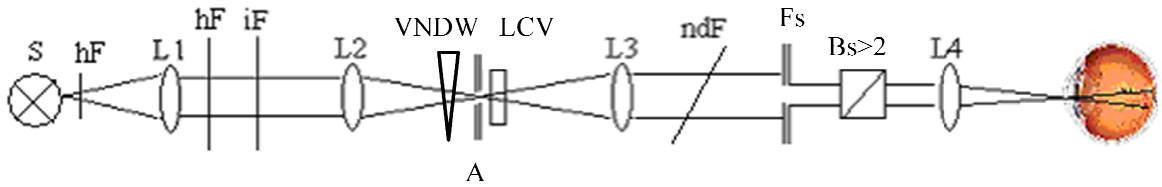

Figure 2.1. A simplified diagram of a single Maxwellian channel. S, light source; hF, IR and UV filter; L1-4 represents the lens with the corresponding number; iF, interference filter; VNDW, 3 $\log_{10}$ unit variable neutral density wedge; A, aperture stop; LCV, liquid-crystal light valve; ndF is the neutral density filter(s) at 30° tilt relative to the vertical plane; Fs is the field stop controlling the size of the stimulus; Bs>2, more than two sequential beam splitters transmit a fraction of the light towards L4, which focuses it within the pupil.

The Maxwellian system had five channels like the one illustrated in Figure 2.1, one of which was used to display a background light. The channel used for the background was like that illustrated in Figure 2.1 but had neither a VNDW nor a liquid crystal light valve (LCV, Displaytech). The LCV had a fast shutter speed (with a rise and fall time less than 50 μs) and was used to provide a pulse-width-modulated output with a pulse frequency of a 400 Hz (the higher frequency components of which were too high to significantly stimulate the human visual system). The pulse-width-modulation allowed the visual stimulus to be modulated between 0% and 92% around its time-averaged mean light level (as defined by the Michelson luminance contrast, Equation 1.4). Modulation over 92% could not be achieved due to the rise and fall times of the shutter.

The light source was a high-pressure 900 W Xenon arc lamp (Osram XBO) that had high luminous efficacy over the visible spectrum and, therefore, allowed the testing of a wide range of luminance levels. An additional advantage of the Maxwellian-view system was that

the stimulus was not affected by the size of the subjects' pupils. The image of the source was focused within the plane of the pupil and an image of the stimulus was focused on the retina. The image of the source at the plane of the pupil was always less (i.e. 1.5 mm) than the minimal pupil size (i.e. 2 mm) so retinal illumination was not affected by the pupil's size. The pupil position and the head of subjects were stabilized by a dental impression stably mounted on a mechanical x, y and z positioner. The positioner and the rest of the apparatus were mounted on a stable steel optical table.

2.1.2 Waveform

An amplitude-modulated signal ($A_m(t)$) was generated according to Equation 2.1, which was the primary temporal waveform of the visual stimuli in later chapters,

$$A_m(t) = 1 + m\sin(2\pi f_c t)\,[0.5 + 0.5\cos(2\pi f_{am} t)] \quad , \qquad \text{Equation 2.1}$$

where f_c is the carrier frequency, f_{am} is the amplitude-modulation frequency and m is the modulation of the carrier frequency (Figure 2.2). The average light intensity over time remained constant during each experiment as the amplitude was modulated around a constant mean.

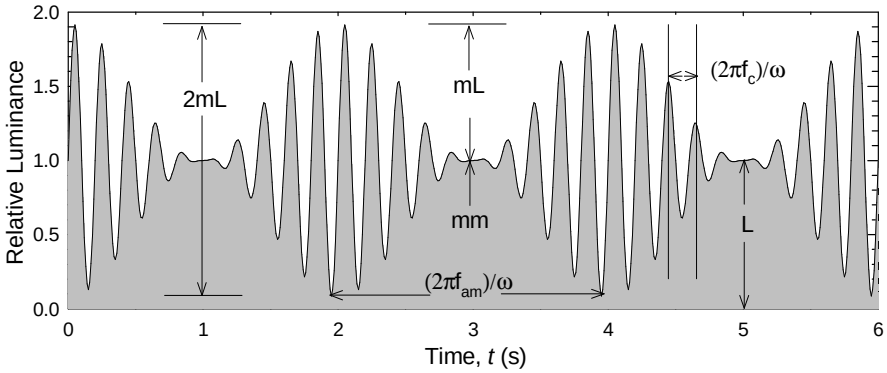

Figure 2.2. The amplitude-modulated stimulus waveform that is most commonly referred to in this project, where f_{am} is the amplitude-modulation frequency (0.5 Hz); f_c is the carrier frequency (5 Hz); ω is the angular frequency; mL is the amplitude and L is the time-averaged luminance or adaptation level, m is the mL:L ratio or the maximum modulation (92%); and mm is the minimum modulation, which was always fixed to 0%.

For the waveform in Equation 2.1, the ratio of the amplitudes of the frequency components, i.e. f_c and the two sidebands $f_c - f_{am}$ and $f_c + f_{am}$, remained constant. The amplitude of the sidebands was equal to half the amplitude of the carrier frequency (Equation 2.2),

$$A_m(t) = 1 + m\begin{Bmatrix} 0.25\sin\left[2\pi\left(f_c - f_{am}\right)t\right] + \\ 0.5\sin\left(2\pi f_c t\right) + 0.25\sin\left[2\pi\left(f_c + f_{am}\right)t\right] \end{Bmatrix}. \qquad \text{Equation 2.2}$$

The main advantage of the amplitude-modulated sinusoidal waveform is that, when it passes through a nonlinearity, a frequency component will be produced at f_{am} (and to a lesser extend at harmonics of f_{am}, f_c, and their sums and differences), which can be measured to infer the frequency characteristics for the pre- and post-nonlinearity stage. The pre- and post-nonlinearity stages are conceived as filters that delay and scale the amplitude of the input signal's frequency components according to their attenuation characteristics.

The pre-nonlinearity stage affects the input to the nonlinearity, and thus the output of the nonlinearity and the amplitudes of distortion products produced by the nonlinearity, while the post-nonlinearity stage affects the output of the nonlinearity (including the distortion products) and the output signal. Therefore, by varying f_c and measuring the threshold for detecting a distortion product at f_{am} (e.g. a colour or brightness change at f_{am}) it is possible to measure the temporal characteristics of the pre-nonlinearity stage. While f_c is varied, f_{am} is kept fixed to control for changes in temporal processing after the nonlinearity. Conversely, by varying f_{am} and measuring the sensitivity to a distortion product at f_{am}, it is possible to estimate the temporal characteristics of the post-nonlinearity stage because a frequency component at f_{am} will be generated at the nonlinearity and only stages after the nonlinearity will attenuate its amplitude. While f_{am} is varied, f_c is kept constant to control for changes in

temporal processing prior to the nonlinearity. The temporal characteristics with respect to the input depend on the properties of the nonlinearity.

When f_c is varied to measure the pre-nonlinearity stage characteristics, f_{am} was fixed at 0.5 Hz. This frequency was chosen because preliminary measurements showed that when f_{am} >0.5 Hz then colour change or brightness change decreases and when and f_{am} <0.5 Hz the experiments were prolonged unnecessarily.

When f_{am} was varied to measure the stages after the pre-nonlinearity stage, f_c was fixed at 30 Hz. The 30 Hz carrier was chosen because it provided a balance between a relatively high sensitivity to the colour or brightness change compared with the flicker itself and a sufficient difference between f_{am} and f_c.

2.1.3 Calibration

Two main types of calibration procedures were carried out: calibration of the Maxwellian system for linearity and daily calibration of the visual stimuli. All instruments were separately calibrated.

The Maxwellian system was calibrated for linearity to ensure that the nonlinearity that was measured was generated by the human visual system and not by the apparatus. The frequency components of the amplitude-modulated waveform were measured using temporal frequency analysers, a photometer (United Detector Technology) at the plane of the pupil with a linear amplifier, and an oscilloscope. The measurements showed that frequency components other than (f_c–f_{am}), f_c andf_c+f_{am}, including any frequencies at the sums and differences of these three frequencies, were at least as low as the mean noise level of the equipment (about 60 dB lower than the carrier frequency), and that consequently any

frequency component near f_{am} must be produced by nonlinearity outside of the apparatus (i.e. in the visual system).

The radiant fluxes of test and background fields were measured daily at the plane of the subject's pupil using a calibrated UDT S370 optometer (Graseby). The mean time-averaged radiance levels of flickering lights of all experimental runs (see section 2.6) are given below. Maximal differences between calibrations of separate experimental runs were <0.05 $\log_{10}$ quanta s^{-1} deg^{-2} over the three years of the study.

This study extends the existing method for measuring changes in appearance of amplitude-modulated lights with a Maxwellian-view system (Stockman & Plummer, 1998) by using up to five channels of the Maxwellian system, which allows more precise measurements of the changes in appearance.

2.2 Extended methodology

The main procedures that were employed to measure the pre- and post-nonlinearity stages of the L- and M-cone pathways carrying temporal contrast sensitivity information are briefly described (Section 2.2.2) after an outline of the data collection procedure that was common to all experiments in this study (Section 2.2.1).

2.2.1 Subjects and data collection

All experiments were carried out on at least two psychophysically experienced subjects (DP, female, aged 21-24; and BH, male, aged 67-70 during the three-year study). Participants had superior (DP) or average (BH) colour discrimination, as determined by the Farnsworth-Munsell 100 Hue Test (Appendix Figure 9.1), and normal (DP) or corrected to normal (BH) visual acuity. Subjects used their right eye in the experiments.

Subjects were experienced and well-trained in using the apparatus and making the various measurements. Two main measurements were made: i) subjects' thresholds to flicker at f_c, and ii) subjects' thresholds to changes in appearance at f_{am} (seen as a change in colour, brightness or saturation), which typically was maximal at the maximum modulation of the amplitude-modulated flickering stimulus. These changes in appearance were forms of distortion produced by the visual nonlinearity. Since the sensitivity to flicker was generally higher than that to distortion, the slow change at f_{am} also appeared to flicker at f_c. The flicker at f_c waxed and waned at at f_{am} depending on whether the modulation was increasing to maximum or decreasing to minimum, respectively. When subjects were setting the thresholds for flicker at f_c they were instructed to ignore the changes in appearance at f_{am} and when they were setting the thresholds for changes in appearance at f_{am} they were instructed to ignore the flicker at f_c. Subjects were able to clearly distinguish and set consistent thresholds, as demonstrated by the relatively small standard errors in their results (Chapters 4-7). Readings were recorded at various frequencies of f_c and f_{am}. The detailed methods and procedures for each experiment are described in the relevant chapters that follow.

Subjects responded to the visual stimulus using an eight button keypad. The method of adjustment was used to measure visual response for the experiments. Forced choice could not be used for measuring sensitivity to changes in appearance at f_{am} because the change in appearance was always accompanied by visible flicker. Errors of habituation (when subjects continue to report seeing the stimulus even below their threshold) and anticipation (when subjects prematurely report seeing the stimulus) were minimized by practice trials and demonstrations, clear instructions, and independent trials (repetitions) of experiments on separate days.

Audio signals and a voice synthesizer provided feedback after each button press. A computer-generated audio signal with frequency equal to f_{am} indicated the peak amplitude-modulation. The audio signal was particularly useful for the phase measurements in Chapter 5. The signal did not affect the mean or standard error of the measurements.

The visual stimulus focused in the plane of the pupil was the only visible light source for the observers in an otherwise dark room. The subjects adapted to the test light for a minimum of two minutes prior to making the first threshold setting in an experimental run. For each experimental condition within an experimental run, three consecutive threshold settings were made. Between the successive settings, subjects randomly adjusted the stimulus' modulation before finding the threshold level again.

Each experiment was repeated three times (or more where so stated) on separate days. The mean of the three settings for each trial were recorded and their overall mean was plotted below.

The error intervals around the means on the graphs in Chapters 4-7 show $\pm$ 1 standard error of the mean (SE). The SE gives the standard deviation of a sample mean estimate of the population mean. The SE is calculated as the sample standard deviation divided by the square root of the sample size (where the sample size is equal to the number of independent experimental runs for each of which the results of the three settings are averaged).

2.2.2 Stimuli and procedures

The visual stimulus in most experiments was a circular target of 4° diameter, which stimulated the fovea and the central 4° of the parafovea. The following paragraphs summarise two of the main new procedures that have been developed in this study and that are explained in more detail in later chapters.

To estimate the properties of the nonlinearity, which needs to be known to estimate the post-nonlinearity function, the distortion in the form of change in appearance at f_{am} needed to be measured. This was measured by matching the colour, brightness and saturation change of an amplitude-modulated flickering target with a sinusoidally-flickering light that had the same frequency as target's f_{am} (Chapter 5).

To compare the pre-nonlinearity, nonlinearity and post-nonlinearity stages in the L-cone pathway with those in the M-cone pathway, the silent cone-substitution technique was extended for use with amplitude-modulated flickering stimuli (Chapters 3-7).

3 The pre-nonlinearity stage

The methodology employed in this study (Chapter 2), allows the temporal characteristics of the pre-nonlinearity stage to be measured in the L- and M-cone pathways carrying temporal contrast sensitivity information that contain a nonlinearity causing colour, brightness and/or saturation change in flickering lights.

Previous studies (see Section 1.3 for details) have estimated the pre-nonlinearity temporal characteristics for L- and M-cones detecting brightness change information using a 560-nm light (Wu et al., 1996) and colour change information using a 650-nm light (Stockman, 1993) as well as measuring the pre-nonlinearity temporal characteristics for the S-cone pathway carrying colour change information (Stockman & Plummer, 1998). These studies found that the pre-nonlinearity stage was band-pass, with a pronounced peak around 16 Hz for most subjects detecting brightness change and a shallow peak around 5 Hz for colour change produced by S-cone stimuli. However, the temporal characteristics of the pre-nonlinearity stage of the L- and M-cone pathways carrying colour change information at long wavelengths and their comparison to those of the L- and M-cone pathways carrying brightness change information are still unknown.

The main aim of this chapter is to provide measures of the temporal characteristics of the pre-nonlinearity stages in the L- and M-cone pathways and to compare them to the temporal contrast sensitivity function (TCSF) for the detection of either colour changes (Sections 3.1, 3.3, 3.4 and 3.5) or brightness changes (Sections 3.3 and 3.4). In addition, the change in appearance at f_{am} will be measured for stimuli that isolate either the L-cone or the M-cone responses (Section 3.5).

The inset curves in the Figures of this Chapter show one cycle of the temporal waveform of the visual stimulus with carrier frequency, f_c, equal to 10 Hz and amplitude-modulation frequency, f_{am}, equal to either 0.5 Hz or 0 Hz. Results for subjects DP and BH are presented in the left and right columns of graphs, respectively, in each Figure. The numbers in the legend of the Figures show the time-averaged radiance of the target in $\log_{10}$ quanta s^{-1} deg^{-2}.

3.1 Initial work on colour changes

Stockman (1993) reported that a 650-nm amplitude-modulated flickering target (with diameter 4°, radiance around 10.33 $\log_{10}$ quanta s^{-1} deg^{-2}, and f_{am}=0.5 Hz) appeared to change colour from red to yellow at peak modulation. He used a similar apparatus and basic methods to those described in Section 2.1.

The purpose of the initial experiments was to compare the sensitivity to the colour change as a function of carrier frequency with the conventional TCSF. The gradient of the frequency attenuation curve for a temporal filter can be related to the number of component stages: the greater the gradient, the greater the number of component stages (for more details see Section 1.2.3). Therefore, if the gradient of the sensitivity curve to colour change is shallower than the gradient for the TCSF (i.e. the sensitivity curve to flicker, which reflects the total attenuation by all the component stages in the visual pathway) then it would indicate that the pre-nonlinearity filter is located relatively early within the visual pathway.

3.1.1 Procedures

A flickering target of 4° diameter, 650 nm and 10.33 $\log_{10}$ quanta s^{-1} deg^{-2} radiance was presented. Subjects were asked to carry out three sets of measurements: i) to set the minimum modulation at which they could just detect the flicker of a continuously-presented sinusoidally-flickering target ($0.25 \leq f_c \leq 60$ Hz and f_{am}=0 Hz); ii) to set the minimum

modulation at which they could just detect the flicker for the amplitude-modulated light at varying f_c ($5 \leq f_c \leq 60$ Hz and f_{am}=0.5 Hz); and iii) to set the minimum modulation at which they could just detect a colour change for the amplitude-modulated light at varying f_c ($5 \leq f_c \leq 60$ Hz and f_{am}=0.5 Hz). Settings ii) and iii) were interleaved, while setting i) was measured separately. Three settings were made for each condition within an experimental run and three experimental runs were carried out as described in Section 2.2.1.

When amplitude-modulated stimuli were used, subjects adjusted the modulation of the carrier frequency and sidebands together so that the ratio of the carrier's amplitude to the sidebands' amplitude remained constant at 1 to 0.5, respectively.

The modulation sensitivity to amplitude-modulated flicker and to the colour change at f_{am} could not be reliably measured at carrier frequencies below about 5 Hz. This is thought to be because the frequency components of the amplitude-modulated flicker were too close to the amplitude-modulation frequency.

3.1.2 Results

The amplitude-modulated flicker appeared as bursts of flicker at f_{am}. The change in appearance at f_{am} was reported by subjects to appear as a slow colour change that flickered at f_c. The colour change appeared as a change from red to yellow and it was most apparent (salient) near the maximum modulation 92%. At lower modulations, where the colour change was still visible but less salient, it was from red to orange. In addition, subjects reported that the saliency of the colour change increased during the first fifteen seconds of adaptation to the target (regardless of whether the target was steady or flickering during this adaptation period).

Subjects found it difficult to make reliable threshold settings for colour-change and for amplitude-modulated flicker when f_c<5 Hz (which is why the minimum f_c in tasks ii and iii in Section 3.1.1 was limited to 5 Hz). For instance, when f_c<5 Hz, the subject's variation in amplitude-modulated flicker and colour-change settings increased and they found it more difficult to distinguish chromatic flicker at the low f_c from the chromatic change at f_{am}. In addition, for each burst of flicker at f_{am} there were fewer cycles of f_c when f_c<5 Hz, which may have led to a change in criteria and further increased the difficulty of making threshold settings at f_c.

Figure 3.1 shows the $\log_{10}$ modulation sensitivities (i.e. the $\log_{10}$ of the reciprocal of the threshold modulations) for sinusoidal flicker (half-black, grey-black symbols), for amplitude-modulated flicker (blue symbols) and for colour change at f_{am} (orange symbols), as functions of the logarithm of carrier frequency. Only sinusoidal-flicker thresholds at f≥5 Hz are plotted in Figure 3.1 so that they can be compared with the amplitude-moduladated flicker and colour-change thresholds, which are also at f_c≥5 Hz. The sinusoidal-flicker thresholds at f<5 Hz are plotted in Figure 3.10 where they are compared with other thresholds at those frequencies.

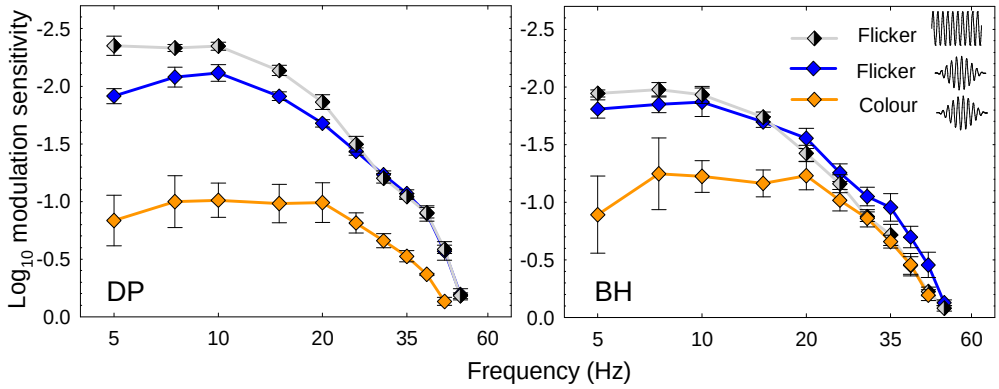

Figure 3.1. Mean ± 1 SE $\log_{10}$ modulation sensitivities for sinusoidal flicker (TCSF, half-black, grey-black symbols), for amplitude-modulated flicker (blue symbols) and for colour change at f_{am} (orange symbols) as a

function of f_c for a 650-nm target at 10.33 $\log_{10}$ quanta s^{-1} deg^{-2}. The inset graph in the top right corner shows one cycle of the temporal waveform used to measure each of the sensitivity curves (at f_c=10 Hz for example and f_{am}=0.5 Hz or f_{am}=0 Hz). The left and right graphs show the data for subject DP and BH, respectively.

The overlapping error bars suggest that there was no significant difference between the curve shapes for sensitivity to sinusoidal and amplitude-modulated flicker at carrier frequencies above 20 Hz. The differences between the absolute sensitivities to sinusoidal flicker and amplitude-modulated flicker above 20 Hz can be related to the two-year difference between the two sets of measurements. At frequencies below 20 Hz, the slope of the sensitivity curve for amplitude-modulated flicker was shallower relative to that for sinusoidal flicker. This relative decrease in sensitivity is consistent with the difficulty in measuring thresholds to amplitude-modulated flicker (and colour change) when f_c<5 Hz and it may also be explained by the decrease in the number of cycles of the carrier frequency per cycle of the amplitude-modulation frequency.

The gradient of the fall-off in sensitivity for colour change was shallower than that for the flicker sensitivity (TCSF) curve. This result was consistent across observers. For DP the result was more apparent than for BH at frequencies above 20 Hz and for both subjects the results were similar below 20 Hz. Below about 10 Hz and above about 25 Hz the gradients of the colour-sensitivity and the flicker sensitivity curves tended to become parallel.

3.1.3 Conclusions

The shallower fall-off in the sensitivity for detecting the colour change at f_{am} compared to the sensitivity for detecting flicker suggests that less attenuation occurs in the visual pathway that determines the sensitivity to colour change than in the visual pathway that determines the sensitivity to flicker. This is consistent with the sandwich model used in the present study. The attenuation that affects the colour-change sensitivity should only reflect that of the pre-

nonlinearity stage whereas the attenuation that affects flicker sensitivity should reflect both the pre-nonlinearity and the post-nonlinearity stages.

3.2 Spectral variation

A range of spectral lights were tested in order to determine the most appropriate wavelengths for investigating the brightness-enhancement and to compare the efficacy of the 650-nm light used in Section 3.1 with other wavelengths in producing a colour change.

Earlier work has been done on investigating the changes in appearance (in hue, brightness and saturation) of flickering lights (see Section 1.3 for review). In general, yellow and blue-green lights are relatively invariant in hue (i.e. a flickering light will appear the same hue as a steady light of the same time-averaged luminance and spectral composition) while red and green lights undergo considerable hue shift towards yellow, and blue undergoes considerable desaturation. The purpose behind the experiments in this subsection was to determine the most suitable wavelengths for investigating changes in brightness and in colour in the L- and M-cone pathways.

3.2.1 Procedures

The target wavelength was varied between 461 nm and 650 nm in 10-20 nm steps. In total, 16 monochromatic targets were calibrated in photopic luminance to be 1330 ph Td, which is equivalent to the photopic luminance of the initial target conditions in Section 3.1.1 (i.e., a 650-nm target of 10.33 $\log_{10}$ quanta s^{-1} deg^{-2}).

The target was amplitude-modulated around the 1329.86 ph Td mean luminance with f_{am} and f_c fixed at 0.5 Hz and 30 Hz, respectively. The frequencies, f_{am}=0.5 Hz and f_c=30 Hz, were chosen because for those frequencies the sidebands in the waveform's frequency

spectrum were very close to the carrier frequency, which means that any difference in sensitivity between the three frequency components of the waveform (29.5 Hz, 30 Hz and 30.5 Hz) would be very small (Section 2.2).

The target's size and position was the same as in Section 3.1.1. The subjects' tasks were to make two sets of measurements: i) to set the modulation threshold at which the amplitude-modulated flicker was just visible; and ii) to set the modulation threshold at which the slow change in appearance at f_{am} (hue, brightness or saturation change) was just visible (as measurements ii and iii in Section 3.1.1). The settings for flicker and appearance change at f_{am} were interleaved as described in Section 3.1.1. The subjects were also asked to compare the appearance of the target at zero modulation with that at maximum modulation (which was indicated by an audio signal) and to report the change in appearance (i.e. the hue, the saturation and the brightness).

A separate experiment was carried out in which the 16 monochromatic targets were all calibrated to be equal radiance at 10.33 $\log_{10}$ quanta s^{-1} deg^{-2} (which is equivalent to the radiance of the initial target conditions in Section 3.1.1) instead of being equated for luminance.

3.2.2 Data and analysis

Figure 3.2 illustrates the sensitivities to flicker and appearance-change at f_{am} for subjects DP and BH as a function of stimulus wavelength for luminances of 1329.86 ph Td. The coloured bars immediately above the x-axis indicate the approximate appearance of the target that was reported by subjects at peak modulation (92%) for each wavelength. The colour of the circles indicates the approximate appearance of the target when steady. The reported appearances are also listed in Table 3.1.

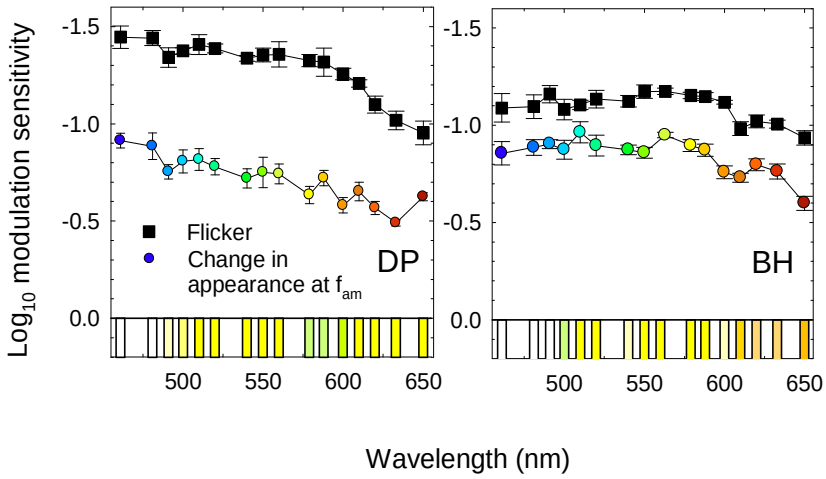

Figure 3.2. Mean ± 1 SE $\log_{10}$ modulation sensitivities to flicker (black squares) and appearance-change at f_{am} (circles) as a functions of wavelength. The monochromatic visual stimuli were calibrated for equal luminance at 1329.86 ph Td. The colour of the circles and the colour of the bars above the x-axis indicate the approximate appearance at 0% and 92% target modulation, respectively.

The results in Figure 3.2 and Table 3.1 indicate that all wavelengths undergo a slow change in appearance at f_{am} (i.e. colour change, brightness change or desaturation).

At equal luminance across wavelengths, the flicker sensitivity should remain approximately constant with wavelength (assuming that flicker sensitivity is limited by the luminance channel). However, a downward trend can be seen above 588 nm, which is particularly apparent for subject DP (Figure 3.2). This suggests that the CIE 1924 luminous efficiency function, which was used to equate the wavelengths for luminance, underestimates the luminous efficiency at long wavelengths.

For both subjects, the sensitivity curves for appearance change at f_{am} approximately parallel the trend of the sensitivity curves for flicker at f_c, apart from slight convergence towards 650 nm in the data of subject DP.

Wavelength	**461**	**481**	**491**	**500**	**510**	**520**	**540**	**550**
Radiance (log_{10} quanta s^{-1} deg^{-2})	**10.41**	**10.07**	**9.90**	**9.74**	**9.55**	**9.41**	**9.6**	**9.29**
DP	White	White	White/ yellow	Pale yellow	Yellow	Yellow	Yellow	Yellow
BH	White	White	White	Pale green/ white	Yellow	Yellow	Yellow/ white	Yellow
Wavelength	**560**	**579**	**588**	**600**	**610**	**620**	**633**	**650**
Radiance (log_{10} quanta s^{-1} deg^{-2})	**9.30**	**9.36**	**9.42**	**9.52**	**9.63**	**9.76**	**9.98**	**10.33**
DP	Brighter/ yellow-green	White/ green/ yellow	White/ green/ yellow	Green/ yellow	Yellow	Yellow	Yellow	Yellow
BH	Brighter/ yellow-green	Yellow	Yellow	Yellow/ white	Yellow/ orange	Orange/ white	Orange/ white	Orange

Table 3.1. The reported appearance at peak modulation (92%) of an amplitude-modulated flickering target of various wavelengths but constant luminance (1329.86 ph Td).

The difference between the sensitivity to flicker and the sensitivity to appearance change at f_{am} was calculated by subtracting the mean of the three settings in each experimental run for the appearance change at f_{am} from the mean of the three settings in each experimental run for the flicker and then plotting the mean and SE for the three values, one for each experimental run (Figure 3.3).

The difference between the sensitivities for flicker and for appearance-change at f_{am} is approximately constant for both subjects (Figure 3.3) as shown by the linear regression curve-fit (black line), which is not significantly different from the horizontal (red dashed line) when considering the 95% confidence band (blue lines). This constancy confirms that at equal luminance the sensitivities to flicker and appearance change at f_{am} are approximately parallel across wavelengths, except for the significant decrease at 650 nm in the data of subject DP. Also, this constancy suggests that the sensitivity to appearance-change at f_{am}, similarly to flicker, is dependent on luminance.

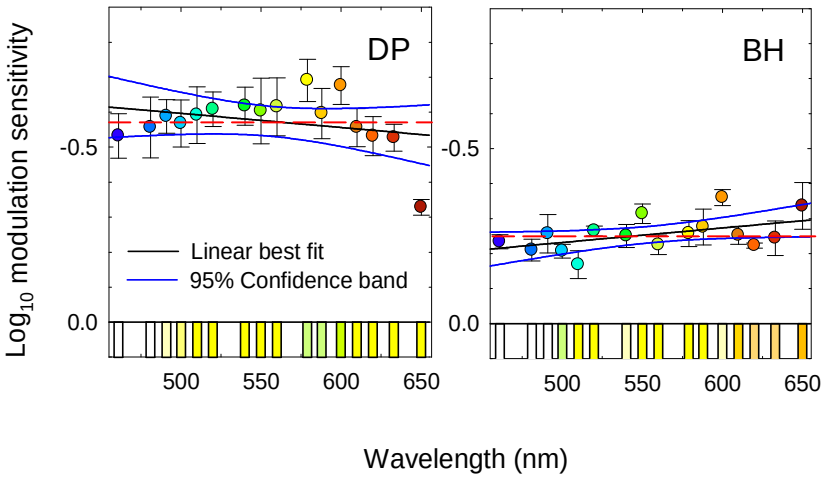

Figure 3.3. Mean ± 1 SE difference in $\log_{10}$ modulation units between the sensitivity to flicker and the sensitivity to change in appearance at f_{am} as a function of wavelength (circles). The black and blue lines show the linear best fit and the 95% confidence band of the fit, respectively. The dashed red line indicates the horizontal. The targets were calibrated for equal luminance at 1329.86 ph Td.

The flicker and distortion sensitivity curves for wavelengths between 461 nm and 650 nm that are matched in radiance are approximately parallel for both subjects except where they converge at short wavelengths for subject BH (Figure 3.4). The convergence for BH is consistent with the subject's reduced flicker sensitivities at short wavelengths, especially below 510 nm. BH has an overall reduced flicker sensitivity compared to DP but this decrease is more apparent at short wavelengths (<510 nm) where the difference between the subjects is ~0.5 log units greater than at long wavelengths (>600 nm) where the difference is only ~0.2 log units. The drop in flicker sensitivity at shorter wavelengths equated for radiance is considerably steeper for BH than the gradual decline at equal luminance conditions (Figure 3.2).

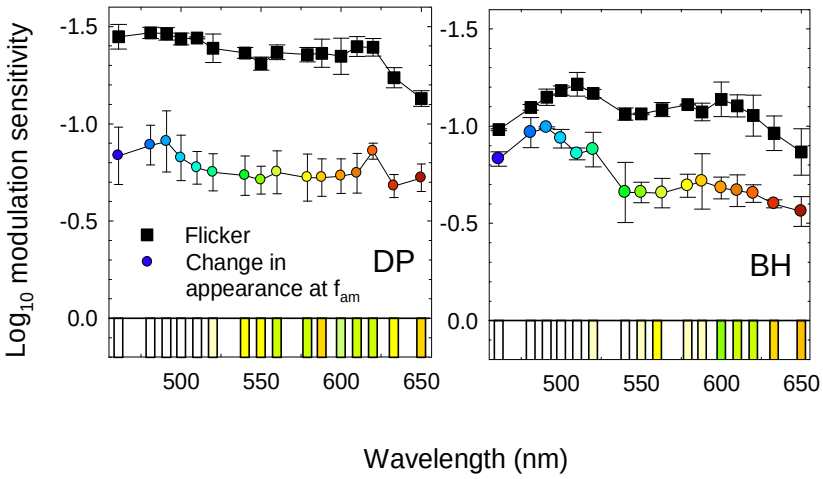

Figure 3.4. Mean ± 1 SE $\log_{10}$ modulation sensitivities to flicker (black squares) and change-in-appearance-at-f_{am} (circles) at equal radiance (10.33 $\log_{10}$ quanta s^{-1} deg^{-2}). The colour of the circles and the colour of the bars above the x-axis indicate the approximate appearance at 0% and 92% target modulation, respectively.

Wavelength	**461**	**481**	**491**	**500**	**510**	**520**	**540**	**550**
DP	White	White	White	White	White	White/ yellow	Yellow	Yellow
BH	White	White	White	White	White	Yellow/ white	White	Yellow/ white
Wavelength	**560**	**579**	**588**	**600**	**610**	**620**	**633**	**650**
DP	Yellow/ green	Yellow/ green	Yellow/ orange	Yellow/ White/ green	Yellow/ green	Yellow/ green	Yellow	Yellow/ Orange
BH	Yellow	Yellow/ white	Yellow/ white	Green	Green/ yellow	Yellow/ green	Yellow/ Orange	Orange

Table 3.2. The reported appearance at peak modulation (92%) of an amplitude-modulated flickering target of various wavelengths but constant radiance (10.33 $\log_{10}$ quanta s^{-1} deg^{-2}).

The strong decline in the $\log_{10}$ sensitivity difference between flicker and change-in-appearance-at-f_{am} below 510 nm (Figure 3.5) can be explained by a simultaneous decrease in flicker sensitivity and increase in change-in-appearance-at-f_{am} sensitivity at short wavelengths (<510 nm), which is more pronounced for subject BH.

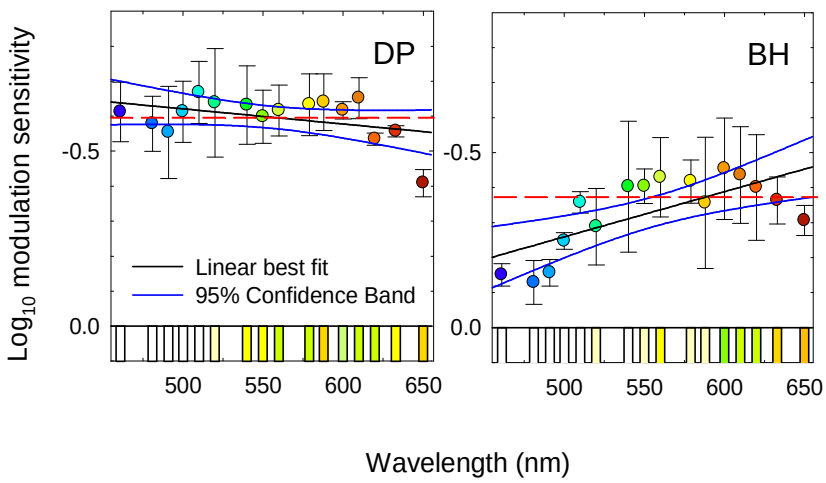

Figure 3.5. Mean ± 1 SE difference in $\log_{10}$ modulation units between the sensitivity to flicker and the sensitivity to change in appearance at f_{am} as a function of wavelength (circles). The black and blue lines show the linear best fit and the 95% confidence band of the fit, respectively. The dashed red line indicates the horizontal. The targets were calibrated for equal time-averaged radiance at 10.33 $\log_{10}$ quanta s^{-1} deg^{-2}.

The reason the flicker sensitivity decreases can be explained by the decrease in overall light levels at short wavelengths where most of the light would be absorbed by a yellowing of the lens with age (as Figure 3.4 shows, flicker sensitivity declines with declining light levels). The decline in flicker sensitivity is more pronounced for subject BH because of the 45 year age gap with (the younger) subject DP.

3.2.3 Discussion

Purdy (1931) reported that 475 nm, 507 nm and 575-nm lights were invariant in hue with intensity. However, he measured only colour changes and not desaturation or brightness changes. Given that Purdy's documented hue changes between the invariant 475 nm and 507 nm are less than 5 nm, it is possible that these two invariant wavelengths are the upper and lower limits of one invariant wavelength that lies in the middle, i.e. 491 nm. The 491-nm and 575-nm wavelengths closely approximate the wavelengths of peak desaturation in Guth's model of light adaptation (Capilla, Luque, Gomez & Palomares, 2001; Guth, 1991). Ball and

Bartley (Ball, 1964; Ball & Bartley, 1971) also reported that the wavelength of peak desaturation with increasing intensity is close to 500 nm. Studies on flickering lights further reported that wavelengths invariant in hue and brightness are around 575 nm, 491 nm and 476 nm (van der Horst & Muis, 1969) and 500 nm (Nilsson & Nelson, 1971). These invariant wavelengths for flickering stimuli are very close to the invariant wavelengths for stimuli of varying intensity reported by Purdy (1931). In addition, the peak at 491 nm, the peak at longer wavelengths and the colour appearance at the 600 nm for equal radiance stimuli (Figure 3.4) suggest a strong relationship with results of the Bezold-Brücke effect (Guth, 1991; Purdy, 1931; Sperling & Lewis, 1959). Consequently, the changes in appearance with increasing intensity are very similar to the changes in appearance with increasing modulation of amplitude-modulated flickering lights. Wavelengths that are invariant in brightness and colour with intensity and modulation coincide with the wavelengths undergoing desaturation for amplitude-modulated flickering stimuli. There appear to be no wavelengths in the visible spectrum that remain invariant in all three properties: hue, brightness and saturation.

For short wavelengths as equal radiance conditions, the older subject, BH, had lower sensitivity to flicker and higher sensitivity to changes in appearance at fam (Figure 3.4) as well as lower $\log_{10}$ modulation difference between the sensitivity to flicker and the sensitivity to change in appearance at f_{am} (Figure 3.5). These changes may be related to the decline of S-cone function with age (Haegerstrom-Portnoy, Hewlett & Barr, 1989; Werner, Bieber & Schefrin, 2000) and increased absorption of short wavelengths by changes in the lens and macula with age. Such changes will also explain BH's concentration of errors in the blue region of the Farnsworth Munsell 100 Hue Test (Appendix Figure 9.1).

The minimum difference between the sensitivity to flicker and the sensitivity to a change in appearance at f_{am} for 650 nm (shown in the data of subject DP, Figure 3.3) as well as easily

detectable colour change from red to yellow (DP) or orange (BH) with no additional desaturation or brightness change at 650 nm indicate that 650 nm is a suitable wavelength for investigating the L- and M-cone pathway carrying colour change information because the flicker will be less salient at the threshold for seeing a colour change at f_{am}.

The 560-nm target was reported by subjects to undergo the most brightness change and the least colour change or desaturation. In addition, there is negligible S-cone sensitivity at 560 nm (over 3 $\log_{10}$ units lower sensitivity than L- and M-cones, Figure 1.1). This wavelength was chosen to compare the results for colour change at 650 nm with those for brightness change for the pre-nonlinearity and post-nonlinearity stages as well as their variation (e.g. in the critical fusion frequency) with intensity.

3.3 Critical fusion frequencies

Having established that 650 nm and 560 nm are suitable wavelengths for testing colour change and brightness change, respectively, an additional experiment was carried out to determine appropriate time-averaged radiance levels to use in later experiments. The critical fusion frequency for flicker (CFF) and the critical fusion frequency for detection of distortion in the form of change in appearance at f_{am} (CFFD) was measured as a function of radiance. It is well known that the CFF shifts to higher frequencies with increasing light intensity due to the shortening of the integration time with adaptation of the visual pathway (e.g. De Lange, 1952; Kelly, 1961a; and more recently Stockman et al., 2006). It is expected that the CFFD will also shift to higher frequencies with increasing light intensity. In principle, the best radiances to use are those at which the difference between the sensitivity to flicker and change in appearance at f_{am} is smallest. Ideally, a failure of the Talbot-Plateau law would occur at certain radiances, which would allow threshold measurements of the change in appearance at f_{am} in isolation from flicker. In addition, the CFF and CFFD measurements will

also provide preliminary information on how the pre-nonlinearity stage adapts (indicated by the CFFD measurements) relative to the overall contrast sensitivity pathway (indicated by the CFF measurements).

3.3.1 Procedures

An amplitude-modulated 560-nm or 650-nm flickering light (92% modulated, f_{am}=0.5 Hz and f_c varied) was presented with the same size and position (i.e., 4° central visual field) as in Section 3.1.1.

The radiance level for the 650-nm target was increased in approximately 0.3-0.45 $\log_{10}$ units from 6.53 to 10.93 $\log_{10}$ quanta s^{-1} deg^{-2} (Figure 3.6). Above 10.93 $\log_{10}$ quanta s^{-1} deg^{-2}, subjects reported a lot of light scatter that made experiments more difficult so no measurements were made above this level.

The radiance level for the 560-nm target was increased from 5.81 to 10.11 $\log_{10}$ quanta in 0.3-0.45 $\log_{10}$ steps (Figure 3.7). Above 10.11 $\log_{10}$ quanta s^{-1} deg^{-2} subjects reported a lot of light scatter and a strong afterimage so no measurements were made above these levels.

The starting f_c for each new intensity level in the experiments was 10 Hz. Subjects were asked to increase or decrease the carrier frequency in steps of 0.5 Hz until they found the maximum frequency at which they could just detect the flicker (triangles, Figures 3.6 and 3.7) or the change in appearance at f_{am} (circles, Figures 3.6 and 3.7).

Subjects made three settings in each of three separate runs of the experiment (Section 2.2.1). After each three settings the mean radiance of the target was increased. Subjects adapted to the new target radiance for a minute before making a setting.

3.3.2 Data and analysis

For the 650-nm target (Figure 3.6), observers reported that the change in appearance at f_{am} was in the form of a brightness change from dark red to bright red at low intensity levels (below about 8 $\log_{10}$ quanta s^{-1} deg^{-2}), and in the form of a colour change at higher levels from red to orange (between about 8 and 9.5 $\log_{10}$ quanta s^{-1} deg^{-2}), from red to yellow (between about 9.5 and 10.5 $\log_{10}$ quanta s^{-1} deg^{-2}) and from red to pale yellow (above 10.5 $\log_{10}$ quanta s^{-1} deg^{-2}). The four radiance levels that were chosen for further experiments were the maximum level before strong glare was reported, 10.93 $\log_{10}$ quanta s^{-1} deg^{-2}; the level at which the CFF and CFFD were closest, 10.33 $\log_{10}$ quanta s^{-1} deg^{-2}; the minimum level at which CFF and CFFD were above 30 Hz, 9.10 $\log_{10}$ quanta s^{-1} deg^{-2}; and an intermediate level, 9.70 $\log_{10}$ quanta s^{-1} deg^{-2}. These four radiances are indicated with arrows on Figure 3.6. The 10.33 and 10.93 $\log_{10}$ quanta s^{-1} deg^{-2} radiance levels were also the levels at which the sensitivity to colour change, amplitude-modulated flicker and sinusoidal flicker have been measured as a function of f_c.

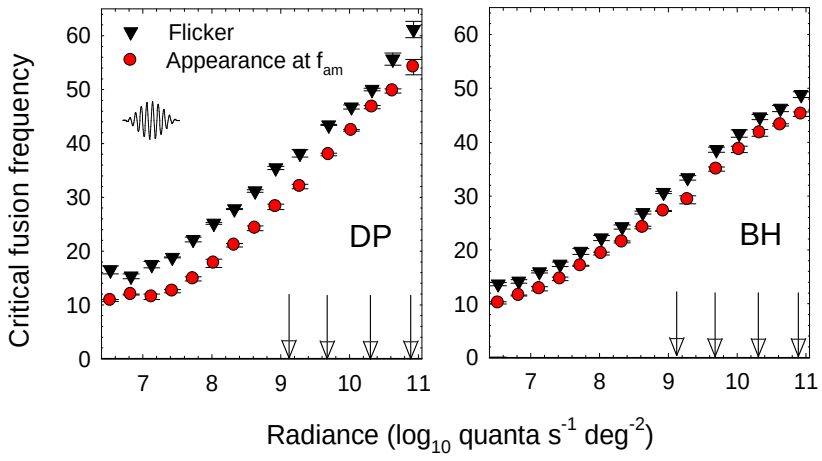

Figure 3.6 Mean ± 1 SE critical fusion frequency for flicker and for a change in appearance at f_{am} in response to a 650-nm, amplitude-modulated flickering target (f_{am}=0.5 Hz and f_c is varied) as a function of time-averaged radiance. The four radiance levels that were chosen for subsequent experiments are indicated by

arrows. The inset graph below the legend shows one cycle of an amplitude-modulated waveform of f_c=10 Hz as example and f_{am}=0.5 Hz.

The CFF and CFFD curves for the 650-nm stimulus (Figure 3.6) increase approximately in parallel with increasing radiance. The two curves increase approximately linearly with a 10 Hz increase for every 1 $\log_{10}$ quanta s^{-1} deg^{-2} increase in radiance over the region in which the Ferry-Porter law applies, above about 7 $\log_{10}$ quanta s^{-1} deg^{-2} for subjects BH and DP. The smoothness and continuity of the two curves above 7 $\log_{10}$ quanta s^{-1} deg^{-2} suggests that there is no change in underlying mechanisms (specifically that the rod mechanism does not intrude on the cone mechanisms at these intensity levels).

For the 560-nm target (Figure 3.7), observers reported that the change in appearance at f_{am} was in the form of a brightness change (from dark to bright at low to high modulations, respectively) for all radiance levels. The four radiance levels that were chosen for further experiments were: the maximum level before strong afterimages were reported by the subjects, 10.11 $\log_{10}$ quanta s^{-1} deg^{-2}; the minimum level at which CFFs and CFFDs were always above 30 Hz, 8.26 $\log_{10}$ quanta s^{-1} deg^{-2}; and two intermediate levels with approximately 0.6 $\log_{10}$ units difference from the other two levels, i.e. 9.51 and 8.86 $\log_{10}$ quanta s^{-1} deg^{-2}). These four radiances are indicated with arrows on Figure 3.7.

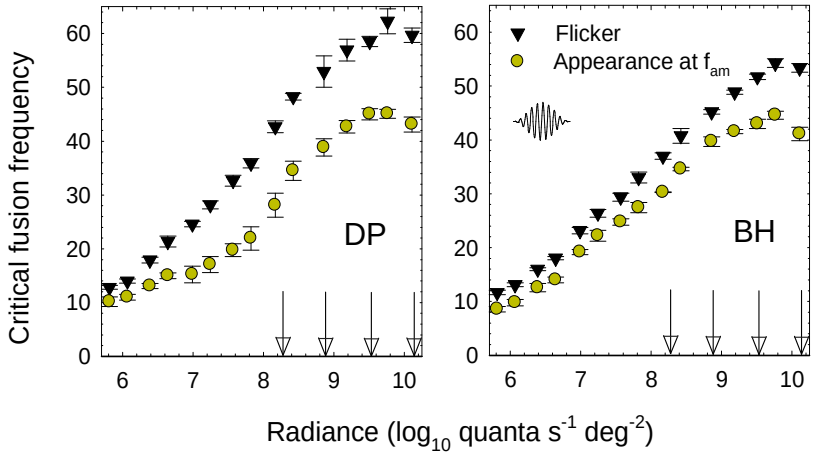

Figure 3.7. Mean ± 1 SE critical fusion frequency for flicker and for a change in appearance at f_{am} in response to a 560-nm, amplitude-modulated flickering target (f_{am}=0.5 Hz and f_c is varied) as a function of radiance. The four radiance levels for each target that were chosen for subsequent experiments are indicated by arrows. The inset graph below the legend shows one cycle of an amplitude-modulated waveform of f_c=10 Hz as example and f_{am}=0.5 Hz.

Unlike the CFF and CFFD curves for 650 nm (Figure 3.6), those at 560 nm (Figure 3.7) show a plateau at high radiances, above 9.19 and 9.77 $\log_{10}$ quanta s^{-1} deg^{-2} for DP and BH, respectively, which indicates that Weber's law holds there (i.e. the ratio of the amplitude to the mean intensity remains constant). Also, unlike the results for the 650-nm target (Figure 3.6), the CFF and CFFD curves are not parallel for 560 nm (Figure 3.7) due to the lower slope for the CFFD curve compared to that for CFF, particularly for DP.

3.3.3 Discussion

The CFF and CFFD results for 650 nm (Figure 3.6) and 560 nm (Figure 3.7) suggest that there is no saturation of the M- and L-cone pathways, which would be indicated by a negative slope of the curves i.e. a decrease in CFF measurements at high intensity levels. Only one data point (at the highest time-averaged radiance) suggests a decrease in the CFF and CFFD with increasing radiance in Figure 3.7 but because it is a single point and its error bars, at least for the CFF, overlap with those of the preceding data point, this decline does not appear

significant. These results are different from those for S-cones, for which CFF and CFFD curves decrease at high intensities (Stockman & Plummer, 1998). Consequently, substantial differences exist in the L- and M-cones compared with the S-cones and these differences are apparent as early as the pre-nonlinearity stage.

The CFF and CFFD curves can be interpreted as the change in sensitivity (caused by, for example, shortening time constant) of the overall temporal contrast sensitivity pathway and the pre-nonlinearity stage, respectively, with increasing intensity. The similar slopes of the CFF and CFFD for a 650-nm target suggest that the mechanisms for adaptation of the overall pathway and its pre-nonlinearity stage are comparable. No additional temporal-frequency-dependent adaptation appears to occur at 650 nm between the pre-nonlinearity filter (indicated by the CFFD) and the end of the contrast sensitivity pathway (indicated by the CFF). Therefore, the post-nonlinearity stage should not show any temporal-frequency-dependent adaptation.

For the 560-nm target, the slightly steeper slope of the CFF curve in comparison to the CFFD curve indicates that limited adaptation and sensitivity changes may occur after the pre-nonlinearity stage i.e. at the post-nonlinearity stage.

The greater change in sensitivity at the pre-nonlinearity stage compared to the post-nonlinearity stage is consistent with physiological evidence that at the early stage of the visual system the photoreceptors show substantial adaptation (Schneeweis & Schnapf, 1999) while at post-nonlinearity stages of the visual system the ganglion cells in the LGN show little or no adaptation at high frequencies (Virsu & Lee, 1983).

3.4 Colour and brightness

A 650 nm and a 560-nm target were chosen (Section 3.2) to test the colour changes and brightness changes, respectively, of amplitude-modulated flickering lights at four different intensity levels (Section 3.3). When the slow change in appearance at f_{am} appears as a colour change away from the steady hue of the stimulus then the stimulus is likely to be processed by the chromatic pathway and when the change in appearance at f_{am} appears as a brightness change then it may be processed by the brightness pathway. This assumption suggests that the procedures in the present study (see Sections 3.1.1 and 3.4.1 in particular) allow the distinction between the chromatic and brightness pathways. If the attenuation characteristics of the pre-nonlinearity stage are found to be the same for the two pathways then this would suggest either that the nonlinearity is located before the separation of the two pathways or that it is at a comparable stage in both pathways.

3.4.1 Procedures

The procedures were the same as in Section 3.1.1 (including tasks i, ii and iii) for seven new targets, each target was presented in a separate experimental run. Three of the targets were 650 nm as in Section 3.1 but of different time-averaged radiance: 9.10, 9.70 and 10.93 $\log_{10}$ quanta s^{-1} deg^{-2}. The other four targets were 560 nm at 8.26, 8.86, 9.51 and 10.11 $\log_{10}$ quanta s^{-1} deg^{-2}.

In a separate experiment, subjects were asked to set the minimum modulation at which they could just detect the amplitude-modulated flicker and the change in appearance at f_{am} (as in tasks ii and iii in Section 3.1.1) for a 529-nm target at one of four time-averaged radiance levels.

The four time-averaged radiance levels for the 560-nm and 529-nm lights were equated for equal L-cone stimulation to the four radiance levels for the 650 nm condition (Figure 3.10).

3.4.2 Data and analysis

Figures 3.8 and 3.9 show the $\log_{10}$ modulation sensitivity curves for sinusoidal flicker (half-black symbols), amplitude-modulated flicker (blue symbols) and colour change at f_{am} (black, red, orange and yellow symbols, Figure 3.8) or brightness change at f_{am} (black, green and yellow symbols, Figure 3.9). The third row of graphs in Figure 3.8 shows the same data as in Figure 3.1. The thresholds for sinusoidal flicker and change in appearance at f_{am} are plotted in terms of modulation in Figures 3.8 and 3.9 and in terms of amplitude in Figures 3.10 and 3.11. Considering that amplitude-modulated flicker and colour-change thresholds could only be measured at $f_c \geq 5$ Hz, Figures 3.8 and 3.9 show data only at and above 5 Hz. The sinusoidal-flicker thresholds for $f < 5$ Hz are shown in Figures 3.10 and 3.11 where they can be compared across time-averaged radiance levels.

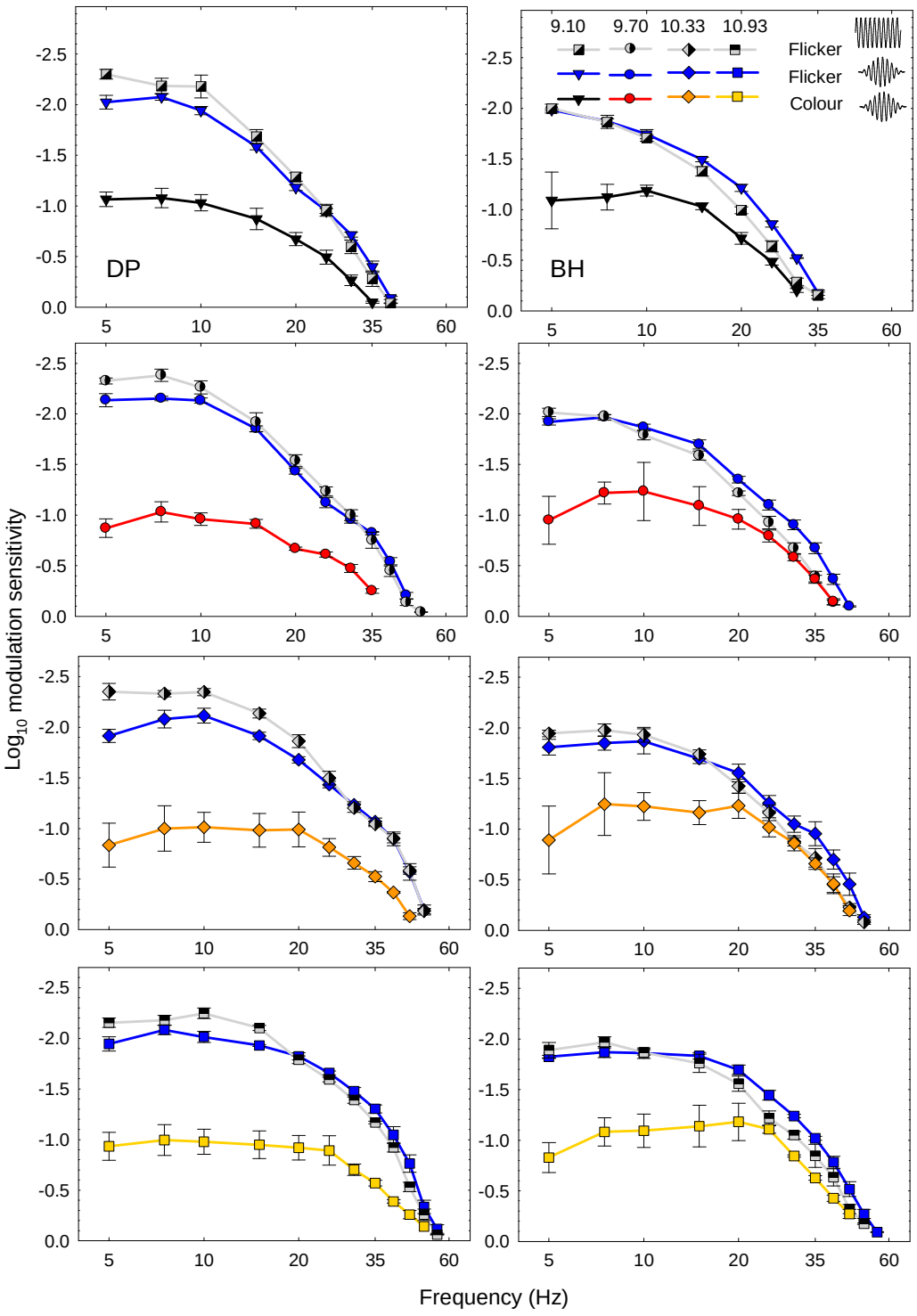

Figure 3.8. Mean ± 1 SE $\log_{10}$ modulation sensitivities for sinusoidal flicker (TCSF, half-black, grey-black symbols), for amplitude-modulated flicker (blue symbols) and for colour change at f_{am} (black, red, orange and yellow symbols) as a function of f_c. The inset graph in the top right corner shows one cycle of the temporal waveform used to measure each of the sensitivity curves (at f_c=10 Hz for example and f_{am}=0.5 Hz or f_{am}=0 Hz). The left and right columns show the data for subject DP and BH, respectively. The rows from top to bottom

show the data for the 560-nm target at time-averaged radiance of 9.10, 9.70, 10.33 and 10.93 $\log_{10}$ quanta s^{-1} deg^{-2}, respectively.

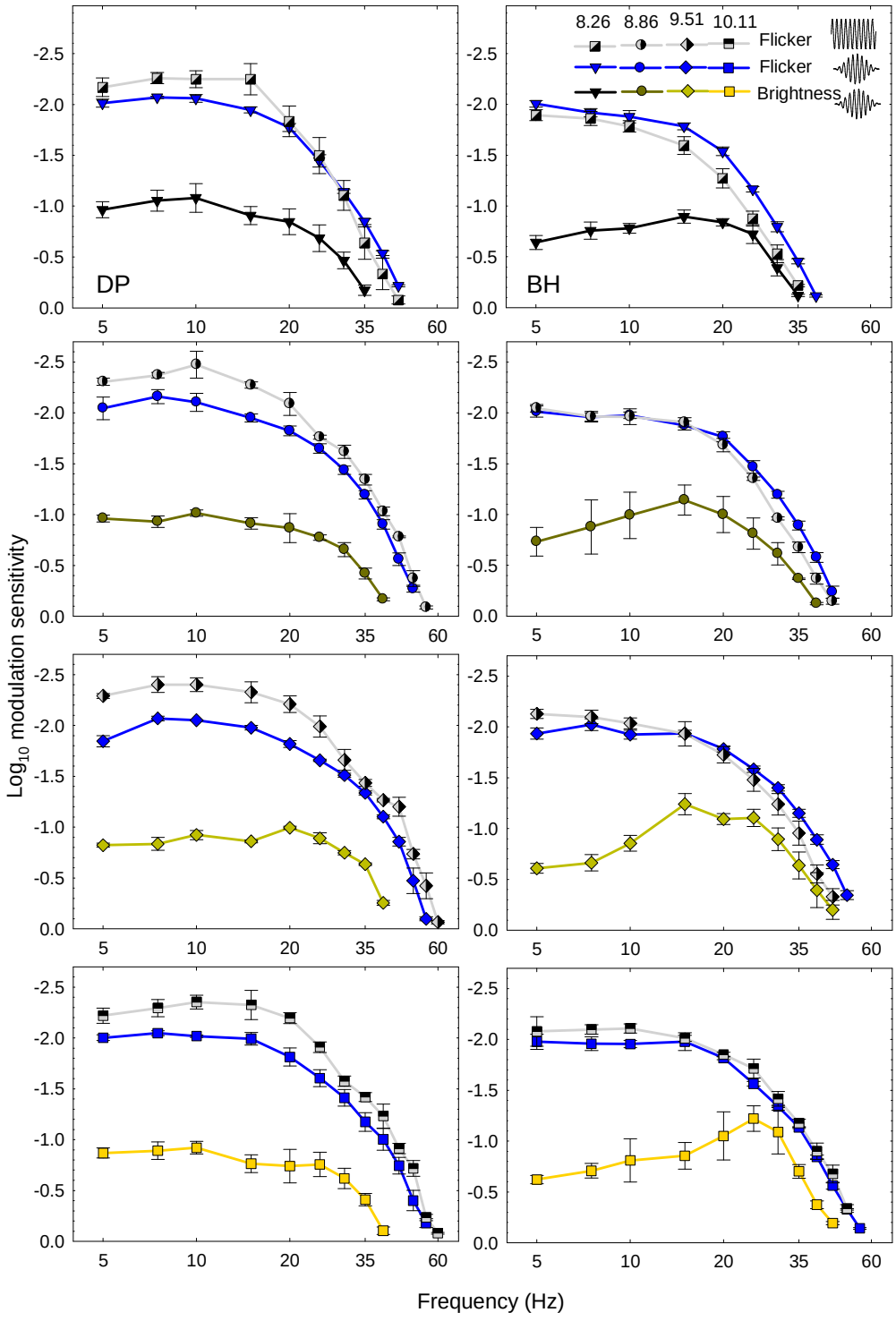

Figure 3.9. Mean ± 1 SE $\log_{10}$ modulation sensitivities for sinusoidal flicker (TCSF, half-black, grey-black symbols), for amplitude-modulated flicker (blue symbols) and for brightness change at f_{am} (black, green and yellow symbols) as a function of f_c. The inset graph in the top right corner shows one cycle of the temporal waveform used to measure each of the sensitivity curves (at f_c=10 Hz for example and f_{am}=0.5 Hz or f_{am}=0 Hz).

The left and right columns show the data for subject DP and BH, respectively. The rows from top to bottom show the data for the 560-nm target at time-averaged radiance of 8.26, 8.86, 9.51 and 10.11 $\log_{10}$ quanta s^{-1} deg^{-2}, respectively.

There is no significant difference between the slope of the sensitivity curves for sinusoidal flicker and amplitude-modulated flicker when f_c >20 Hz. As the frequency decreases (when $f_c \leq 20$ Hz) the sensitivity to amplitude-modulated flicker decreases (Figures 3.8 and 3.9) and fails to provide a measure of the true flicker sensitivity because of the increasingly small number of cycles. Both of these observations (at f_c >20 Hz and $f_c \leq 20$ Hz) as well as the ability to set sinusoidal-flicker thresholds but not amplitude-modulated flicker thresholds (Figures 3.10 and 3.11) are consistent across wavelengths, intensities and observers including results from Section 3.1.2. Considering the higher and more reliable thresholds for sinusoidal flicker at $f_c \leq 20$ Hz as well as the ability to make threshold measurements at f<5 Hz (which will be particularly useful later in Chapter 7), sensitivity to sinusoidal flicker rather than sensitivity to amplitude-modulated flicker was used as an indicator of the overall attenuation characteristics of the temporal contrast sensitivity pathway in Section 3.5 and Chapter 7. In experiments where the carrier frequency was fixed at 30 Hz (e.g. Chapters 4-7) the sensitivity to amplitude-modulated flicker can be assumed to be equal to the sensitivity to sinusoidal flicker.

The sensitivity curves for detecting a colour-change at 650 nm (Figure 3.8) and brightness-change at 560 nm (Figure 3.9) have a shallower fall-off in sensitivity than the curves for detecting sinusoidal flicker at 650 nm and 560 nm above about 10 Hz. The sensitivity curve to amplitude-modulated flicker and sinusoidal flicker are similar but subjects are typically relatively more sensitive to low-frequency sinusoidal flicker. Sinusoidal flicker instead of amplitude-modulated flicker was used in subsequent experiments because it allowed measurements at low frequencies.

In order to show the change in the sensitivity curves to sinusoidal flicker and appearance change at f_{am} with changes in the time-averaged radiance level on the same graph, the threshold settings made by the subjects were plotted as amplitudes (Figures 3.10 and 3.11) instead of modulation sensitivities (Figures 3.1, 3.8 and 3.9). The amplitudes were calculated as the sum of the $\log_{10}$ modulation sensitivity value and the time-averaged radiance in $\log_{10}$ quanta s^{-1} deg^{-2}. (The sensitivities to amplitude-modulated flicker were not re-plotted in the same way due to their unreliability at low carrier frequencies, e.g. see Section 3.1.)

For 650 nm (Figure 3.10) and 560 nm (Figure 3.11), DP had slightly higher sensitivity to flicker, higher sensitivity to changes in appearance at f_{am} for low carrier frequencies (below about 7.5 Hz for the 650 nm conditions and 15 Hz for the 560 nm conditions) and lower sensitivity to changes in appearance at f_{am} for high carrier frequencies compared to BH. Consequently, the frequency at which subjects are most sensitive to changes in appearance at f_{am} is higher for BH than for DP (DP's results hare more low-pass characteristics under some conditions). The peak brightness-change sensitivity at 560-nm target (bottom row, Figure 3.11) occurred about 5 Hz higher for BH (except at 9.81 $\log_{10}$ quanta s^{-1} deg^{-2} where it is 7.5 Hz higher) and 2.5 Hz higher for DP (except at 9.81 $\log_{10}$ quanta s^{-1} deg^{-2} where it is 10 Hz higher) compared with the peak of the colour-change sensitivity curve at 650nm (bottom row, Figure 3.10). No significant shift was observed in the frequency of peak flicker sensitivity between the 650 nm conditions (top row, Figure 3.10) and the 560 nm conditions (top row, Figure 3.11).

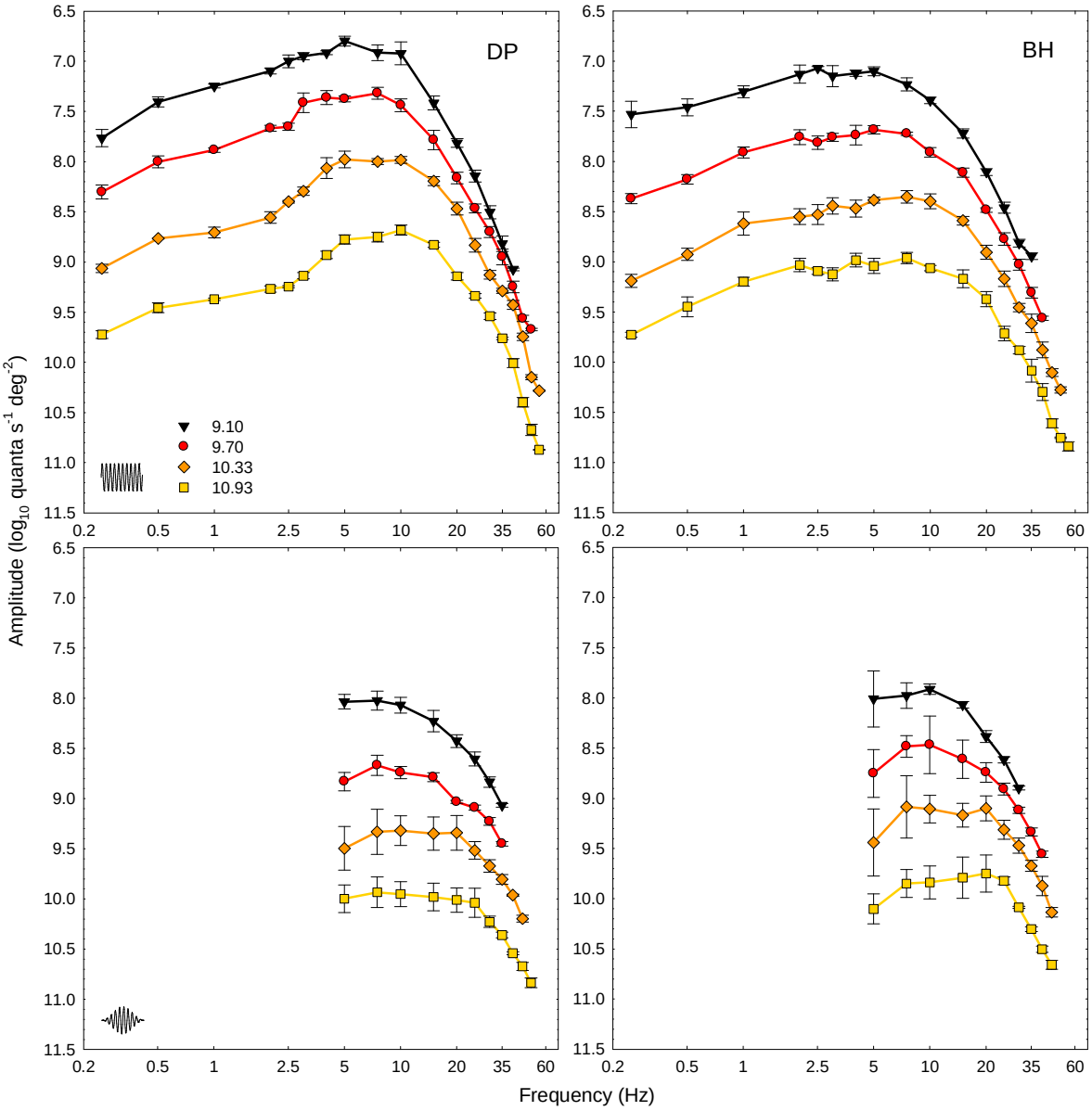

Figure 3.10. Mean ± 1 SE amplitude required for subjects to detect sinusoidal flicker (top row) and colour change at f_{am} (bottom row) as a function of f_c. The inset graph in the bottom left corner of each row shows the temporal waveform used to measure the sensitivity curves in each row of graphs (at f_c=10 Hz for example and f_{am}=0.5 Hz or f_{am}=0 Hz). The left and right columns show the data for subject DP and BH, respectively. The numbers in the legend show the time-averaged radiance level of the four 650-nm targets in $\log_{10}$ quanta s^{-1} deg^{-2}.

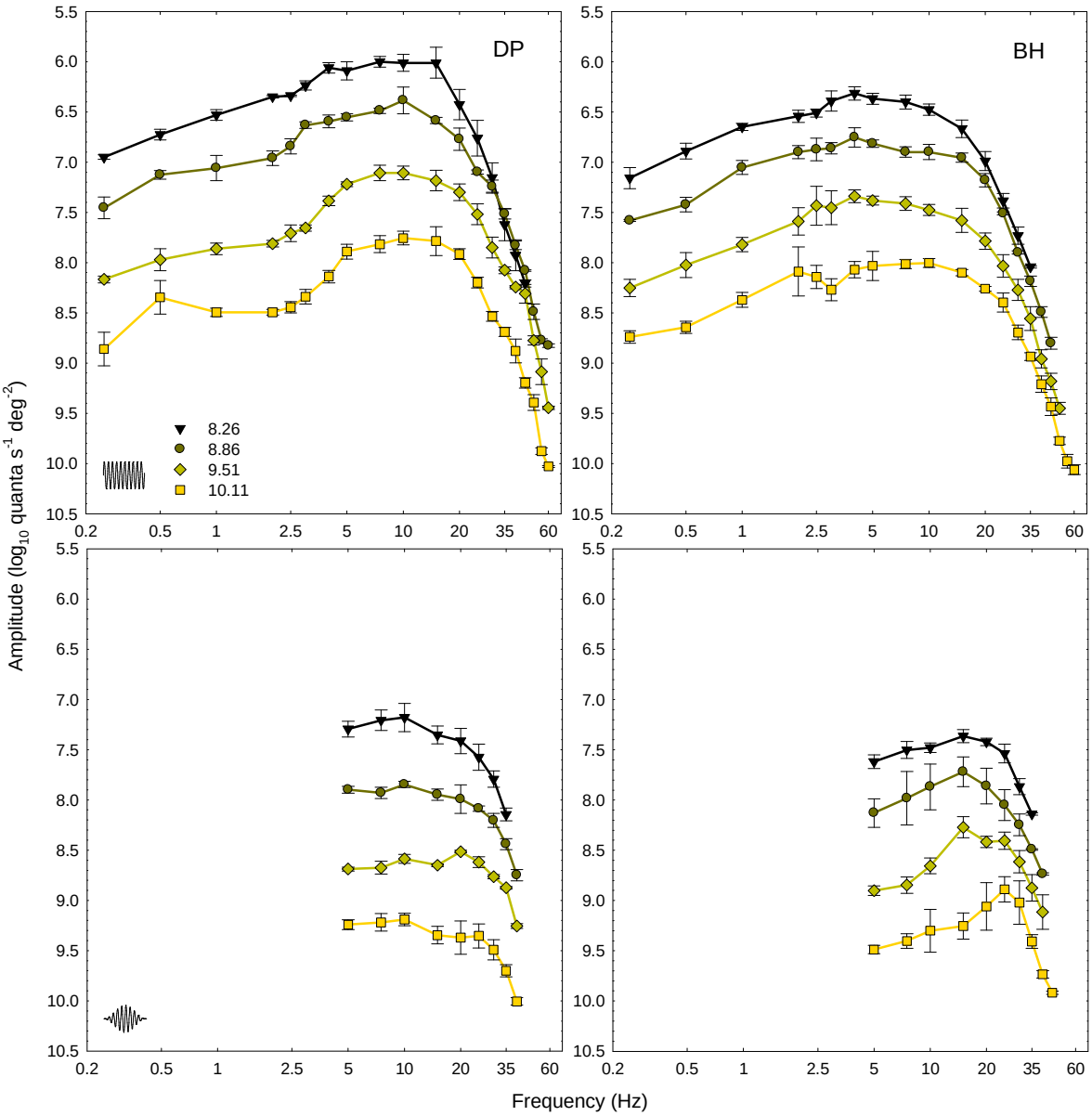

Figure 3.11. Mean ± 1 SE amplitude required for subjects to detect sinusoidal flicker (top row) and brightness change at f_{am} (bottom row) as a function of f_c. The inset graph in the bottom left corner of each row shows the temporal waveform used to measure the sensitivity curves in each row of graphs (at f_c=10 Hz for example and f_{am}=0.5 Hz or f_{am}=0 Hz). The left and right columns show the data for subject DP and BH, respectively. The numbers in the legend show the time-averaged radiance level of the four 560-nm targets in $\log_{10}$ quanta s^{-1} deg^{-2}.

The sensitivity curves to sinusoidal flicker for the 650-nm target (Figure 3.10) and 560-nm target (Figure 3.11) show three main changes as result of adaptation with increasing intensity: low-frequency attenuation increases and the peak of the flicker sensitivity curve

becomes more pronounced, the cut-off frequency shifts to higher frequencies and the extrapolated sensitivities at high frequencies tend towards a common asymptote consistent with high-frequency linearity. All three of these observations are consistent with earlier measurements of the TCSF function (De Lange, 1958a; Kelly, 1961b).

The same three changes as result of adaptation with increasing intensity can also be observed for the sensitivity curves for detecting colour change (Figure 3.10) and for detecting brightness change (Figure 3.11). This means that the changes in sensitivity with intensity for the TCSF curve are consistent the changes in the sensitivity with intensity for the appearance change at f_{am} (i.e. the sensitivities to colour change and brightness change).

In addition to the 560 nm and 650-nm targets, a 529-nm target was also used to measure the sensitivity to sinusoidal flicker and to changes in appearance at f_{am} (Figure 3.12).

Subjects reported that the change in appearance at f_{am} for the 529 nm stimuli appeared as a slow colour change from green (at minimum, 0%, modulation) to yellow (at peak, 92%, modulation). (The colour change was seen to flicker at f_c because the flicker sensitivity was always higher than the colour-change sensitivity.)

The sensitivities for amplitude-modulated flicker and change in appearance at f_{am} for 529 nm (Figure 3.12) were very similar to those for 560 nm (Figure 3.11). For instance, the peak sensitivity to flicker shifted from around 5 Hz to around 10 Hz over a 1.8 $\log_{10}$ unit increase in time-averaged radiance and the peak sensitivity to change in appearance at f_{am} shifted from around 10 Hz to around 20 Hz over the same range. Also, subject DP showed a less pronounced peak than subject BH, similarly to the inter-subjective differences for 560 nm (Figures 3.11).

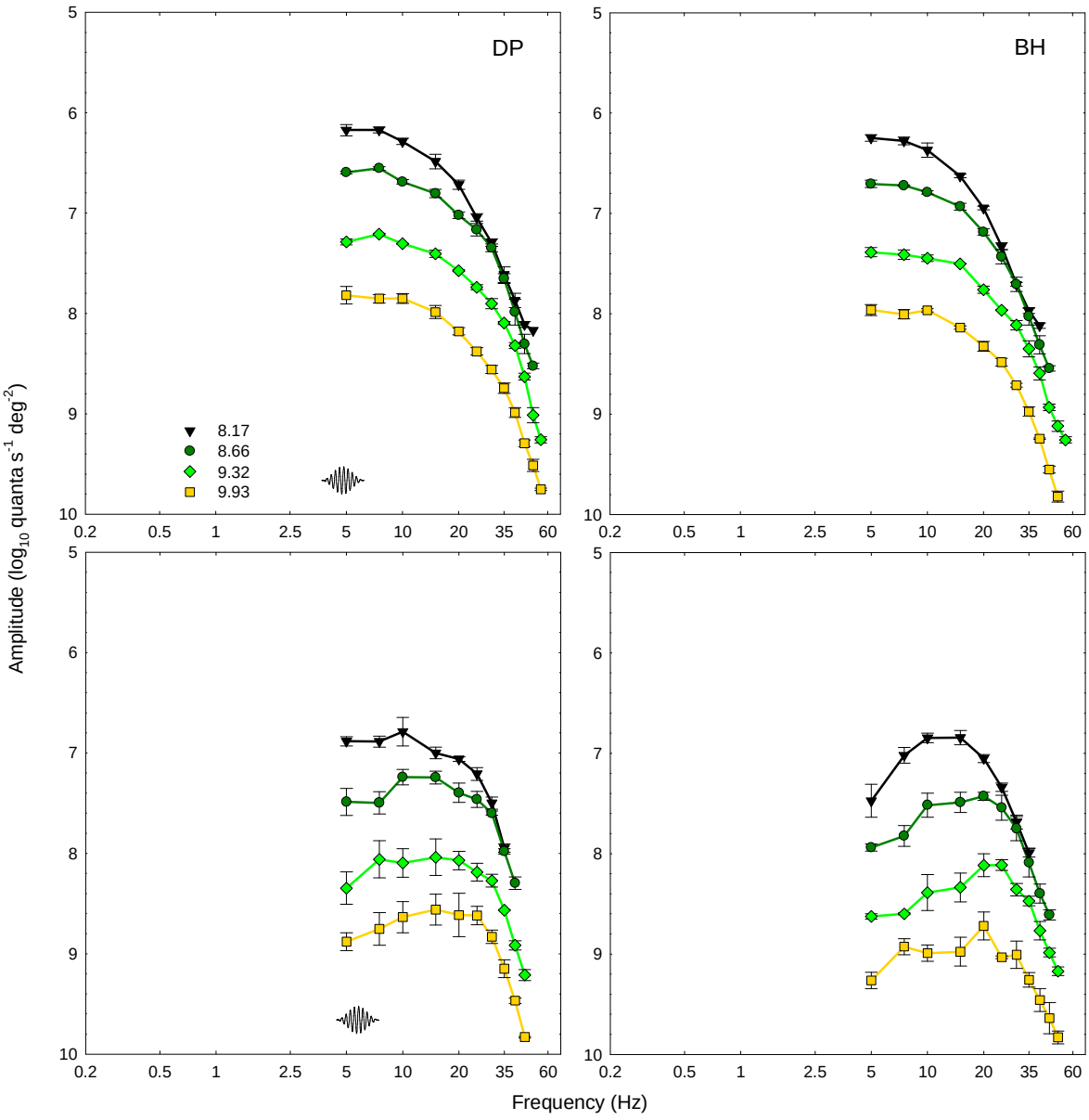

Figure 3.12. Mean ± 1 SE amplitude required for subjects to detect sinusoidal flicker (top row) and colour-change-at-f_{am} (bottom row) as a function of f_c. The inset graph in the bottom left corner of each row shows the temporal waveform used to measure the sensitivity curves in each row of graphs (at f_c=10 Hz for example and f_{am}=0.5 Hz). The left and right columns show the data for subject DP and BH, respectively. The numbers in the legend show the time-averaged radiance level of the four 529-nm targets in $\log_{10}$ quanta s^{-1} deg^{-2}.

3.4.3 Discussion

The sensitivity curves for detecting changes in appearance at f_{am} have shallower high-frequency slopes than the curves for detecting sinusoidal flicker. These results confirm the

earlier results in Section 3.1 where the colour-change sensitivity is attenuated less than the temporal contrast sensitivity to flicker.

The variation in sinusoidal flicker sensitivity with intensity, which reflects the adaptation of the overall temporal contrast sensitivity pathway, are consistent with the variation in colour-change sensitivity with intensity (bottom row, Figure 3.10) and brightness-change sensitivity (bottom row, Figure 3.11), which are assumed to reflect adaptation at the pre-nonlinearity stage in the L-/M-cone chromatic pathway and the brightness pathway, respectively. Thus, much of the adaptation is occurring before the nonlinearity in the two pathways.

The results suggest that the pre-nonlinearity stage for the L- and M-cone chromatic pathway (bottom row, Figure 3.10) as well as for the brightness pathway (bottom row, Figure 3.11) is slightly band-pass with the peak for the brightness pathway being relatively more pronounced and occurring at higher frequencies (between 10 Hz and 25 Hz). The peak sensitivity to appearance-change-at-f_{am} shifts by approximately 10 Hz to higher frequencies over the 1.8 $\log_{10}$ unit increase in mean intensity for both the chromatic and the brightness pathways. This suggests that both pathways have similar adaptation characteristics.

At all intensity levels for the 650-nm target (Figure 3.10) and 560-nm target (Figure 3.11), the peak sensitivity to appearance-change-at-f_{am}, which reflects the pre-nonlinearity temporal characteristics, occurs at higher frequencies than the peak sensitivity for flicker, which peaks at 2.5-10 Hz and reflects the temporal characteristics of stages before and after the nonlinearity.

The similarities between the pre-nonlinearity stages of the chromatic and brightness pathways for the L- and M-cones suggest that the pre-nonlinearity stage, and consequently

the nonlinearity, may be either at a similar stage in each pathway or at a stage prior to the separation of chromatic and brightness information.

The pre-nonlinearity measurements in the present study show smoother curves than the inferred pre-nonlinearity temporal characteristics obtained by Wu et al. for brightness enhancement at 560 nm. The overall shape of their pre-nonlinearity data indicates a shallow peak with little low-frequency attenuation similar to the data for the 8.26 $\log_{10}$ quanta s^{-1} deg^{-2} radiance level in the bottom row of Figure 3.11. The peaks for pre-nonlinearity stage characteristics of the brightness pathway in the present study (10-25 Hz in the bottom row of Figure 3.11) correspond well to the peak for the pre-nonlinearity stage characteristics inferred by Wu et al. (16 Hz in the majority of cases, Figure 7, Wu et al., 1996) .

Although the data for DP at 650 nm (Figure 3.10) and 560 nm (Figure 3.11) is consistent with a low-pass pre-nonlinearity filter while the data for BH clearly show a band-pass filter, the results for DP have to be extended to lower frequencies before a definite conclusion about the shape of the pre-nonlinearity filter can be made (see Section 7.1).

3.5 L- and M-cone pathways

In addition to measuring the pre-nonlinearity stage in the pathways carrying chromatic and brightness information (Section 3.4), it was also measured using isolated-L-cone and isolated-M-cone stimuli (employing silent-cone substitution to isolate the cone responses) as described in the present section.

The silent-cone substitution technique has been used previously (Estévez & Cavonius, 1975; Estévez & Spekreijse, 1974; Estévez & Spekreijse, 1982) to measure the temporal and spatial contrast sensitivity of isolated L- and M-cone pathways. Of course, since M- and L-cone signals feed into both luminance and chromatic pathways such data reflect the mixed

properties of later visual mechanisms and not single cones (Kelly & van Norren, 1977; Smith, Pokorny, Davis & Yeh, 1995).

Nonetheless, if the pre-nonlinearity stage reflects the temporal filter characteristics of the photoreceptors themselves (as suggested by MacLeod et al., 1992; Stockman & Plummer, 1998; Wu, Burns & Elsner, 1995) then it would be possible to reveal the temporal characteristics of the separate L- and M-cones using the new combination of the silent-cone substitution technique with the sandwich model (where nonlinear distortion manifests as a visible change in appearance at f_{am}) as outlined in this section.

3.5.1 Procedures

The silent-cone substitution technique was first proposed by Rushton et al. (1973a; 1973b). Using this technique to isolate M-cone responses, for instance, the intensities of two wavelengths are adjusted so that they produce equal L-cone excitation. Thus, if the L-cones are *n* times more sensitive to λ_1 than to λ_2, then λ_2 must be *n* times more intense to have the same effect on the L-cones.

Silent-cone substitution was produced by superimposing a 4°, 650-nm light and a 4°, 529-nm light that were both amplitude-modulated (as described in Section 2.2). Both lights were undergoing amplitude-modulated flicker with their f_c 180° out-of-phase and f_{am} in-phase. The 529-nm light was used because it allowed a large difference in M- and L-cone excitation relative to the 650-nm light while avoiding a significant contribution from S-cones and thus allowed the best cone-isolation conditions.

Four time-averaged radiance levels were used to measure the influence of radiance on the pre-nonlinearity stage. The four time-averaged radiance levels for the L-cone isolation conditions were calibrated to produce approximately the same L-cone excitation as the four

time-averaged radiance levels used for the 650-nm condition (Figure 3.10). The four time-averaged radiance levels for the M-cone isolation condition were calibrated for approximately equal M-cone excitation at peak to those of the L-cone excitation condition. The sensitivity to the change in appearance at f_{am} was much lower at the lowest radiance level for the M-cone condition compared to the lowest radiance level for the L-cone condition. Therefore, the time-averaged radiance level for the M-cone isolating condition was increased by another approximately 0.6 $\log_{10}$ units to measure a fifth, higher radiance level.

Apart from the target wavelengths and radiance levels, the procedures were the same as in Section 3.1.1.

3.5.2 Data and analysis

The presence of two lights flickering out-of-phase reduced the maximum possible modulation for each cone type from around 92% to an effective cone modulation around 78%. The effective modulation (m_c) was calculated for each threshold setting according to Equation 3.1 (i.e. Michelson contrast as in Equation 1.4 but for the isolated cone type),

$$m_c = m_m \left(\frac{10^{cs+ss} - 10^{ci+si}}{10^{cs+ss} + 10^{ci+si}} \right) , \qquad \text{Equation 3.1}$$

where m_m is the measured modulation at each setting, cs is the calibrated time-averaged radiance (in $\log_{10}$ quanta s^{-1} deg^{-2}) of the stimulating light (i.e. 529 nm in the case of M-cones and 650 nm in the case of L-cones), ss is the isolated-cone's logarithmic sensitivity to the stimulating light, ci is the calibrated radiance for the isolating light that allows silent substitution (i.e. 650 nm in the case of M-cones and 529 nm in the case of L-cones) and si is the isolated-cone's logarithmic sensitivity to the isolating light. The M- and L-cone sensitivities were taken from the most recent human cone spectral sensitivity data (Stockman & Sharpe, 2000b). An example of the m_m, cs, ci, ss and si units is shown in Figure 3.13 for

the L-cone isolating stimulus at the lowest time-averaged radiance level that was used in the experiments.

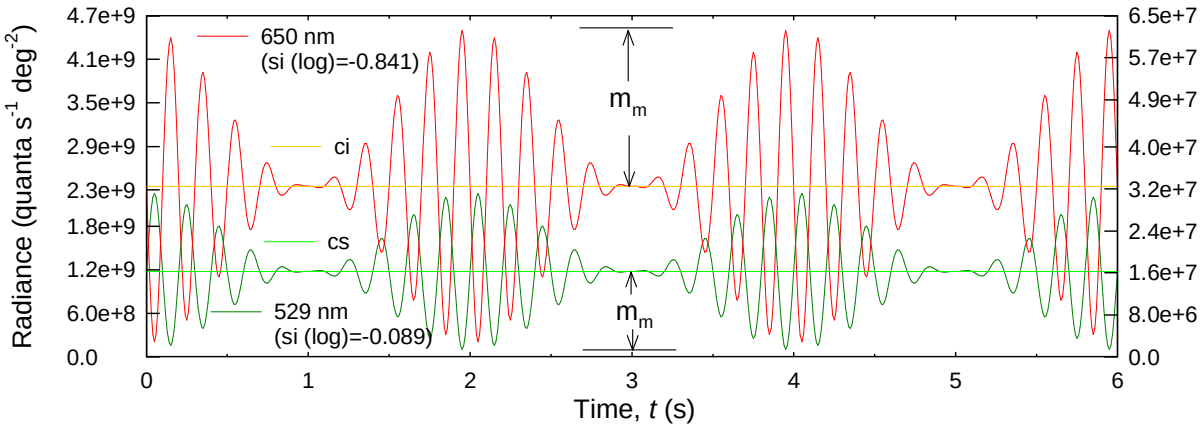

Figure 3.13. A schematic of the units in Equation 3.1 for calculating the effective L-cone modulation for an equal-M-cone stimulus, where m_m is the modulation (92%), *cs* is the time-averaged radiance of the 650-nm light ($10^{9.37}$ quanta s^{-1} deg^{-2} left y-axis), *ss* is the L-cone sensitivity to 650 nm, *ci* is the time-averaged radiance for the 529-nm light ($10^{7.51}$ quanta s^{-1} deg^{-2} right y-axis), *si* is the L-cone sensitivity to 529 nm. L-cone sensitivities are in $\log_{10}$ units according to the Stockman and Sharpe fundamentals (2000b).

The average calibrations (in $\log_{10}$ quanta s^{-1} deg^{-2}) for the 529-nm and 650-nm lights that composed the cone-isolating stimuli are shown in Figures 3.14 and 3.15 in the format "650 nm radiance/529 nm radiance" for the L-cone isolation conditions and "529 nm radiance/650 nm radiance" for the M-cone isolation conditions. One cycle of the temporal waveform is shown next to the legend (where a 529 nm and a 650-nm lights are 180° out-of-phase, f_{am}=0.5 or f_{am}=0 and f_c=10 Hz for example).

The subjects reported that the change in appearance at f_{am} appeared as a colour change from orange-red to yellow for L-cone stimuli (Figure 3.14) and as a colour change from yellow-green to yellow for M-cone stimuli (Figure 3.15). They also reported that at frequencies below about 10 Hz the flicker appeared coloured i.e. alternating from red to green. The chromatic flicker can be explained by the 180º out-of-phase flickering of the 650-nm light (which appears red in isolation) and 529-nm light (which appears green in isolation).

Subjects also reported that as the colour of the flicker increased, the slow change in appearance at f_{am} became less obvious.

Figures 3.14 and 3.15 do not show the sensitivities for amplitude-modulated flicker because these showed similar trends relative to the sensitivities for sinusoidal flicker as those reported in Sections 3.1 and 3.4.

The amplitudes required for subjects to detect sinusoidal flicker or change in appearance at f_{am} were plotted to compare changes across various radiance levels (Figures 3.14 and 3.15). The linear amplitudes for silent-cone substitution experiments (A_c) were calculated according to Equation 3.2,

$$A_c = m_m(10^{cs+ss} - 10^{ci+si}) \quad , \qquad \text{Equation 3.2}$$

where the values m_c, ci, cs, si and ss are as described for Equation 3.1. The values in Figures 3.14 and 3.15 are plotted as $\log_{10}$ of A_c.

For all subjects, the sinusoidal flicker sensitivities for the cone-isolation conditions (Figures 3.14 and 3.15) show less low-frequency attenuation than the flicker sensitivities for the monochromatic conditions (Figures 3.10 and 3.11), especially below 10 Hz. This is consistent with previous results (see results by: Estévez & Spekreijse, 1982; Kelly, 1983; Kelly & van Norren, 1977). The flicker sensitivity measurements below 5 Hz show a secondary peak, in addition to the peak that is visible around 7.5 Hz, at around 1 Hz for the cone-isolation conditions (Figures 3.14 and 3.15) that is absent for the monochromatic conditions (Figures 3.10 and 3.11). The flicker sensitivities for the M-cone conditions (Figure 3.15) are generally higher at frequencies below 2.5 Hz compared to those for the L-cone conditions (Figure 3.14), which means that the peak around 1 Hz is often higher than the peak around 7.5 Hz for the M-cone conditions, unlike for the L-cone condition. For DP, the flicker

sensitivity was slightly higher than for BH at frequencies below about 10 Hz but the curve shapes for the subjects were similar.

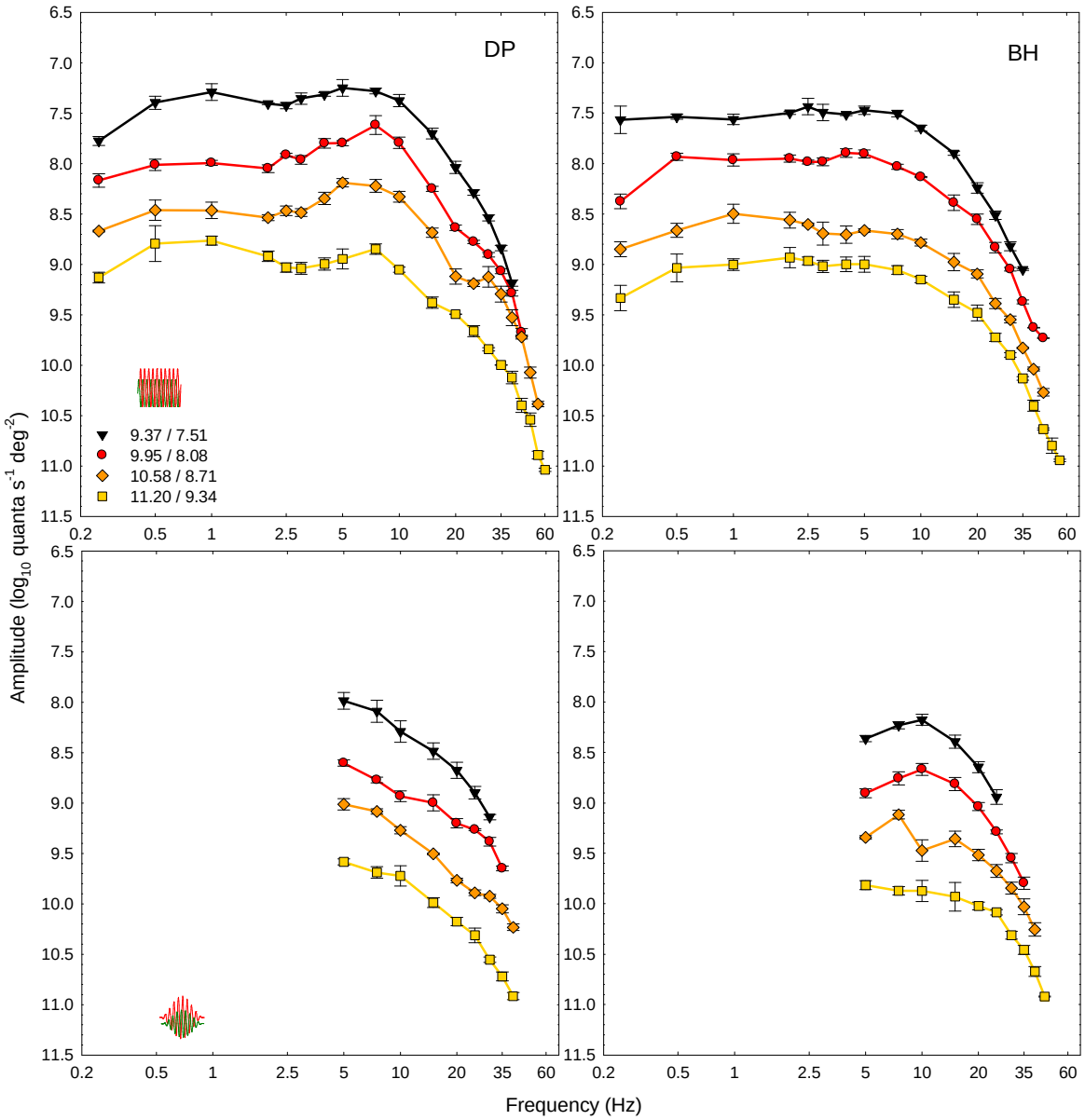

Figure 3.14. Mean ± 1 SE amplitude required for subjects to detect sinusoidal flicker (top row) and colour change at f_{am} (bottom row) as a function of f_c. The inset graph in the bottom left corner of each row shows the temporal waveform used to measure the sensitivity curves in each row of graphs (at f_c=10 Hz for example and f_{am}=0.5 Hz or f_{am}=0 Hz). The left and right columns show the data for subject DP and BH, respectively. The stimulus was a 650-nm light superimposed on a 529-nm light (numbers in legend show the time-averaged radiance for 650 nm/529 nm in $\log_{10}$ quanta s^{-1} deg^{-2}) with f_c 180º out-of-phase and f_{am} in-phase (L-cone isolating stimulus).

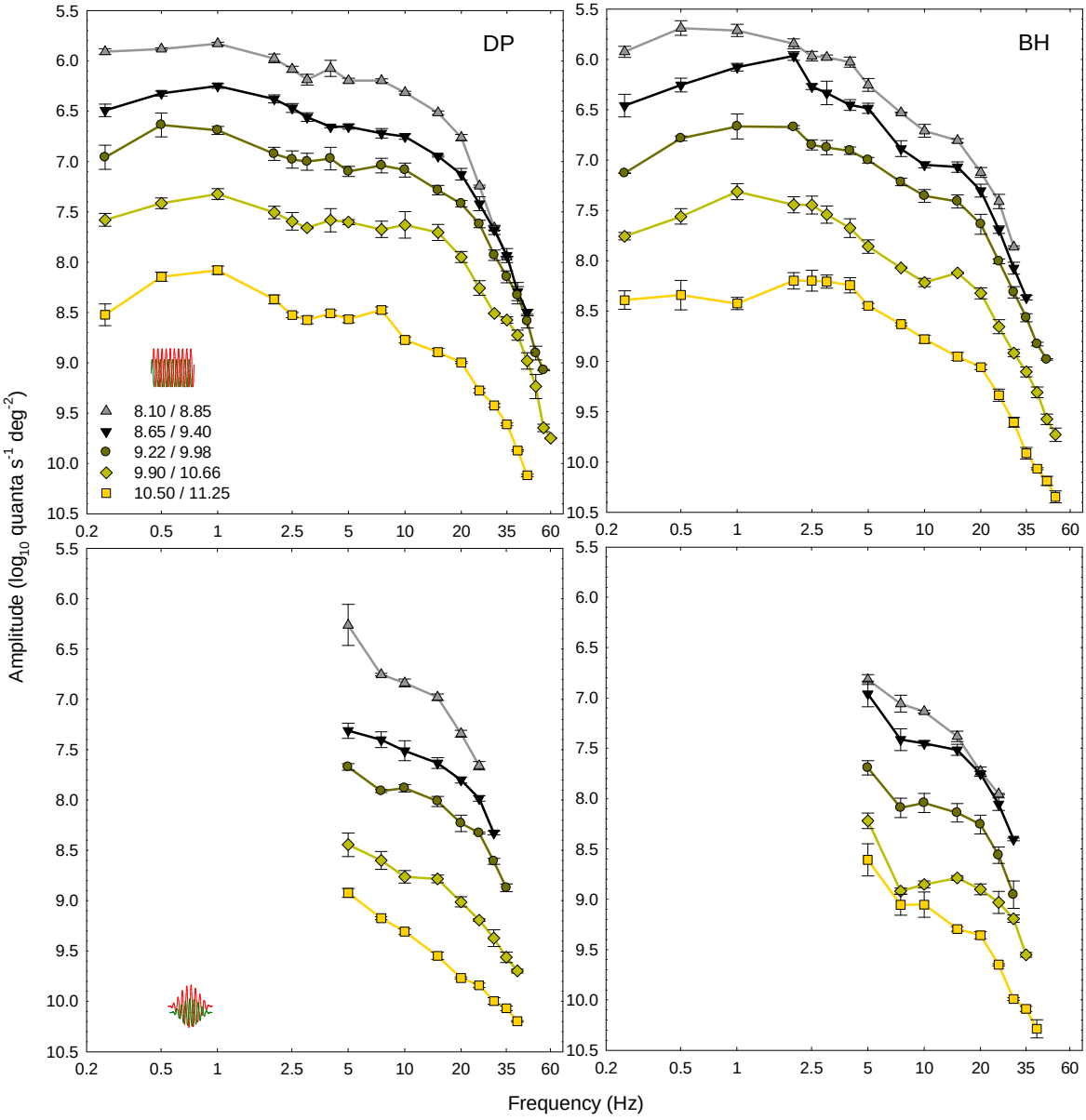

Figure 3.15. Mean ± 1 SE amplitude required for subjects to detect sinusoidal flicker (top row) and colour change at f_{am} (bottom row) as a function of f_c. The inset graph in the bottom left corner of each row shows the temporal waveform used to measure the sensitivity curves in each row of graphs (at f_c=10 Hz for example and f_{am}=0.5 Hz or f_{am}=0 Hz). The left and right columns show the data for subject DP and BH, respectively. The stimulus was a 529-nm light superimposed on a 650-nm light (numbers in legend show the time-averaged radiance for 529 nm/650 nm in $\log_{10}$ quanta s^{-1} deg^{-2}) with f_c 180º out-of-phase and f_{am} in-phase (M-cone isolating stimulus).

The colour-change sensitivities for all subjects also show higher values at frequencies at and below 10 Hz for the cone-isolation conditions (Figures 3.14 and 3.15) compared to the

colour- and brightness-change sensitivities for monochromatic conditions (Figures 3.10 and 3.11).

The L-cone data (Figure 3.14) confirms earlier results (Sections 3.1 and 3.4) that the fall-off in sensitivity of the curve for detecting changes in appearance at f_{am} is shallower than the slope of the curve for detecting flicker. The two curves tend to be parallel above 25 Hz as in Section 3.4.

Unlike the L-cone data (Figure 3.14) and earlier data in Sections 3.1 and 3.4, the M-cone data (Figure 3.15) shows that at frequencies below 10 Hz, the sensitivity curve for the change in appearance at f_{am} rapidly increases. This increase leads to greater parallels in slope between the curves for flicker and colour change.

3.5.3 Discussion

Combining the silent-cone substitution technique with the nonlinear distortion analysis in this section may reveal the temporal characteristics of the early (pre-nonlinearity) stage of the cone pathways that reflect the temporal response of cones more closely than when using silent-cone substitution alone. (The isolation of an early stage of the cone pathways is supported by the results that show shallower slopes for the appearance-change-at-f_{am} sensitivity curves compared to the flicker sensitivity curves, as supported by previous evidence in Sections 3.1 and 3.4.) These pre-nonlinearity stages are similar between the L- and M-cone pathways but have both similarities (e.g. a shift in sensitivity to higher frequencies with increasing time-averaged radiance) and differences (e.g. less low frequency attenuation) compared to the pre-nonlinearity stages in the brightness and colour pathways (Section 3.4). This suggests that the M-cone flicker and L-cone flicker signals must interact before the nonlinearity.

The results suggest that the pre-nonlinearity stage can be described as band-pass for monochromatic conditions (most pronounced for the 560 nm conditions, Figure 3.11) and more low-pass for cone-isolation conditions (most pronounced for the L-cone conditions, Figure 3.14). However, in order to validate these suggestions, it is necessary to infer the response of the pre-nonlinearity stage at low frequencies (see Section 7.1).

For cone-isolation conditions, the higher sinusoidal flicker sensitivity at low frequencies, compared to that for monochromatic conditions, may be explained by the activation of the chromatic pathway at low-frequencies. These observations are consistent with previous studies showing that for silent-cone-substitution conditions, the flicker sensitivity at low frequencies can be described by the chromatic pathway while that at high frequencies can be described by the achromatic pathway (Kelly & van Norren, 1977; Lennie, 1984; Smith et al., 1995). This is not surprising considering that subjects report chromatic flicker at low frequencies when the two lights that produce the cone-isolation conditions are flickered out-of-phase.

The comparison of the attenuation characteristics measured so far allows the inference of the relative sequence in visual processing since cascading filters (except for compensation or differentiation) tend to increase the slope of high-frequency attenuation (Kelly, 1976; Levinson, 1968; Watson, 1986). Figures 3.8 and 3.9 show that the sensitivity curves for changes in appearance at f_{am} have a shallower slope than the sensitivity curves for sinusoidal flicker, which suggests that there is a late (post-nonlinearity) stage that attenuates high frequencies in the TCSF pathway. At low frequencies, the sensitivity curve for changes in appearance at f_{am} tends to be parallel to the sensitivity for sinusoidal flicker (Figures 3.8 and 3.9), which suggests that the post-nonlinearity filter attenuates low frequencies equally i.e. it is likely to be low-pass.

This chapter met its aim to provide a measure of the pre-nonlinearity stage preceding the nonlinearity for the pathways under investigation. The differences between the pre-nonlinearity stages and the TCSF for the various conditions indicate that a post-nonlinearity stage is also present, which selectively attenuates frequency components in the temporal contrast sensitivity pathways (see Chapter 4).

4 The stages after the pre-nonlinearity stage

The results in Chapter 3 showed that the pre-nonlinearity stage of the temporal contrast sensitivity pathway can be measured at frequencies ≥5 Hz. The difference in the attenuation characteristics between the pre-nonlinearity stage and the overall temporal contrast sensitivity function (TCSF) can be explained by an additional frequency-dependent stage that follows the pre-nonlinearity stage and the nonlinearity (i.e., a post-nonlinearity stage), which is consistent with the sandwich model (Section 1.2).

Estimates of the post-nonlinearity stage's attenuation characteristics have been rare, e.g. there has been a single study on the S-cone pathway (Stockman & Plummer, 1998), partly because of the difficulties in accounting for the effect of the nonlinearity on the measured sensitivities (addressed in Chapter 5). Neither Wu et al.'s, (1996) nor MacLeod and He's (1992) techniques and analyses allowed the measurement of the post-nonlinearity stage. However, the techniques and analysis outlined in the present study make it possible to measure the attenuation characteristics of the stages after the pre--nonlinearity stage in the L- and M-cone pathways. The effect of the nonlinearity on these measurements and the consequent estimate of the post-nonlinearity stage are considered in the next two chapters.

Chen et al. (1993) attempted to measure the pre-nonlinearity and post-nonlinearity stages of spatial summation by varying the spatial frequency and the orientation, respectively, of two laser interference fringes that evoked the perception of an illusory low-frequency grating generated by a nonlinearity in the visual system. However, they do not distinguish the stages after the pre-nonlinearity stage from the post-nonlinearity i.e., they did not consider that by keeping the spatial frequency of the laser interference fringes and varying their orientation (and measuring the sensitivity to the illusory grating) they would keep the output of the pre-

nonlinearity stage constant but they would vary the output of the nonlinearity as well as the output of the post-nonlinearity stage. Therefore, their measurements would not reflect just the attenuation by the post-nonlinearity stage but they would also reflect the change in amplitude due to the input-output function of the nonlinearity. The complex curve they use to fit their results may be simplified by accounting for the effect of the nonlinearity.

In the present chapter, the sensitivity to the illusory colour or brightness change for amplitude-modulated flickering stimuli is measured as a function of amplitude-modulation frequency (f_{am}) for a fixed carrier frequency (f_c). By keeping f_c fixed, the signal's attenuation by the pre-nonlinearity stage is kept constant. In effect, then the output of the post-nonlinearity stage is measured relative to the input of the nonlinearity. However, the output (and distortion) of the nonlinearity will vary as a function of the input modulation. To estimate the temporal characteristics of the post-nonlinearity stage, it is necessary to correct for the effect of the nonlinearity. The relationship between input modulation and output distortion is investigated in the next chapter. To reiterate, the measurements in this chapter reflect the temporal characteristics of the post-nonlinearity filter convolved with the effects of the nonlinearity.

4.1 Procedures

The same targets (used in Sections 3.1, 3.4 and 3.5) were also used to measure the stages after the pre-nonlinearity stage in the brightness pathway, the L- and M-cone chromatic pathway, the L-cone pathway and the M-cone pathway. The temporal waveform of the target was again amplitude-modulated flicker (as described in Section 2.1.2) but instead of varying the carrier frequency (f_c) and keeping the amplitude-modulation frequency (f_{am}) fixed at 0.5 Hz (as in Chapter 3), f_c was fixed at 30 Hz (see Section 3.2.1) and f_{am} was varied between 0.25 and 5 Hz.

Subjects were asked to adjust the modulation of the amplitude-modulated flickering target in 0.10 and 0.02 $\log_{10}$ unit steps until the change in appearance at f_{am} was just at threshold. The f_{am} was either systematically increased or it was systematically decreased between 0.25 Hz and 5 Hz in alternative experimental runs.

4.2 Results

Figures 4.1 and 4.4 show the $\log_{10}$ modulation sensitivities to the change in appearance at f_{am} as a function of f_{am}. The amplitudes for detecting a change in appearance at f_{am} in response to monochromatic stimuli (Figures 4.2 and 4.3) and cone-isolating stimuli (Figure 4.5) were calculated as described in Section 3.4.2 and 3.5.2, respectively.

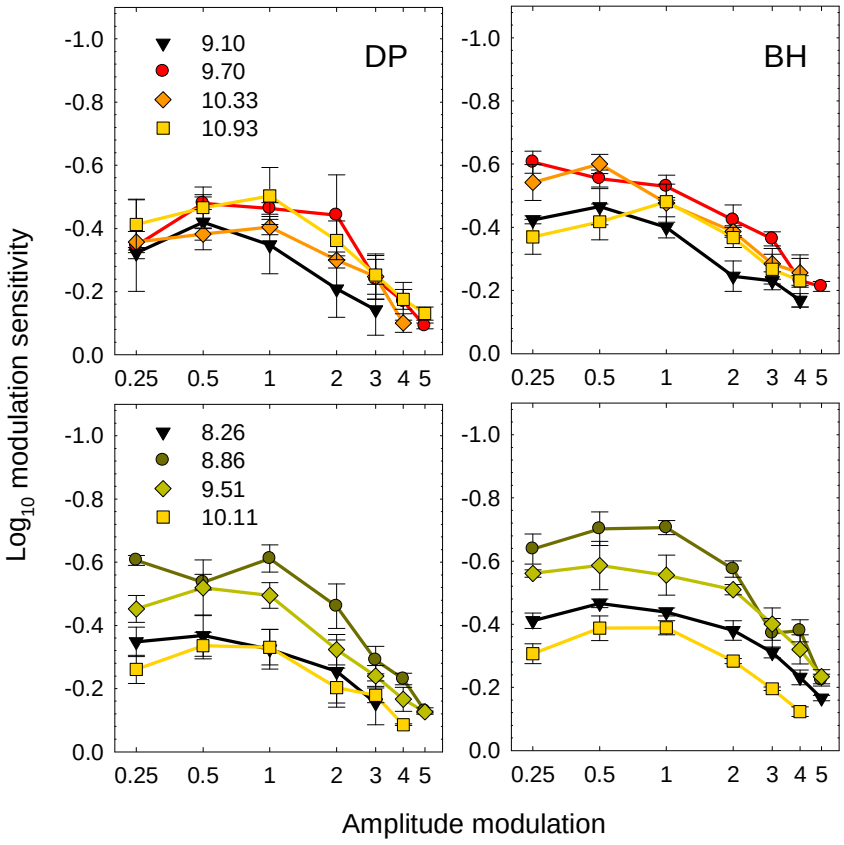

Figure 4.1. Mean ± 1 SE $\log_{10}$ modulation sensitivities for colour change at f_{am} for an amplitude-modulated 650-nm target (top row) and brightness change at f_{am} for an amplitude-modulated 560-nm target (bottom row) as

a function of f_{am}. The left and right columns show the data for subject DP and BH, respectively, and the legend shows the time-averaged radiance level of the targets in $\log_{10}$ quanta s^{-1} deg^{-2}.

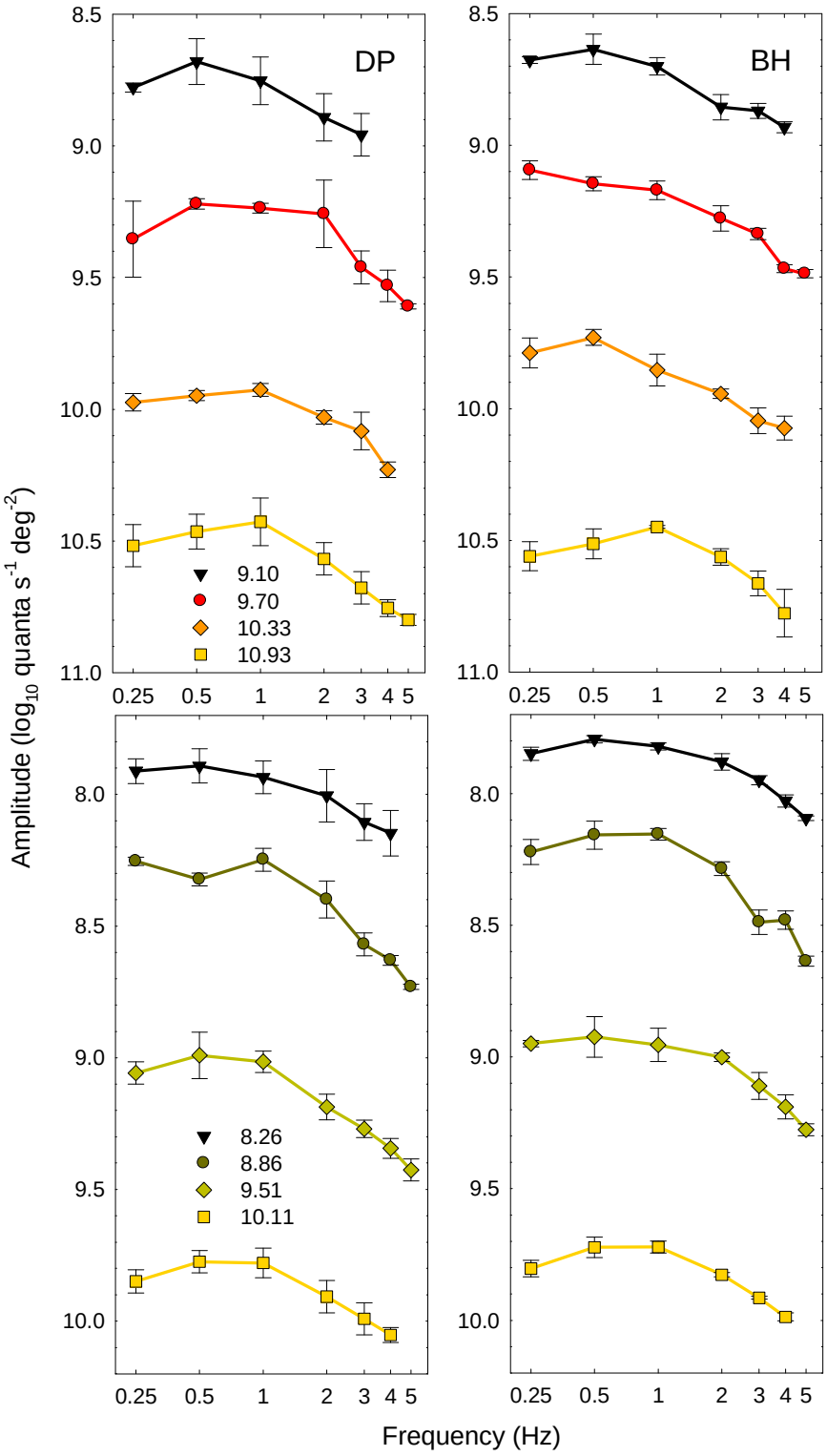

Figure 4.2. Mean ± 1 SE amplitude required for subjects to detect colour change at f_{am} for an amplitude-modulated 650-nm target (top row) and brightness change at f_{am} for an amplitude-modulated 560-nm target

(bottom row) as a function of f_{am}. The left and right columns show the data for subject DP and BH, respectively, and the legend shows the time-averaged radiance level of the targets in $\log_{10}$ quanta s^{-1} deg^{-2}.

The sensitivity to colour change at f_{am} as a function of f_{am} was also measured for the 529-nm targets used in Section 3.4 (Figure 4.3).

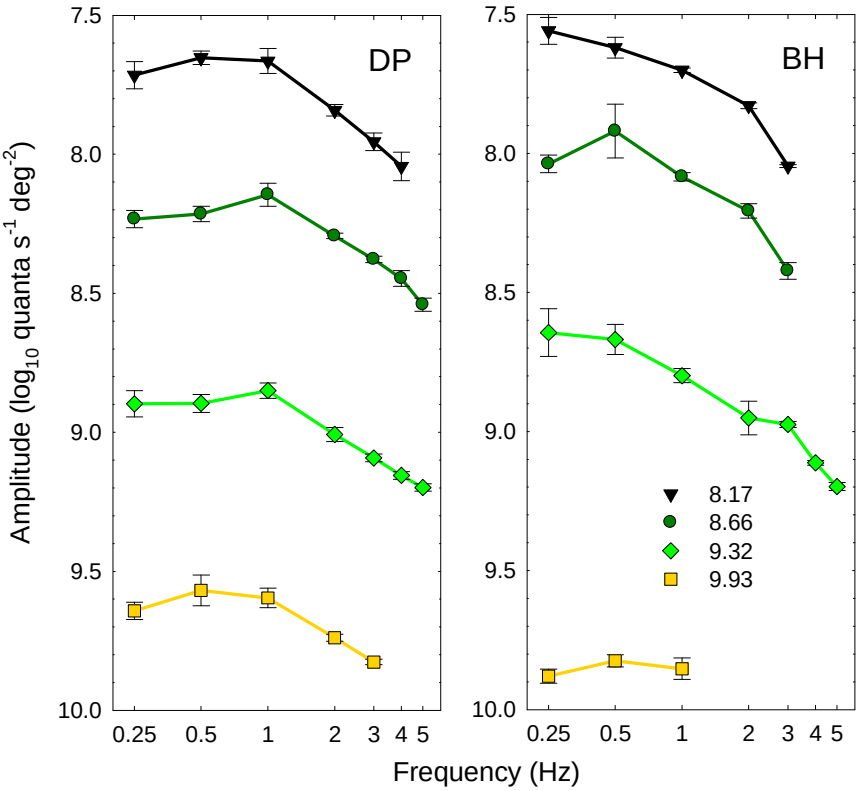

Figure 4.3. Mean ± 1 SE amplitude required for subjects to detect colour change at f_{am} for an amplitude-modulated 529-nm target as a function of f_{am}. The left and right columns show the data for subject DP and BH, respectively, and the legend shows the time-averaged radiance level of the targets in $\log_{10}$ quanta s^{-1} deg^{-2}.

The results for both colour change and brightness change (Figures 4.1-4.3) indicate low-pass filter characteristics that fall-off in sensitivity above about 1 Hz. There is no systematic change in the curve shapes for colour change and brightness change with variation in the time-averaged radiance level. Furthermore, the majority of the error bars overlap when the curves are normalised to peak sensitivity, which suggests that there are no significant differences in the shapes of the curves for the 529 nm, 560 nm and 650 nm across subjects.

For cone-isolating conditions (Figures 4.4 and 4.5), where 650-nm and 529-nm lights were superimposed, subject BH showed a relatively higher sensitivity to L-cone stimuli while subject DP showed relatively higher sensitivity to M-cone stimuli.

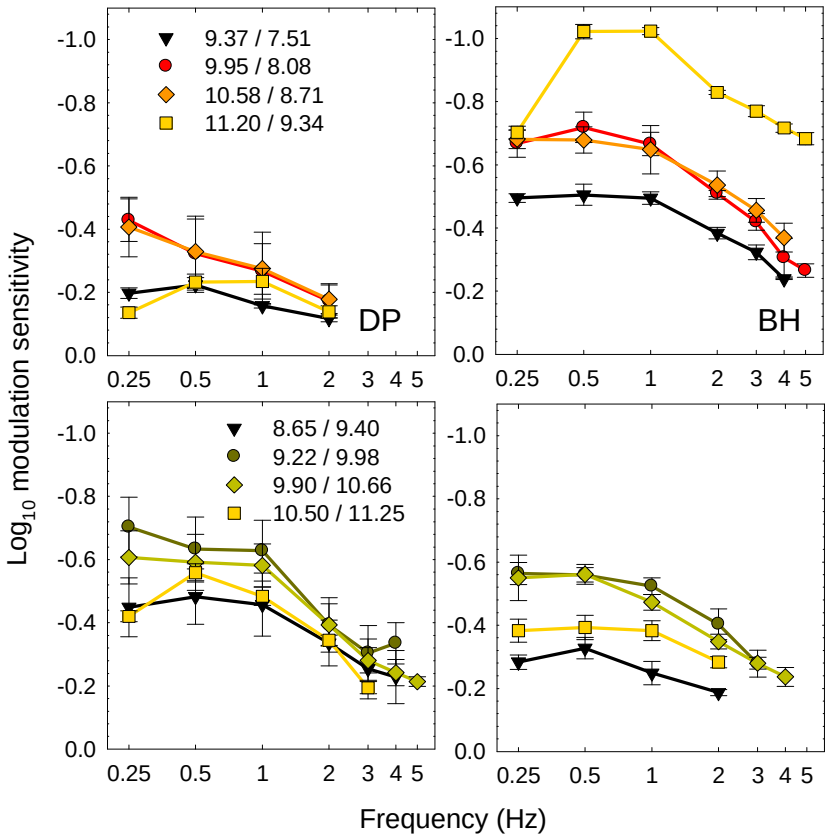

Figure 4.4. Mean ± 1 SE $\log_{10}$ modulation sensitivities for colour change at f_{am} as a function of f_{am} for an L-cone stimulus or an M-cone stimulus amplitude-modulated stimulus. The legend shows the radiance (in $\log_{10}$ quanta s^{-1} deg^{-2}) of the 650 nm/529 nm (top row) and 529 nm/650 nm (bottom row) component lights.

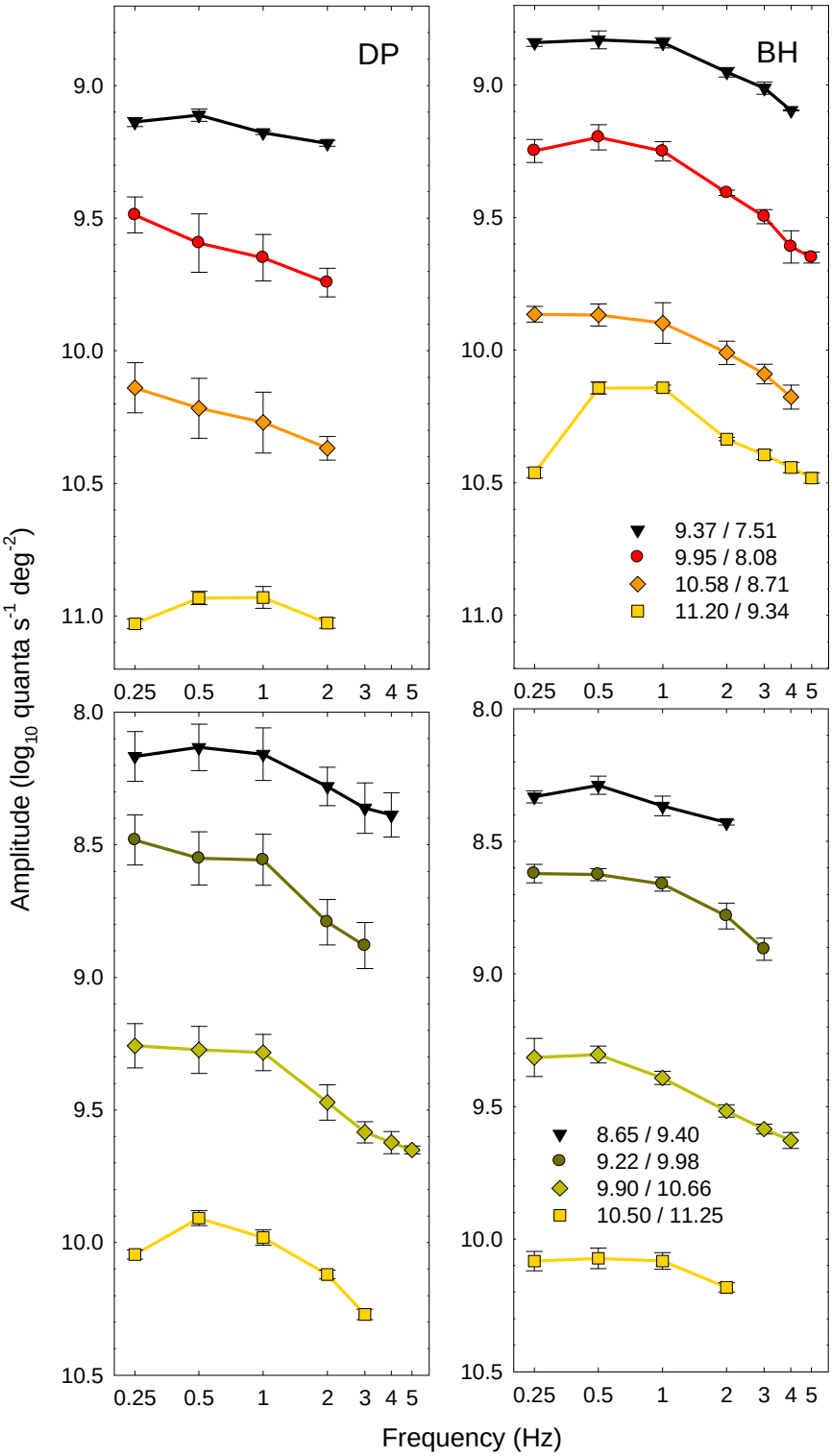

Figure 4.5. Mean ± 1 SE amplitude required for subjects to detect colour change at f_{am} as a function of f_{am} for an L-cone (top row, legend shows the radiance of the 650 nm / 529 nm component lights) or M-cone (bottom row, legend shows the radiance of the 529 nm / 650 nm component lights) amplitude-modulated stimulus.

The results for cone-isolating stimuli (Figures 4.4 and 4.5) show similar low-pass characteristics (including a cut-off frequency near 1 Hz) to the results for monochromatic conditions (Figures 4.1-4.3). Similarly, there is no systematic change in the curve shapes for colour change with variation in the time-averaged radiance level of cone-isolating targets and the majority of the error bars overlap when the curves are normalised to peak sensitivity, which suggests that there are no significant differences in the shapes of the curves across targets and subjects. However, at the highest time-averaged radiance level, each of the four targets (650 nm, 560 nm, L-cone and M-cone conditions) have a higher threshold at 0.25 Hz compared with that at 1 Hz (apart from the data for BH at 560 nm, Figure 4.1), which may indicate transition from low-pass characteristics to band-pass characteristics at very high time-averaged radiance levels.

4.3 Discussion

The results for the combined effect of the nonlinearity and post-nonlinearity stages (Figures 4.1 and 4.4) indicate low-pass characteristics with a cut-off frequency around 1 Hz (i.e., maximum sensitivity occurs below about 1 Hz amplitude-modulation frequency and then falls-off at higher frequencies). This means that the pre-nonlinearity stage is best measured when f_{am} <1 Hz so that there is minimal attenuation by subsequent stages when f_{am} is fixed and the widest possible frequency range can be measured for the pre-nonlinearity stage. Therefore, f_{am}=0.5 Hz was a suitable frequency to use for measuring the pre-nonlinearity stage in Chapter 3 because it provided the highest sensitivity to the colour or brightness change.

The similarity between the sensitivities to changes in appearance at f_{am} as a function of f_{am} for all four L- and M-cone conditions (isolating the colour pathway, brightness pathway,

L-cone pathway and M-cone pathway) indicates that the temporal characteristics after the pre-nonlinearity stage are likely to be independent of the L:M cone ratio.

The differences between subjects for L-cone conditions (for which BH has higher sensitivities than DP, top row Figure 4.4) and M-cone conditions (for which DP has higher sensitivities than BH, bottom row Figure 4.4) may be attributed to different L- and M-cone populations between subjects e.g. different L:M ratios (Kremers, Scholl, Knau, Berendschot & Sharpe, 2000). The maintenance of the shape of the sensitivity curve for appearance change at f_{am} as a function of f_{am} despite these differences (Figure 4.4) suggests that the stages after the pre-nonlinearity are little influenced, if at all, by differences in L- and M-cone ratios.

The critical amplitude-modulation frequency above which subjects could no longer see a change in appearance at f_{am} varied very little across intensity levels ($\leq$3 Hz). In addition, the similarity of the data across intensity levels indicates that the combined characteristics of the nonlinearity and the post-nonlinearity stage vary little, if at all, with the intensity level (i.e., they adapt little, if at all, with light intensity).

This chapter provided a measure of the stages after the pre-nonlinearity stage (i.e., the combined effect of the nonlinearity and the post-nonlinearity). However, as previously noted, the intervening nonlinearity between the pre-nonlinearity and post-nonlinearity stages is likely to change the input to the post-nonlinearity stage relative to the input to the visual system. In order to estimate the late (post-nonlinearity) filter from the measurements in this chapter, it is first necessary to determine the properties of the nonlinearity (see Chapter 5).

5 The nonlinearity

In Chapter 4, the output of the post-nonlinearity stage was measured relative to the input modulation to the nonlinearity. However, to estimate the attenuation characteristics of the post-nonlinearity stage in isolation it is necessary to know the relationship between the input modulation to the nonlinearity and its output distortion. The purpose of this chapter is to measure the output distortion of the nonlinearity as a function of the input modulation in order to scale the measurements of Chapter 4 to allow a true estimate of the post-nonlinearity stage, which will be given in Chapter 6. In addition, the results in the present chapter will allow comparison between the characteristics of the various nonlinearity(ies) lying in the L- and M-cone pathways (see Sections 5.5 and 7.2).

Several experimental methods for measuring the input to the post-nonlinearity stage were tested in pilot experiments (Section 5.1) at the end of which two matching techniques were chosen that were found to be suitable for measuring the brightness change (Sections 5.2 and 5.3) and the colour change (Section 5.4) of the flickering targets (used in Sections 3.1, 3.4 and 3.5).

5.1 Experimental design

In order to measure the output distortion of the nonlinearity, it is necessary to measure the change in appearance produced by the nonlinearity as a function of the input modulation to the nonlinearity. Henceforth, this function will be referred to as the input-modulation vs. output-appearance-change-at-f_{am} function or the IMOAC function for brevity.

Several methods for quantifying the change in appearance at f_{am} as a function of input modulation have been used before, e.g. interleaving the target and a matching stimulus (Wu

et al., 1996) and nulling the colour change (Stockman & Plummer, 1998). (The majority of early studies that investigated changes in appearance of flickering lights did not measure the change in appearance as a function of input modulation but varied the wavelength of the target and matching stimuli to match the change in colour or brightness appearance at f_{am} for a fixed modulation, see Section 1.3.)

Wu et al. (1996) interleaved one cycle of an amplitude-modulated target stimulus undergoing a brightness change (with f_{am}=0.5 Hz and high f_c) with one cycle of the matching stimulus that consisted of a raised cosine also of 0.5 Hz. The wavelength of the target and matching stimuli was the same (560 nm). They adjusted the amplitude of the matching stimulus until the brightness of both the target and the matching stimuli appeared equal.

For S-cone stimuli undergoing a colour change, Stockman & Plummer (1998) cancelled (i.e., nulled) the colour change of an S-cone stimulating 440-nm amplitude-modulated flickering light (at f_{am}=0.5 Hz and high f_c), which appeared to change colour from blue to yellow, by adding a 440-nm sinusoidally-flickering light (nulling stimulus) with a frequency equal to f_{am} and its peak approximately synchronised with the peak modulation.

In the present study, the target and matching stimuli were not interleaved or alternated. The initial experiments in this study focused on measuring the brightness change, which were technically easier because only one wavelength was required to match the brightness change. Later experiments focused on measuring the colour change of amplitude-modulated lights, which were technically more complex because two or more wavelengths were required.

For brightness enhancement using 560-nm targets (as described in Section 3.4), nulling the brightness change was only possible at low stimulus modulations. For changes in colour, using 650-nm targets (as described in Sections 3.1 and 3.4), residual colour changes always

remained when nulling the colour change with single (650 nm) and mixed (650 nm and 560 nm) stimuli. Consequently, the nulling technique could not be used to measure the IMOAC curves either for brightness change or for colour change of L- and M-cone stimuli.

Subsequent pilot experiments focused on matching techniques (Bartley, 1951a; Nilsson & Nelson, 1971; Pokorny, Smith & Yamashita, 1987; see original developments by Rayleigh, 1881; for variations of the matching technique see: van der Horst & Muis, 1969; Walters & Harwerth, 1978)). Several parameters were initially varied for the technically simpler brightness-enhancement matching for which the target and matching lights were both 560 nm. In initial matching experiments, vertically oriented target and matching half-fields of 4° were presented separated by 1 º, 0.5º, 0.25º and 0º. The separating band was a steady light with the same wavelength and time-averaged radiance as the target. Fixation was central, as always. Subjects were able to make matches most consistently when there was no separating band (0°). (The success of the minimal border for the matching conditions can be explained by the fact that colour and brightness changes were most salient when centrally fixated and that subjects did not have to move their eyes from the target to the matching stimulus, thus they avoided the additional factor of episodic memory for the change in appearance.) The target and matching lights were on continuously between settings. Subjects adapted for minimum of two minutes before they made their first setting and for a minute at the start of every new modulation level. They were instructed to fixate the centre of the border between the target and matching lights.

The appearance change at f_{am} for each of the 560-nm targets described in Section 3.4.1 was measured using two methods (described in Sections 5.2.1 and 5.3.1), which differed in the matching stimulus that was used.

5.2 Brightness matching with varying modulation around the mean

Brightness enhancement was initially measured using target and matching stimuli of equal time-averaged radiance in order to keep the adaptation level of the two stimuli the same.

5.2.1 Procedures

The time-averaged radiance of the 560-nm matching stimulus was calibrated to be equal to the time-averaged radiance of the 560-nm target stimulus at each of the four intensity levels so that the mean adaptation levels were the same (Figure 5.1). Subjects confirmed that the target and the matching stimulus appeared the same when steady (in hue, brightness and saturation) before starting the experiment.

The time-averaged radiance remained fixed when the target and matching light were modulated around the mean. Each experimental run was repeated three times on separate days and consisted of ten trials each with three settings (as described in Section 2.2.1). The ten trials either decreased in modulation (from the maximum modulation of 92% to 2% in steps of 10%) or increased in modulation (in steps of 10%). The descending and ascending modulations alternated between every experimental run.

The amplitude-modulation frequency was 0.5 Hz (i.e. the same f_{am} that was used to measure the pre-nonlinearity stage in Chapter 3) and the carrier frequency was 30 Hz (i.e. the same f_c that was used to measure the stages after the pre-nonlinearity stage in Chapter 4). The experiments were also repeated for two additional carrier frequencies, f_c=20 Hz and f_c=10 Hz.

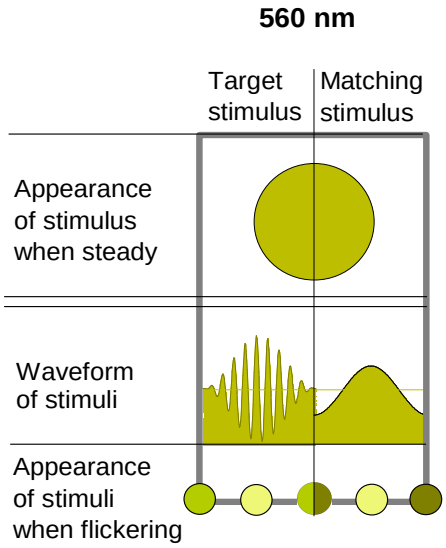

Figure 5.1. Schematic of the visual stimulus used to match the brightness enhancement of a 560-nm amplitude-modulation flickering target (f_{am}=0.5 Hz and f_c=10 Hz, left half of the panel) by varying the modulation of a sinusoidal stimulus of the same wavelength and time-averaged radiance (f=0.5 Hz, right half of the panel). The disk at the top of the panel indicates the approximate appearance of the target (left half) and the matching stimulus (right half) when both are steady around 9.51 $\log_{10}$ quanta s^{-1} deg^{-2}. The small circles at the bottom of the panels indicate the approximate appearance of the target at the minimum and maximum modulation and of the matching field at the trough and peak.

Subjects had two main tasks during the experiment: to set the modulation (Section 5.2.1.1) and to set the phase (Section 5.2.1.2) of the matching stimulus.

5.2.1.1 Modulation settings

Subjects adjusted the depth of modulation of the matching light (sinusoidally flickering with frequency equal to f_{am} of the target) using large steps (0.1 $\log_{10}$ units) or small steps (0.02 $\log_{10}$ units) until the peak brightness of the matching light matched the appearance of the peak brightness enhancement of the target (Figure 5.2). If there was a range of sinusoidal modulations that matched the maximum brightness enhancement then subjects were instructed to set the minimum modulation needed to attain the best possible match in appearance.

In this version of the method, subjects were asked to ignore the appearance of the matching stimulus at the trough when making their match (because the aim of the task was to match the peak of the brightness enhancement) but to report the appearance of the matching stimulus at the trough compared to the appearance of the target stimulus at minimum modulation. Subjects reported that even if the target and matching stimuli were matched at the peak brightness they appeared different at the trough, which was a drawback of this matching technique.

5.2.1.2 Phase settings

The subjects also adjusted the phase of the matching stimulus relative to the target until the peak brightness of the matching stimulus was synchronised with the peak brightness enhancement of the target (Figure 5.3). Subjects could advance or retard the phase of the matching stimulus by 2° steps or invert the phase by 180º, which allowed them to check their settings (e.g. if subjects were close to the right phase setting then inverting the signal by 180° would lead to maximum flicker and if they were about 90° away from the correct setting then the inversion would lead to very little noticeable change). If there was a range of phase measurements at which the maximum change in appearance at f_{am} appeared to be in phase with the peak of the matching light then subjects were instructed to set the middle of the range.

Adjustment of the phase allowed more precise matching because if the matching stimulus was not precisely in phase with the peak brightness change then the subjects would underestimate the magnitude of the brightness change. The starting phase at the beginning of each experimental condition was 0º i.e. the peak amplitude for the sinusoidally-flickering matching light was in phase with the peak modulation for the amplitude-modulated target.

The phase at the start of each subsequent setting in the experiment was equal to the last phase setting made by the subject in the previous setting. In practice, the phase settings were relatively small.

For each setting, subjects were asked to adjust the modulation, then to adjust the phase and subsequently to repeat this procedure (adjusting the modulation and the phase) until they found the best possible match.

5.2.2 Results

Subjects reported that the target appeared the same in hue and brightness as the matching field when both were steady. However, the matching stimulus at its trough, which coincided with the point of minimum modulation of the target, always appeared darker than the target at its minimum modulation. Nevertheless, a good match at the peak modulation was generally possible.

Figure 5.2 shows that the IMOAC curves for DP and BH are approximately linear at low time-averaged radiance levels. As the time-averaged radiance level is increased, the slopes of the IMOAC curves for DP tend to accelerate with increasing modulation while those for BH tend to decelerate with increasing modulation.

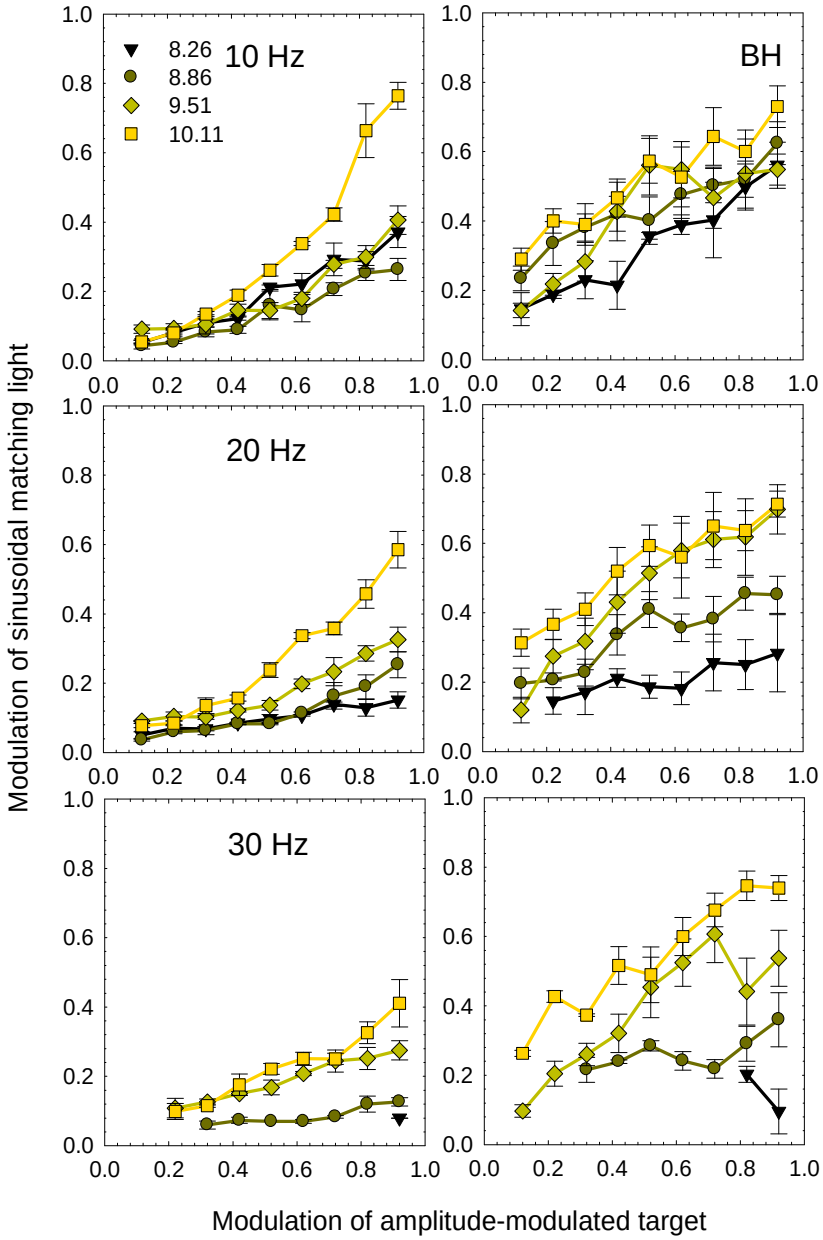

Figure 5.2. Mean ± 1 SE modulation of a 560-nm sinusoidally-flickering light (f=0.5 Hz) needed for the appearance at the peak amplitude of the sinusoid to match the peak brightness enhancement of a 560-nm, amplitude-modulated flickering target (f_{am}=0.5 Hz and f_c=10 Hz for the top row, f_c=20 Hz for the middle row or f_c=30 Hz for the bottom row). For each carrier frequency, the target and matching light had equal time-averaged radiance at one of four levels (indicated in the legend in $\log_{10}$ quanta s^{-1} deg^{-2}).

The carrier frequency does not affect the relative shape of the IMOAC curves in Figure 5.2. However, it affects the magnitude of the IMOAC curves at low intensities, as a result of which at low carrier frequencies the IMOAC curves at low time-averaged intensities can be

measured over a greater range of modulations (see, e.g., the 8.26 $\log_{10}$ quanta s^{-1} deg^{-2} data in Figure 5.2). The change in appearance at f_{am} reaches threshold around 30 Hz for 8.26 $\log_{10}$ quanta s^{-1} deg^{-2} (black symbols, bottom row, Figure 5.2). This threshold value is consistent with the data in the top row of Figure 3.11, which shows that the critical carrier frequency for detecting change in appearance at f_{am} for 560 nm at 8.26 $\log_{10}$ quanta s^{-1} deg^{-2} is 35 Hz. Considering that the sensitivity to change in appearance at f_{am} increases with increasing input modulation then the greater the attenuation by the pre-nonlinearity stage (e.g. at frequencies above the peak frequency ~10 Hz) the smaller the output of the nonlinearity.

Figure 5.3 shows the phase adjustments for each modulation setting in Figure 5.2 at f_c=10 Hz (top row), f_c=20 Hz (middle row) and f_c=30 Hz (bottom row). The dashed red line in Figure 5.3 (as well as in Figures 5.7, 5.11 and 5.13) indicates 0° phase, which is when the peak amplitude of the matching sinusoid is synchronous with the peak modulation of the amplitude-modulated target. The solid lines (in Figure 5.3 as well as Figures 5.7, 5.11 and 5.13) indicate the linear regression of the data points at each time-averaged radiance level. For BH at f_c=30 Hz the regression lines at 9.51 and 8.26 $\log_{10}$ quanta s^{-1} deg^{-2} overlap each other (Figure 5.3). (The deviations in slope for BH at the lowest time-averaged radiance level for f_c=30 Hz can be attributed to the fewer data points at this level compared to higher time-averaged radiance levels.)

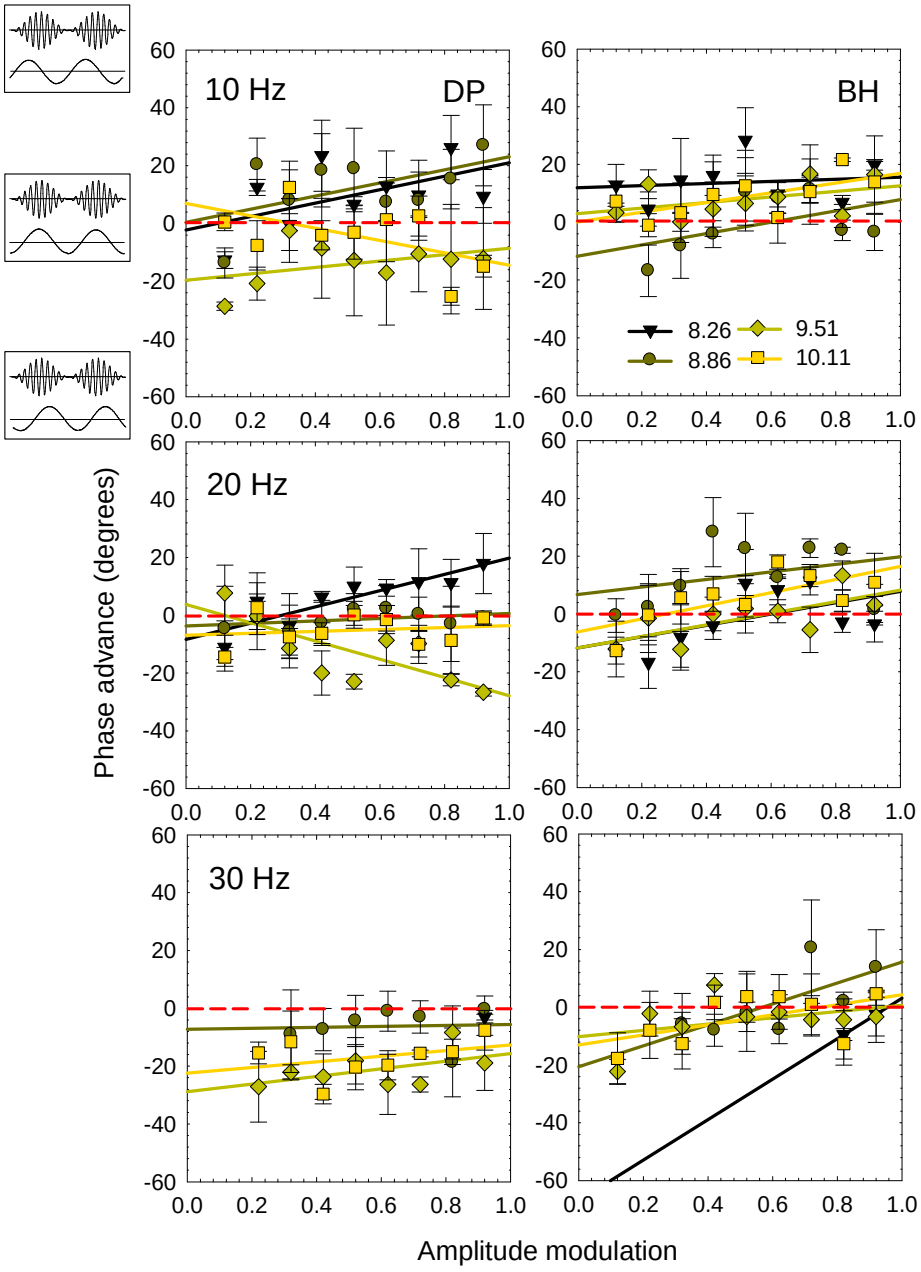

Figure 5.3. Mean ± 1 SE phase advance of a 560-nm sinusoidally-flickering matching light (f=0.5 Hz) relative to a 560-nm amplitude-modulated flickering target (f_{am}=0.5 Hz and f_c=10 Hz for the top row, f_c=20 Hz for the middle row or f_c=30 Hz for the bottom row) so that the brightness changes of the two flickering lights are matching and in phase. For each carrier frequency, the target and matching light had equal time-averaged radiance at one of four levels (indicated in the legend in $\log_{10}$ quanta s^{-1} deg^{-2}). The waveforms in the top left show the approximate advance of the matching stimulus at 60°, 0° and -60° relative to the target stimulus. The dashed red horizontal line indicates a phase advance of 0° and solid lines indicate linear regression of the data.

The majority of the linear regression lines in Figure 5.3 have a positive slope. However, when the 95% confidence intervals of the linear regression fits are plotted (Appendix Figures 9.2-9.4) they do not show a statistically significant deviation from a horizontal line, except at the 8.26 $\log_{10}$ quanta s^{-1} deg^{-2} time-averaged radiance level for f_c=20 Hz (Figure 9.3), and are significantly different from the phase=0º line only in half of the graphs in Figures 9.2-9.4.

A potential complication of matching the brightness change with a sinusoidal stimulus of the same time-averaged radiance as the target is that at high sinusoidal modulations the appearance of the matching light at its trough appears significantly darker than the appearance of the target at its minimum amplitude-modulation. Potentially, this could offset the match by, for example, spatial or temporal brightness induction.

In order to reduce this complication, the IMOAC curves for the brightness enhancement conditions at f_c=30 Hz (bottom row, Figure 5.2) were re-measured using the method described in Section 5.2.1.2.

5.3 Brightness matching with a pedestal

Brightness enhancement was subsequently measured using target and matching stimuli with matched minimum brightness levels (but varying time-averaged radiance levels) in order to keep the appearance-change between the two stimuli similar.

5.3.1 Procedures

The sinusoidally-flickering 560-nm matching light was superimposed on a steady light (i.e. a pedestal). The pedestal had the same wavelength as the target, 560 nm, and was calibrated to have the same radiance as the time-averaged radiance of the amplitude-modulated target at each of the four intensity levels (Figure 5.4). Before proceeding with the

experiment, subjects confirmed that when the target stimulus was steady it appeared the same (in hue, brightness and saturation) as the pedestal.

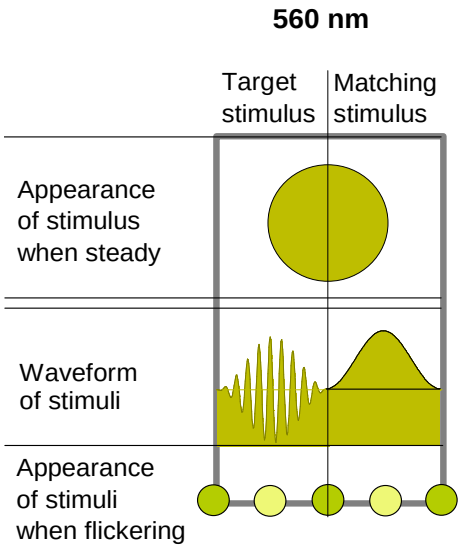

Figure 5.4. Schematic of the visual stimulus used to match the brightness enhancement of a 560-nm amplitude-modulated flickering target (f_{am}=0.5 Hz and f_c=10 Hz, left half of the panel) by varying the relative intensity of a 92% modulated sinusoidal stimulus of the same wavelength (f=0.5 Hz, right half of the panel) superimposed on a pedestal of the same wavelength and time-averaged radiance as the target. The disk at the top of the panel indicates the approximate appearance of the target (left half) and the pedestal (right half) when both are steady around 9.51 $\log_{10}$ quanta s^{-1} deg^{-2}. The small circles at the bottom of the panels indicate the approximate appearance of the target at the minimum and maximum modulation and of the matching field at the trough and peak.

The match was achieved by varying the time-averaged radiance of the sinusoidally-flickering matching light, which was always modulated at 92% and superimposed on the pedestal. The subjects adjusted the mean intensity of the 560-nm sinusoid in ±1/150 $\log_{10}$ unit steps, until the appearance at the peak of the matching light matched the appearance of the brightness enhancement at the target's maximum change in appearance at f_{am} (Figure 5.4). Again, subjects were asked to ignore the appearance of the matching stimulus at the trough when making their match but to report the appearance of the matching stimulus at the trough compared to the appearance of the target at minimum modulation. If there was a range of

intensities that matched the maximum change in appearance at f_{am} then subjects were instructed to set the minimum intensity needed to attain the best possible match of the maximum brightness enhancement (in order to minimise decreases in sensitivity with adaptation). As in the previous method, the subject also varied the phase (as in Section 5.2.1.2).

In practice, this technique produced a better match at the minimum modulation of the amplitude-modulated waveform than that described in Section 5.2.1.1 and thus facilitated matches of the change in appearance at f_{am}.

5.3.2 Results

To allow comparisons between intensity levels (in Chapter 6), the radiances of the sinusoidal matching stimulus modulations (in quanta sec^{-1} deg^{-2}) that matched 92% input modulation were normalised to 0.92, as shown in Figure 5.6. (Whether the relative change in appearance at f_{am} was plotted in radiance units, luminance units or cone-excitation units did not affect the shape of the IMOAC curve if only one wavelength was used for the sinusoidal stimulus to match the change in appearance at f_{am}.) To allow comparison between the data in Figure 5.2 and 5.6, the data in Figure 5.2 were also normalised to the same point as in Figure 5.6 (0.92, 0.92), as shown in Figure 5.5.

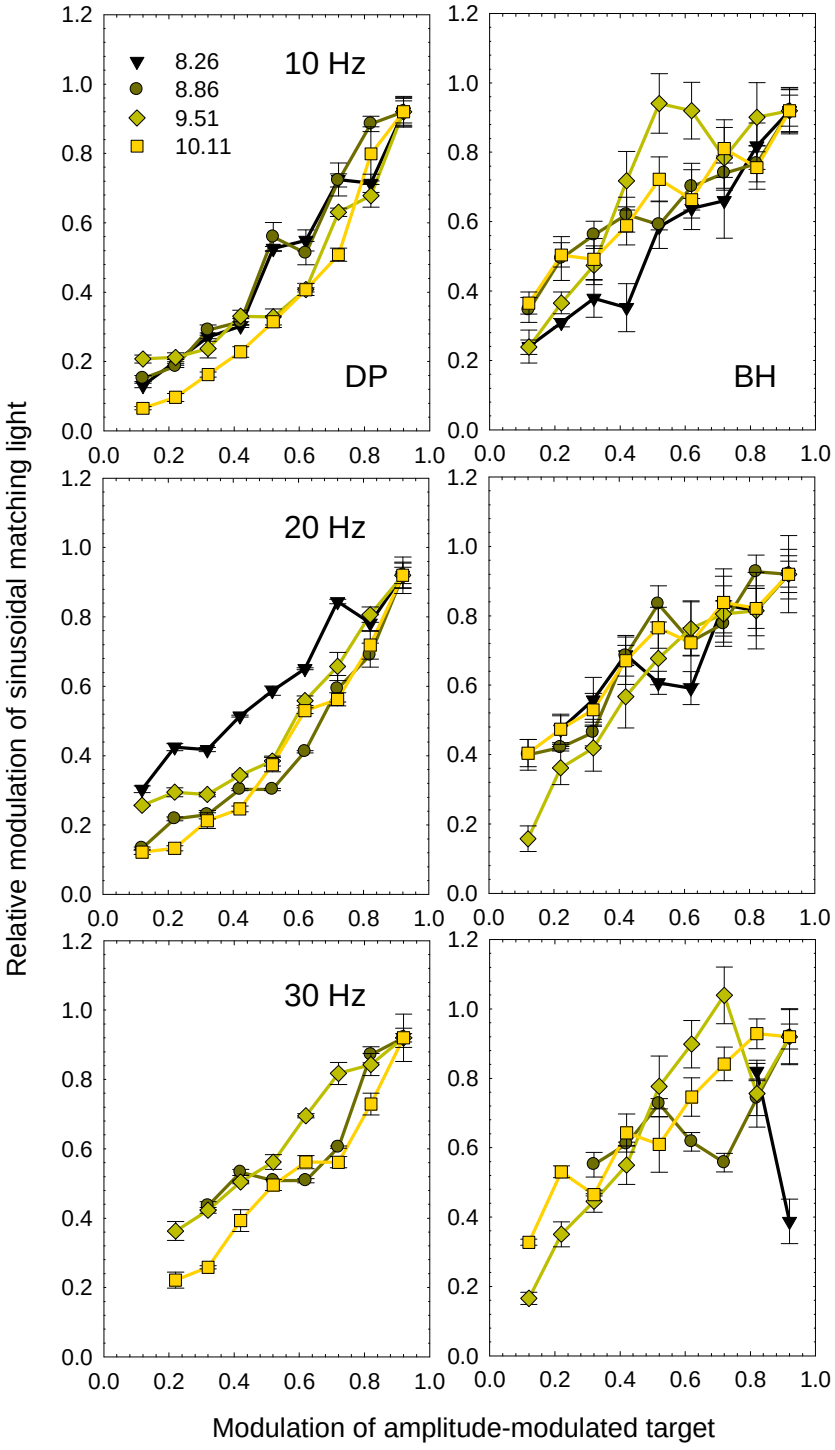

Figure 5.5. Mean ± 1 SE relative modulation of a 560-nm sinusoidally-flickering light (f=0.5 Hz) needed for the appearance at the peak amplitude of the sinusoid to match the peak brightness enhancement of a 560-nm, amplitude-modulated target (f_{am}=0.5 Hz and f_c=10 Hz for the top row, f_c=20 Hz for the middle row or f_c=30 Hz for the bottom row). For each carrier frequency, the target and matching light had equal time-averaged radiance at one of four levels (indicated in the legend in $\log_{10}$ quanta s^{-1} deg^{-2}). All curves were normalised to 0.92 except for the black curve in the bottom right panel, which was normalised to 0.82.

Both subjects show the greatest deceleration for the IMOAC curves at high modulations and the highest mean intensity level (yellow symbols, Figure 5.6), and the least deceleration for the second lowest mean intensity level (dark green symbols, Figure 5.6). At the lowest intensity level, indicated by the black symbols, the sensitivity to brightness change is near threshold and the one or two data points that are present are not enough to determine the shape of the IMOAC curve).

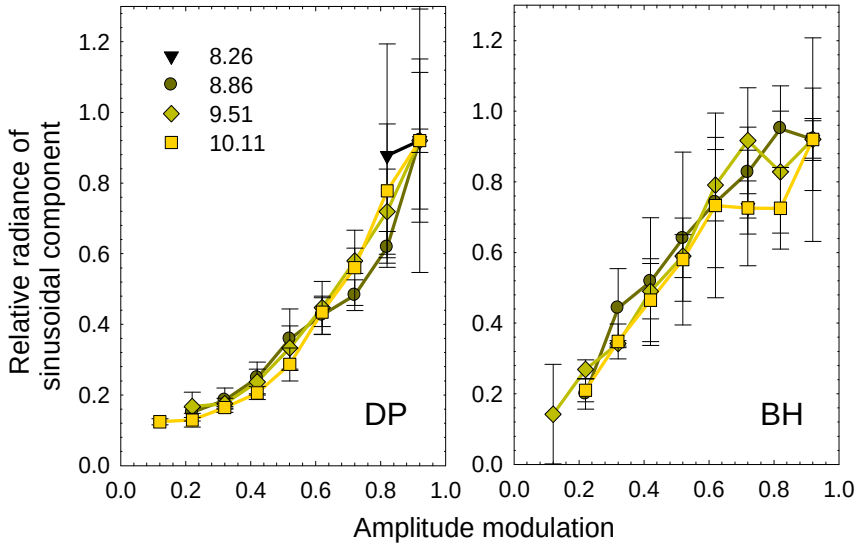

Figure 5.6. Mean ± 1 SE relative radiance of a 92% modulated 0.5 Hz sinusoidally-flickering 560-nm light (superimposed on a pedestal of the same wavelength and time-averaged radiance as the target) needed to match the brightness enhancement of an amplitude-modulated 560-nm target (f_{am}=0.5 Hz and f_c=30 Hz) at four time-averaged radiance levels (legend shows the radiance levels of the target in $\log_{10}$ quanta s^{-1} deg^{-2}).

The phase of the sinusoidally-flickering matching stimulus relative to the amplitude-modulated target for each match of brightness enhancement made by the subjects in Figure 5.6 is shown in Figure 5.7. Subjects made the settings so that the brightness changes of the target and the matching stimuli were in phase. The phase settings were not significantly different from the horizontal line phase=0º at the 95% confidence interval (Appendix Figure 9.5 shows the 95% confidence intervals for the phase settings in Figure 5.7). (The deviations

in slope at the lowest time-averaged radiance level can be attributed to the fewer data points at this level compared to higher time-averaged radiance levels.)

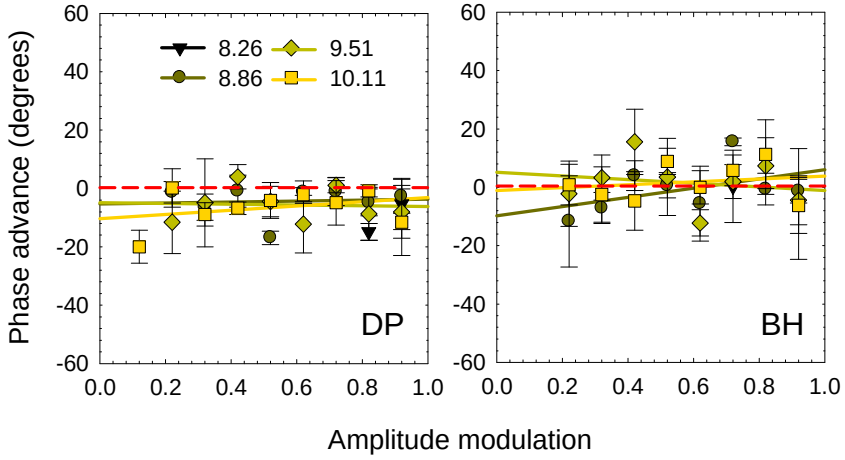

Figure 5.7. Mean ± 1 SE phase advance of a 92% modulated sinusoidally-flickering 560-nm light (superimposed on a pedestal of the same wavelength and time-averaged radiance as the target) relative to a 560-nm amplitude-modulated flickering target (f_{am}=0.5 Hz and f_c=30 Hz) so that the brightness changes of the two flickering lights are matching and in phase at four time-averaged radiance levels (legend shows the radiance levels of the target in $\log_{10}$ quanta s^{-1} deg^{-2}). The dashed red horizontal line indicates a phase advance of 0° and solid lines indicate linear regression of the data.

5.4 Colour matching

The method described in Section 5.3.1 could be used not only for measuring brightness changes but also for measuring colour changes and saturation changes as described in Section 5.4.1. For colour changes, two or more superimposed lights of different wavelengths would be necessary.

5.4.1 Procedures

The amplitude-modulated flickering target was presented in the left half of the central 4º visual field and the 92% modulated, sinusoidally-flickering matching light was presented in

the right half of the central 4º visual field as described in Section 5.2.1. The flicker frequencies and the subjects' tasks were as in Section 5.3.1.

5.4.1.1 Monochromatic stimuli

The 650-nm target that was used to test colour change was the same as described in Sections 3.1 and 3.4 (i.e. presented at four different time-averaged radiance levels). The radiance of the pedestal in the matching stimulus (of equal wavelength to the target, 650 nm) was calibrated to be equal to the time-averaged radiance of the target at each of the four intensity levels. Subjects confirmed that, when steady, the target stimulus and the pedestal appeared the same (in hue, brightness and saturation) before proceeding with the experiment.

A 560-nm, 92% modulated sinusoidally-flickering light was superimposed on the 650-nm pedestal (as described in Section 5.3.1). In pilot experiments, a range of wavelengths were tested and subjects reported that they could match the colour changes best with the 560 nm.

If subjects reported a desaturation of the amplitude-modulated light (e.g. from red to pale yellow) then they had the option to add a 491-nm 92% modulated, sinusoidally-flickering light superimposed on top of the pedestal and the 560-nm sinusoid to complete the match (as shown in Figure 5.8). (In pilot experiments, the 491-nm wavelength was found to produce a suitable desaturation of the matching field.) The 49- nm sinusoidal flicker was always in-phase with the 560-nm sinusoidal flicker (so when the 560-nm sinusoidally–flickering light was varied in phase relative to the target, the phase of the 491-nm light was similarly adjusted).

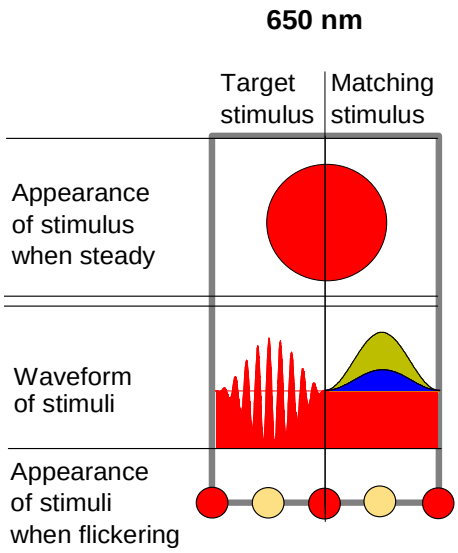

Figure 5.8. Schematic of visual stimulus used to match the colour change and desaturation of a 650-nm amplitude-modulated flickering target (f_{am}=0.5 Hz and f_c=10 Hz, left half of the panel) by varying the relative intensity of two 92% modulated sinusoidal stimuli (at 560 nm and 491 nm with f=0.5 Hz, right half of the panel) superimposed on a pedestal of the same wavelength and time-averaged radiance as the target. The disk at the top of the panel indicates the approximate appearance of the target (left half) and the pedestal (right half) when both are steady around 10.33 $\log_{10}$ quanta s^{-1} deg^{-2}. The small circles at the bottom of the panels indicate the approximate appearance of the target at the minimum and maximum modulation and of the matching field at the trough and peak.

Subjects were asked to adjust the phase of the 560-nm light (and, if present, the 491-nm light) until the colour change of the matching field was synchronised with the colour change of the target. They were also asked to vary the time-averaged radiance of the 560-nm sinusoid, (and also that of the 491-nm sinusoid when present), in ±1/150 $\log_{10}$ unit steps until the appearance at the peak of the sinusoidal stimulus matched the maximum colour change of the amplitude-modulated flicker.

5.4.1.2 Cone-isolation stimuli

A related method to that in Section 5.4.1.1 was also used for L- and M-cone-isolating stimuli. The L-cone-isolation and M-cone-isolation targets were described in Section 3.5 (i.e. amplitude-modulated 650-nm and 529-nm lights were flickered with f_c 180º out-of-phase and

f_{am} in-phase). The stimuli were either equated for M-cone excitation (i.e. L-cone stimuli) or equated for L-cone excitation (M-cone stimuli). Four radiance levels were used in each case as described in Section 3.5.1.

For the cone-isolation conditions, the wavelength of the steady pedestal was varied until the subject found a wavelength the hue of which closely matched the hue of the target when steady. Subjects then adjusted the radiance of the pedestal until its brightness matched the brightness of the non-flickering cone-isolating target. The wavelength selection and brightness adjustment were repeated for each subject at each time-averaged radiance level for the L- and M-cone-isolating targets.

A 92% modulated sinusoidally-flickering light at 0.5 Hz was superimposed on the pedestal (Figure 5.9). The wavelength of this light was chosen by subjects in a pilot experiment. In the pilot experiment, subjects were asked to match the colour change at various target modulations by adjusting the time-averaged radiance of the sinusoidal light, which was initially set to 560 nm (as in Section 5.4.1.1). If subjects were not able to match the colour change at all target modulations using the 560-nm light then the wavelength was progressively increased or decreased away from 560 nm until they were able to match the colour change at all target modulations. This pilot experiment was repeated for each subject and for each time-averaged radiance level of the L- and M-cone-isolating targets.

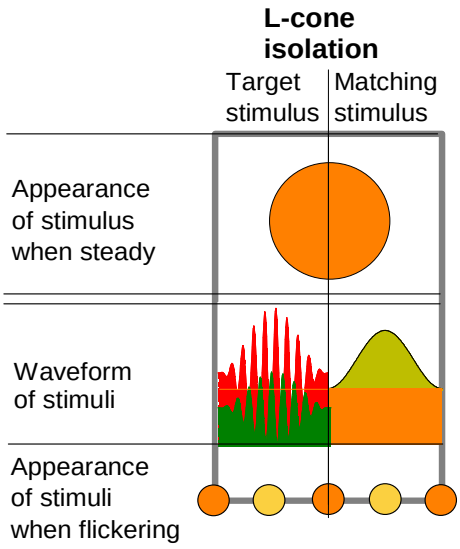

Figure 5.9. Schematic of visual stimulus used to match the colour change of an L-cone-isolating target (using 650-nm and 529-nm amplitude-modulated flickering lights with f_c 180° out-of-phase and f_{am} in phase, left half of the panel) by varying the relative intensity of a 92% modulated sinusoidal stimulus (e.g. 560 nm at the low time-averaged target radiances) superimposed on a pedestal (e.g. 630 nm at the low time-averaged target radiances) matched in appearance to the target when steady. The disk at the top of the panel indicates the approximate appearance of the target and the pedestal when both are steady and the 650-nm light is around 10.58 $\log_{10}$ quanta s^{-1} deg^{-2}The small circles at the bottom of the panels indicate the approximate appearance of the target at the minimum and maximum modulation and of the matching field at the trough and peak.

Once the wavelengths for the pedestal and the superimposed sinusoidally-flickering light were chosen, subjects were asked to vary the time-averaged radiance of the sinusoidally-flickering light in ±1/150 $\log_{10}$ unit steps until the appearance at the peak of the sinusoidal stimulus matched the maximum colour change. They were also asked to adjust the phase of the sinusoidally-flickering light (as described in Section 5.2.1.2) until the colour change of the matching field was synchronised with the colour change of the target. In practice, M-cone matching proved to be impossible for the reasons given below.

5.4.2 Results

When the colour change of the amplitude-modulated target was matched by the peak of the sinusoid, at the trough of the sinusoidally-flickering light, the matching field appeared

approximately the same hue and brightness as the pedestal, which matched the appearance of the target at minimum modulation.

The data for the matches of colour change in a 650-nm amplitude-modulated flickering light are presented in Figure 5.10. At the highest time-averaged radiance level for the target (10.93 $\log_{10}$ quanta s^{-1} deg^{-2}), BH reported that, although he could match the colour change with the 560-nm sinusoid, he experienced difficulties because the target also appeared desaturated at the peak amplitude modulation. Therefore, a 491-nm light was added to the matching stimulus, for this condition only, as described in Section 5.4.1.1. The yellow squares in Figure 5.10 indicate the matches for the colour change with a 560-nm light. The blue triangles (Figure 5.10) indicate the matches for the colour and desaturation changes with 560-nm and 491-nm lights, respectively.

When two wavelengths were used to match the change in appearance at f_{am} (i.e. 560 nm and 491 nm) then the change in appearance at f_{am} is plotted in cone excitation units relative to the wavelength of peak cone sensitivity.

The matches for DP are accelerating functions except at the highest radiance, at which the function saturates at high modulations. The data for BH also shows evidence of saturation at the highest radiance. His functions at lower radiance levels vary between accelerating and linear.

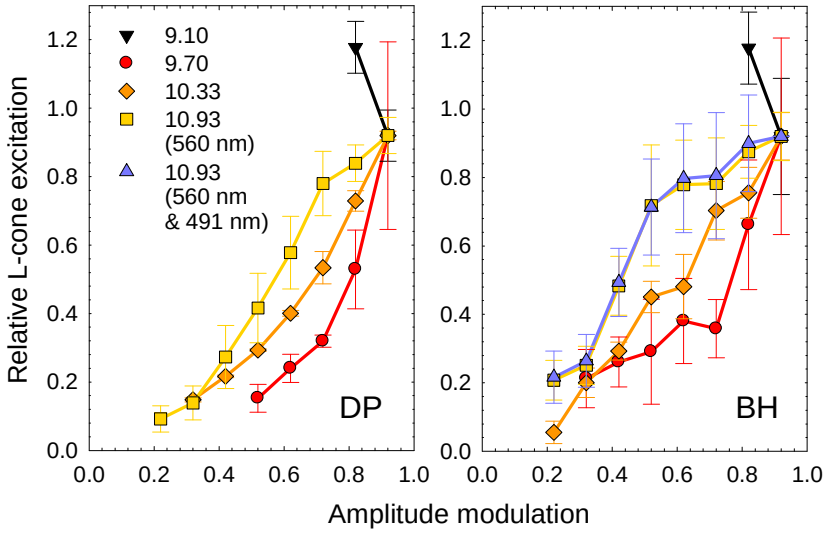

Figure 5.10. Mean ± 1 SE relative radiance of a 92% modulated, 0.5 Hz sinusoidally-flickering 560-nm light (superimposed on a pedestal of the same wavelength and time-averaged radiance as the target) needed to match the colour change of an amplitude-modulated 650-nm target (f_{am}=0.5 Hz and f_c=30 Hz) at four time-averaged radiance levels (legend shows the radiance levels of the target in $\log_{10}$ quanta s^{-1} deg^{-2}).

The phase settings (Figure 5.11) made for the colour-change matches (Figure 5.10) are not significantly different at the 95% level (see Appendix Figure 9.6 for confidence intervals) from the phase=0º line for subject BH. The phase settings for subject DP differ by about 5º from the phase=0º but with increasing modulation the phase settings do not show statistically-significant difference at the 95% level from a horizontal line. (The deviations in slope at the lowest time-averaged radiance level can be attributed to the fewer data points at this level compared to higher time-averaged radiance levels.)

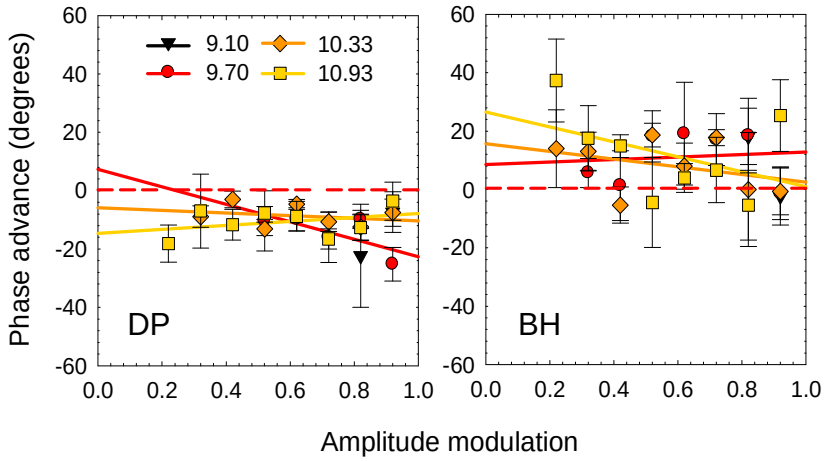

Figure 5.11. Mean ± 1 SE phase advance of a 92% modulated, sinusoidally-flickering 560-nm light (superimposed on a pedestal of the same wavelength and time-averaged radiance as the target) relative to a 650-nm amplitude-modulated flickering target (f_{am}=0.5 Hz and f_c=30 Hz) so that the colour changes of the two flickering lights are matching and in phase at four time-averaged radiance levels (legend shows the radiance levels of the target in $\log_{10}$ quanta s^{-1} deg^{-2}). The dashed red horizontal line indicates a phase advance of zero degrees and solid lines indicate linear regression of the data.

Following the matching data for the 650-nm target, the matching data for the L-cone-isolation conditions are presented in Figure 5.12. In general, for the highest L-cone-isolation target intensity and for the M-cone-isolation conditions, subjects found it impossible to match the change in appearance at f_{am}, so these measurements could not be made. Subjects reported that the change in appearance at f_{am} was more subtle for cone-isolation conditions than for monochromatic conditions, which is also in agreement with the lower critical fusion frequency for the change in appearance at f_{am} as a function of f_c for these conditions (Figures 3.14 and 3.15). In addition, silent cone substitution reduced the maximum effective modulation of the cone signal to about 78%, which reduced the maximum saliency of the flicker and the change in appearance at f_{am}.

For the three lowest time-averaged radiance levels for the L-cones (from lowest to highest, respectively), subject BH used 630 nm, 633 nm and 640 nm for the pedestal

wavelength and 560 nm, 560 nm and 540 nm for the sinusoidally-flickering light superimposed on the pedestal. Subject DP always used 630 nm for the pedestal and a 560 nm for the sinusoidally-flickering light.

For the L-cone conditions (Figure 5.12) the IMOAC curve for subject DP is accelerating at the lowest intensity level and tends to linearity at higher levels. For subject BH, the curves accelerate at low intensity levels and low modulations but then saturate at high intensity levels and high modulations.

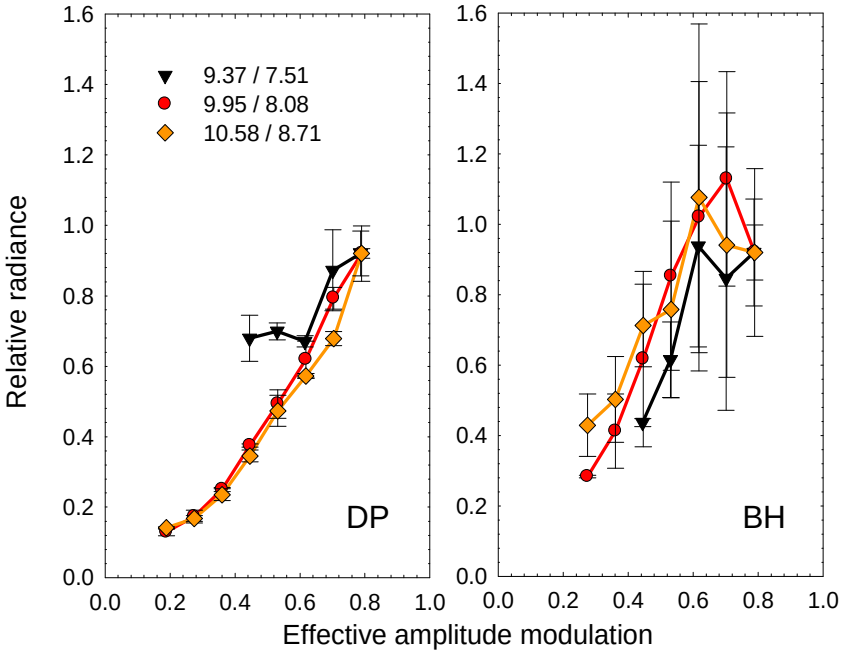

Figure 5.12. Mean ± 1 SE relative radiance of a 92% modulation, 0.5 Hz sinusoidally-flickering light (superimposed on a pedestal matched in hue and brightness to the target when steady) needed to match the colour change of an amplitude-modulated L-cone-isolating amplitude-modulated flickering target (f_{am}=0.5 Hz and f_c=30 Hz) at four time-averaged radiance levels (legend shows the radiance levels of the 650 nm/529 nm target lights in $\log_{10}$ quanta s^{-1} deg^{-2}).

The phase settings (Figure 5.13) made for the colour-change matches of L-cone-isolation conditions (Figure 5.12) are not significantly different at the 95% level (see Appendix Figure 9.7 for confidence intervals) from the phase=0º line for subject BH. The phase settings for subject DP differ by about 10º from the phase=0º but with increasing modulation the phase

settings do not show statistically-significant difference at the 95% level from a horizontal line. (The deviations in slope at the lowest time-averaged radiance level can be attributed to the fewer data points at this level compared to higher time-averaged radiance levels.) These results are similar to the results of both subjects for the 650-nm target.

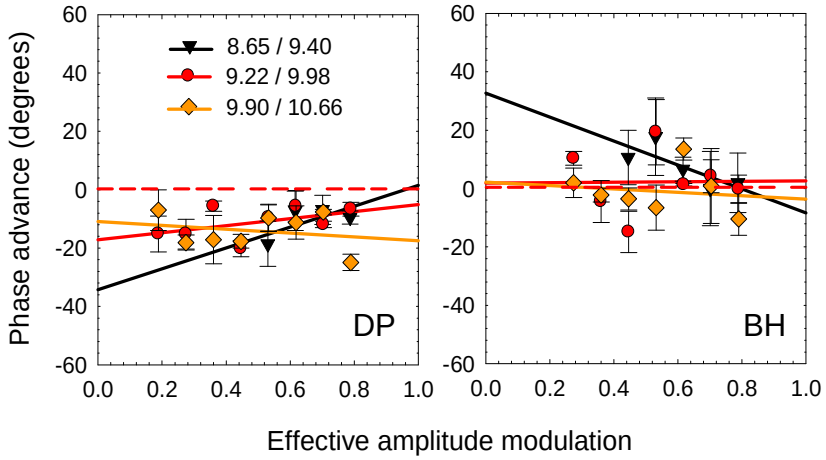

Figure 5.13. Mean ± 1 SE phase advance of a 92% modulated, sinusoidally-flickering light (superimposed on a pedestal matched in hue and brightness to the target when steady) needed to match the colour change of an amplitude-modulated L-cone-isolating amplitude-modulated flickering target (f_{am}=0.5 Hz and f_c=30 Hz) so that the colour changes of the two flickering lights are matching and in phase at four time-averaged radiance levels (legend shows the radiance levels of the 650 nm/529 nm target lights in $\log_{10}$ quanta s^{-1} deg^{-2}). The dashed red horizontal line indicates a phase advance of zero degrees and solid lines indicate linear regression of the data.

5.5 Discussion

Any visual stimulus including the sinusoidal (matching light) has to pass through the pre-nonlinearity stage, the nonlinearity and the post-nonlinearity stage. It is conceivable, therefore, that the matching sinusoidal stimulus may also undergo distortion at the nonlinearity, which may change its appearance. However, as discussed in Section 7.2, distortion of the sinusoidal stimulus is unlikely when using the pedestal method because the modulation of the sinusoid is decreased by the pedestal.

Overall, the results in this chapter show that the IMOAC curves for subject DP tend to be accelerating while those for subject BH are more linear but at high radiances and modulations tend to saturate (decelerate). This trend is clearly apparent for the 560-nm target data (Figures 5.5 and 5.6) gathered using both methods (Sections 5.2.1 and 5.3.1) as well as for the 650-nm target (Figure 5.10) and the L-cone-isolation target (Figure 5.12). Therefore, the L- and M-cone pathways carrying brightness and colour information may have a common nonlinearity. This might suggest that the nonlinearity is prior to the separation of the brightness and chromatic channels.

The side-by-side matching method has an advantage over the nulling method (Section 5.1) because the superimposed nulling light decreases the effective amplitude-modulation of the amplitude-modulated target. Temporally interleaved target and matching stimuli also proved harder to match than side-by-side stimuli perhaps because of local adaptation effects.

With the pedestal method used in conjunction with the side-by-side matching method, it was possible to measure the change in appearance at f_{am} as a function of modulation for a wide variety of stimuli that undergo brightness, colour, desaturation or a combination of these changes (e.g. for any of the stimuli of the visible spectrum that were used in Section 3.2).

However, when using the pedestal method, the state of adaptation changes with the amplitude modulation because subjects needed to increase the time-averaged radiance of the matching light in order to match the change in appearance at f_{am}. This may slightly change the gain of the system but such slight effects are not considered in subsequent analysis because they are unlikely to affect the shapes of the IMOAC curves (e.g. similar appearance of the target and matching light suggests that they evoke similar adaptation levels).

The precise measurement of the IMOAC curve shape (as shown by the pedestal method) is of importance for the correct scaling of the measurements of the stages after the pre-nonlinearity stage (Chapter 4) in order to estimate the temporal attenuation characteristics of the post-nonlinearity stage (Chapter 6).

6 The post-nonlinearity stage

Now that the input-modulation (at f_c) vs. output-appearance-change (at f_{am}) (IMOAC) functions have been measured (Chapter 5), the temporal characteristics of the late filter (after the nonlinearity) can be estimated from the measurements reported in Chapter 4. Recall that these measurements reflect the joint characteristics of the nonlinearity and the late filter combined. These joint characteristics represent the threshold output modulation of the post-nonlinearity stage relative to the input modulation of the nonlinearity. In this study it is assumed that the output modulation of the nonlinearity is proportional to the change in appearance at f_{am} and the input modulation to the nonlinearity is proportional to the amplitude-modulation of the visual stimulus (scaled at f_c by the attenuation of the early filter, measured in Chapter 3). The IMOAC function for the nonlinearity defines the effective relative input modulation at f_{am} to the late filter after the nonlinearity (measured in Chapter 5). If the IMOAC function is linear, the late filter will have the same slope as the joint nonlinearity and late filter curves. If the IMOAC function is accelerating, the late filter will be steeper and if it is decelerating, the late filter will be shallower. Thus, depending on the IMOAC function, the measured functions in Chapter 4 will have to be scaled accordingly.

In previous work, the late filter (after a nonlinearity that produces colour or brightness changes) either was assumed to be represented by the joint temporal characteristics of the nonlinearity and the late filter ignoring any effects of the nonlinearity on the temporal characteristics (Chen et al., 1993) or the influence of the nonlinearity was discounted because its effects were shown to be approximately linear over a certain range (Stockman & Plummer, 1998). In the latter study, the linear approximation of the IMOAC function for the S-cone pathway (on the basis of which the scaling of the temporal characteristics of the

stages after the pre-nonlinearity stage was discounted before estimating the post-nonlinearity) was based on data only up to about 62% input modulation because a nulling procedure was used (Figure 6 in Stockman & Plummer, 1998). However, any non-linearity in the IMOAC function becomes particularly apparent above about 62% (as shown in Figures 5.2, 5.6, 5.10 and 5.12). Extending measurements to higher modulations might have revealed an accelerating or decelerating slope.

In this chapter, the temporal characteristics of the post-nonlinearity stage are estimated from the measurements in Chapters 4 and 5.

6.1 Procedures

Each of the three threshold settings used to calculate the mean values in Chapter 4 were individually scaled by the mean IMOAC functions (measured using the pedestal method) shown in Chapter 5. The three scaled values for each target condition are plotted in this chapter as threshold amplitudes in $\log_{10}$ quanta s^{-1} deg^{-2} (as explained in Chapter 3).

Figure 6.1 shows an example of the scaling for subject DP based on the matching data for the 650-nm target at 10.33 $\log_{10}$ quanta s^{-1} deg^{-2}. The amplitude modulation on the x-axis is equivalent to the physical amplitude-modulation of the stimulus and, since f_c is fixed, it differs by a constant from the modulation at the input to the nonlinearity (the constant is equivalent to the attenuation by the pre-nonlinearity stage at 30 Hz). The y-axis gives the relative radiance of the monochromatic sinusoidally-flickering light needed to match the colour or brightness change produced by the amplitude-modulation (as described in Chapter 5). It is assumed that the match is directly proportional to the colour or brightness change caused by distortion at f_{am} at the output of the nonlinearity.

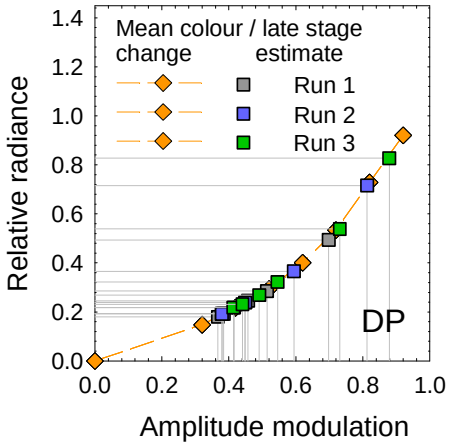

Figure 6.1. Mean ± 1 SE thresholds for detecting colour change at various amplitude-modulation frequencies (vertical grey lines from the x-axis) are scaled (horizontal grey lines to y-axis) by relative radiance needed to match the colour change (diamonds). The dashed line shows linear interpolation between the data points for relative radiance. Three different threshold settings were made for each experimental condition (indicated by grey, blue and green squares). The f_c for the threshold settings and matching settings was fixed at 30 Hz and f_{am} was either varied (threshold settings) or fixed at 0.5 Hz (matching settings).

Linear interpolation was used for threshold data points falling between the measured matching points. It was assumed that 0% modulation produced 0 radiance in addition to that of the pedestal (i.e. if there was no amplitude-modulation there would be no colour change at f_{am}). Thus it was possible to estimate the relative radiances for data points below the measured range.

6.2 Results

The measured thresholds from Chapter 4, for detecting the colour change (top row in Figure 6.2 and Figure 6.3) and brightness change (bottom row in Figure 6.2) of amplitude-modulated stimuli as a function of f_{am} for fixed f_c, are shown with non-black symbols (these data are also presented in Figure 4.2 and top row in Figure 4.5). The same thresholds, after scaling by the IMOAC curve that describes the nonlinearity, are shown by the half-black symbols in Figures 6.2 and 6.3. The four intensity levels for each target are distinguished by

four different colours. Where only non-black symbols are shown for a particular intensity level the shape of the IMOAC curves are linear so no relative adjustment is needed.

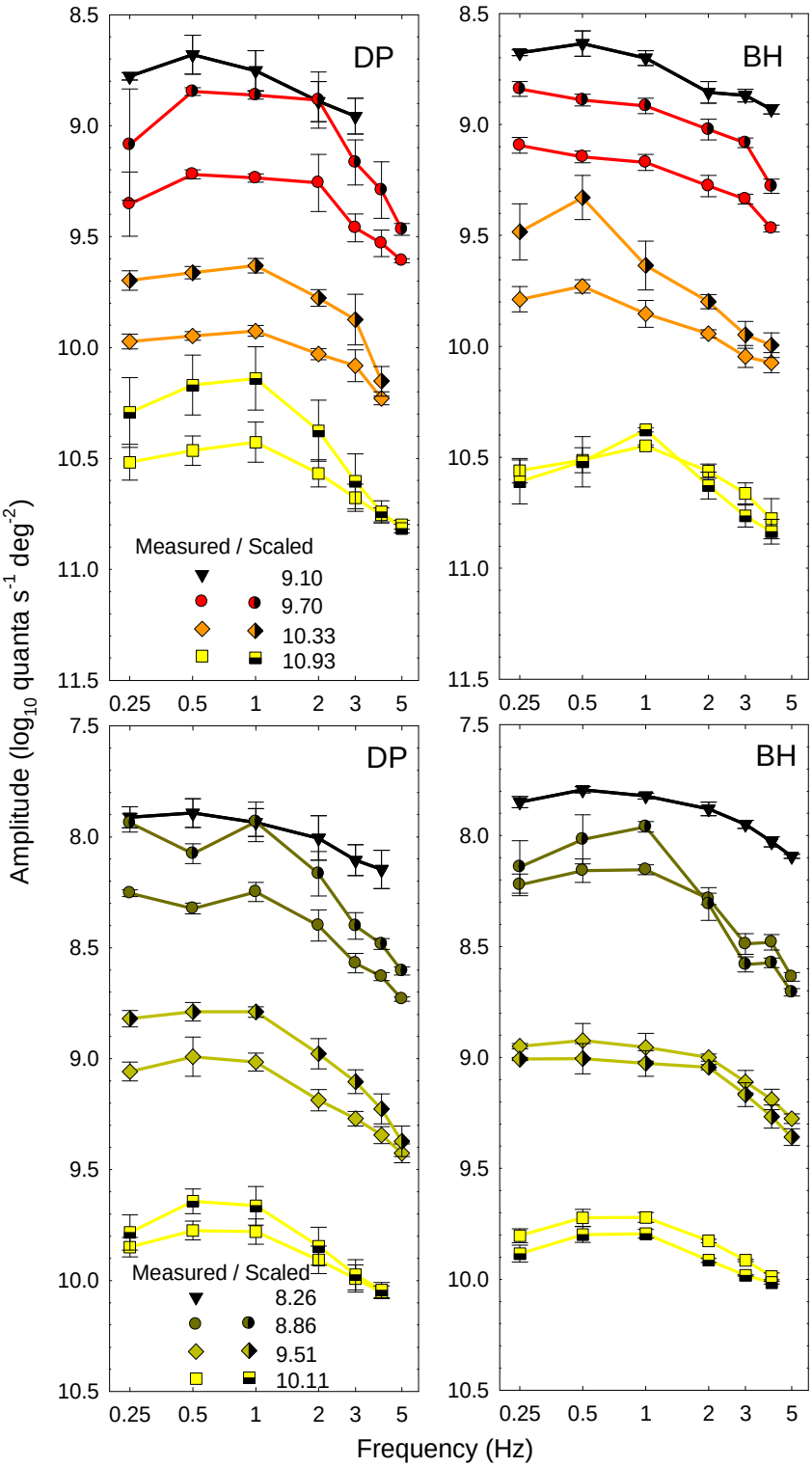

Figure 6.2. Mean ± 1 SE relative amplitude change by the stages after the pre-nonlinearity stage (non-black symbols) and by the post-nonlinearity stage (half-black symbols) for 650 nm (top row) and 560 nm (bottom

row) as a function of amplitude-modulation frequency. Legends show the radiance levels of the targets in $\log_{10}$ quanta s^{-1} deg^{-2}.

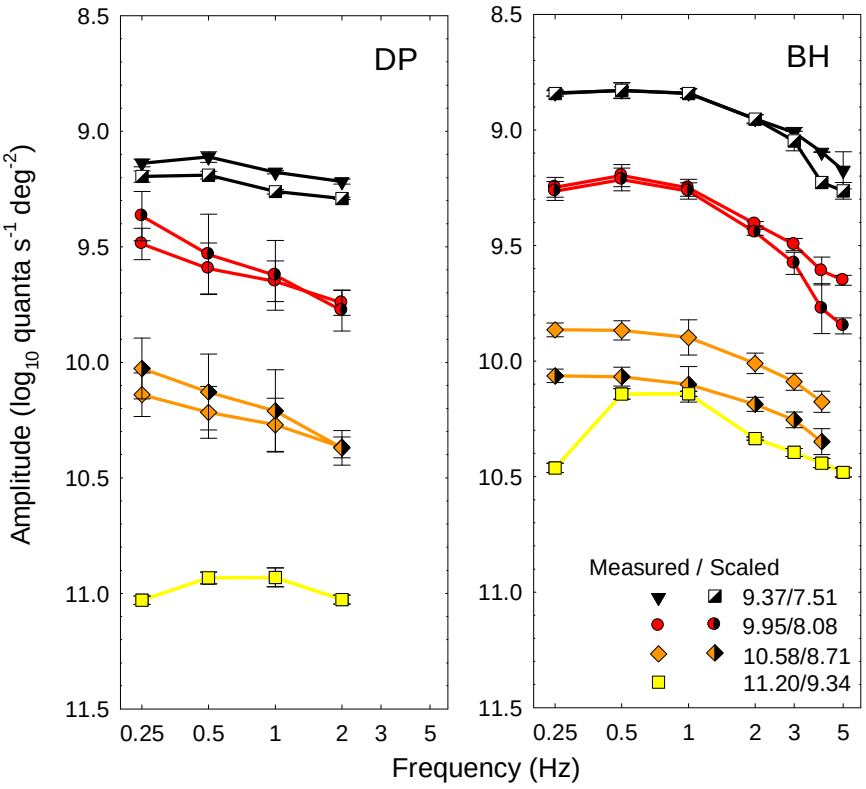

Figure 6.3. Mean ± 1 SE relative amplitude change by the stages after the pre-nonlinearity stage (non-black symbols) and by the post-nonlinearity stage (half-black symbols) for an L-cone-isolating stimulus using a 650-nm light and a 529-nm light out-of-phase (650 nm/529 nm radiances in $\log_{10}$ quanta s^{-1} deg^{-2} are shown in the legend) as a function of amplitude-modulation frequency.

The vertical positions of the late filter functions are arbitrarily fixed at the radiance at which the modulation is maximal (i.e. 92%). At this radiance the unscaled and scaled functions are the same.

After scaling, the threshold curves shown in Figure 6.2 and 6.3 are generally falling-off steeper for subject DP than for subject BH. This is due to the generally more expansive and more compressive IMOAC curves for subjects DP and BH, respectively (as shown in Chapter 5).

The estimated attenuation by the late filter (post-nonlinearity stage) is similar across intensity levels and target conditions for each subject. Figure 6.4 (where the range of the y-axis is 1.1 log units) shows the estimated attenuation by the late filter in Figures 6.2 and 6.3 normalised to a maximum of 0.

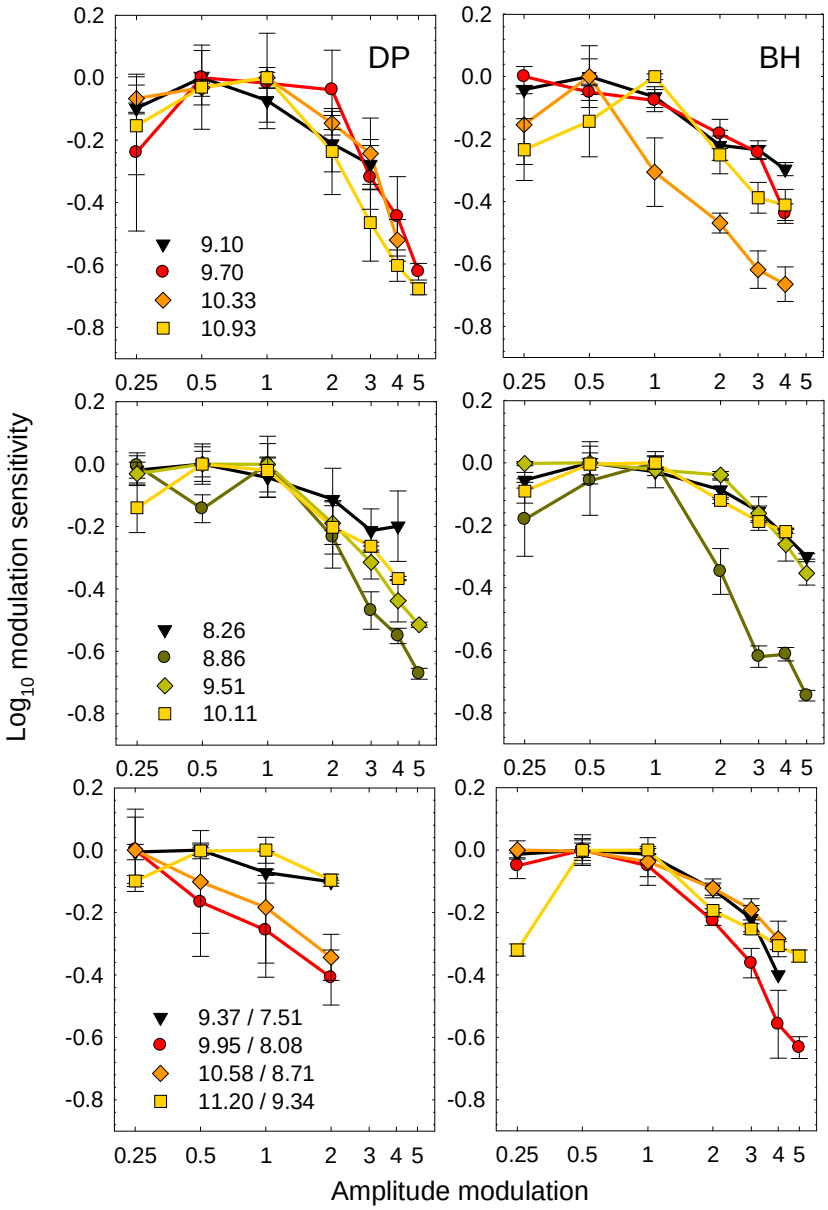

Figure 6.4. Mean ± 1 SE estimated $\log_{10}$ modulation sensitivity of the late filter for colour change at 650 nm (top row), brightness change at 560 nm (middle row) and colour change for L-cone stimuli (bottom row) as a function of amplitude-modulation frequency. Every curve is normalized to 0 at its peak. Legends show the time-averaged radiance levels of the targets in $\log_{10}$ quanta s^{-1} deg^{-2}.

6.3 Discussion

The results in this chapter (half-black symbols, Figures 6.2 and 6.3) suggest that the post-nonlinearity stage has low-pass filter characteristics with a cut-off frequency near 1 Hz. The existence of a low-pass filter with a cut-off frequency around Hz and located at a stage after the retina is also consistent with a hypothesis put forward by Lee et al. (1990) that a central low-pass filter would have a cut-off frequency at least a factor of 2 lower than the cut-off of the tonic and phasic ganglion cells' frequency responses.

The sensitivity to colour change for a 650-nm 10.33 $\log_{10}$ quanta s^{-1} deg^{-2} target flickering at f_c =30 Hz and f_{am} =0 Hz (i.e. sinusoidally-flickering) was also measured relative to a steady annulus of the same wavelength and luminance (for more details of methods and results see Appendix 9.3). When subjects set the minimum modulation at which the target changed colour relative to the annulus (Figure 9.10), their settings were not significantly different from their settings at f_{am}=1 Hz in the top row of Figures 4.1 for the same time-averaged intensity. This supports that the post-nonlinearity stage is low-pass even as the frequency approaches 0 Hz.

In addition, the results of Figure 9.10 link the distortion of amplitude-modulated lights to a wide-set of visual effects e.g. colour changes for non-amplitude-modulated flickering lights, the Brücke-Bartley effect and the Broca-Sulzer effect (see Section 1.3 for details). The advantage of using amplitude-modulated stimuli (as in this study) over non-amplitude-modulated lights (as in studies described in Section 1.3) for studying nonlinearities producing colour and brightness changes is that the former allow the measurement not only of the pre-nonlinearity stage (by varying f_c) but also of subsequent stages (by varying f_{am}).

For targets where the colour change and brightness change were near threshold (e.g. M-cone conditions at f_c=30 Hz in Chapter 4), the colour-change and brightness-change matches oscillate around a constant radiance with increasing modulation. Consequently, for those targets, the IMOAC curve is approximately linear and the thresholds set in Chapter 4 may be scaled by a constant but their relationship (i.e. the shape of the threshold curve) would not be changed by the nonlinearity i.e. the attenuation by the post-nonlinearity stage can be assumed to be proportional to the threshold measurements in Chapter 4.

The slopes of the estimated attenuation curves for the late filter in Figures 6.2 and 6.3 at higher frequencies are very similar across subjects and across time-averaged radiance levels (Figure 6.4). No systematic changes can be seen with increasing radiance. This suggests that the temporal characteristics of the late filter are not affected over this frequency range. Whether the late filter shows adaptation at frequencies (above 5 Hz) can be inferred from the difference between the early filter and the temporal characteristics of the whole pathway (i.e. the TCSF function) as outlined in Chapter 7.

7 Modelling and discussion

The stage before the nonlinearity that produces colour or brightness changes in flickering lights has been described as band-pass (Chapter 3) while the stage after the nonlinearity has been described as low-pass (Chapter 6). However, the measurements for both stages have been limited by the frequency ranges over which the subjects could detect the colour or brightness changes. Section 7.1 describes how the temporal characteristics of the pre-nonlinearity and post-nonlinearity stages can be inferred at frequencies where they cannot be measured directly.

The post-nonlinearity stage was estimated only after the change in appearance at f_{am} introduced by the nonlinearity was measured with the input-modulation vs. output-appearance-change-at-f_{am} (IMOAC) function, as described in Chapter 5. In addition to helping to estimate the post-nonlinearity stage, the IMOAC function can be used to infer the input-output function of the nonlinearity. This will be discussed in Section 7.2.

The characteristics of the pre-nonlinearity, nonlinearity and post-nonlinearity stages can be correlated to physiological cell responses to identify possible physiological substrates for these stages (see Section 7.3).

7.1 The temporal properties of the L- and M-cone pathways

In the present study it is assumed that the nonlinearity separates the pre-nonlinearity stage from the post-nonlinearity stage in a serial sequence within a pathway (Section 1.2), that the nonlinearity is frequency-independent (Chapter 5), and that the temporal contrast sensitivity function (TCSF) provides a measure of the temporal sensitivity of the whole pathway (Chapter 3). Consequently, the difference in log units between the TCSF for the

whole pathway (in Chapter 3) and the attenuation by the post-nonlinearity stage (in Chapter 6) reflects the attenuation by the pre-nonlinearity stage (Petrova, Henning & Stockman, 2010a). This difference (henceforth called the inferred pre-nonlinearity function), together with the directly measured pre-nonlinearity function, provides an estimate of the attenuation by the pre-nonlinearity stage. (Comparably, the difference between the TCSF for the whole pathway and the attenuation by the pre-nonlinearity stage should reflect the attenuation by the post-nonlinearity stage.) However, a difficulty in characterising the overall pre- and post-nonlinearity stages is the alignment of the inferred and the measured functions. Alignment methods are developed below.

7.1.1 Parametric equations

Equations 7.1 shows that the attenuation by the overall visual pathway ($TCSF_{total}$, measured in Chapter 3) is the product of the attenuation by its component early filter ($TCSF_{pre}$, measured in Chapter 3) and its late filter ($TCSF_{post}$, estimated in Chapter 6) in linear units (also equivalent to the sum of the attenuation by the two filters in log units),

$$TCSF_{total} = TCSF_{pre}TCSF_{post} . \qquad \text{Equation 7.1}$$

These three levels of the visual system are measured, respectively, by the temporal contrast sensitivity to flicker (TCSF measurements in Chapter 3), the contrast sensitivity to colour- or brightness-change-at-f_{am} as a function of f_c (Chapter 3) and the contrast sensitivity to colour- or brightness-change-at-f_{am} as a function of f_{am} following correction for changes of the signal's amplitude by the nonlinearity (Chapter 6).

Equation 7.1 in log units was used to infer the pre-nonlinearity characteristics at frequencies below 5 Hz where they could not be measured but where the post-nonlinearity characteristics and those of the whole visual pathway could be measured. Similarly, Equation

7.1 was used to infer the post-nonlinearity characteristics at frequencies above 5 Hz where they could not be measured but where the pre-nonlinearity characteristics and those of the whole visual pathway could be measured.

To infer the pre-nonlinearity characteristics at frequencies below 5 Hz for each experimental condition, the $\log_{10}$ estimate of the post-nonlinearity stage for each individual experimental run (from Chapter 6) was subtracted from the mean $\log_{10}$ measurement of the TCSF for all experimental runs (from Chapter 3). Consequently, there were three inferred pre-nonlinearity values (one for each experimental run). To calculate the inferred post-nonlinearity characteristics at frequencies above 5 Hz for each experimental condition, the $\log_{10}$ estimate of the pre-nonlinearity stage for each individual experimental run (from Chapter 3) was subtracted from the mean $\log_{10}$ measurement of the TCSF for all experimental runs (from Chapter 3). Consequently, there were three inferred post-nonlinearity values (one for each experimental run). The mean and standard error (SE) were then taken from the three inferred values for each condition and they were plotted as the half-black symbols in Figures 7.1-7.6.

The inferred functions were shifted relative to the measured functions for the pre- and post-nonlinearity stages until the inferred and measured functions for each stage approximately aligned. This rough estimate of the shift was used to fit a parametric curve that allowed further refinements of the shift between the two curve sections. No parametric equations have been previously reported for the pre- and post-nonlinearity stages, which are subject of this study.

Various methods were tried for deriving a smooth parametric function that could be applied across different radiance levels for a particular target condition. In one method, equations in the TableCurve 2D library (made up of about three thousand equations) were

used to fit each of the data sets for the pre- and post-nonlinearity stages (i.e. for each of the four target types and for each of the four intensity levels for these targets). The equations were grouped by parametric count and in order of decreasing r^2 values. The curve fits were plotted and the figures were ranked according to the following main criteria: the equation for the parametric fit had to have a finite solution; it had to have the lowest possible parametric count that could describe the data with a high r^2 value; it had to be continuous over a suitable range that included the data and a suitable range of extrapolation (the range that was tested was from about 10^{-4} to about 10^4 Hz); and the same equation (but with different parameter values) had to fit the data for all four intensity levels of each target condition.

This method was successful in obtaining a function to describe the post-nonlinearity stage. A four-parameter logistic sigmoid was used, as in Equation 7.2,

$$y = \frac{a_1}{1+(\frac{x}{c_1})^{(d_1)}} + b_1 \,, \qquad \text{Equation 7.2}$$

where x is the frequency in linear units, y is the attenuation by the post-nonlinearity stage in $\log_{10}$ units, and a_n, b_n, $c_n$and d_n are constants.

It was not possible to find a standard equation that provides suitable curve fits (according to the above criteria) for the pre-nonlinearity data at both high and low time-averaged radiance levels. Considering that the pre-nonlinearity stage acts as a band-pass filter and that band-pass filters can be modelled as a combination of a low-pass and a high-pass filter, where the high-pass filter can be an inhibitory physiological stage with low-pass characteristics, a second method was developed to curve fit the pre-nonlinearity data by adding two component functions. One of the component functions predominated at the low-frequencies (below the peak sensitivity around 10 Hz) and a second predominated at high-frequencies (above the peak sensitivity). The two component functions were separately determined using the first

method. The values for the pre-nonlinearity stage frequencies below peak sensitivity could be fitted by the four-parameter sigmoid in Equation 7.3 while those above peak sensitivity could be fitted by the two-parameter polynomial in Equation 7.4,

$$y = \frac{a_2}{1+e^{\left(-\frac{x-d_2}{c_2}\right)}} + b_2 \ , \qquad \text{Equation 7.3}$$

$$y = a_3 x^{1.5} + b_3 \ . \qquad \text{Equation 7.4}$$

A sigmoid was more suitable than a polynomial (or another function that might describe a high-pass filter) for describing the low-frequency data because it did not provide discontinuity at the intersection with the equation that described high-frequency data.

The pre-nonlinearity stage can be modelled by the sum of Equations 7.3 and 7.4, which simplify to give a five-parameter Equation 7.5,

$$y = \frac{a_2}{1+e^{\left(-\frac{x-d_2}{c_2}\right)}} + a_3 x^{1.5} + b \ , \qquad \text{Equation 7.5}$$

where $b = b_2 + b_3$ (from Equations 7.3 and 7.4, respectively). The new equation (Equation 7.5) provides a mean r^2 value of 0.97 for the curve fits of the data in Figures 7.1-7.4.

The band-pass and low-pass characteristics of the early and late filters are consistent with previous research (see Section 1.2.3). The parametric equations for the pre- and post-nonlinearity stages were subsequently used to refine the shift of the inferred functions relative to the measured functions. The inferred functions were shifted relative to the measured functions until the r^2 value of the curve fit with the parametric equation was maximised. The alignment (and the curve fit for that alignment) that gave the highest r^2 value are plotted in the figures of Section 7.1.2 using SigmaPlot 11.0.

7.1.2 Pre-nonlinearity stage

Figures 7.1-7.4 show that the model fits using Equation 7.5 fit well the combined measured and inferred data for the pre-nonlinearity stage across observers, time-averaged radiance levels and L- and M-cone conditions e.g. the function can capture the changes in shape with increasing time-averaged radiance and changing L:M cone ratio.

The pre-nonlinearity stage in the L- and M-cone pathways when both cone types are stimulated by monochromatic lights acts like an early band-pass filter with a peak close to the peak of the TCSF (top row in Figures 3.10 and 3.11) near 10 Hz for colour change (Figure 7.1) and near 15 Hz for brightness change (Figure 7.2). The data suggest a substantial decrease in low-frequency sensitivity with increasing intensity.

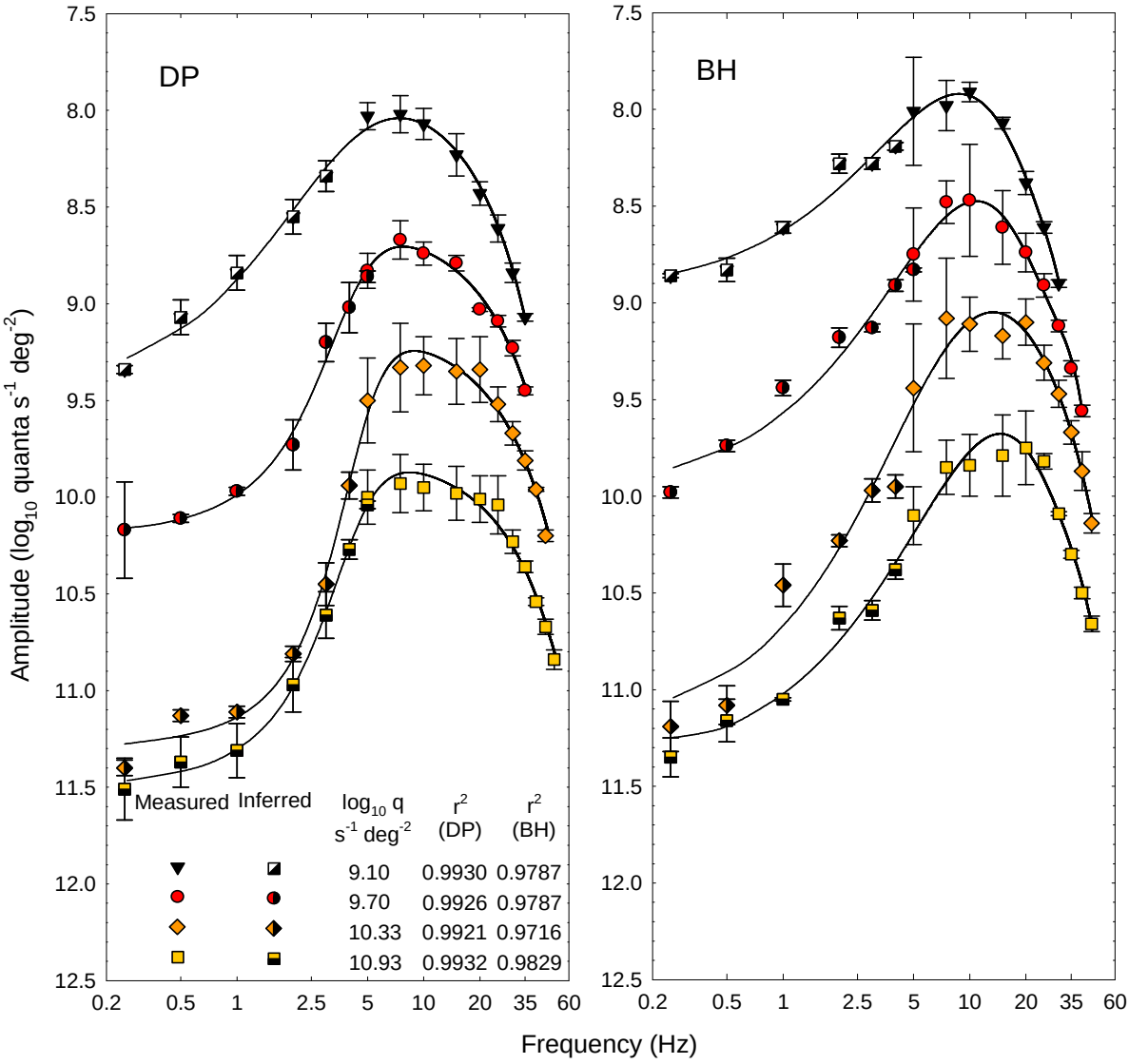

Figure 7.1. Mean ± 1 SE measured (non-black symbols) and inferred (half-black symbols) amplitudes for detecting colour change in an amplitude-modulated flickering 650-nm target as a function of carrier frequency. The legend shows the four time-averaged radiance levels of the target (in $\log_{10}$ quanta s^{-1} deg^{-2}) and the r^2 values of the curve fits using the parametric equations.

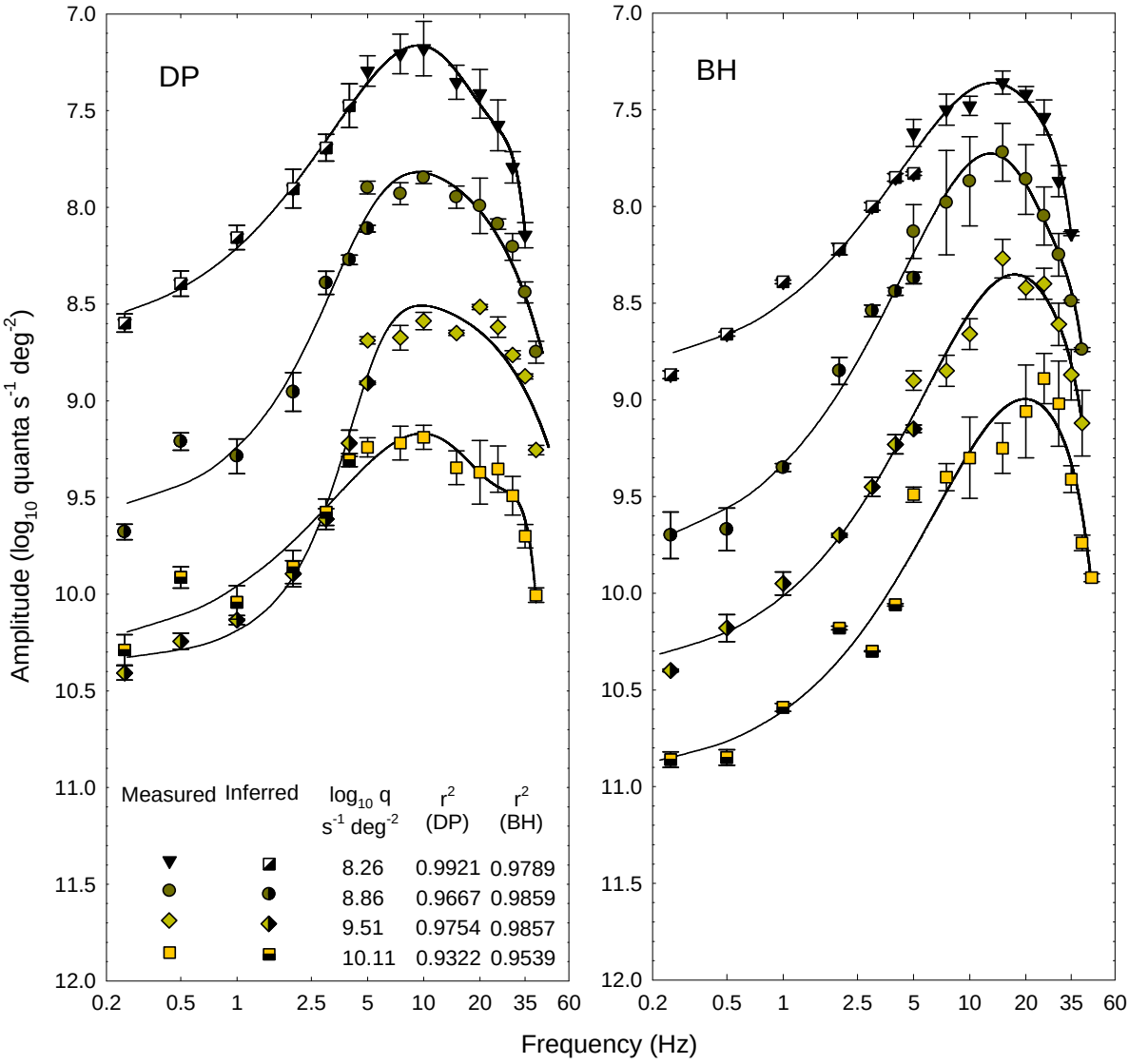

Figure 7.2. Mean ± 1 SE measured (non-black symbols) and inferred (half-black symbols) amplitudes for detecting brightness change in an amplitude-modulated flickering 560-nm target as a function of carrier frequency. The legend shows the four time-averaged radiance levels of the target (in $\log_{10}$ quanta s^{-1} deg^{-2}) and the r^2 values of the curve fits using the parametric equations.

Compared with the early filter for monochromatic L- and M-cone conditions (Figures 7.1 and 7.2), the early filter for isolated M- and L-cone conditions has less low-frequency attenuation (Figures 7.3 and 7.4). The early filter for isolated M- and L-cone conditions has similar characteristics to the early filter for isolated S-cone conditions (Figure 11 in Stockman & Plummer, 1998) in that for all three cone types the early filter is broad-band, with increased attenuation below 2 Hz and above 15 Hz. This similarity suggests that the

three cone types, which have to contribute to the early filter, have approximately similar temporal characteristics.

However, when more than one cone type is active (e.g. at 650 nm and 560 nm) then, at a level of cone interaction (e.g. at retinal ganglion cells), low-pass inhibition is likely to contribute to the early filter and depress sensitivity to low-frequencies (Figures 7.1 and 7.2). This likelihood is also supported by the difference in the peak of the band-pass early filter between monochromatic conditions i.e. the peak is more pronounced for the 560 nm where the M- and L-cones are approximately equally sensitive (that can lead to greater interaction between cone signals and greater low-pass inhibition) than at 650 nm where the L-cones are predominantly active (that can lead to decreased interaction between cone signals and decreased low-pass inhibition).

For BH, the pre-nonlinearity stage for L-cone-isolation conditions (Figure 7.3) is more narrow-band with a shallow peak around 10 Hz compared to the pre-nonlinearity stage for M-cone-isolation conditions where no peak is present for either subject (Figure 7.4).

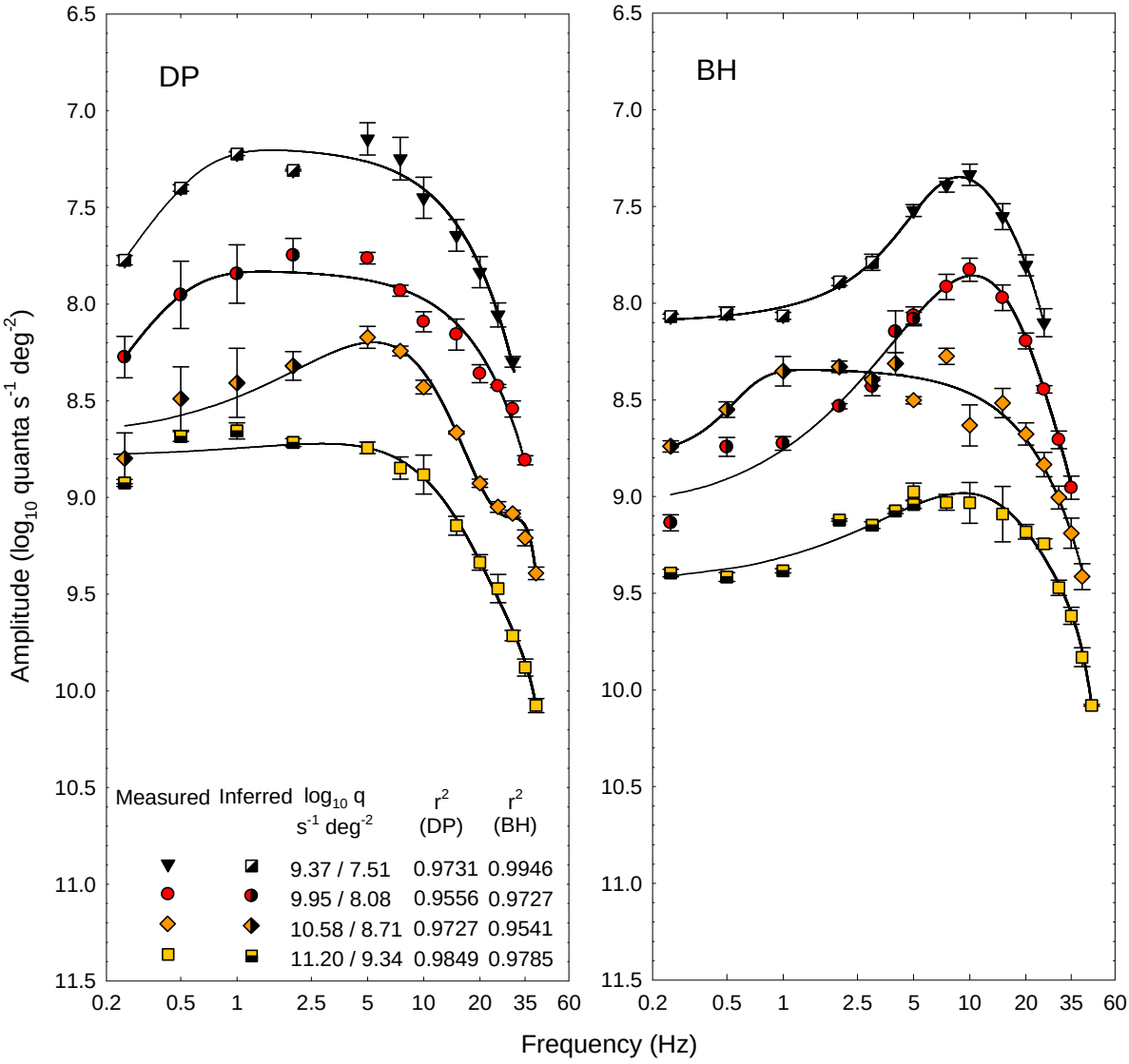

Figure 7.3. Mean ± 1 SE measured (non-black symbols) and inferred (half-black symbols) amplitudes for detecting colour change in an amplitude-modulated flickering L-cone-isolating stimulus as a function of carrier frequency. The legend shows the four time-averaged radiance levels (in $\log_{10}$ quanta s^{-1} deg^{-2} of 650 nm/529-nm lights used to produce the stimulus) and the r^2 values of the curve fits using the parametric equations.

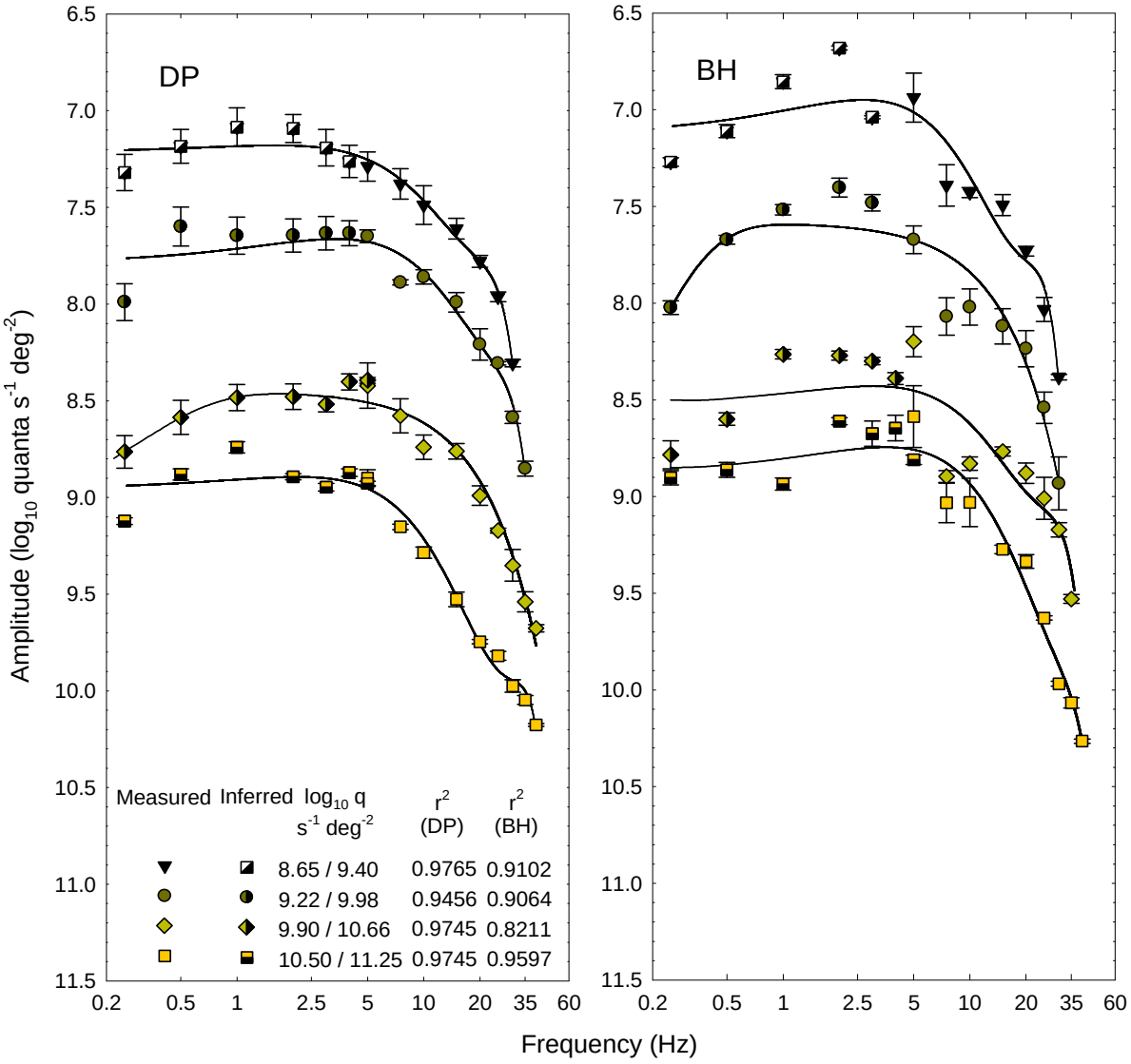

Figure 7.4. Mean ± 1 SE measured (non-black symbols) and inferred (half-black symbols) amplitudes for detecting colour change in an amplitude-modulated flickering M-cone-isolating stimulus as a function of carrier frequency. The legend shows the four time-averaged radiance levels (in $\log_{10}$ quanta s^{-1} deg^{-2} of 529 nm/650-nm lights used to produce the stimulus) and the r^2 values of the curve fits using the parametric equations.

The curve fits of the data allow extrapolation to higher frequencies, which shows that the attenuation by the pre-nonlinearity stage tends to a common asymptote at high frequencies regardless of the time-averaged radiance. This confirms earlier suggestions (Chapter 3) that the pre-nonlinearity stage shows similar linearity at high frequencies (i.e. lack of adaptation) as the TCSF functions.

In addition to the attenuation by the pre-nonlinearity stage, the post-nonlinearity stage also provides important attenuation of temporal frequencies that contributes to the overall temporal resolution of the visual system.

7.1.3 Post-nonlinearity stage

The adjusted data (from Chapter 6) and the inferred data for the post-nonlinearity stage can be suitably modelled and aligned using Equation 7.2 across observers, time-averaged radiance levels and L- and M-cone conditions. However, it was difficult to curve-fit the estimated and inferred post-nonlinearity data for cone-isolating conditions because both data sets were approximately flat without a significant gradient. The decreased significance in the gradient was possibly due to the shallower gradient at cone-isolating conditions compared to monochromatic conditions for the flicker-sensitivity function used to infer the post-nonlinearity data at high frequencies. Due to the insignificant gradient, the r^2 value tended to 1 as the shift between the estimated and inferred post-nonlinearity characteristics tended to infinity.

The post-nonlinearity stage for L- and M-cone conditions (Figures 7.5 and 5.6) can be described as a late low-pass filter within the visual system, with cut-off frequency around 1 Hz. These filter characteristics are similar to those suggested by the measurements in Chapter 4 of the changes in the amplitude after the pre-nonlinearity stage, which also showed low-pass characteristics with a cut-off frequency around 1 Hz. However, there is a tendency for the functions to plateau at the highest frequencies.

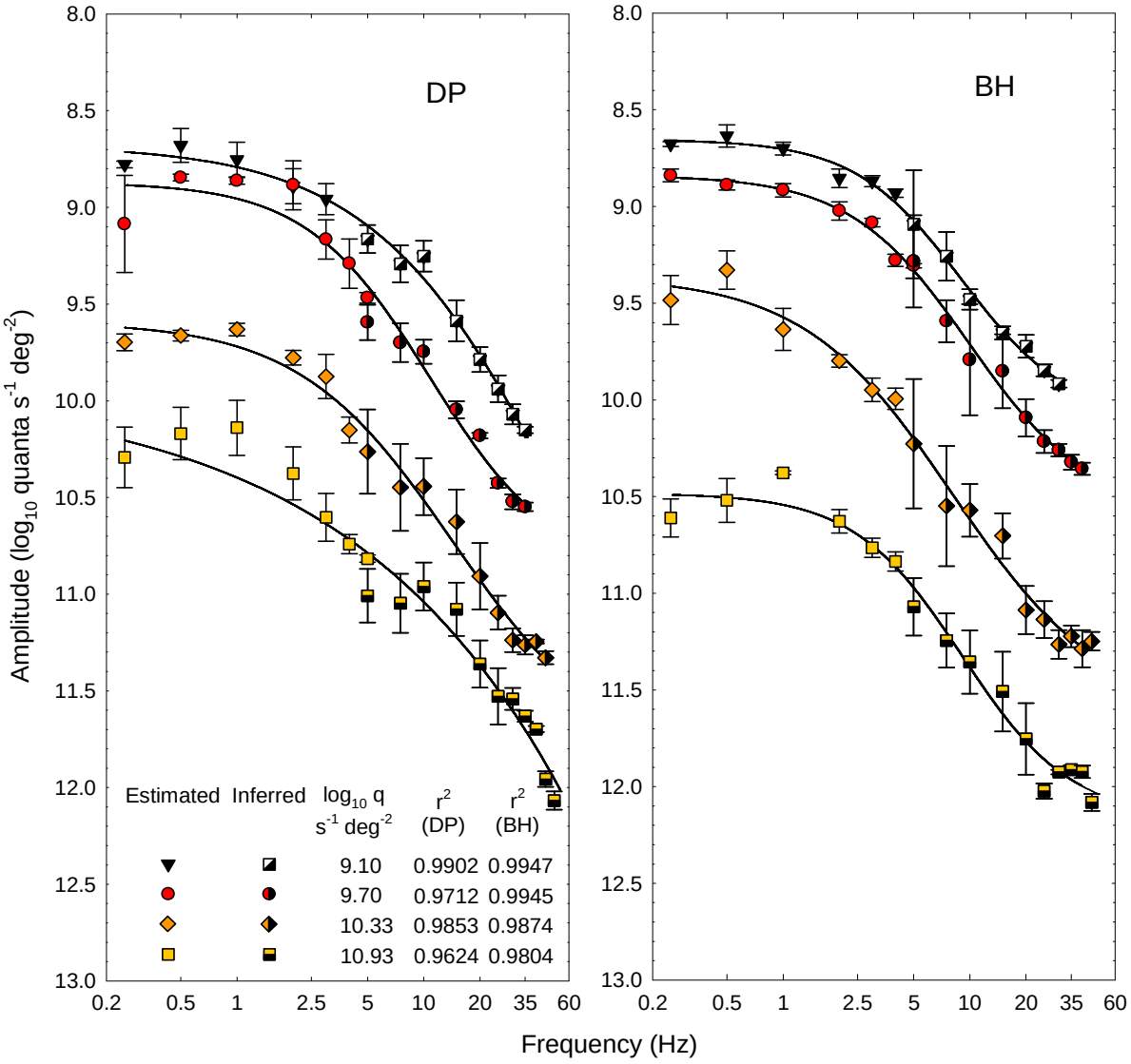

Figure 7.5. Mean ± 1 SE estimated (non-black symbols) and inferred (half-black symbols) amplitudes for detecting colour change in an amplitude-modulated flickering 650-nm target as a function of amplitude-modulation frequency. The legend shows the four time-averaged radiance levels of the target (in $\log_{10}$ quanta s^{-1} deg^{-2}) and the r^2 values of the curve fits using the parametric equations.

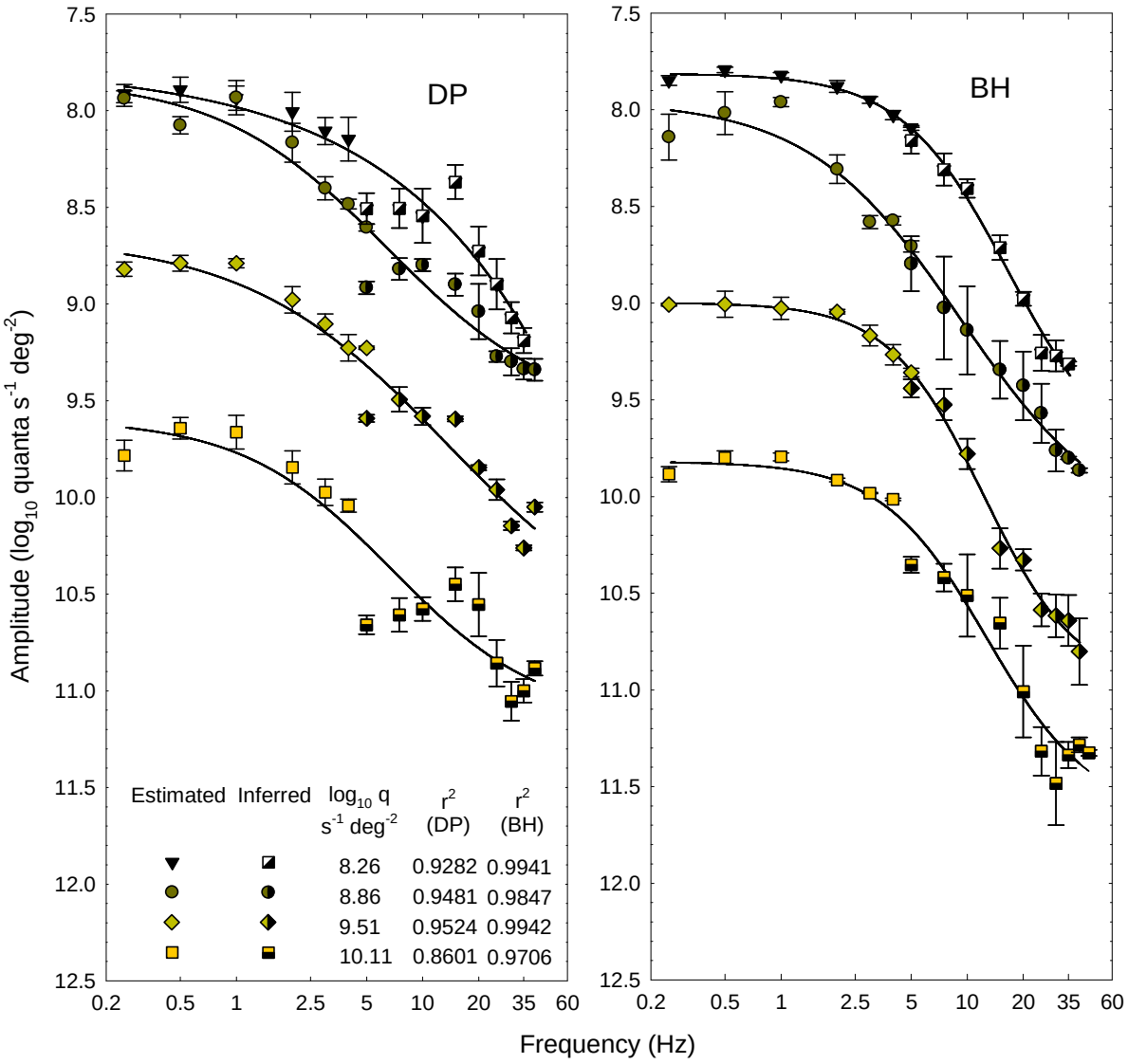

Figure 7.6. Mean ± 1 SE estimated (non-black symbols) and inferred (half-black symbols) amplitudes for detecting brightness change in an amplitude-modulated flickering 560-nm target as a function of amplitude-modulation frequency. The legend shows the four time-averaged radiance levels of the target (in log_{10} quanta s^{-1} deg^{-2}) and the r^2 values of the curve fits using the parametric equations.

The curve fits and the extrapolations for the post-nonlinearity stage are approximately parallel for the different time-averaged radiance levels within each condition at low frequencies (as suggested by the measurements in Chapter 4) and at high frequencies. (This similarity in curve shapes across intensities is unlike the curve shapes for the pre-nonlinearity stage that only tend to a common slope for extrapolations to high frequencies, Section 7.1.2.) The maintenance of the curve shape across intensity levels suggests that the time constant for

the post-nonlinearity stage varies very little, if at all, with intensity. In addition, the approximately equal separation between the curves suggests that there is also little or no change in sensitivity of the post-nonlinearity stage with intensity. (Only the inferred functions have been shifted vertically and the estimated functions have not been shifted.) The invariance of the integrating-time constant and the sensitivity with intensity indicate lack of adaptation at the post-nonlinearity stage of the visual system. The slight decrease in sensitivity at 0.25 Hz relative to 0.5 Hz at high intensities implies the activation of a very slow inhibitory stage but no data was available at lower frequencies <0.25 Hz because they were impractical for the purposes of this study.

The temporal characteristics of the post-nonlinearity stage, described for the L- and M-cone pathways in this chapter, are similar to those described for the S-cone pathway by Stockman & Plummer (1998). For the pathways of all three cone types, the stage after the nonlinearity can be described as a first-order low-pass filter with a cut-off frequency near 1 Hz. These estimates of the post-nonlinearity stage would not be possible without knowledge about how the nonlinearity changed the input signal to the visual system (Chapter 5 and Section 7.2).

7.2 The input-output function of the nonlinearity

The results in Chapter 5 suggest that the nonlinearity is frequency-independent and static. In this section, the input-output function of the nonlinearity is estimated from the input-modulation vs. output-appearance-change-at-f_{am} (IMOAC) results in Chapter 5.

The input-output function of the nonlinearity is different from the IMOAC function measured in Chapter 5. Previous studies of comparable nonlinearities (e.g. MacLeod et al., 1992; Wu et al., 1996) did not make a clear distinction between the measurable input-

modulation vs. output-appearance-change functions that they measured and the input-output functions of the nonlinearities they assumed underlied those measurements.

The input-modulation vs. output-appearance-change functions characterise the appearance change produced at the output of the nonlinearity as a function of the input modulation to the nonlinearity. The visible distortion produced by the nonlinearity, i.e. the contrast of the change in appearance of an amplitude-modulated light at f_{am} (C_{am}), can be represented as the amplitude of the amplitude-modulation frequency (A_{am}) at the output of the nonlinearity relative to the amplitude of the output DC (A_{DCo}), as in Equation 7.6,

$$C_{am} = \frac{A_{fam}}{A_{DCo}} \ . \qquad \text{Equation 7.6}$$

The C_{am} term in Equation 7.6 can be used as a perceptual 'index of the nonlinearity'. Comparable indexes of nonlinearity have used the second harmonic of the fundamental frequency, such as the Hochstein and Shapley index used in cellular physiology (Hochstein & Shapley, 1976), which will not be useful for studies on visual perception because the second harmonic will not be perceived at higher fundamental frequencies.

A sinusoid can be used to measure the relative change in C_{am} as a function of input modulation by matching the appearance of the colour or brightness change of an amplitude-modulated flickering stimulus with the appearance of the sinusoid at its peak, as in the pedestal method in Chapter 5. In this study it is assumed that the nonlinearity will not distort significantly the sinusoid and it will thus not affect the relative measurements of the colour or brightness changes (i.e. the IMOAC curves) because the effective modulation of the sinusoid is reduced by the pedestal.

MatLab 7.1 was used for all calculations and simulations in this section, and to generate the fast Fourier transform (FFT) of the input and output signals before and after the assumed

nonlinearity. The MatLab code written for the simulations, which gives the parameters of the simulations in detail, is included in Appendix 9.4.1. The amplitude-modulated input signal to the nonlinearity was generated according to Equation 2.1.

Because the frequency sample rate and the sampling window for the FFT calculations could not be infinite but had to be physically limited by the program, there was a certain spread of the power spectrum for each frequency component. However, this spread had negligible effect on the frequency amplitudes.

Figure 7.7 gives an example of how a signal is changed by the input-output function of a nonlinearity. A smooth, compressive nonlinearity is used as an example (equation shown in legend of Figure 7.7). The input DC (DC_i) and the modulation for each signal are also shown in the legend. The input signal (bottom graph, Figure 7.7) with the lowest DC_i and modulation (black line) undergoes the least compression by the nonlinearity. As the modulation increases (light grey line) and/or the DC_i increases (dark grey line) then the signal undergoes greater distortion by the nonlinearity. Each of the three output signals (top right graph, Figure 7.7) has a different A_{fam} and A_{DCo}.

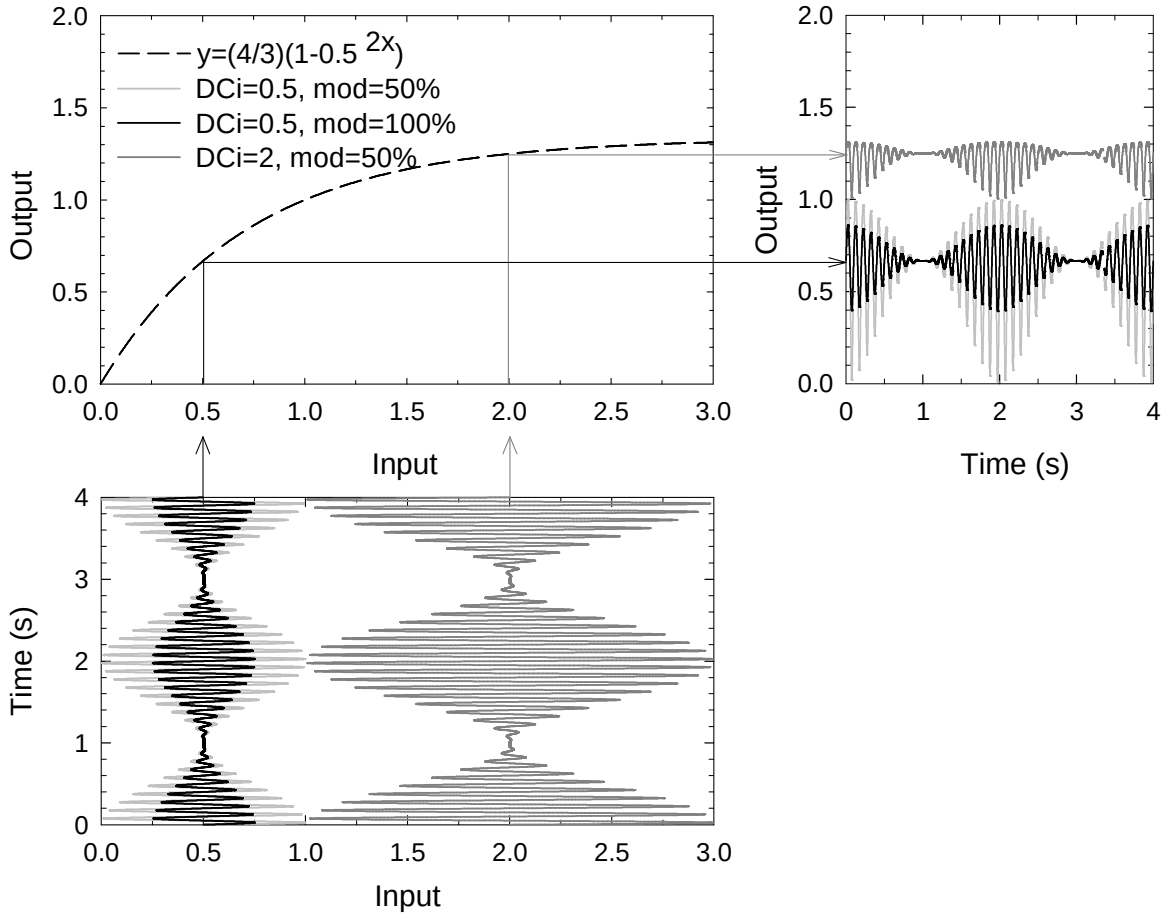

Figure 7.7. Three input signals (input DC and modulation shown in legend, bottom graph) pass through a smooth, compressive, nonlinear input-output function (equation in legend, top left graph) to produce three output signals (top right graph). The vertical arrows and straight lines show the input DC and the horizontal ones show the corresponding output for that input level.

A wide range of possible input-output functions were tested, including: rectifying nonlinearities, polynomial, sigmoidal, logarithmic and exponential functions. The input-output functions were scaled so that they had inputs signals with input DCs lying between 0 and 2 units (as in Figure 7.7). For each function the input DC of the input signal was varied between 0 and 2, for each of the input DC levels the modulation of the signal was varied between 0-100%, and for each of these modulations the A_{fam}:A_{DCo} ratio was calculated. This

sequence of events (transcribed to MatLab code in Appendix 9.4.1) allowed 3D graphs to be plotted like those in Figures 7.8-7.10.

Figure 7.8 shows three examples of common input-output functions that were tested (left column) and the change in appearance at f_{am} that they could produce (right column) as a function of input DC and input modulation. All three examples of input-output functions go through the coordinate (1, 1) i.e. do not change the DC of an input signal with a DC of 1.

The right column of Figure 7.8 shows how the contrast at f_{am} at the output of the nonlinearity (z-axis) varies as a function of the input DC level (x-axis) and the input modulation (y-axis). The 3D graph illustrating the input modulation, input DC and output contrast will henceforth be referred to as an IMIDOC graph while the 2D curves illustrating just the input modulation and output contrast at f_{am} will be referred to as IMOC curves. (The MatLab code in Appendix 9.4.1 was used to generate the IMIDOC and IMOC functions from the input-output equation of a nonlinearity.) The IMOC curves are proportional to the IMOAC curves in Chapter 5 because the contrast at f_{am} is proportional to the colour change or brightness change at f_{am}.

The top row of Figure 7.8 shows the input-output function (top left panel) and the IMIDOC graph (top right panel) of a hard saturating nonlinearity that transduces input signals below the ceiling, i.e. $<\sqrt{2}$, in a linear fashion but clips any parts of the signal $>\sqrt{2}$. Such a nonlinearity cannot explain the IMOAC curves in Chapter 5 because: i) the contrast at f_{am} would be negative i.e. at peak amplitude-modulation a flickering target would appear darker and not brighter compared to a similar non-flickering light; and ii) the top right panel in Figure 7.8 shows that mainly decelerating IMOAC curves can be explained by such a nonlinearity but not linear or accelerating IMOAC curves, which are shown to be present for the nonlinearity measured in Chapter 5.

The middle row of Figure 7.8 shows an expansive quadratic nonlinearity. Such a nonlinearity can produce brightness enhancement at peak input modulation but only as an expansive function of the input modulation. Expansive slopes cannot explain the deceleration at high modulations found in the IMOAC curves (e.g. in Figure 5.10).

Smooth, compressive input-output functions (bottom row, Figure 7.8), similar to those commonly cited to underlie colour changes (see Section 1.3.1), produce darkness enhancement instead of brightness enhancement at maximum input modulation for an amplitude-modulated stimulus. Consequently, smooth compressive functions cannot explain the brightness enhancement for a 560-nm light. In addition, such functions can explain only accelerating IMOAC curves but not the linear or decelerating IMOAC curves in Chapter 5.

Therefore, hard compressive, smooth compressive and smooth expansive input-output functions cannot explain the rapidly decelerating IMOAC curves at high modulations and brightness enhancement (Chapter 5). Simple sigmoidal nonlinearities were also ruled out because they produced a roughly linear region around their point of 180º rotational symmetry, where no distortion would be found. However, there is no evidence for such a region in the data of this study (see Chapter 5).

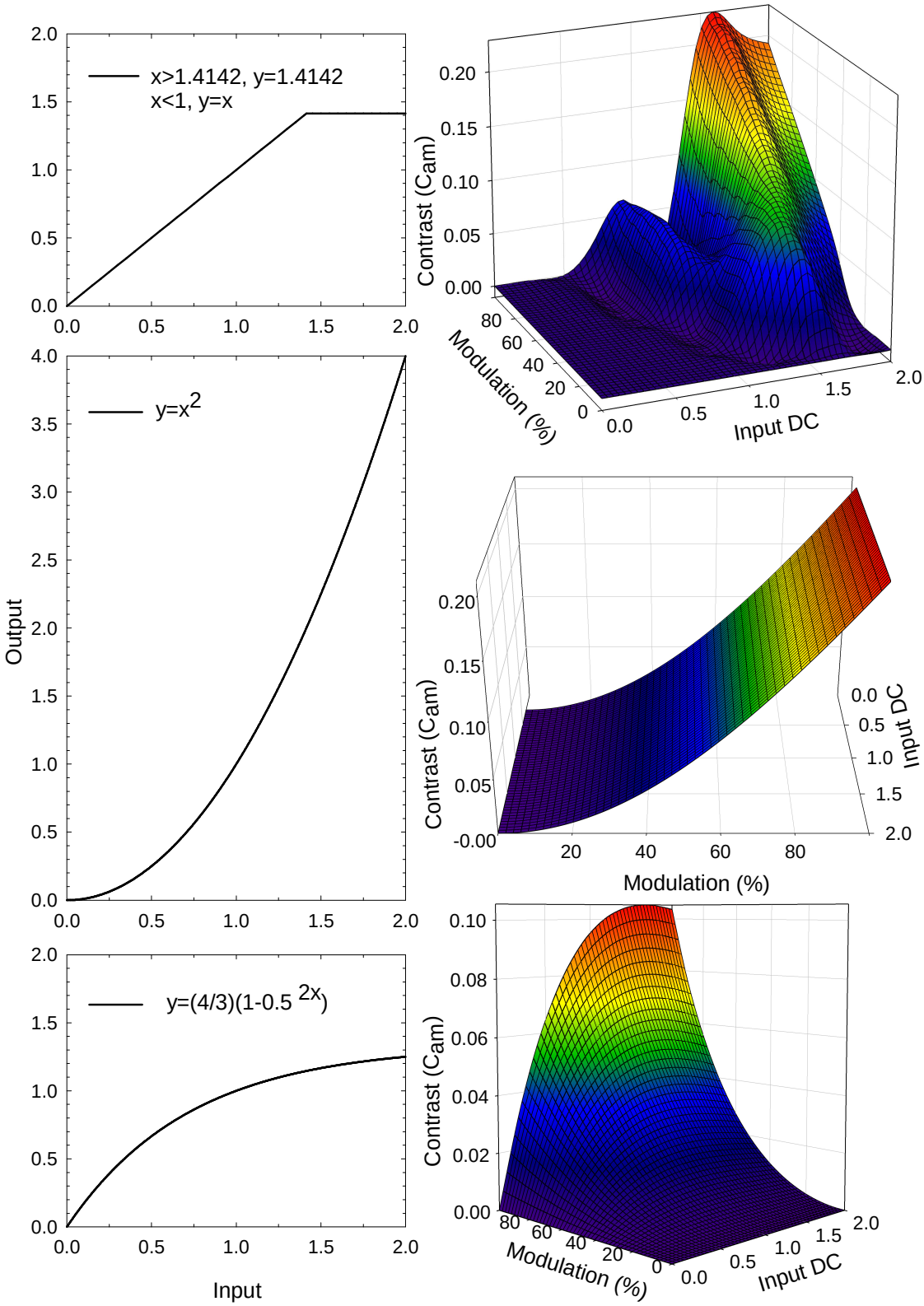

Figure 7.8. Three examples of input-output functions (left column), and the contrast at f_{am} that they produce (right column) as a function of input DC (x-axis) and input modulation (y-axis). Top, middle and bottom rows show hard compressive, smooth expansive and smooth compressive nonlinearities, respectively.

Following simulation of various families of functions, the input-output function that best simulated the IMOAC results in Chapter 5 was found to be an expansive nonlinearity with a ceiling (described by Equation 7.7 and Figure 7.9),

$y = kx^2$ when $x < \sqrt{2},\ k = 1,$

$y = 2$ when $x \geq \sqrt{2},$ Equation 7.7

where x is the input and y is the output of the input-output nonlinearity function (left panel, Figure 7.9).

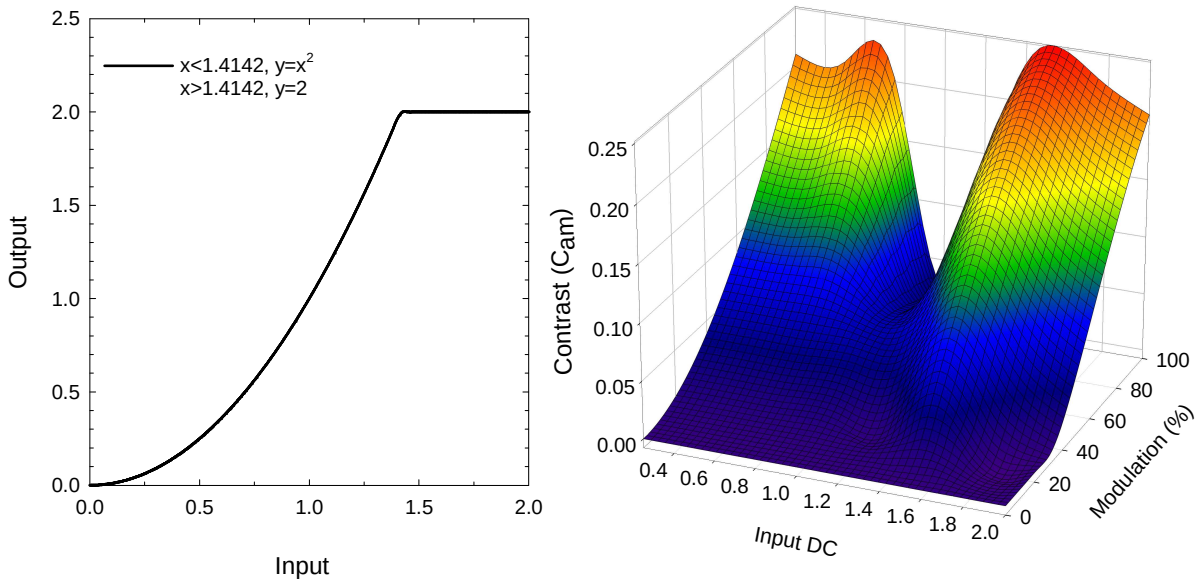

Figure 7.9. An expansive quadratic nonlinearity whose output reaches a ceiling at high inputs (left panel), and the contrast at f_{am} that it produces (right panel) as a function of input DC (x-axis) and input modulation (y-axis).

At DC_i levels $<\sqrt{2}$, the IMIDOC graph (right panel of Figure 7.9) can explain brightness enhancement with increasing modulation. As the DC_i level is increased from 0 to 1, the IMIDOC graph has accelerating, near-linear and decelerating slopes of contrast at f_{am} as a function of modulation (right panel, Figure 7.9). At DC_i levels $>\sqrt{2}$, the IMIDOC graph can

explain the increase in darkness enhancement with increasing modulation. As the DC_i level is increased from 1 to 2, the IMIDOC graph has decelerating and near-linear slopes of contrast as a function of modulation. The results in the present study can be explained by varying the DC_i levels between 0 and 1 (see Figure 7.11).

Varying the input-output function (while keeping the input signal constant) can produce IMIDOC graphs of similar form to the one in the right panel of Figure 7.9 where the DC_i of the input signal is varied (while keeping the input-output function constant). For instance, either varying the input and output level of the input-output function at which the ceiling occurs (while keeping the accelerating slope of the curve constant and the DC_i of the input signal constant) or varying the acceleration of the slope of the expansive function by varying *k* in Equation 7.7 along with the output level above which the ceiling occurs (while keeping the input level at which the ceiling occurs constant and the DC_i of the input signal constant) can produce similarly-shaped graphs to the IMIDOC graphs in the right panel of Figure 7.9.

Figure 7.10 shows the change in the DC by the nonlinearity (top left panel), the amplitude at f_{am} (top right panel) and the total amplitude of the carrier and two sidebands (bottom panel) as a function of input DC and modulation. Note that although the amplitude at f_{am} increases markedly with the input DC, the contrast at f_{am} does not because the output DC also increases. The IMIDOC graph in the right panel of Figure 7.9 is equal to the ratio of the output-DC 3D graph and the amplitude-at-f_{am} 3D graph (top right panel, Figure 7.10). The total amplitude at the output of the nonlinearity for the frequency components centred on the carrier frequency (bottom panel, Figure 7.10) is proportional (after scaling by the pre-nonlinearity filter) to the flicker sensitivity measured in Chapter 3 (top row, Figures 3.10-3.12 and 3.14-3.15). For instance, the summed amplitude of the three frequency components near

f_c as a function of input DC at maximum modulation (bottom panel, Figure 7.10) is similar to the flicker sensitivity curve as a function of radiance in Figures 3.6 and 3.7.

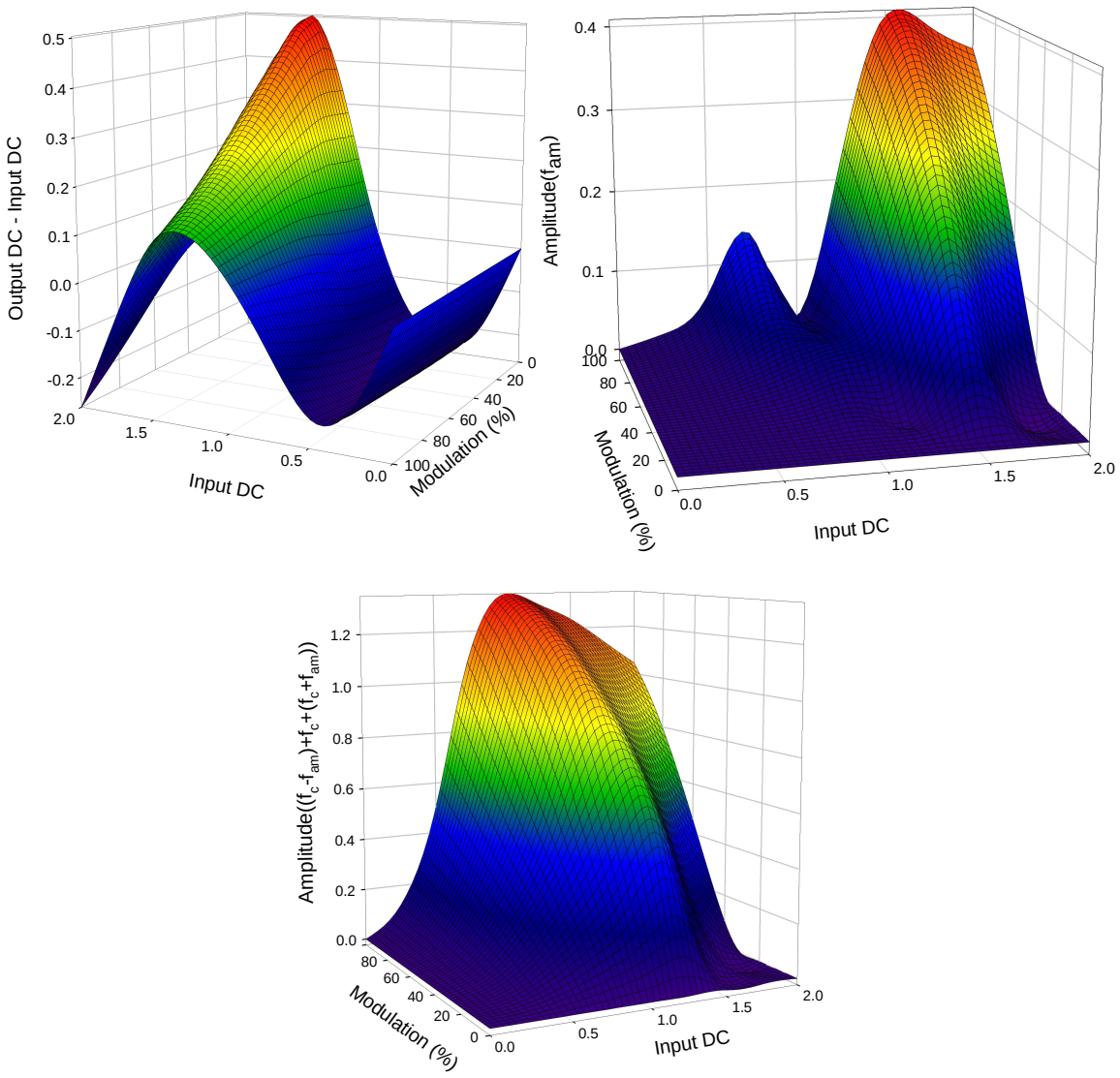

Figure 7.10. 3-D plots showing the effect of varying the modulation and the input DC level on the change in the DC (top left), the amplitude of f_{am} (top right) and the combined amplitude of the frequency components around the carrier frequency (bottom centre).

Since the IMOC curves are assumed to be proportional to the input-modulation vs. output-appearance-change-at-f_{am} curves (IMOAC) they, in principle, can be used to curve fit the IMOAC results from Chapter 5 (Figure 7.11). In curve-fitting the IMOAC curves of

Figures 5.6, 5.10 and 5.12 with the IMOC curve in Figure 7.9, three parameters were varied: i) the scalar of the IMOC curve (where *m*IMOC is the product of the IMOC curve and the scalar *m*); ii) the transpose of the IMOC curve (in the form *m*IMOC+*c* where *c* is the transpose); and iii) the DC_i of the input signal. The transpose of the IMOC curve is equal to the y-intercept in Figure 7.11. Where a range of DC_i values are given in Figure 7.11 (i.e. $0<DC<0.75$), over this DC_i range the IMOC curves do not vary with DC_i and have the same scalar, transpose and r^2 values for describing the data.

The IMOC curves show high precision ($0.932<r^2<0.999$, Figure 7.11) in describing the IMOAC data. This strongly suggests that the nonlinearity underlying brightness and colour change in the L- and M-cone pathways is an expansive nonlinearity that reaches a ceiling at high input-DC levels with an input-output function similar to that in Figure 7.9. Consequently, the nonlinearity is likely to be located prior to the separation of the brightness and chromatic pathways and to have input from single cone types (also, see Section 1.3.2).

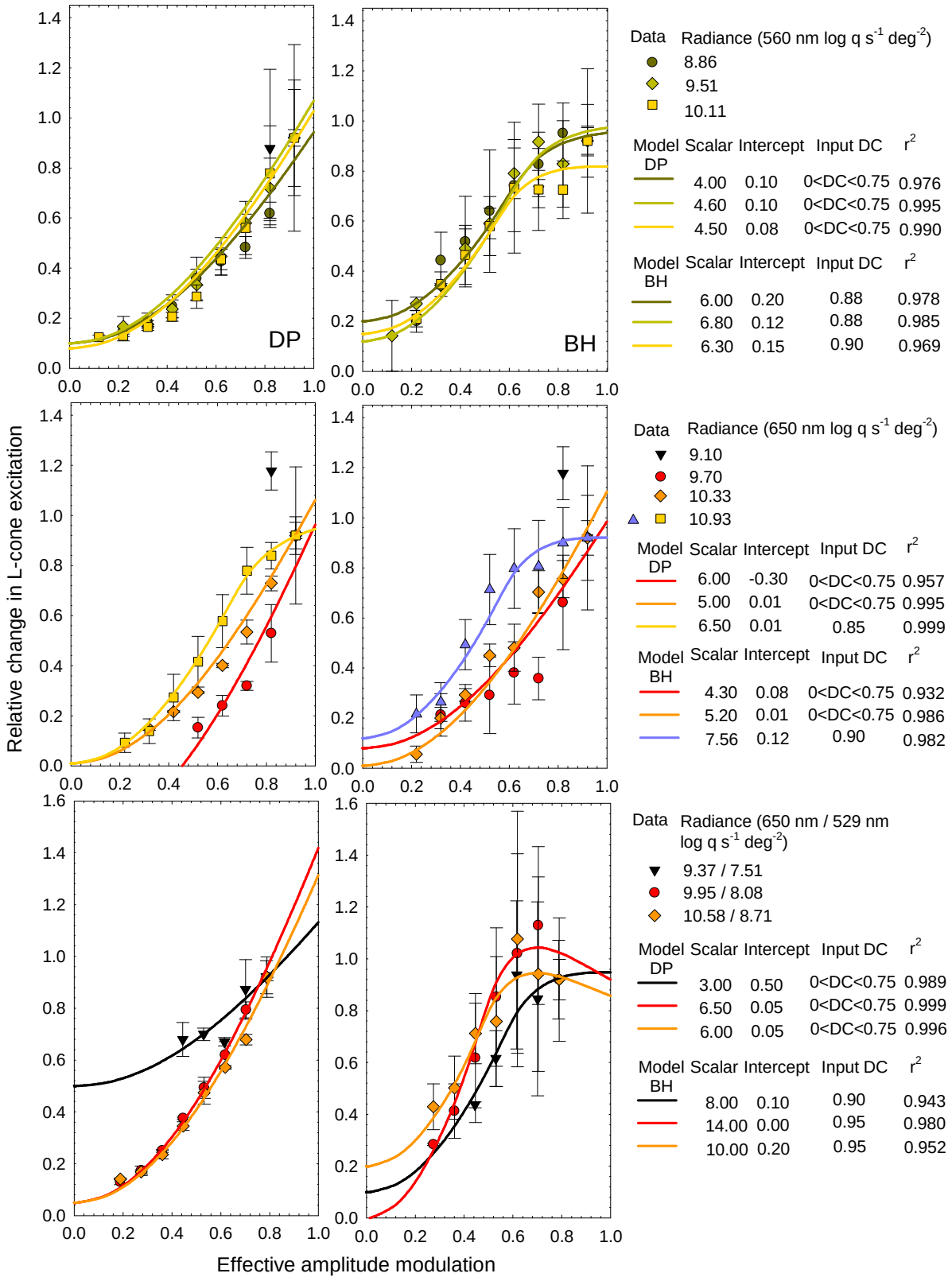

Figure 7.11. Mean ± 1 SE for the relative change in L-cone excitation produced by the nonlinearity as a function of input-modulation (symbols) for brightness change at 560 nm (top row), colour change at 650 nm (middle row) and colour change at L-cone-isolation conditions (bottom row) can be described with high

precision (r^2 values on the right) by the contrast at f_{am} as a function of input modulation (solid lines) of an expansive quadratic nonlinearity with an output ceiling of 2. The scaling factor affecting the gradient of the curve, the y-intercept of the curves and the input DC over which the curves apply are shown to the left of the r^2 values. The time-averaged radiance levels for the targets are shown at the top of the legend for each row.

The difference between brightness enhancement and colour change produced by the nonlinearity can be explained by the difference in the input from L- and M-cone signals. For instance, if the mean input DC (DC_i) from the two cone types is approximately equal, e.g. around 560 nm, then the mean output of the nonlinearity for both cone signals will be changed similarly (with a higher mean for high-modulation inputs than for low-modulation inputs) and the ratio of the cone signals will remain the same. Therefore, brightness enhancement but no colour change will be perceived for high-modulation stimuli around 560 nm. Conversely, if the DC_i from the two cone types is different, e.g. around 650 nm where the DC_i from L-cones is greater than the DC_i from M-cones, then the ratio of cone signals will be changed at the output of the nonlinearity. For instance, if the DC_i of the L-cones is assumed to be 1 and the DC_i of the M-cones is assumed to be 0.5 then as the modulation of the L-cone signal approaches the saturation level and the M-cone signal does not reach the saturation level (for an output ceiling of 2), the amplitude at f_{am} of the L-cones will be lower than the amplitude at f_{am} of the M-cones (A_{am} values in Figure 7.12), which will also contribute to the DC_o of the L-cones increasing more slowly than the DC_o of the M-cones. Consequently, as the L-cone signal approaches saturation and the M-cone signal does not, the L:M cone ratio at the output of the nonlinearity will tend towards 1:1 (Figure 7.12). As the ratio tends towards 1:1, a colour change will occur towards yellow.

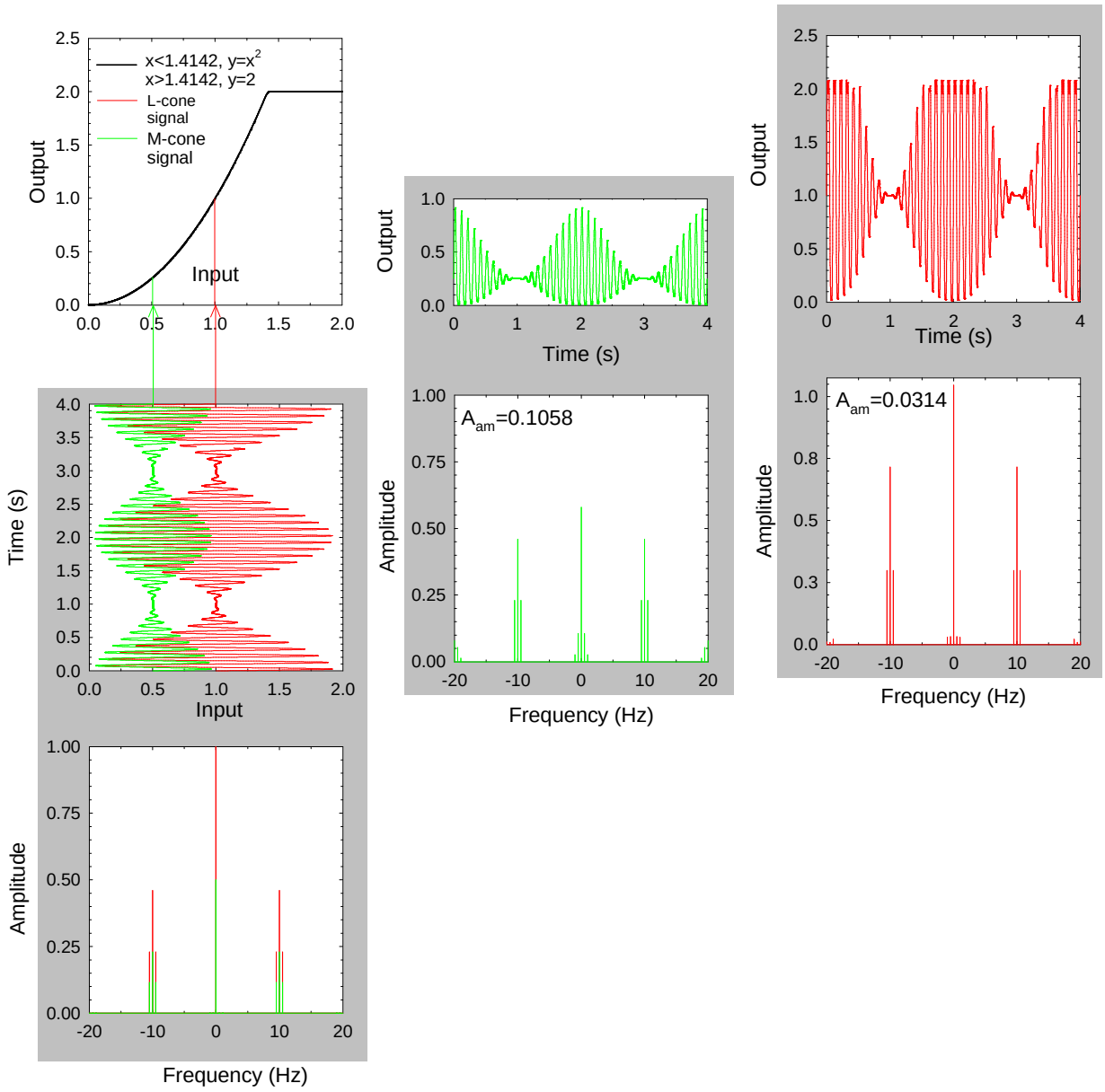

Figure 7.12. An expansive nonlinearity with an output ceiling of 2 (top left) changes two amplitude-modulated input signals with 92% modulation and mean level (DC) equal to 0.5 (green lines, left grey panel) and 1 (red lines, left grey panel) to produce an output signal in the middle and right grey panels, respectively. Each grey panel gives the signal in the time domain (upper graph) and the Fourier domain (lower graph). A_{am} refers to the amplitude of the amplitude-modulation frequency.

The applicability of an expansive nonlinearity, which rapidly saturates at high input levels (as shown in Figure 7.9), to explain IMOAC curves not just for L- and M-cone stimuli (Figure 7.11) but also for S-cone stimuli (Figure 7.13) was tested. S-cone IMOAC data was used from Figure 6 in Stockman & Plummer (1998). The data was plotted (black symbols,

Figure 7.13) against the IMOC curve (blue line, Figure 7.13) of the expansive input-output function with a ceiling (Figure 7.9) and the IMOC curve (purple line, Figure 7.13) of a linear input-output function with a ceiling (top row, Figure 7.8) i.e. the nonlinearities proposed by this study and by Stockman & Plummer, respectively. The three parameters that were varied for the IMOC curve in Figure 7.11 (i.e. scalar, transpose and DC_i) were also varied for the IMOC curves in Figure 7.13. The second IMOC curve (purple line) is produced by a linear input-output function with a ceiling (as in the top row of Figure 7.8) that was proposed by Stockman & Plummer for their data. The input-output functions, which produce each of the IMOC curves, both saturate at $DC_i=\sqrt{2}$.

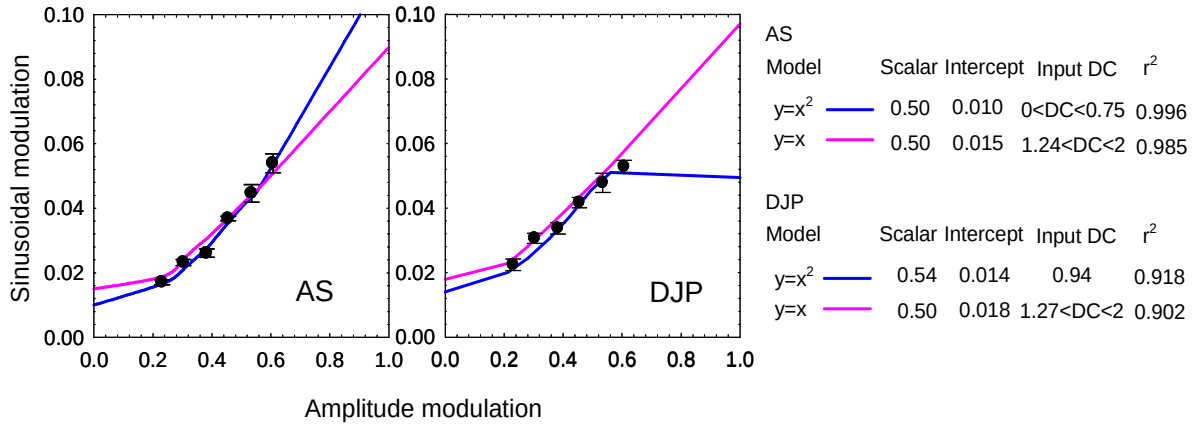

Figure 7.13. Mean ± 1 SE sinusoidal modulation needed to cancel the colour change produced by an amplitude-modulated S-cone-isolating stimulus (black symbols, from Figure 6 in Stockman & Plummer, 1998) can be described by the contrast at f_{am} as a function of input modulation (solid lines) with higher precision (r^2 values on the right) for an expansive quadratic nonlinearity with an output ceiling of 2 (blue line) than a linear input-output function with an output ceiling of 2 (purple line). The scaling factor affecting the gradient of the curve, the y-intercept of the curves and the input DC over which the curves apply are shown to the left of the r^2 values.

Although the IMOC curves of both input-output functions give generally high r^2 values, the IMOC curve of the expansive input-output function with a ceiling (present model) consistently gives higher r^2 values for curve-fitting the IMOAC S-cone data of both subjects

in Figure 7.13 compared to the IMOC curve of the linear input-output function with a ceiling (Stockman & Plummer model). The DC_i range over which the data for AS and DJP in Figure 7.13 can best be described by the IMOC curve of the Stockman & Plummer model includes $DC_i=\sqrt{2}$. This DC_i is the 100% from the saturation level, which is consistent with the Stockman & Plummer model where the input DC level in their experiment is close to the saturation limit of the input-output function.

The IMOC curves of the present model can consistently describe IMOAC data from L-, M- and S-cone stimuli with higher r^2 values than alternative models including smooth compressive, smooth expansive or rapidly saturating nonlinearities. Consequently, the nonlinearity for cone stimuli at photopic light levels that causes colour and brightness changes can be described as an expansive nonlinearity that rapidly saturates at high input levels and occurs at a stage common to the pathways of all three cone types.

7.3 Physiological substrates

In this section, the pre-nonlinearity characteristics shown previously in Section 7.1 (Figures 7.1-7.4) are compared with the frequency responses of different cell types. Previous studies have suggested that comparable nonlinearities as the one investigated in this study lie at an early level of the visual system perhaps close to the photoreceptor (MacLeod et al., 1992) and after an early stage of surround inhibition (Chen et al., 1993; Stockman & Plummer, 1998; Wu et al., 1996). This means that the nonlinearity is likely to be retinal. Consequently, although there may not be a direct correspondence between psychophysical data and cell data, the present section compares the frequency response of the pre-nonlinearity data with the frequency responses of cones and P and M cells at the retinal ganglion cell (RGC) and lateral geniculate nucleus (LGN) levels.

If the nonlinearity investigated in this study is located after a stage of surround inhibition then the pre-nonlinearity stage should show some low-frequency attenuation of the monochromatic flickering lights that stimulate both the centre and surround of concentric retinal receptive fields. Such low-frequency attenuation is indeed present in the pre-nonlinearity data (Figures 7.1 and 7.2).

In addition, if the nonlinearity occurs after a stage of surround inhibition then the pre-nonlinearity data could reveal whether a cone-specific surround (also supported by some psychophysical studies e.g. Kelly, 1983; Lee, Kremers & Yeh, 1998; Martin, Lee, White, Solomon & Rüttiger, 2001; Reid & Shapley, 1992; Reid & Shapley, 2002; Wiesel & Hubel, 1966) or a mixed-cone surround (Mollon & Bowmaker, 1992; Packer, Williams & Bensinger, 1996; Roorda, Metha, Lennie & Williams, 2001) is more likely to be present at the pre-nonlinearity stage. If a cone-specific surround is present then there should be no low-frequency attenuation for cone-isolation conditions if the surround and centre are cone opponent However, if a mixed-cone surround is present then some low-frequency inhibition should be present for cone-isolating conditions but this should be less than for monochromatic conditions of similar time-averaged radiance – this was found to be the case (see Figures 7.3 and 7.4). Consequently, the data in this study support that the nonlinearity is located at or after a stage of surround inhibition. The surround inhibition can explain the low-frequency attenuation by a sluggish surround and a centre-surround delay (where the surround is slower than the centre). Previous research suggests that centre-surround delays vary from 15 ms (Gouras & Zrenner, 1979) to 3-8 ms (Lee, Martin & Valberg, 1989a). A centre-surround delay of 15 ms and 3-8 ms also means that centre and surround signals would be synchronous at 33 Hz or 166.7-62.5 Hz, respectively, (i.e. cone signals would add instead of subtract). The surround attenuation presumably also varies with wavelength and light

adaptation levels as can be seen, for instance, by the variance in low-frequency attenuation for different targets in Chapter 3.

The frequency response of L-cones was calculated from the Fourier transform of the impulse response shown in Figure 6B of Schneeweis & Schnapf (1999). Schneeweis & Schnapf reported that there were no significant differences in the impulse responses of L- and M-cones. They used circularly-symmetric stimuli of 180 μm diameter and 10 ms duration in their study. In the experiment for their Figure 6A (the data that was used in plotting the cone response in Figures 7.14-7.7.17), Schneeweis & Schnapf subtracted the response of a rod-excitatory 500-nm stimulus (5.56 $\log_{10}$ quanta s^{-1} deg^{-2}) from a rod- and cone-excitatory 660 nm stimulus (8.41 $\log_{10}$ quanta s^{-1} deg^{-2}) to estimate the impulse response of the cone without rod input. The cone's response to a flash without a background was similar to the cones' response to a flash with a background (compare Figures 6A and 9A, respectively, of Schneeweis & Schnapf, 1999). Although the cone's response to a flash without a background may appear less comparable to the pre-nonlinearity data in this study (in which the cones adapt to a continuously presented stimulus) than the cone's response to a flash with a background, it was chosen for the comparisons in Figures 7.14-7.17 of the present study because it was less noisy in the frequency domain than the response with the background.

The frequency responses of the parvocellular RGC responding to chromatic stimuli (Pc RGC) and luminance stimuli (Pl RGC) as well as the magnocellular RGC (M RGC) were replotted from Figure 6 in Lee et al. (1994). Lee et al. used two LEDs (of 554 nm and 638 nm, with time average chromaticity of 595 nm) that were sinusoidally flickering in-phase and 180° out-of-phase to produce luminance and chromatic stimuli, respectively. The total approximate intensity of their stimulus with average chromaticity 595 nm was 9.62 $\log_{10}$ quanta s^{-1} deg^{-2} and it subtended 4.7°. This field size was similar to the one used in the

present study and its luminance fell between the time-averaged luminances for the lowest two intensities of the cone-isolation conditions in the present study.

The pre-nonlinearity data were also compared with P LGN and M LGN responses from Figures 7A and 12A, respectively, in Derrington & Lennie (1984). Derrington & Lennie used drifting gratings of various speeds and constant, optimal spatial frequency to maximize the cell response (5.2 cycles/degree for the data in their Figures 7A and 12A). The drifting grating was presented as an elliptical stimulus of dimensions 3.3° by 2.7° and with time-averaged luminance of 200 cd m^{-2}. This luminance is close to that of the 560-nm target at the lowest two intensity settings, which are equivalent to 142.16 cd m^{-2} and 565.93 cd m^{-2}.

Considering that Derrington & Lennie (1984) used chromatic stimuli to identify the P LGN cells and distinguish them from the M LGN cells then it is likely that the P LGN cells they recorded received inputs from P_c RGCs similar to those later recorded by Lee et al. (1994).

Figures 7.14-7.17 show the inferred (half-black symbols) and measured (non-black symbols) data corresponding to the pre-nonlinearity stage (as aligned in Figures 7.1-7.4). They are plotted here as $\log_{10}$ modulation sensitivities normalised to peak at zero. The cell responses are aligned with the measured data (i.e. at frequencies of 5 Hz and above) by using the least-squares method and varying the y-axis intercept of the curves. The measured data were used for the alignment because the inferred data are less certain. The numbers next to the lines in the legends show the correlation between the cell responses and the measured data in terms of the r^2 values. The r^2 values for correlation of the cell responses with the measured, inferred and overall (including both measured and inferred data) pre-nonlinearity data are shown in Tables 9.1-9.4.

The r^2 values for the measured pre-nonlinearity data at 650-nm and the cell responses (Figure 7.14 and Table 9.1) show that at the two lowest intensities the parvo cells provide the best fits (cones and other parvo cells providing the second-best fits) and at the two highest intensities the magno cells provide the best fits (with the parvo cells providing the second-best fits). For the 560 nm measured data (Figure 7.15 and Table 9.2), the magno cells provide the highest r^2 values and the parvo cells provide the second-highest r^2 values, except at the two highest intensity levels for BH where the magno cells have the two highest r^2 values.

DP's inferred data for the 560-nm conditions and both subjects' inferred pre-nonlinearity data for the 650-nm conditions correlate with magno-cell data at low intensities and parvo-cell data at high intensities. BH's inferred data for the 560-nm condition shows strong magnocellular correlation at all intensities, with weaker parvocellular correlation at intermediate intensities.

For the overall pre-nonlinearity data (including both inferred and measured data), parvo cells show the highest correlations at low intensities and magno cells show the highest correlations at high intensities for both subjects in response to the 650-nm conditions. For the 560-nm conditions for both subjects, predominantly the magno cells show the highest correlation and the parvo cells show the second highest correlation. The high correlation of the inferred data with the magnocellular functions is likely to be because the inferred data were derived from the difference between the overall TCSF, whose origin may be luminance flicker, and the estimated late filter.

The above correlations are suggestive but not definitive. Considering that parvo cells carry chromatic information whereas magno cells do not then the pre-nonlinearity stage measured using colour-change sensitivity to a 650-nm stimulus is likely to include parvo cells and not magno cells. In addition, considering that the results for the nonlinearity (Chapter 5)

are consistent with a single input-output function (Section 7.2), and consequently a single nonlinearity for both colour change at 650 nm and brightness change at 560 nm, then it seems reasonable to suppose that the parvo cells account for the pre-nonlinearity stage measured with both a 650-nm stimulus and a 560-nm stimulus.

In the measured pre-nonlinearity data, the apparent shift in correlation with increasing intensity from parvo to magno cells may be attributed to the increase in the steepness of the high-frequency slope, the increase in the peak frequency and the increase in the CFF of the measured pre-nonlinearity data with increasing intensity. Considering that four intensity levels are used to measure the pre-nonlinearity data and only one intensity level is used for the parvocellular and magnocellular frequency responses in the comparisons then the increase in the slope of the measure pre-nonlinearity data with increasing intensity will shift in correlation from parvo cells (which have relatively shallower slopes) to magno cells (which have relatively steeper slopes).

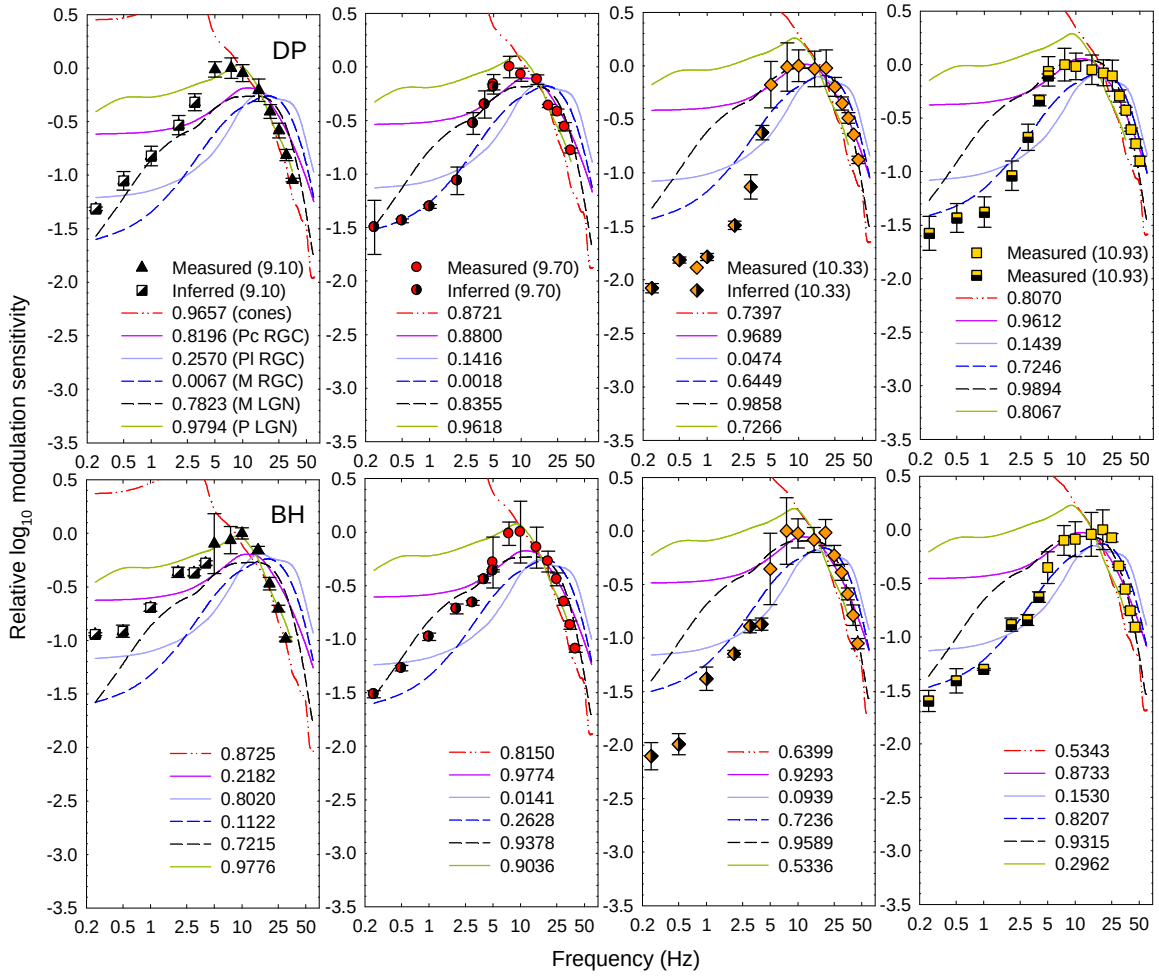

Figure 7.14. Mean ± 1 SE normalised measured (non-black symbols) and inferred (half-black symbols) $\log_{10}$ modulation sensitivities of the pre-nonlinearity stage in response to a 650-nm target (numbers in brackets show the four time-averaged radiance levels of the target in $\log_{10}$ quanta s^{-1} deg^{-2} that apply for each column). Results are shown for subjects DP (top row) and BH (bottom row). The numbers noted against each line show the correlation (r^2) of the measured data ≥5Hz and physiological data: the line 'cones' indicates the cone responses replotted from a Fourier transform of Figure 6B in Schneeweis & Schnapf (1999); the lines 'P_c RGC', 'P_l RGC' and 'M RGC' indicate chromatic parvocellular, luminance parvocellular and magnocellular retinal ganglion cell responses, respectively, replotted from Figure 6 in Lee et al. (1994); the lines 'P LGN' and 'M LGN' indicate parvocellular and magnocellular LGN responses replotted from Figures 7A and 12A, respectively, in Derrington & Lennie (1984).

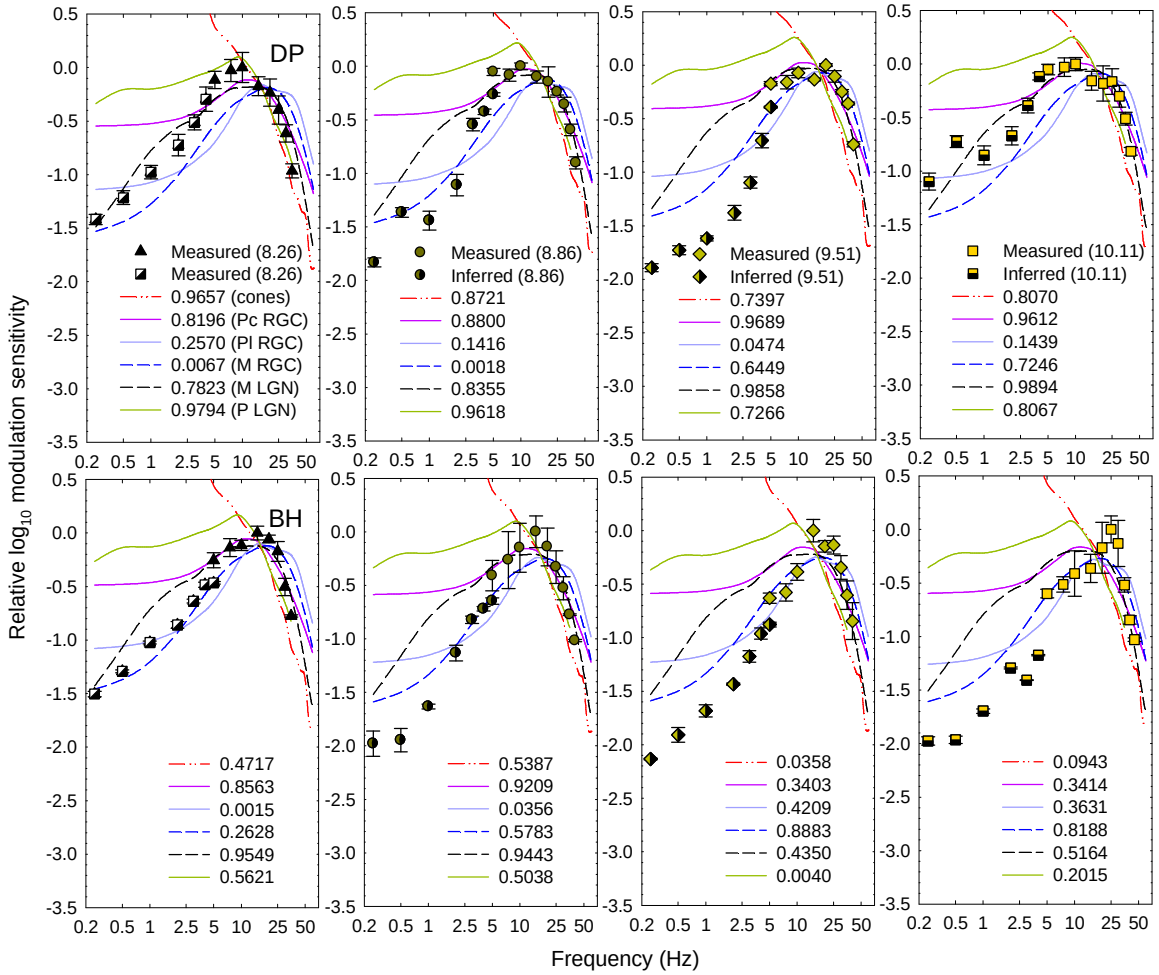

Figure 7.15. Mean ± 1 SE normalised measured (non-black symbols) and inferred (half-black symbols) $\log_{10}$ modulation sensitivities of the pre-nonlinearity stage in response to a 560-nm target (numbers in brackets show the four time-averaged radiance levels of the target in $\log_{10}$ quanta s^{-1} deg^{-2} that apply for each column). Results are shown for subjects DP (top row) and BH (bottom row). The numbers noted against each line show the correlation (r^2) of the measured data ≥5Hz and physiological data: the line 'cones' indicates the cone responses replotted from a Fourier transform of Figure 6B in Schneeweis & Schnapf (1999); the lines 'P_c RGC', 'P_l RGC' and 'M RGC' indicate chromatic parvocellular, luminance parvocellular and magnocellular retinal ganglion cell responses, respectively, replotted from Figure 6 in Lee et al. (1994); the lines 'P LGN' and 'M LGN' indicate parvocellular and magnocellular LGN responses replotted from Figures 7A and 12A, respectively, in Derrington & Lennie (1984).

For DP's measured pre-nonlinearity data at L-cone-isolation conditions (Figure 7.16 and Table 9.3) and for both subjects' measured data at M-cone-isolation conditions (Figure 7.17 and Table 9.4) cones and P LGN cells unvaryingly provide the highest and second highest r^2 values, respectively. However, the two highest r^2 values for BH at L-cone-isolation

conditions vary between parvo cells and either cones (at low intensities) or magno cells (at high intensities).

P LGN and M LGN cells provide the highest and second highest correlations, respectively, to DP's inferred pre-nonlinearity data for the L-cone-isolation conditions. This is also generally true for both subjects at M-cone-isolating conditions, except for several good fits by cone functions. BH's inferred data for L-cone-isolation conditions show high correlation with parvo cells at low intensities and magno cells at high intensities.

For both subjects' overall pre-nonlinearity data at L- and M-cone conditions, cones and parvo cells unvaryingly provide the highest and second highest correlations, respectively, with some exceptions for BH at L-cone conditions where parvo cells provide better correlation than cones.

The differences between the pre-nonlinearity data at low frequencies (<10 Hz) and the cone responses may be attributed to residual rod responses not accounted for in the calculations by Schneeweis & Schnapf (1999) as well as differences between actual cone responses and recorded cone responses due to the removal of the cones from their natural surrounding medium during recordings. However, the general similarity between the overall pre-nonlinearity data for M-cone conditions (Figure 7.17) and the cone responses by Schneeweis & Schnapf suggests that the nonlinearity (and consequently the pre-nonlinearity stage) reflects mainly the responses of the cones (more so than the data for L-cone and monochromatic conditions).

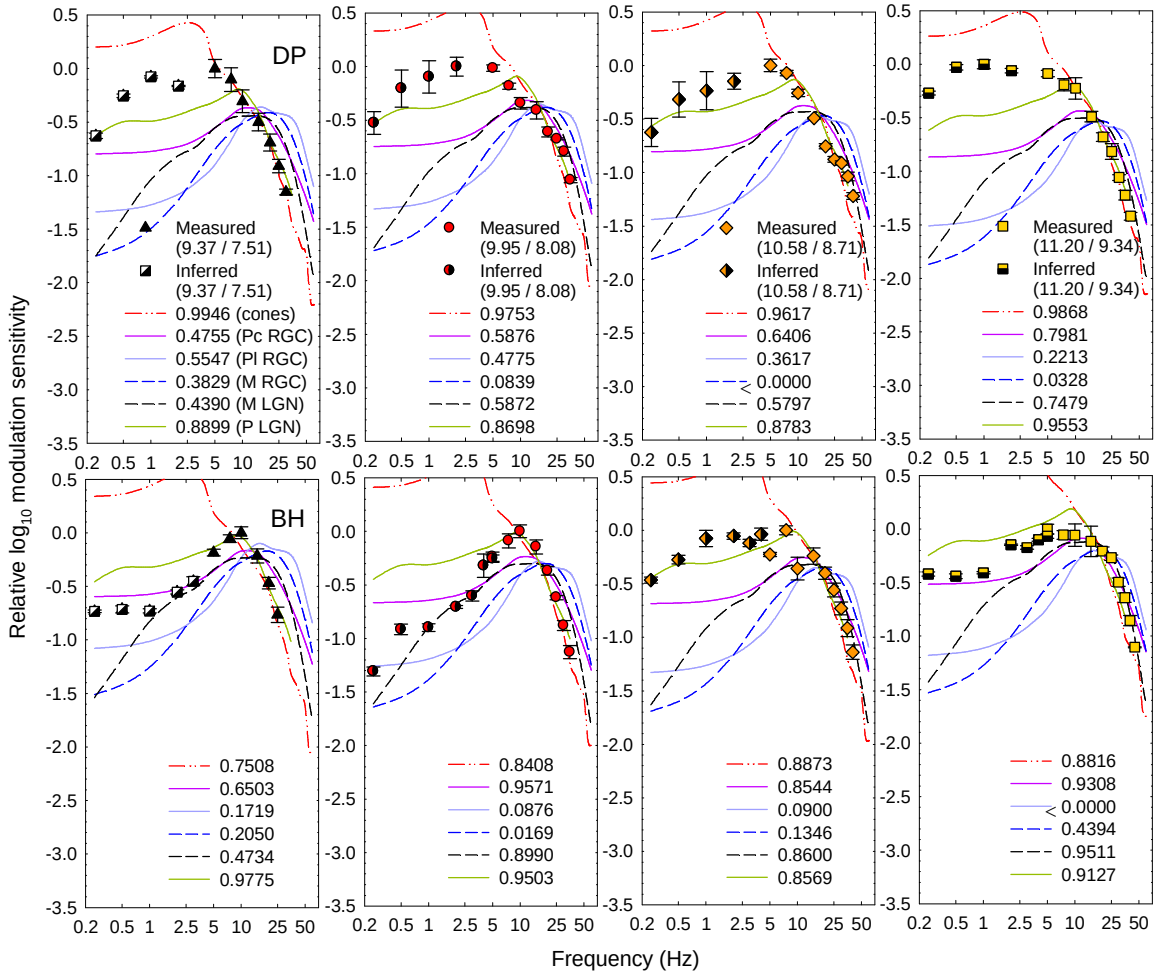

Figure 7.16. Mean ± 1 SE normalised measured (non-black symbols) and inferred (half-black symbols) $\log_{10}$ modulation sensitivities of the pre-nonlinearity stage in response to an L-cone-isolating stimulus (numbers in brackets show the four time-averaged radiance levels in $\log_{10}$ quanta s^{-1} deg^{-2} of the counter-phase flickering 650-nm and 529-nm lights used to produce the stimulus for each column). Results are shown for subjects DP (top row) and BH (bottom row). The numbers noted against each line show the correlation (r^2) of the measured data ≥5Hz and physiological data: the line 'cones' indicates the cone responses replotted from a Fourier transform of Figure 6B in Schneeweis & Schnapf (1999); the lines 'P_c RGC', 'P_l RGC' and 'M RGC' indicate chromatic parvocellular, luminance parvocellular and magnocellular retinal ganglion cell responses, respectively, replotted from Figure 6 in Lee et al. (1994); the lines 'P LGN' and 'M LGN' indicate parvocellular and magnocellular LGN responses replotted from Figures 7A and 12A, respectively, in Derrington & Lennie (1984).

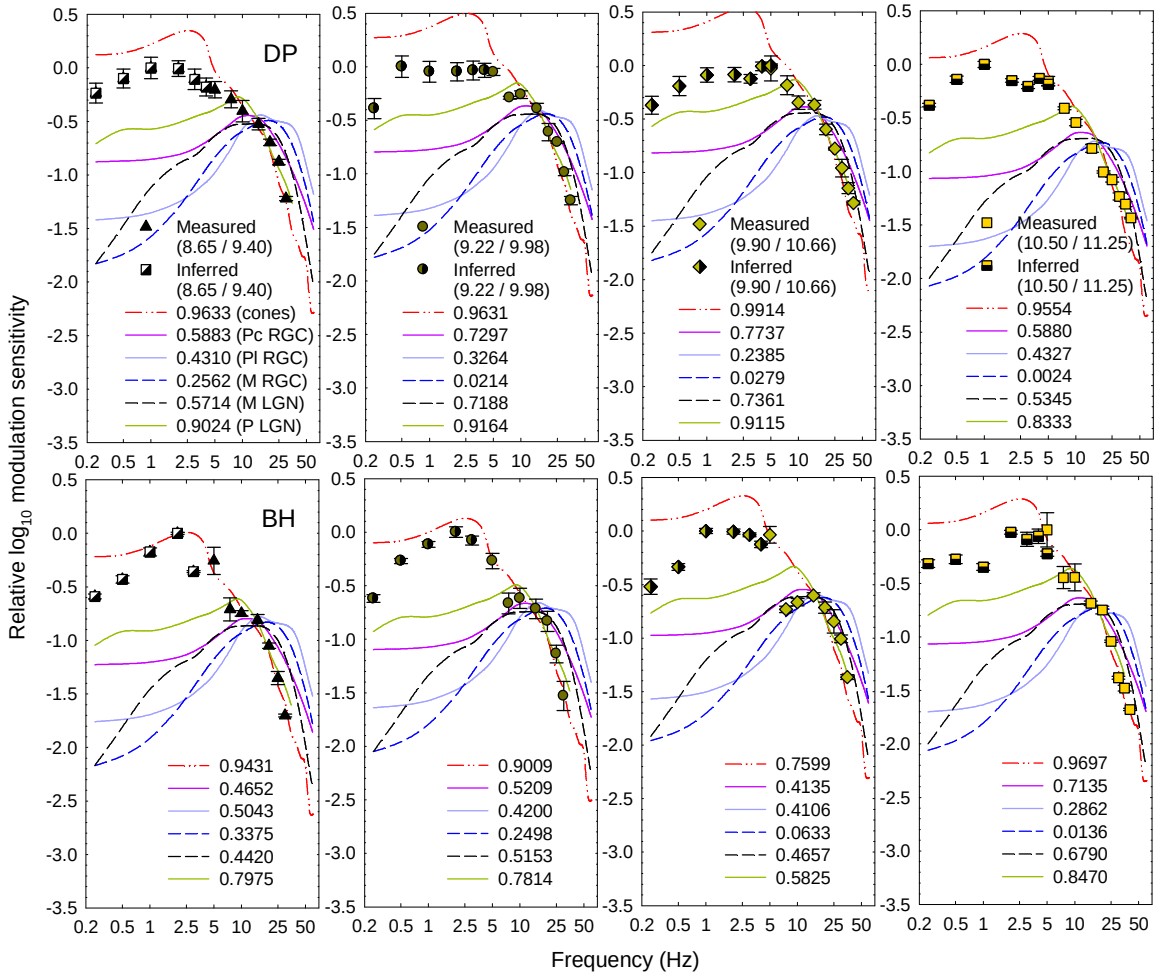

Figure 7.17. Mean ± 1 SE normalised measured (non-black symbols) and inferred (half-black symbols) $\log_{10}$ modulation sensitivities of the pre-nonlinearity stage in response to an M-cone-isolating stimulus (numbers in brackets show the four time-averaged radiance levels in $\log_{10}$ quanta s^{-1} deg^{-2} of the counter-phase flickering 529-nm and 650-nm lights used to produce the stimulus for each column). Results are shown for subjects DP (top row) and BH (bottom row). The numbers noted against each line show the correlation (r^2) of the measured data ≥5Hz and physiological data: the line 'cones' indicates the cone responses replotted from a Fourier transform of Figure 6B in Schneeweis & Schnapf (1999); the lines 'P_c RGC', 'P_l RGC' and 'M RGC' indicate chromatic parvocellular, luminance parvocellular and magnocellular retinal ganglion cell responses, respectively, replotted from Figure 6 in Lee et al. (1994); the lines 'P LGN' and 'M LGN' indicate parvocellular and magnocellular LGN responses replotted from Figures 7A and 12A, respectively, in Derrington & Lennie (1984).

Considering the high correlation of the pre-nonlinearity data for cone-isolation conditions with the cone data at both low and high frequencies (Figures 7.16-7.17 and Tables 9.3-9.4), the cone-isolation conditions differ from the monochromatic conditions by having less low-

frequency attenuation. The lack of low-frequency attenuation shifts the peak sensitivity to lower frequencies and makes the high frequency slope shallower.

If the low-frequency inhibition is due to a mixed-cone surround inhibition of a cell with a centre-surround structure and single-cone input to its centre (e.g. a midget parvo retinal ganglion cell), then low-frequency attenuation would be present for both monochromatic and cone-isolating stimuli but less so for the cone-isolating stimuli because fewer cones in the surround would be stimulated (due to the null of the non-isolated cone types in cone-isolation conditions). This is what was found in this study. The results in this section support existing studies that suggest the surround of RGCs receive mixed input from M- and L-cone types (Mollon & Bowmaker, 1992; Packer et al., 1996; Roorda et al., 2001).

The low-frequency attenuation is higher for L-cone conditions (Figure 7.16) than for M-cone conditions (Figure 7.17), which suggests that there is higher surround inhibition for L-cone conditions than for M-cone conditions despite silent cone substitution. This surround inhibition is likely to be from the same cone type that is being isolated. Considering that L-cone conditions lead to stronger surround inhibition than M-cone conditions, this suggests that there are more L-cones in the surround than M-cones to provide the stronger inhibition. A high L:M cone ratio is also consistent with physiological studies (e.g. Bowmaker, Parry & Mollon, 2003). The low-frequency attenuation is relatively higher for BH than for DP during L-cone-isolation conditions (Figure 7.16) and relatively higher for DP than for BH during M-cone-isolation conditions (Figure 7.17). This difference in the attenuations between subjects may be explained by inter-subjective variation in the L:M cone ratio, with a higher ratio for subject BH than for subject DP.

Sensitivities to changes in appearance at f_{am} in response to monochromatic and cone-isolating conditions represent the early filter in the presence of substantial low-frequency

inhibition and with reduced low-frequency inhibition, respectively. Consequently, it is possible to estimate roughly the attenuation characteristics of the inhibition by subtracting the sensitivities to changes-in-appearance-at-f_{am} for the monochromatic conditions away from the sensitivity to changes-in-appearance-at-f_{am} for the cone-isolating conditions, when both conditions have approximately the same luminance, as shown in Figure 7.18. Higher luminances were required for the M-cone conditions compared with the other conditions so the highest M-cone luminance level was higher than other luminance levels and could not be used for inferring the characteristics of the inhibition. The three or four luminance levels for each condition are indicated in increasing order by 'I. 1-4' in Figure 7.18 (the $\log_{10}$ quanta s^{-1} deg^{-2} for these conditions can be found in Figures 7.1-7.4). The standard error intervals in Figure 7.18 have been estimated as the total standard error of the two sensitivities used in calculating the $\log_{10}$ modulation difference. The $\log_{10}$ modulation differences were normalised to 0 in order to emphasise variation with intensity.

If the low-frequency inhibition is assumed to be due to centre-surround inhibition then the 'L_{cone}-650_{nm}' and 'L_{cone}-560_{nm}' graphs in Figure 7.18 indicate the attenuation characteristics of the surround when it receives input from cones other than L-cones (i.e. M-cone input and negligible S-cone input at these conditions). Similarly, the 'M_{cone}-650_{nm}' and 'M_{cone}-560_{nm}' graphs in Figure 7.18 show the attenuation characteristics of a surround when it receives input from cones other than M-cones, which would provide input to the centre of the P_c RGC. If the surround receives input from the same cone type as the centre then its effect would not be accounted for by the attenuation characteristics inferred in Figure 7.18.

An important source of variability in the inferred low-frequency inhibition is the luminance level at which cone-isolating conditions and monochromatic conditions are comparable, which is influenced by the different weights of the cone types providing input to

P RGCs as well as by the adaptation level and the differences in relative cone numbers (for reviews, see Sharpe, Stockman, Jägle & Nathans, 1999; Stockman, Sharpe, Merbs & Nathans, 2000).

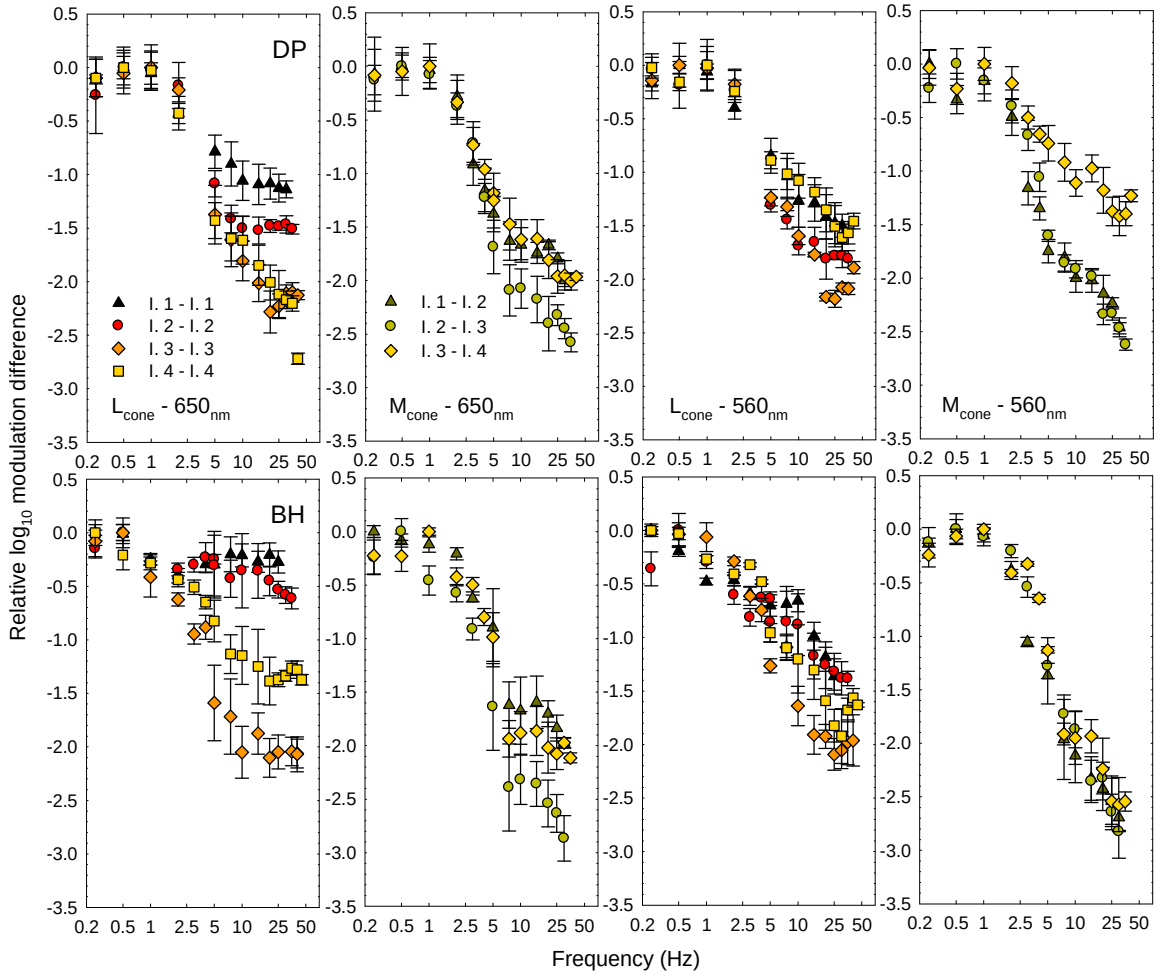

Figure 7.18. Relative differences ± 1 SE between the $\log_{10}$ modulation sensitivities for colour change of cone-isolating stimuli and either $\log_{10}$ modulation sensitivities for colour change (at 650 nm) or brightness change (at 560 nm) of monochromatic stimuli. 'I. 1-4' indicates the four time-averaged intensity levels for each stimulus in increasing order (subtractions were carried for levels of approximately the same luminance).

The M-cones providing surround inhibition (columns one and three in Figure 7.18) show generally greater variation in sensitivity with intensity and shallower slopes at low intensity levels for the relative $\log_{10}$ modulation differences than the L-cones providing surround inhibition (columns two and four in Figure 7.18). For both cone types providing surround inhibition, the steepest part of the $\log_{10}$ modulation-difference slope extends to higher

frequencies at intermediate intensity levels (usually the second-highest intensity level) before reaching a plateau. This suggests that low-frequency attenuation also extends to the higher frequencies at intermediate intensity levels. Furthermore, the slope at intermediate intensity levels (the steepest slope) is approximately the same for all conditions i.e. around 2 $\log_{10}$ units per decade, which is consistent with a second-order filter. A second-order inhibitory filter is close to but different from the first-order inhibitory filter used by Watson to model low-frequency inhibition of TCSF at photopic light conditions (see Section 1.2.3 above and Figure 6.4 in Watson, 1986).

For the last two columns in Figure 7.18, brightness-change sensitivity at 560 nm is subtracted from colour-change sensitivity at cone-isolation conditions. If colour change and brightness change are both carried by the same cells (e.g. double-duty parvocellular ganglion cells) then such subtraction would give an indication of the frequency response by the cells' surround. However, if different cells carried brightness-change and colour-change information, e.g. luminance and chromatic parvocellular ganglion cells, then the $\log_{10}$ modulation differences would not indicate the frequency response by the cells' surround.

If the pre-nonlinearity stage is attributed to filtering at and before P RGC then the post-nonlinearity stage could be attributed to filtering after the P RGC. The low-pass characteristics of the post-nonlinearity stage (Chapter 6 and Section 7.1.3) suggest that the frequency-dependent stages after P RGC are also low-pass without low-frequency inhibition. The average maximum gradient of the post-nonlinearity function described in Figures 7.5-7.6 is -1 $\log_{10}$ unit per decade, which is equivalent to -20 dB per decade or to a first-order filter. A first-order filter in a physiological pathway suggests that there is one synapse in the pathway that would affect the frequency response in the visible range by acting as a low-pass filter (as each site of processing would increase the slope of the overall frequency-attenuation

function). Synapses that do not affect the frequency response in the visible range can still signal the presence or absence of flicker but in a non-frequency-dependent manner (e.g. as for example suggested by Stockman, Williams & Smithson, 2004).

A low-order low-pass filter is consistent with previous studies suggesting a first-order central filter (1990; Stockman & Plummer, 1998). Considering the extensive processing by the visual cortex, a low-order low-pass filter suggests that much of the central processing is not temporal-frequency dependent.

8 Conclusion

This study demonstrated how making use of nonlinearities within the visual system can allow its non-invasive dissection into early (pre-nonlinearity) and late (post-nonlinearity) stages.

In order to estimate the input-output function of the nonlinearity and the attenuation characteristics of the stages after the nonlinearity, a side-by-side matching method was developed. This method was found to be more effective then nulling methods and allowed greater flexibility since the same technique could be used to measure changes in colour, brightness and saturation produced by flickering lights. The L- and M-cone pathways were also investigated by combining the M- and L-cone silent-substitution technique with the above method.

The measurements and inferred estimates of the pre-nonlinearity stage show that it acts as a band-pass filter for monochromatic lights. The results show increase in low-frequency attenuation and shortening of the time constant with increasing intensity similar to the changes in TCSF for comparative conditions, which suggest that most of the adaptation in the visual pathway occurs before the nonlinearity. The low-frequency attenuation of the filter is clearly apparent for monochromatic conditions but not for cone-isolation conditions, which suggests that the pre-nonlinearity stage has a centre-surround structure. In this structure, the surround was found to act approximately as a second-order low-pass filter whose frequency range increases at intermediate intensities and provides mixed-cone inhibition.

The results suggest that the nonlinearity is frequency independent, static and common to the cone pathways carrying colour and brightness information. The colour-change or brightness-change at f_{am} was modelled as the ratio of the f_{am}:DC amplitudes at the output of

the nonlinearity. Based on measurements of this ratio as a function of the input modulation, the input-output function was modelled as an expansive nonlinearity that reaches a ceiling at high input levels in the cone pathways. This result contradicts theories that the colour- and brightness changes accompanying flicker are due to compressive and expansive nonlinearities, respectively. As a result of statistical analysis, it was found that a plausible location for the nonlinearity is at or near the midget parvocellular retinal ganglion cell (P_m RGC), perhaps at the bipolar cell level supplying the inputs to P_m RGC.

The estimates of the post-nonlinearity stage suggest that it acts as a first-order low-pass filter with a cut-off frequency near 1 Hz, which exhibits little or no temporal-frequency-dependent adaptation with changes in intensity or wavelength. The results demonstrated that the late filter was common to the pathways carrying colour, brightness, L-cone and M-cone information. The similarity of the results to the first-order low-pass late filter with a cut-off frequency near 1 Hz that was reported for the S-cone pathway by Stockman & Plummer (1998), also suggests that the late filter is common for all three cone types.

In summary, the temporal contrast sensitivity function (which is around a fifth-order filter, Figures 3.10, 3.11, 3.14 and 3.15) can be modelled approximately, as shown in Appendix 9.4.2, by a fourth-order low-pass filter (as suggested by the pre-nonlinearity measurements for cone-isolation conditions, Figures 7.3 and 7.4) followed by an inhibitory second-order low-pass filter (as suggested by the estimates in Figure 7.18) with negligible attenuation at high frequencies and succeeded by a first-order low-pass filter (as suggested by the estimates in Figures 7.5 and 5.6). Because the early filter undergoes substantial light adaptation (Chapters 3 and 7), such modelling of the centre-surround characteristics of the early filter only applies for a narrow range of photopic light conditions and long-wavelength conditions.

The wavelengths that appear invariant in hue for amplitude-modulated flickering lights were found to be similar to the wavelengths that appear invariant in hue for lights varying in intensity. In addition, the changes in appearance for amplitude-modulated flickering lights were found to be similar to those for non-amplitude-modulated sinusoidally-flickering lights. These results suggest that the methods and outcomes of this study on amplitude-modulated flickering lights can apply to a wide body of literature on non-amplitude-modulated flickering lights, and to lights varying in intensity (i.e. the Bezold-Brücke effect). In addition, non-invasive dissection of the human visual system into an early retinal stage and a late stage may have further applications in clinical work including the screening and diagnosis of retinal diseases or changes in retinal function. In conclusion, the outcomes of this study may have applications to basic research, cybernetics, bioengineering and clinical work. The future beneficiaries of this research are likely to be scientists, clinicians and patients.

9 Appendices

9.1 Colour discrimination

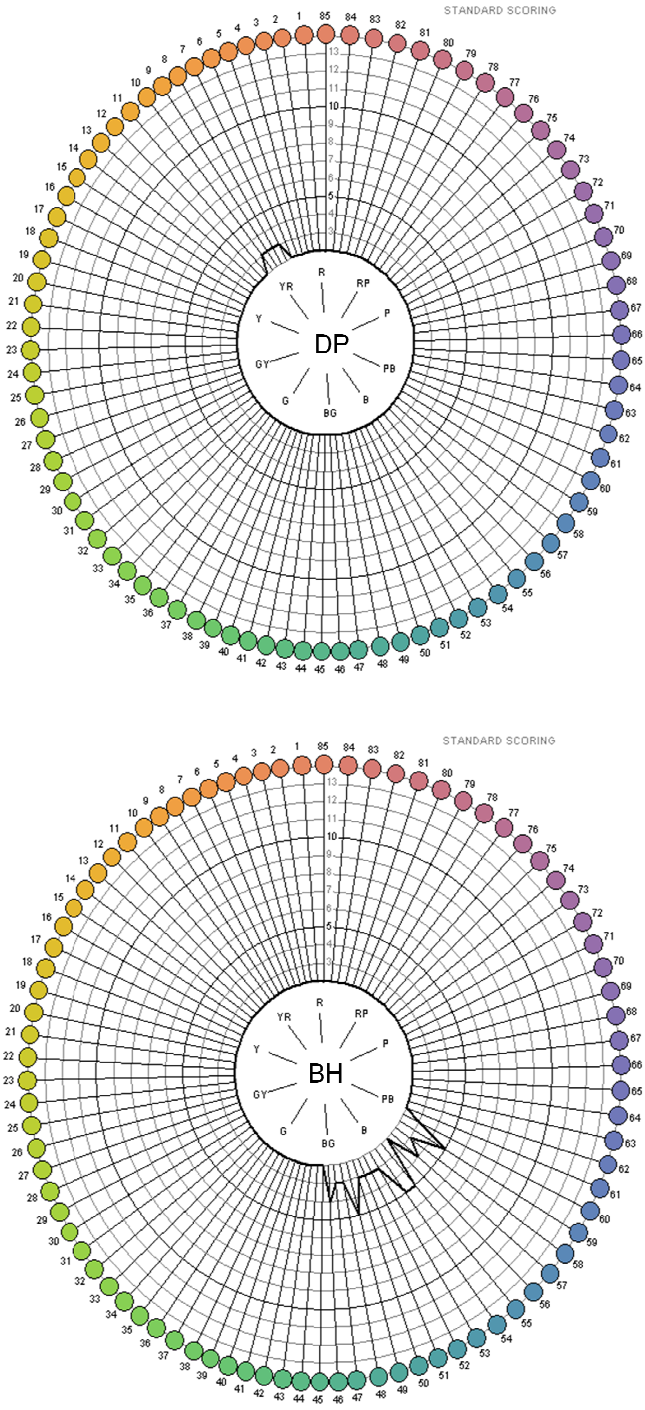

Figure 9.1. Farnsworth-Munsell 100 Hue Test results for subjects DP (top graph) and BH (bottom graph). The following hues are indicated: red (R), red-purple (RP), purple (P), purple-blue (PB), blue (B), blue-green (BG), green (G), green-yellow (GY), yellow (Y), yellow-red (YR).

9.2 Nonlinearity phase

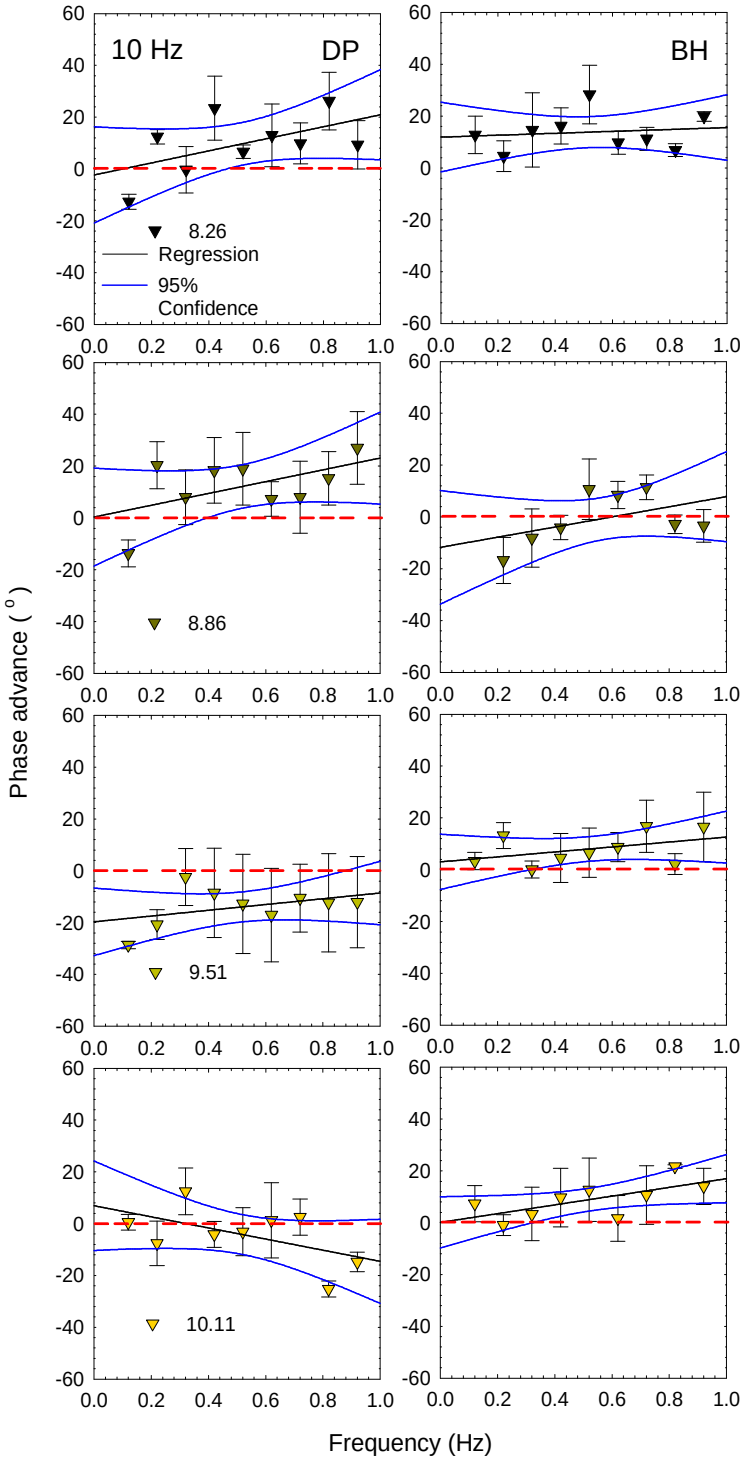

Figure 9.2. Mean ± 1 SE phase advance of a sinusoidally-flickering matching light (f=0.5 Hz) relative to a 560-nm amplitude-modulated flickering target of the same time-averaged radiance (f_c=10 Hz and f_{am}=0.5 Hz) so that the brightness changes of the two flickering lights are in phase. The legends show the time-averaged radiance of the target in $\log_{10}$ quanta s^{-1} deg^{-2} for each row of data. The dashed red horizontal line indicates a

phase advance of zero degrees, the black lines show the linear regression of the data and the blue lines show the 95% confidence interval of the linear regression.

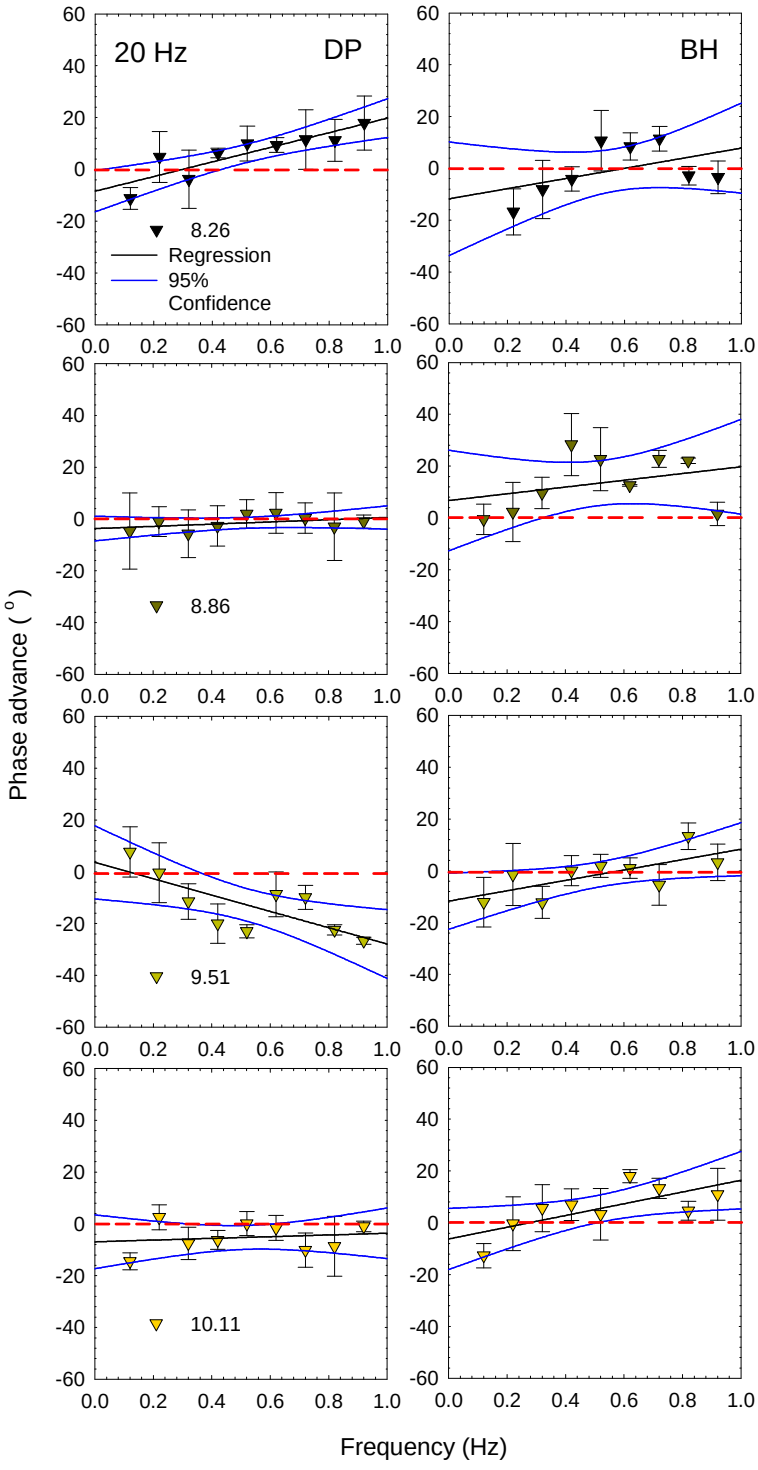

Figure 9.3. Mean ± 1 SE phase advance of a sinusoidally-flickering matching light (f=0.5 Hz) relative to a 560-nm amplitude-modulated flickering target of the same time-averaged radiance (f_c=20 Hz and f_{am}=0.5 Hz) so that the brightness changes of the two flickering lights are in phase. The legends show the time-averaged radiance of the target in $\log_{10}$ quanta s^{-1} deg^{-2} for each row of data. The dashed red horizontal line indicates a

phase advance of zero degrees, the black lines show the linear regression of the data and the blue lines show the 95% confidence interval of the linear regression.

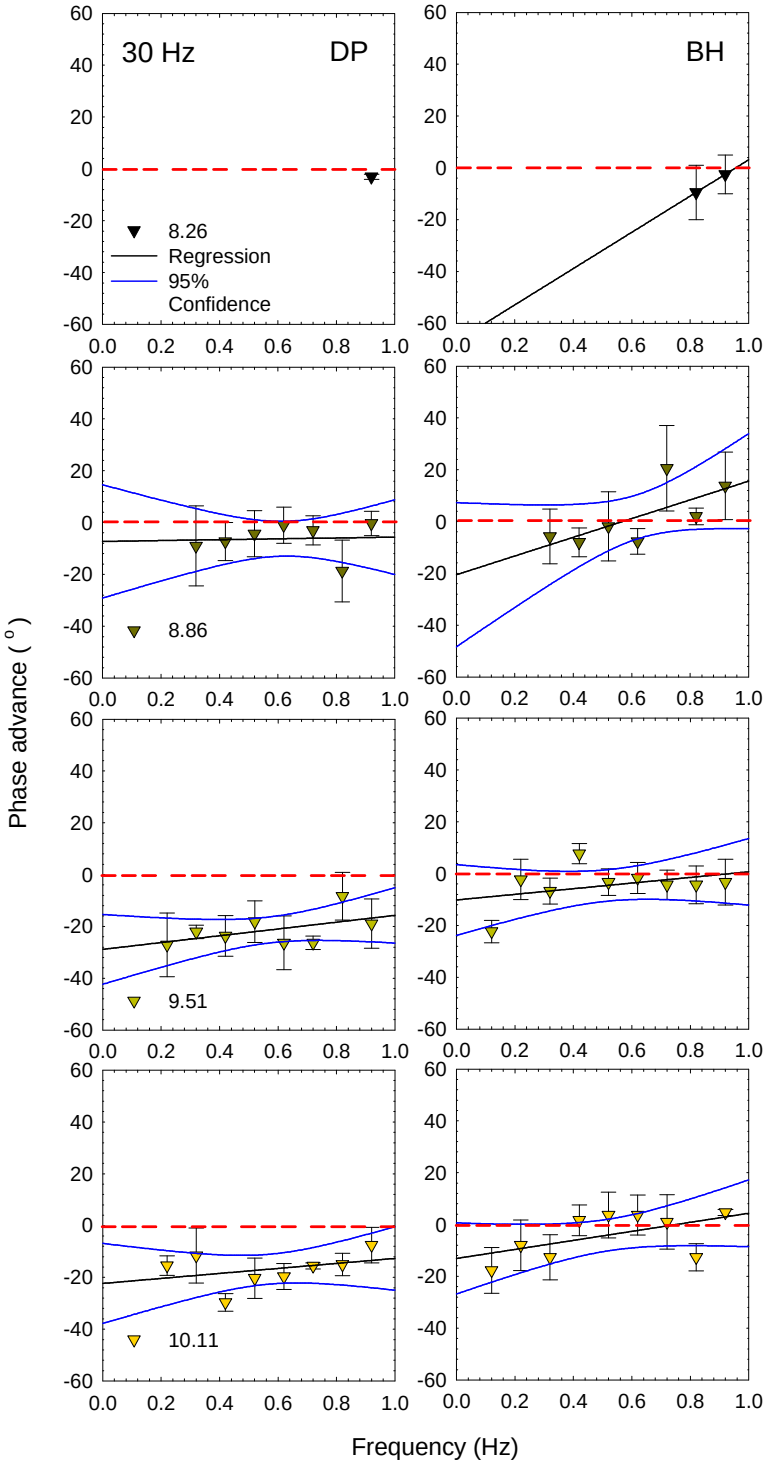

Figure 9.4. Mean ± 1 SE phase advance of a sinusoidally-flickering matching light (f=0.5 Hz) relative to a 560-nm amplitude-modulated flickering target of the same time-averaged radiance (f_c=30 Hz and f_{am}=0.5 Hz) so that the brightness changes of the two flickering lights are in phase. The legends show the time-averaged radiance of the target in $\log_{10}$ quanta s^{-1} deg^{-2} for each row of data. The dashed red horizontal line indicates a

phase advance of zero degrees, the black lines show the linear regression of the data and the blue lines show the 95% confidence interval of the linear regression.

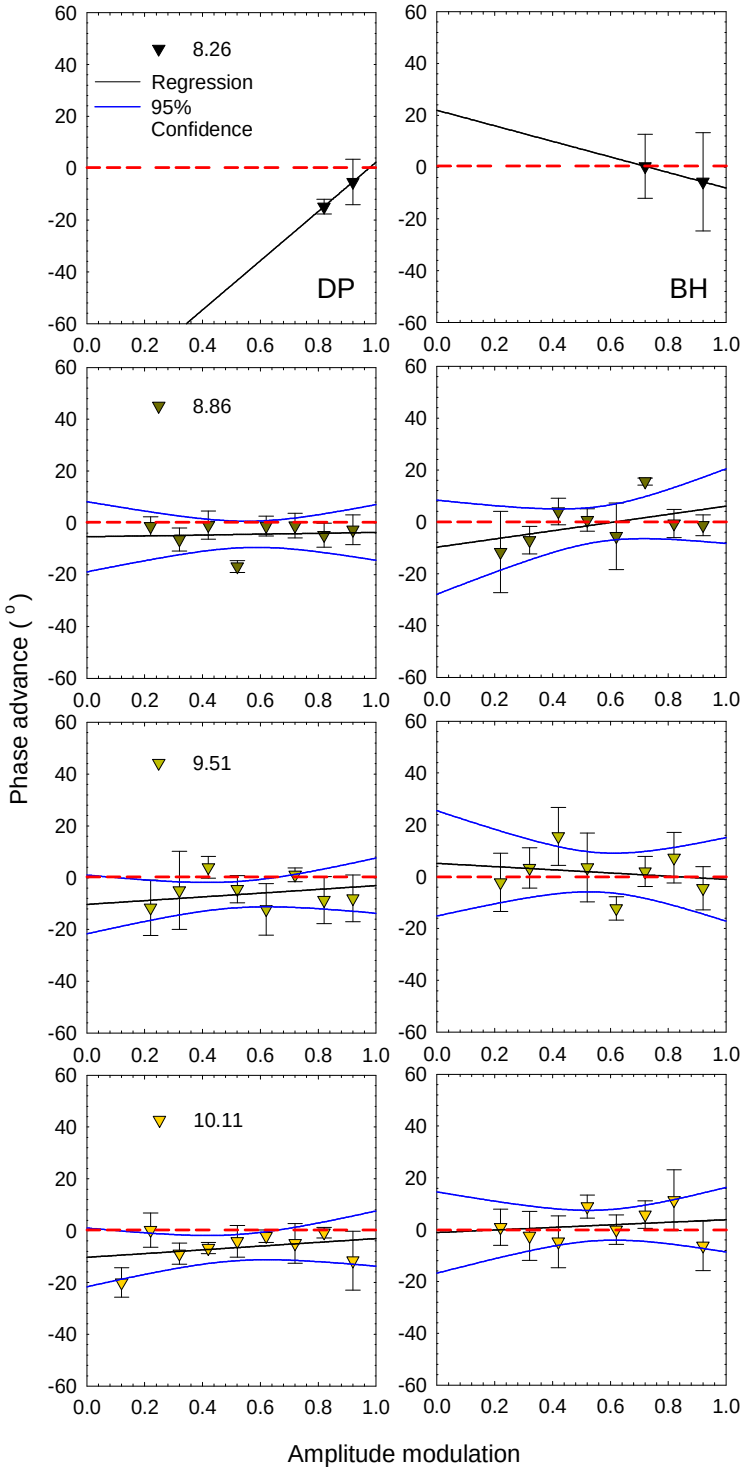

Figure 9.5. Mean ± 1 SE phase advance of a sinusoidally-flickering matching light superimposed on a pedestal relative to a 560-nm amplitude-modulated flickering target so that the brightness changes of the two flickering lights are in phase. The legends show the time-averaged radiance of the target in $\log_{10}$ quanta s^{-1} deg^{-2} for each row of data. The dashed red horizontal line indicates a phase advance of zero degrees, the black lines

show the linear regression of the data and the blue lines show the 95% confidence interval of the linear regression.

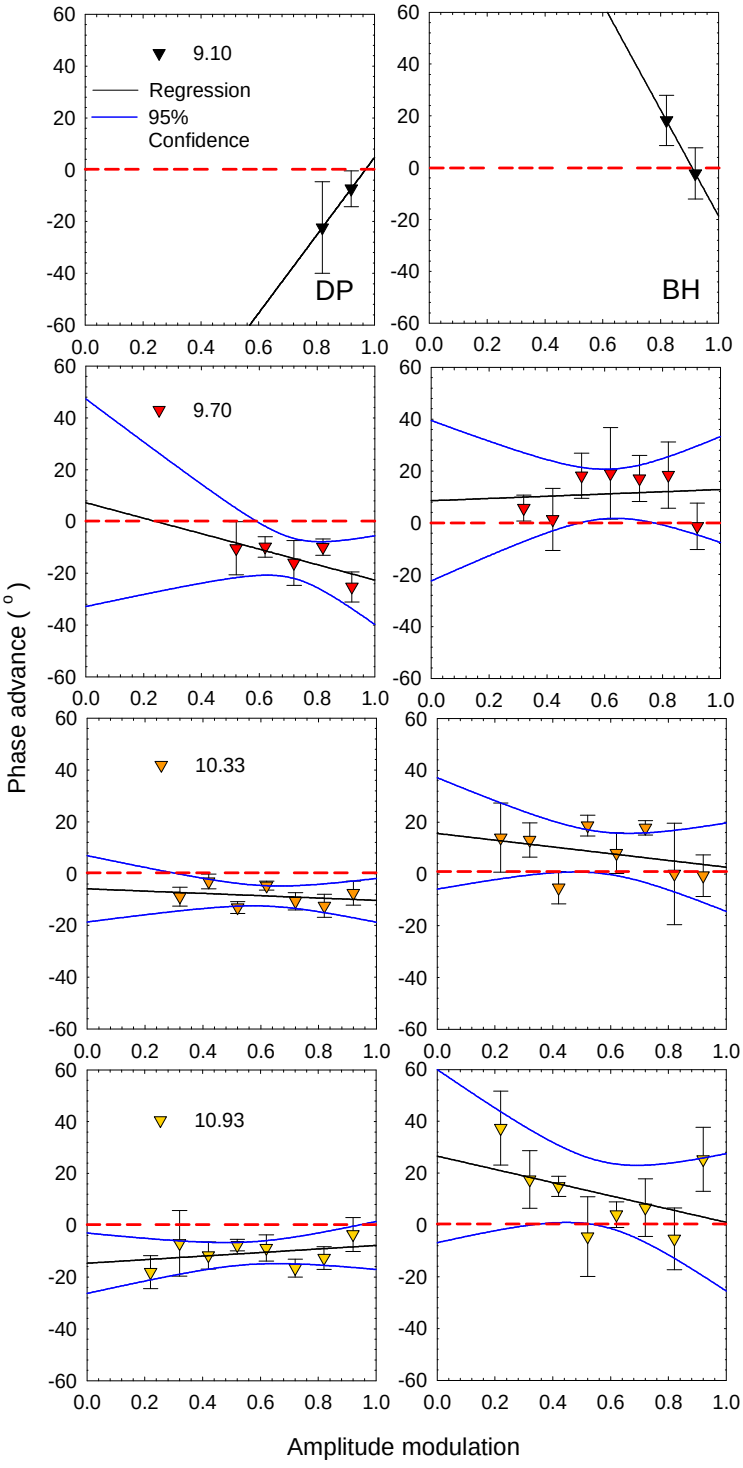

Figure 9.6. Mean ± 1 SE phase advance of a sinusoidally-flickering matching light superimposed on a pedestal relative to a 650-nm amplitude-modulated flickering target so that the colour changes of the two flickering lights are in phase. The legends show the time-averaged radiance of the target in $\log_{10}$ quanta s^{-1} deg^{-2} for each row of data. The dashed red horizontal line indicates a phase advance of zero degrees, the black lines

show the linear regression of the data and the blue lines show the 95% confidence interval of the linear regression.

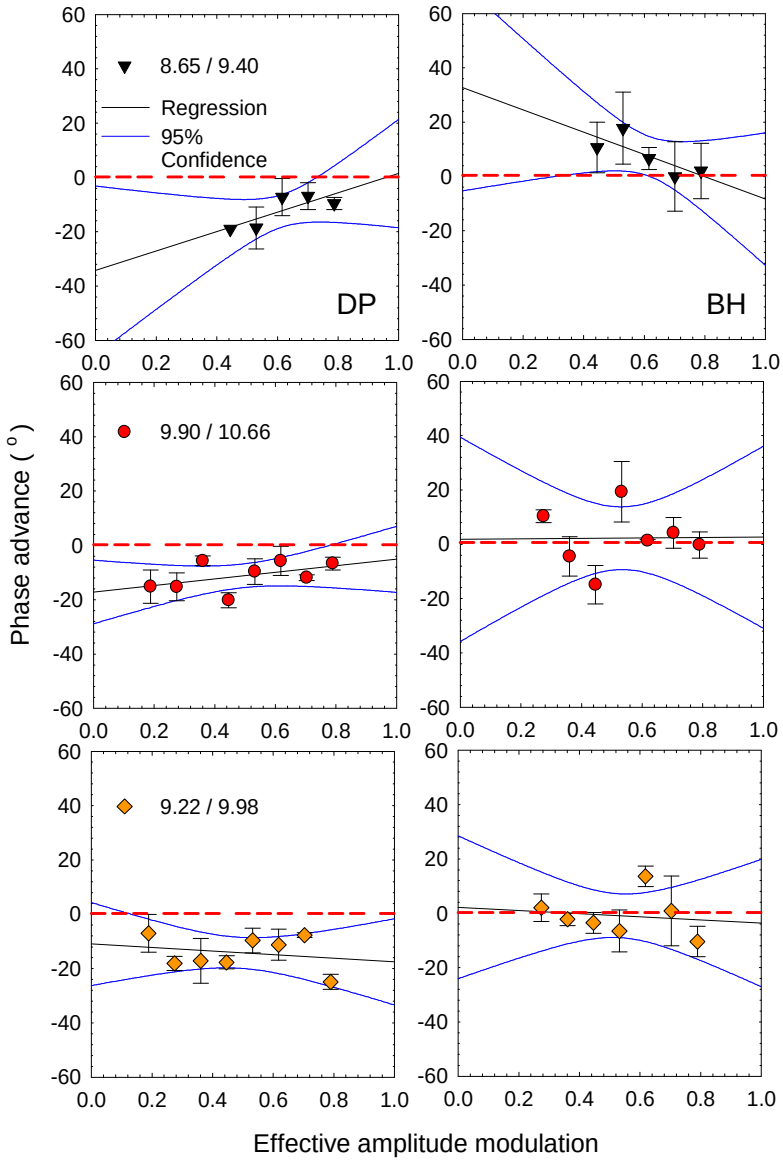

Figure 9.7. Mean ± 1 SE phase advance of a sinusoidally-flickering matching light superimposed on a pedestal relative to an L-cone isolating amplitude-modulated flickering target so that the colour changes of the two flickering lights are in phase. The legends show the time-averaged radiance of the 650nm and 529-nm lights used for the L-cone-isolating stimulus (650 nm / 529 nm) in $\log_{10}$ quanta s^{-1} deg^{-2} for each row of data. The dashed red horizontal line indicates a phase advance of zero degrees, the black lines show the linear regression of the data and the blue lines show the 95% confidence interval of the linear regression.

9.3 Target with annulus

A flickering target with sharp contrast to the background can evoke transient flicker at its border i.e. border transients. These border transients may increase the flicker sensitivity relative to the colour-change sensitivity. A steady annulus with the same chromaticity and time-averaged intensity as the flickering target can decrease border transients. In order to test whether the targets used in this investigation, where there was sharp contrast between the target and the surround, evoked significant border transients, the flicker sensitivities and colour-change sensitivities were measured in the presence of a matching annulus.

The same target was used as described in Section 3.1.1 (650-nm target with time-averaged radiance 10.33 $\log_{10}$ quanta s^{-1} deg^{-2} and 4° diameter). This wavelength and intensity of the target were chosen because the difference between the flicker sensitivity and colour-change sensitivity was smallest at this condition (Figure 3.6) and therefore, if the flicker sensitivity is reduced relative to the colour-change sensitivity by the introduction of the annulus, a failure of the Talbot-Plateau law would be most likely. Consequently, this experiment could also be used to test whether the Talbot-Plateau law fails under certain conditions for L- and M-cone stimuli, as it has been found to fail for S-cone stimuli by Stockman & Plummer (1998).

An annulus was introduced around the target, with an inner diameter of 4° and an outer diameter of 9°. It had the same wavelength and the same time-averaged radiance as the target. Subjects confirmed that the colour and brightness appearance of the annulus matched the colour and brightness appearance of the target.

In the first experiment, subjects were presented only with the target (without an annulus) and their tasks were to set the minimum modulation at which they could detect a flicker at f_c

(which varied from 5 Hz to CFF) and the minimum modulation at which they could detect a colour change at f_{am} (which was fixed at 0.5 Hz). In the subsequent experiment the target and annulus were both presented and the subjects' tasks were to set the minimum modulation for detecting the flicker and the minimum modulation for detecting a colour change in the target away from the colour or the annulus.

Figure 9.8 shows the sensitivities to flicker (triangles) and colour-change (circles) for the target alone (grey symbols) compared to the target with the annulus (red and pink symbols).

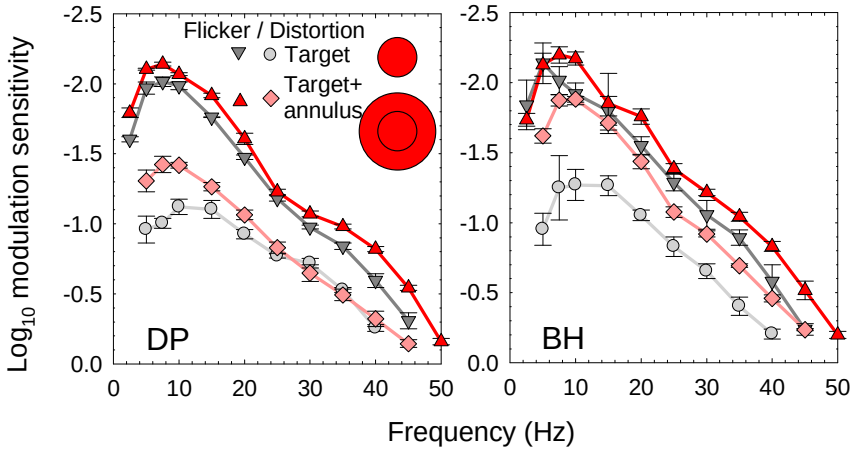

Figure 9.8. Mean ± 1 SE $\log_{10}$ modulation sensitivities for flicker and colour-change as a function of carrier frequency of a 650-nm amplitude-modulated flickering target (f_{am}=0.5 Hz) presented alone (grey symbols) and with an annulus (red and pink symbols).

The flicker sensitivities with and without the annulus have very similar curve shapes and relative values but the absolute values for the flicker sensitivities with the annulus show slightly higher sensitivities. The higher flicker sensitivity in the presence of an annulus is contrary to initial expectations but in agreement with previous studies that show an equiluminant steady annulus enhances modulation sensitivity at all frequencies (Harvey, 1970; Kelly, 1959) and increases CFF (Berger, 1953; Lythgoe & Tansley, 1929).

The colour-change sensitivities with and without the annulus have similar curve shapes at high frequencies (>25 Hz), with higher absolute sensitivities for the annulus condition. However, the colour-change sensitivity curves have slightly different shapes because the annulus enhances colour-change sensitivity at low frequencies (<25 Hz) relatively more than at higher frequencies.

Considering that the flicker sensitivity indicates the overall attenuation and that the colour-change sensitivity as a function of the carrier frequency indicates attenuation by the pre-nonlinearity stage, the difference between the flicker and colour-change sensitivities gives an indication of the attenuation characteristics by the post-nonlinearity stage (see Section 7.1). Figure 9.9 shows the differences between the flicker and colour-change sensitivities from the results in Figure 9.8.

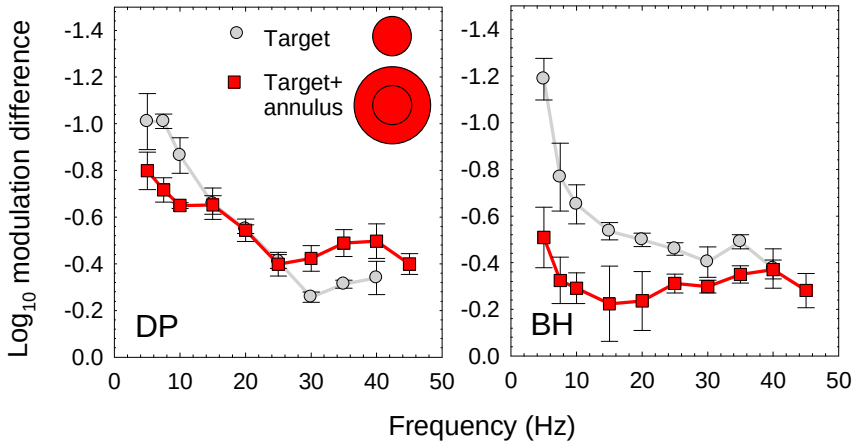

Figure 9.9. Mean ± 1 SE $\log_{10}$ modulation difference between flicker and colour-change sensitivities as a function of the carrier frequency of a 650-nm amplitude-modulated flickering target (f_{am}=0.5 Hz) presented alone (grey symbols) and with an annulus (red symbols).

The results in Figure 9.9 show that for the target-only condition the curve for the $\log_{10}$ modulation difference steadily decreases until it reaches a plateau at about 30 Hz while for the target-with-annulus condition the curve decreases less steeply to a lower frequency (25

Hz for DP and 15 Hz for BH). This can also be detected from the relative increase in colour-sensitivity at low frequencies, which makes the colour-sensitivity curve more parallel to the flicker-sensitivity curve.

In two separate subsequent experiments, using the same target-only and target-with-annulus conditions as described above but this time with the carrier frequency fixed at 30 Hz and the amplitude-modulation frequency varying, the subjects set the minimum modulation at which they could detect a colour change (target-only condition) or a colour change away from the annulus (target-with-annulus condition). The results are shown in Figure 9.10.

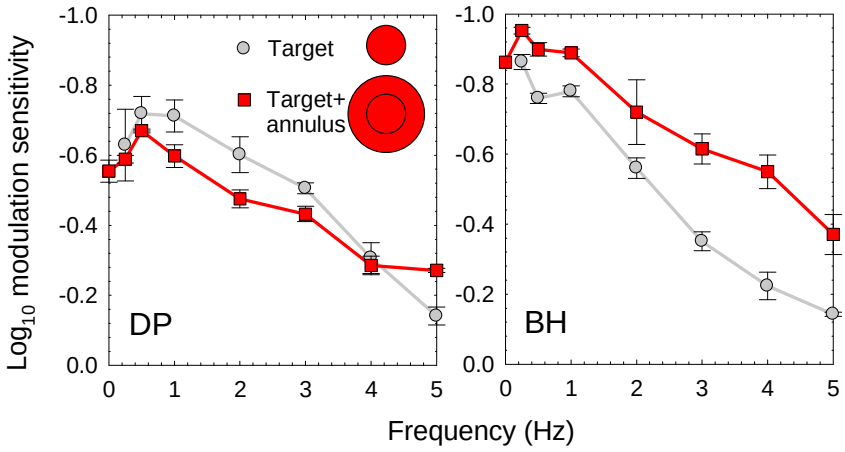

Figure 9.10. Mean ± 1 SE $\log_{10}$ modulation sensitivities for colour-change as a function of amplitude-modulation frequency of a 650-nm amplitude-modulated flickering target (f_c=30 Hz) presented alone (grey symbols) and with an annulus (red symbols).

The results in Figure 9.10 show that in the presence of the annulus the shape of the curve becomes shallower. Considering that the colour-change sensitivity as a function of amplitude-modulation frequency reflects the change in amplitude by both the nonlinearity and the post-nonlinearity function (Chapter 6) and that the input-output function of the nonlinearity contributes approximately equally for the target-only and target-with-annulus conditions, the shallower curve in the presence of the annulus suggests that the attenuation by the post-

nonlinearity stage becomes shallower in the presence of the annulus. This is consistent with the inferred attenuation by the nonlinearity stage at high frequencies in Figure 9.9.

An advantage of the target-with-annulus condition over the target-only condition is that it allows measurement of the colour-change when f_{am}=0 Hz i.e. it allows measurement of the sensitivity to a colour change of a flickering light relative to a steady light of the same chromaticity and time-averaged radiance. This is useful to confirm whether the post-nonlinearity function is indeed low-pass or whether it tends to be more band-pass as it approaches 0 Hz. The colour-change sensitivity at f_{am}=0 Hz in Figure 9.10 is not significantly different from the colour-change sensitivity at 1 Hz (where 1 Hz is close to the cut-off frequency of the post-nonlinearity stage in Chapter 6 and Section 7.1). This confirms earlier results in Chapter 6 and Section 7.1 that the post-nonlinearity stage acts as a low-pass rather than a band-pass filter.

9.4 Modelling software

9.4.1 Estimating the input-output function of a nonlinearity

```
clear all

close all

%% Define constants

fs = 1000;                                          % Sample frequency (Hz)

t = 0:1/fs:10-1/fs;                                 % Sampling window (10 s)

fc=10;                                              % Carrier frequency

fam=0.5;                                            % Amplitude-modulation frequency

offset=1;                                           % Make stimulus positive

ModDis=[];                                          % Define matrix for data


%% Calculate the input-modulation vs. output-distortion-at-f_am as a function of input DC

for offset2=0:0.25:2                                % Input DC level

%% Calculate output-distortion as a function of input-modulation

for modulation=[0 0.02 0.12 0.22 0.32 0.42 0.52 0.62 0.72 0.82 0.92 1] % Input modulation


%% Plot input signal to nonlinearity in time domain

CarSin=modulation*sin(2*pi*fc*t);                   % Carrier wave

AmpSin=0.5+0.5*cos(2*pi*fam*t);                     % Modulation wave

AmpModOffset=((CarSin.*AmpSin)+offset)*offset2;     % Amplitude-modulated wave


%% Convert input signal to frequency domain

m = length(AmpModOffset);                           % Window length
```

```
yInfft = fft(AmpModOffset,m);                    % FFT of the output
yInOffset = fftshift(yInfft);                    % Centre the power spectrum
powerInOffset = yInOffset.*conj(yInOffset)/m;    % Take complex conjugate
yIn=sqrt(powerInOffset)/100;                     % Extract amplitude of power spectrum

%% Input-output function of nonlinearity in time domain
for i=1:m                                        % For discontinuous functions define loop
if AmpModOffset(i)<1.5                           % Define interval of saturation
SinModOffsetACDC(i)=AmpModOffset(i).^2;          % Define slope of acceleration
else
SinModOffsetACDC(i)=2.25;                        % Define level of saturation
end
end

%% Convert output signal to frequency domain
yOutACDCfft = fft(SinModOffsetACDC,m);           % FFT of the output
yOutOffsetACDC = fftshift(yOutACDCfft);          % Centre the power spectrum
powerOutOffsetACDC = yOutOffsetACDC.*conj(yOutOffsetACDC)/m;   % Take complex conjugate
yOut=sqrt(powerOutOffsetACDC)/100;               % Extract amplitude of power spectrum

%% Extract data
DCIn=yIn(5001);
DCOut=yOut(5001);
DCchange=DCOut-DCIn;
FamOut=yOut(5006)+yOut(4996);          % Amplitude of fam
```

```
ACchange=FamOut/DCOut;              % Proportional to magnitude of change in appearance at fam

TwoFamOut=yOut(5011)+yOut(4991);    % 2nd harmonic of fam (2fam)

FcFamOut=yOut(5096)+yOut(4906);     % Sideband (fc-fam)

FcOut=yOut(5101)+yOut(4901);        % Amplitude of fc

ModDis=[ModDis; DCchange ACchange FamOut/TwoFamOut FcOut+2*FcFamOut]; % Matrix of data


%% Additional frequency components

TwoFcTwoFamOut=yOut(5191)+yOut(4811);           % 2fc-2fam

TwoFcFamOut=yOut(5196)+yOut(4806);              % 2fc-fam

TwoFcOut=yOut(5201)+yOut(4801);                 % 2fc

end

end
```

9.4.2 Simulink model

The results in this investigation can be used to create a Simulink model (Figure 9.12) for simulating the responses of the visual system to various stimuli. The input variables whose effects have been investigated in this study are the radiance (in $\log_{10}$ quanta s^{-1} deg^{-2}), modulation, carrier frequency, amplitude-modulation frequency and wavelength (Figure 9.12).

The pre-nonlinearity stage has been modelled as a centre filter and a surround filter determining the centre and surround responses, respectively, of a centre-surround cell (Figure 9.12) and a subsequent combination stage (as discussed in Section 7.3).

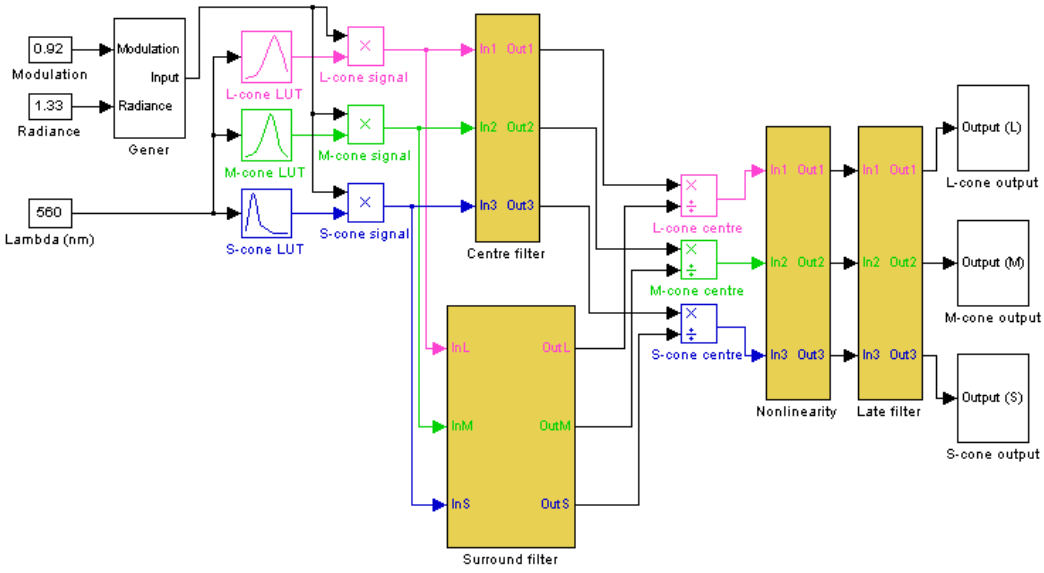

Figure 9.11. Simulink model of the pre-nonlinearity (centre and surround filters), nonlinearity and post-nonlinearity (late filter) stages in the cone pathways. Yellow rectangles show stages investigated in this study. Gener: generates the input signal. LUT: look-up-table according to the Stockman and Sharpe (2000b) 2º cone fundamentals.

9.5 Physiological substrates

Data	Cell response	R squared values for DP's data				R squared values for BH's data			
		I. 1	I. 2	I. 3	I. 4	I. 1	I. 2	I. 3	I. 4
Measured only	Cones	0.9657	0.8721	0.7397	0.8070	0.8725	0.8150	0.6399	0.5343
	Pc RGC	0.8196	0.8800	0.9689	0.9612	0.8020	0.9774	0.9293	0.8733
	Pl RGC	0.2570	0.1416	0.0474	0.1439	0.2182	0.0141	0.0939	0.1530
	M RGC	0.0067	0.0018	0.6449	0.7246	0.1122	0.2628	0.7236	0.8207
	M LGN	0.7823	0.8355	0.9858	0.9894	0.7215	0.9378	0.9589	0.9315
	P LGN	0.9794	0.9618	0.7266	0.8067	0.9776	0.9036	0.5336	0.2962
Inferred only	Cones	0.9390	0.0127	0.2960	0.0326	0.7176	0.0031	0.7163	0.5841
	Pc RGC	0.8810	0.9611	0.9810	0.9876	0.7941	0.8261	0.7624	0.8818
	Pl RGC	0.9301	0.9792	0.9705	0.9955	0.8692	0.8881	0.8405	0.9348
	M RGC	0.9711	0.9682	0.9320	0.9677	0.9338	0.9533	0.9158	0.9710
	M LGN	0.9535	0.7731	0.7402	0.7742	0.9066	0.9765	0.9511	0.9026
	P LGN	0.9216	0.8674	0.8630	0.8809	0.8109	0.9449	0.8351	0.9082
Total (inferred and measured)	Cones	0.0131	0.0908	0.1964	0.0604	0.0346	0.0018	0.1247	0.1111
	Pc RGC	0.7513	0.6700	0.2804	0.3243	0.6944	0.7505	0.3510	0.4053
	Pl RGC	0.1670	0.5378	0.7798	0.6750	0.0995	0.3642	0.7208	0.7280
	M RGC	0.3866	0.7888	0.9452	0.9197	0.2611	0.6336	0.9266	0.9246
	M LGN	0.7433	0.8459	0.6790	0.7196	0.5246	0.9263	0.8114	0.8061
	P LGN	0.4207	0.0792	0.0777	0.1233	0.6356	0.2321	0.0953	0.0987

Table 9.1. R squared values showing correlation between physiological cell responses and the pre-nonlinearity data for subjects DP and BH in response to a 650-nm target. The columns 'I. 1-4' indicate the four time-averaged intensity levels of the stimulus in increasing order. Orange and yellow indicate the highest and second highest r^2 values, respectively, across cell responses for each stimulus.

Data	Cell response	R squared values for DP's data				R squared values for BH's data			
		I. 1	I. 2	I. 3	I. 4	I. 1	I. 2	I. 3	I. 4
Measured only	Cones	0.8498	0.7935	0.4415	0.7700	0.4717	0.5387	0.0358	0.0943
	Pc RGC	0.9009	0.9055	0.7218	0.8442	0.8563	0.9209	0.3403	0.3414
	Pl RGC	0.1168	0.0231	0.0156	0.0366	0.0015	0.0356	0.4209	0.3631
	M RGC	0.0159	0.2726	0.5428	0.2401	0.2628	0.5783	0.8883	0.8188
	M LGN	0.9180	0.9605	0.8708	0.9218	0.9549	0.9443	0.4350	0.5164
	P LGN	0.9092	0.8761	0.3096	0.8538	0.5621	0.5038	0.0040	0.2015
Inferred only	Cones	0.5416	0.0031	0.0608	0.2700	0.0054	0.0088	<0.0000	0.6347
	Pc RGC	0.9130	0.9023	0.9924	0.8975	0.8418	0.8595	0.9046	0.7847
	Pl RGC	0.9579	0.9347	0.9905	0.8907	0.9024	0.9215	0.9518	0.8500
	M RGC	0.9875	0.9493	0.9483	0.8612	0.9670	0.9806	0.9903	0.9038
	M LGN	0.9250	0.8291	0.7698	0.7200	0.9581	0.8888	0.9244	0.8751
	P LGN	0.9307	0.9423	0.8417	0.9103	0.9487	0.8857	0.9365	0.7706
Total (inferred and measured)	Cones	0.0170	0.1001	0.3136	0.0095	0.1527	0.1422	0.3638	0.3270
	Pc RGC	0.7716	0.4853	0.3198	0.6306	0.6764	0.4865	0.2843	0.1649
	Pl RGC	0.3883	0.5929	0.8225	0.3705	0.6608	0.6987	0.8915	0.8759
	M RGC	0.6581	0.8522	0.9559	0.6487	0.8667	0.9194	0.9760	0.9315
	M LGN	0.8940	0.8684	0.7162	0.8458	0.9201	0.8748	0.7142	0.5682
	P LGN	0.1949	0.0748	0.0187	0.1386	0.0351	0.0755	0.0215	0.0530

Table 9.2. R squared values showing correlation between physiological cell responses and the pre-nonlinearity data for subjects DP and BH in response to a 560-nm target. The columns 'I. 1-4' indicate the four time-averaged intensity levels of the stimulus in increasing order. Orange and yellow indicate the highest and second highest r^2 values, respectively, across cell responses for each stimulus.

Data	Cell response	R squared values for DP's data				R squared values for BH's data			
		I. 1	I. 2	I. 3	I. 4	I. 1	I. 2	I. 3	I. 4
Measured only	Cones	0.9946	0.9753	0.9617	0.9868	0.7508	0.8408	0.8873	0.8816
	Pc RGC	0.4755	0.5876	0.6406	0.7981	0.6503	0.9571	0.8544	0.9308
	Pl RGC	0.5547	0.4775	0.3617	0.2213	0.1719	0.0876	0.0900	<0.0000
	M RGC	0.3829	0.0839	<0.0000	0.0328	0.2050	0.0169	0.1346	0.4394
	M LGN	0.4390	0.5872	0.5797	0.7479	0.4734	0.8990	0.8600	0.9511
	P LGN	0.8899	0.8698	0.8783	0.9553	0.9775	0.9503	0.8569	0.9127
Inferred only	Cones	0.4210	0.6858	0.6573	0.2091	0.8030	0.0063	0.5631	0.0041
	Pc RGC	0.3285	0.6203	0.5964	0.1531	0.9580	0.8683	0.4301	0.8134
	Pl RGC	0.3910	0.6772	0.6524	0.1981	0.9475	0.9014	0.5079	0.8680
	M RGC	0.4771	0.7480	0.7228	0.2652	0.9077	0.9228	0.6073	0.9112
	M LGN	0.7830	0.9392	0.9201	0.5611	0.6265	0.8930	0.8935	0.7846
	P LGN	0.8138	0.9709	0.9785	0.7297	0.6909	0.9799	0.7377	0.7874
Total (inferred and measured)	Cones	0.6996	0.8122	0.7724	0.9528	0.0173	0.0087	0.7909	0.4986
	Pc RGC	0.0258	0.0762	0.2920	0.1880	0.7614	0.8872	0.3295	0.8219
	Pl RGC	0.2700	0.3526	0.2515	0.4568	0.2798	0.1986	0.2467	0.0070
	M RGC	0.1219	0.1617	0.0802	0.2610	0.3989	0.4005	0.0672	0.0311
	M LGN	0.0001	0.0002	0.0365	0.0029	0.4754	0.7089	0.0635	0.4294
	P LGN	0.7765	0.7492	0.6567	0.5369	0.6375	0.4367	0.5846	0.5614

Table 9.3. R squared values showing correlation between physiological cell responses and the pre-nonlinearity data for subjects DP and BH in response to an L-cone-isolating target. The columns 'I. 1-4' indicate the four time-averaged intensity levels of the stimulus in increasing order. Orange and yellow indicate the highest and second highest r^2 values, respectively, across cell responses for each stimulus.

Data	Cell response	R squared values for DP's data				R squared values for BH's data			
		I. 1	I. 2	I. 3	I. 4	I. 1	I. 2	I. 3	I. 4
Measured only	Cones	0.9633	0.9631	0.9914	0.9554	0.9431	0.9009	0.7599	0.9697
	Pc RGC	0.5883	0.7297	0.7737	0.5880	0.4652	0.5209	0.4135	0.7135
	Pl RGC	0.4310	0.3264	0.2385	0.4327	0.5043	0.4200	0.4106	0.2862
	M RGC	0.2562	0.0214	0.0279	0.0024	0.3375	0.2498	0.0633	0.0136
	M LGN	0.5714	0.7188	0.7361	0.5345	0.4420	0.5153	0.4657	0.6790
	P LGN	0.9024	0.9164	0.9115	0.8333	0.7975	0.7813	0.5825	0.8470
Inferred only	Cones	0.2859	0.2606	0.0019	0.0544	0.5026	0.7051	0.7144	0.3375
	Pc RGC	0.0201	0.1713	0.5724	0.0051	0.1341	0.4371	0.2460	0.2296
	Pl RGC	0.0024	0.2128	0.6251	0.0129	0.2057	0.5212	0.3311	0.2983
	M RGC	0.0053	0.2730	0.6947	0.0358	0.2985	0.6213	0.4481	0.4061
	M LGN	0.1758	0.5277	0.8888	0.2228	0.5885	0.9084	0.7737	0.4175
	P LGN	0.0670	0.5947	0.8072	0.1864	0.3632	0.8309	0.5484	0.7043
Total (inferred and measured)	Cones	0.9483	0.9040	0.9207	0.9575	0.9090	0.8949	0.8394	0.9418
	Pc RGC	0.0273	0.0517	0.2281	0.0575	0.0274	0.0279	0.0005	0.1698
	Pl RGC	0.6412	0.4742	0.4092	0.6568	0.5809	0.5495	0.5410	0.4742
	M RGC	0.4430	0.2514	0.1687	0.3795	0.3847	0.3507	0.2862	0.2151
	M LGN	0.1224	0.0081	0.0083	0.0181	0.0857	0.0636	0.0159	0.0001
	P LGN	0.5439	0.7664	0.5739	0.4947	0.4973	0.4773	0.4870	0.5372

Table 9.4. R squared values showing correlation between physiological cell responses and the pre-nonlinearity data for subjects DP and BH in response to an M-cone-isolating target. The columns 'I. 1-4' indicate the four time-averaged intensity levels of the stimulus in increasing order. Orange and yellow indicate the highest and second highest r^2 values, respectively, across cell responses for each stimulus.

9.6 Equiluminant flicker

Sensitivity to chromatic flicker is much lower than sensitivity to luminance flicker at high frequencies (Kelly and van Norren, 1977). Chromatic flicker was used in this experiment to test whether the Talbot-Plateau law fails for amplitude-modulated chromatic flicker. (The law states that a flickering light above the CFF should appear the same colour and brightness as a non-flickering light of the same chromaticity and time-averaged intensity.) If a failure of the Talbot-Plateau law is found then it poses the advantage of measuring the colour-change sensitivity in the absence of flicker.

Chromatic flicker can be produced by cancelling the luminance flicker at f_c with a second flickering stimulus, which has a different wavelength and is ~180° out of phase. However, in practice, subjects often have to make minor adjustments in the phase away from 180° in order to achieve optimum cancellation (e.g. ~14° at 20-55 Hz in Cushman & Levinson, 1983; and ~9° at 6 Hz and 4° at 14 Hz in De Lange, 1958b). Larger phase delays for red and green lights have also been reported (Lindsey, Pokorny & Smith, 1986; Stockman et al., 2005; Swanson, Pokorny & Smith, 1987). In addition, due to the effects of light adaptation in speeding-up the responses of cones, phase and amplitude differences will appear between M- and L-cones if the two cone types are differentially adapted (e.g. Baylor, Nunn & Schnapf, 1984). Due to the large differences in M- and L-cone sensitivities at 650 nm, individual modulation settings as well as phase were recorded for each subject in the present experiment (Table 9.5).

Subjects adapted for two minutes to the 4° 650 nm 10.33 $\log_{10}$ s^{-1} deg^{-2} target described in Section 3.1.1 (which flickered at f_c =30 Hz, f_{am}=0 Hz and 92% modulation) before adding a dim, superimposed 560-nm light (which flickered at f_c =30 Hz and was always 180° out-of-phase with the f_c component of the 650-nm light, f_{am}=0 Hz and 92% modulation). The 650-

nm 10.33 $\log_{10}$ s^{-1} deg^{-2} initial target were chosen because the difference between the flicker sensitivity and colour-change sensitivity was smallest at these conditions (Figure 3.6) and therefore, if the flicker sensitivity is reduced relative to the colour-change sensitivity, a failure of the Talbot-Plateau law would be most likely. The subjects' task was to adjust the time-averaged radiance of the 560-nm light until they minimised the flicker of the 650-nm light (i.e. they flicker-photometrically matched the two lights).

An annulus was introduced around the target to limit border transients and narrow the difference between the flicker sensitivity and the colour-change sensitivity as described in Appendix 9.3. Subjects adjusted the wavelength of the annulus until its hue matched the hue of the steady target (i.e. the 650-nm light, and the superimposed 560-nm light at the intensity set in the previous experiment, both lights at 0% modulation) and then they adjusted the intensity of the annulus until its brightness matched the brightness of the target.

Subsequently, subjects first adjusted the modulation of the f_c=20 Hz and f_{am}=0.5 Hz flickering 650-nm target light (in the presence of a steady 560-nm light) and second adjusted the modulation of the f_c=20 Hz and f_{am}=0.5 Hz flickering 560-nm light (in the presence of a steady 650-nm light) until they could just perceive the flicker of each light. Once they had set the two modulations, the two lights were superimposed at those modulations with f_c 180° out-of-phase (f_{am} in phase) and subjects adjusted the f_c phase of the 560-nm light relative to that of the 650-nm light until the combined flicker of the two lights was minimised. The f_c was increased by 5 Hz up to CFF and the subjects set the modulations and phase for the 650-nm and 560-nm lights at each f_c (results in Table 9.5).

Carrier frequency (Hz)	650 nm modulation (%)		560 nm modulation (%)		Phase of 560 nm (°)	
	DP	BH	DP	BH	DP	BH
20	0.17	0.10	0.12	0.15	176	166
25	0.23	0.60	0.18	0.60	181	192
30	0.24	0.60	0.27	0.60	190	194
35	0.13	0.60	0.15	0.60	191	186
40	0.23	0.52	0.30	0.76	192	200

Table 9.5. Equiluminance matches: the percentage modulation for the 650-nm and 560-nm lights and the relative phase of the 560-nm light relative to the 650-nm light at various carrier frequencies.

The results in Table 9.5 show that below f_c =25 Hz the 560-nm light leads relative to its theoretical 180° displacement. However, between f_c =25 and f_c =40 the phase of the 560-nm light becomes increasingly delayed relative to its theoretical 180° displacement.

Once the above settings were made, subjects adjusted the modulation of the two lights together (keeping the ratio between the modulations in Table 9.5 constant) in the presence of the annulus until they found the minimum modulation at which they could detect flicker and, in a separate experiment, the minimum modulation at which they could detect a colour change at f_{am} for a flickering target of f_{am} =0.5 Hz and $20 \leq f_c \leq 50$ Hz.

Figure 9.12 shows $\log_{10}$ modulation sensitivity for flicker (triangles) and colour-change (non-black circles) in response to a flickering 650-nm target (non-black symbols in Figure 9.12, also shown in Figure 9.8) and the L-cone contrast for flicker sensitivity (squares) and colour-change sensitivity (half-black, circles) in response to a chromatically-flickering target composed of a 650-nm light and a superimposed 560-nm light (half-black symbols in Figure 9.12).

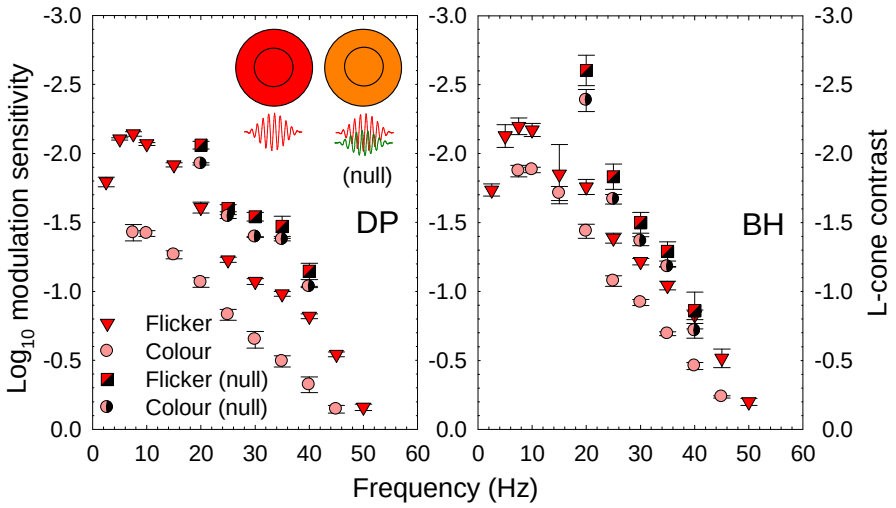

Figure 9.12. Mean ± 1 SE $\log_{10}$ modulation sensitivities to flicker (triangles) and colour-change (non-black circles) in response to flicker (non-black symbols) and mean ± 1 SE L-cone contrast for flicker sensitivity (squares) and colour-change sensitivity (half-black circles) in response to chromatic flicker (where the luminance flicker has been nulled, half-black symbols). The discs represent the approximate hue of the stimuli and below them is indicated the approximate waveform of the target: a 650-nm target and annulus are presented in the left disc and a 650-nm with a superimposed 560-nm light are presented in the right disc.

Subject BH found it relatively more difficult than DP to null the 650-nm flicker with the 560-nm light. Although the flicker sensitivity was decreased relative to the colour-change sensitivity, flicker sensitivity always remained higher than colour-change sensitivity. These results show that the Talbot-Plateau law holds for L- and M-cone stimuli, unlike for S-cone stimuli (Stockman & Plummer, 1998). The difference in the failure of the law between cone types can be related to the fact that S-cones saturate at high intensities while M- and L-cones do not (Figures 3.6 and 3.7).

The presence of visible flicker in all cases where colour change was visible also meant that a forced-choice method could not be used for measuring colour-change sensitivities (since subjects would always be able to tell which of the two trials contained the amplitude-modulated stimulus by the visible flicker).

The results in Figure 9.12 also show that for chromatic (equiluminant) flicker the shape of the colour-change sensitivity curve remains approximately the same as that for luminance flicker, which suggests that the nonlinearity is the same for the chromatic and luminance pathways.

References

Ayama, M., Nakatsue, T., & Kaiser, P.E. (1987). Constant hue loci of unique and binary balanced hues at 10, 100, and 1000 Td. *Journal of the Optical Society of America A, 4*, 1136-1144.

Ball, R.J. (1964). An investigation of chromatic brightness enhancement tendencies. *American Journal of Optometry and Physiological Optics, 41*, 333-361.

Ball, R.J., & Bartley, H. (1965). Effects of temporal manipulation of photic stimulation on perceived brightness hue and saturation. *American Journal of optometry and archives of American Academy of optometry, 2* (10), 8.

Ball, R.J., & Bartley, S.H. (1966). Changes in brightness index, saturation and hue produced by luminance-wavelength-temporal interactions. *Journal of the Optical Society of America, 66*, 695-699.

Ball, R.J., & Bartley, S.H. (1971). Several aspects of visual perception. *Journal of the American Optometry Association, 42*, 649-652.

Bartley, S.H. (1938). A central mechanism in brightness enhancement. *Proceedings of the Society for Experimental Biology and Medicine, 38*, 535-536.

Bartley, S.H. (1939). Some effects of intermittent photic stimulation. *Journal of Experimental Psychology, 25*, 462-480.

Bartley, S.H. (1951a). Brightness comparisons when one eye is stimulated intermittently and the other steadily. *Journal of Psychology, 34*, 165-167.

Bartley, S.H. (1951b). Brightness enhancement in relation to target intensity. *Journal of Psychology, 32*, 57-62.

Bartley, S.H. (1959). Central mechanisms of vision. In: H.W. Magoun (Ed.) *Handbook of Physiology*, 1 Neurophysiology (Washington, D. C.: Am. Physiol. Soc.

Bartley, S.H., & Nelson, T.M. (1960). Certain chromatic and brightness changes associated with rate of intermittency of photic stimulation. *Journal of Psychology, 50,* 323-332.

Bartley, S.H., Nelson, T.M., & Ranney, J.E. (1961). The sensory parallel of the reorganization period in the cortical response in intermitted retinal stimulation. *J. Psychology, 52,* 127-147.

Bartley, S.H., Paczevitz, G., & Valsi, E. (1957). Brightness enhancement and the stimulus cycle. *J. Psychology, 52,* 127-147.

Baylor, D.A., Nunn, B.J., & Schnapf, J.L. (1984). The photocurrent, noise and spectral sensitivity of rods of the monkey Macaca fascicularis. *Journal of Physiology, 357,* 575-607.

Bedrosian, E., & Rice, S.O. (1971). The output properties of Volterra systems (nonlinear systems with memory) driven by harmonic and Gaussian inputs. *Pro. IEEE., 59,* 1688-1707.

Benton, C.P., & Johnston, A. (1999). Contrast inconstancy across changes in polarity. *Vision Res., 39,* 4076-4084.

Berger, C. (1953). Illumination of surrounding field and flicker fusion frequency with foveal images of different sizes. *Acta Physiol., Scand. 30,* 161-170.

Billock, V.A. (1995). Cortical Simple Cells Can Extract Achromatic Information from the Multiplexed Chromatic and Achromatic Signals in the Parvocellular Pathway. *Vision Research, 35* (16), 2359-2369.

Bimler, D.L., & Paramei, G.V. (2005). Bezold–Brücke effect in normal trichromats and protanopes. *J Opt Soc Am A 22* (10), 2120-2136.

Bleck, F.C., & Craig, E.A. (1965). Brightness enhancement and hue II. Hue shift as a function of steady and intermittent photic stimulation. *Journal of Psychology, 59,* 251-258.

Bloch, A.M. (1985). Experiences sur la vision. *C. R. Seances Soc.Biol. , 37,* 3.

Bowmaker, J.K., Parry, J.W.L., & Mollon, J.D. (2003). The arrangement of L and M cones in human and a primate retina. *Normal and defective color vision* (pp. 39-50). Oxford: Oxford University Press.

Boycott, B.B., & Wässle, H. (1991). Morphological classification of bipolar cells of the primate retina. *European Journal of Neuroscience, 3*, 1069-1088.

Boynton, R.M. (1979). Human Color Vision. (New York: Holt, Rinehart and Winston.

Brewster, D. (1838). On the influence of succession of light upon the retina. *Philosophical Magazine, 4*, 241.

Brindley, G.S. (1962). Beats produced by simultaneous stimulation of the human eye with intermittent light and intermittent or alternating electric current. *Journal of Physiology, 164*, 157-167.

Broca, A., & Sulzer, D. (1902). La sensation humineuse en function du temps. *J. Physiol Patbol Gen., 6*, 55-68.

Broca, A., & Sulzer, D. (1903). Sensation lumineuse en fonction du temps pour les lumieres colores; techniques et resultats. *Acad. Sei. Paris, 137*, 3.

Broca, A., & Sulzer, D. (1904). La sensation humineuse en function du temps. *J.Physiol.Patbol Gen., 6*, 55-68.

Brücke, E. (1848). Über die Nutzeffect intermitterender Netzhautreizungen. *Sitzungsberichte der Mathematisch-Naturwissenschaftlichen Classe der Kaiserlichen Akademie der Wissenschaften, 49*, 128-153.

Brücke, E.W. (1878). Über einige Empfindungen im Gebiete der Sehnerven. *Sitzungsberichte der Akademie der Wissenschaften in Wien, Mathematisch-Naturwissenschaftliche Klasse, Abteilung 3, 77*, 39-71.

Burns, S.A., Elsner, A.E., & Kreitz, M.R. (1992). Analysis of nonlinearities in the flicker ERG. *Optometry and Vision Science, 69*, 95-105.

Burton, G.J. (1973). Evidence for non-linear response processes in the human visual system from measurements on the thresholds of spatial beat frequencies. *Vision Research, 13*, 1211-1225.

Capilla, P., Luque, M.J., Gomez, J., & Palomares, A. (2001). On Saturation and Related Parameters Following Guth's ATD Colour-Vision Model. *Color research and application, 26* (4), 305-321.

Casagrande, V., & Kaas, J. (1994). The afferent, intrinsic, and efferent connections of primary visual cortex in primates. In: A. Peters, & K. Rockland (Eds.), *Cerebral cortex,* 10 (pp. 201–259). New York: Plenum.

Cavonius, C.R., & Estévez, O. (1975). Contrast sensitivity of individual colour mechanisms of human colour vision. *Journal of Physiology, 248*, 649-662.

Chander, D., & Chichilnisky, E.J. (2001). Adaptation to Temporal Contrast in Primate and Salamander Retina. *Journal of Neuroscience, 21* (24), 9904–9916.

Chang, Y., Burns, S.A., & Kreitz, M.R. (1993). Red-green flicker photometry and nonlinearities in the flicker electroretinogram. *Journal of the Optical Society of America A, 10*, 1413-1422.

Chen, B., Makous, W., & Williams, D.R. (1993). Serial spatial filters in vision. *Vision Research, 33,* 413-427.

Cole, G.R., Hine, T., & McIlhagga, W. (1993). Detection mechanisms in L-, M-, and S-cone contrast space. *Journal of the Optical Society of America A, 10*, 38-51.

Cushman, W.B., & Levinson, J.Z. (1983). Phase shift in red and green counter-phase flicker at high frequencies. *Journal of the Optical Society of America, 73*, 1557-1561.

De Lange, H. (1952). Experiments on flicker and some calculations on an electrical analogue of the foveal systems. *Physica, 18*, 935-950.

De Lange, H. (1958a). Research into the dynamic nature of the human fovea-cortex systems with intermittent and modulated light. I. Attenuation characteristics with white and colored light. *J. Opt. Soc. Am., 48*, 777-784.

De Lange, H. (1958b). Research into the dynamic nature of the human fovea-cortex systems with intermittent and modulated light. II. Phase shift in brightness and delay in color perception. *Journal of the Optical Society of America, 48*, 784-789.

De Monasterio, F.M. (1978). Properties of concentrically organised X and Y ganglion cells of macaque retina. *Journal of Neurophysiology, 41*, 1394-1417.

De Monasterio, F.M., & Gouras, P. (1975). Functional properties of ganglion cells of the rhesus monkey retina. *Journal of Physiology, 251*, 167-195.

De Valois, R.L., & De Valois, K.K. (1993). A multi-stage color model. *Vision Research, 33*, 1053-1065.

Derrington, A.M., Krauskopf, J., & Lennie, P. (1984). Chromatic mechanisms in lateral geniculate nucleus of macaque. *Journal of Physiology, 357*, 241-265.

Derrington, A.M., & Lennie, P. (1984). Spatial and temporal contrast sensitivities of neurones in the lateral geniculate nucleus of macaque. *Journal of Physiology, 357*, 219-240.

Ebenezer, N.D., Michaelides, M., Jenkins, S.A., Audo, I., Webster, A.R., Cheetham, M.E., Stockman, A., Maher, E.R., Ainsworth, J.R., Yates, J.R., Bradshaw, K., Holder, G.E., Moore, A.T., & Hardcastle, A.J. (2005). Identification of novel RPGR ORF15 mutations in X-linked progressive cone-rod dystrophy (XLCORD) families. *Investigative Ophthalmology and Visual Science, 46*, 1891-1898.

Eisner, A., & MacLeod, D.I.A. (1980). Blue sensitive cones do not contribute to luminance. *Journal of the Optical Society of America, 70*, 121-123.

Eisner, A., & MacLeod, D.I.A. (1981). Flicker photometric study of chromatic adaptation: selective suppression of cone inputs by colored backgrounds. *Journal of the Optical Society of America, 71*, 705-718.

Estévez, O., & Cavonius, C.R. (1975). Flicker sensitivity of the human red and green color mechanisms. *Vision Research, 15*, 879-881.

Estévez, O., & Spekreijse, H. (1974). A spectral compensation method for determining the flicker characteristics of the human color mechanisms. *Vision Research, 14*, 823-830.

Estévez, O., & Spekreijse, H. (1982). The "silent substitution" method in visual research. *Vision Research, 22*, 681-691.

Forsyth, D.M. (1860). Use of Fourier model in describing the fusion of complex visual stimuli. *J. Optical Society America, 50*, 337-341.

Fuortes, M.G.F., & Hodgkin, A.L. (1964). Changes in time scale and sensitivity in the ommatidia of *limulus*. *Journal of Physiology, 172*, 239-263.

Gouras, P., & Zrenner, E. (1979). Enhancement of luminance flicker by color-opponent mechanisms. *Science, 205*, 587-589.

Green, D.G. (1968). The contrast sensitivity of the colour mechanisms of the human eye. *Journal of Physiology, 196*, 415-429.

Guth, S.L. (1991). A model for color vision and light adaptation. *Journal of the Optical Society of America A, 8*, 976-993.

Guth, S.L., Alexander, J.V., Chumbly, J.I., Gillman, C.B., & Patterson, M.M. (1968). Factors affecting luminance additivity at threshold among normal and color-blind subjects and elaborations of a trichromatic-opponent color theory. *Vision Research, 8*, 913-928.

Guth, S.L., & Lodge, H.R. (1973). Heterochromatic additivity, foveal spectral sensitivity, and a new color model. *Journal of the Optical Society of America, 63*, 450-462.

Guth, S.L., Massof, R.W., & Benzschawel, T. (1980). Vector model for normal and dichromatic color vision. *Journal of the Optical Society of America, 70*, 197-212.

Haegerstrom-Portnoy, G., Hewlett, S.E., & Barr, S.A. (1989). S cone loss with aging. In: B. Drum, & G. Verriest (Eds.), *Documenta Ophthalmologica Proceeding Series, Ninth Symposium of the International Research Group on Colour Vision Deficiencies,* Colour Vision Deficiencies, IX (pp. 345-352). Dordrecht, The Netherlands: Kluwer Academic Publishers.

Harvey, L.O. (1970). Flicker sensitivity and apparent brightness as a function of test field and surround configuration. *Journal of the Optical Society of America, 60,* 860-864.

Hendry, S., & Yoshioka, T. (1994). A neurochemically distinct third channel in the macaque dorsal lateral geniculate nucleus. *Science, 264,* 575–577.

Hering, E. (1878). Zur Lehre vom Lichtsinne. Sechs Mittheilungen an die Kaiserliche Akademie der Wissenschaften in Wien. (Wien: Carl Gerold's Sohn.

Hess, R.F., Mullen, K.T., & Zrenner, E. (1989). Human photopic vision with only short wavelength cones: Post-receptoral properties. *Journal of Physiology, 417,* 150-169.

Hess, R.F., & Snowden, R.J. (1992). Temporal properties of human visual filters: number, shape and spatial covariance. *Vision Research, 32* (47-59), 150-169.

Hochstein, S., & Shapley, R.M. (1976). Linear and nonlinear spatial subunits in Y cat retinal ganglion cells. *Journal of Physiology, 262*, 265-284.

Hurvich, L.M., & Jameson, D. (1955). Some quantitative aspects of an opponent-colors theory. II. Brightness, saturation, and hue in normal and dichromatic vision. *Journal of the Optical Society of America, 45*, 602-616.

Hurvich, L.M., & Jameson, D. (1957). An opponent-process theory of color vision. *Psychological Review, 64,* 384-404.

Ikeda, M., Yaguchi, H., Yoshimatsu, K., & Ohmi, M. (1982). Luminous-efficiency functions for point sources. *Journal of the Optical Society of America A, 72*, 68-73.

Ingling, C.R., Grigsby, S.S., & Long, R.C. (1992). Comparison of spectral sensitivity using heterochromatic flicker photometry and an acuity criterion. *Color Research & Application, 17*, 187-196.

Ingling, C.R., Jr., Barley, J.P., & Ghani, N. (1996). Chromatic content of spectral lights. *Vision Research, 36*, 2537-2551.

Ingling, C.R., Jr., & Martinez-Uriegas, E. (1983). The relationship between spectral sensitivity and spatial sensitivity for the primate r-g X-channel. *Vision Research, 23*, 1495-1500.

Ingling, C.R., Jr., & Martinez-Uriegas, E. (1985). The spatiotemporal properties of the r-g X-cell channel. *Vision Research, 25*, 33-38.

Ingling, C.R., Jr., & Martinez, E. (1983). The spatio-chromatic signal of the r-g channels. In: J.D. Mollon, & L.T. Sharpe (Eds.), *Colour Vision: Physiology and Psychophysics* (pp. 433-444). London: Academic.

Ingling, C.R., Jr., & Tsou, H.B.-P. (1977). Orthogonal combination of the three visual channels. *Vision Research, 17*, 1075-1082.

Ingling, C.R., Jr., & Tsou, H.B.-P. (1988). Spectral sensitivity for flicker and acuity criteria. *Journal of the Optical Society of America A, 5*, 1374-1378.

Ives, H.E. (1922). Critical frequency relations in scotopic vision. *Journal of the Optical Society of America and Review of Scientific Instruments, 6*, 254-268.

Jacobs, H.G., & Wascher, C.T. (1967). Bezold-Brücke Hue Shift: Further Measurements. *J Opt. Soc.Amer., 57*, 1155-1156.

Jameson, D., & Hurvich, L.M. (1955). Some quantitative aspects of an opponent-colors theory. I. Chromatic responses and spectral saturation. *Journal of the Optical Society of America, 45*, 546-552.

Judd, D.B. (1949). Standard response functions for protanopic and deuteranopic vision. *Journal of the Optical Society of America, 39*, 505.

Kaiser, P.K., & Comerford, J.P. (1975). Flicker photometry of equally bright lights. *Vision Research, 15*, 1399-1402.

Kaiser, P.K., Lee, B.B., Martin, P.R., & Valberg, A. (1990). The physiological basis of the minimally distinct border demonstrated in the ganglion cells of the macaque retina. *Journal of Physiology, 422*, 153-183.

Kaplan, E., Lee, B.B., & Shapley, R.M. (1990). New views of primate retinal function. In: N. Osborne, & J. Chader (Eds.), *Progress in retinal research*, 9 (pp. 273-336). New York: Pergamon Press.

Kaplan, E., & Shapley, R.M. (1986). The primate retina contains two types of ganglion cells, with high and low contrast sensitivity. *Proc. Natl. Acad. Sci. USA, 83* (8)

Kelly, D.H. (1959). Effects of sharp edges in a flickering field. *Journal of the Optical Society of America, 49*, 730-732.

Kelly, D.H. (1961a). Flicker fusion and harmonic analysis. *Journal of the Optical Society of America, 51*, 917-918.

Kelly, D.H. (1961b). Visual responses to time-dependent stimuli I. Amplitude sensitivity measurements. *Journal of the Optical Society of America, 51*, 422-429.

Kelly, D.H. (1961c). Visual responses to time-dependent stimuli II. Single-channel model of the photopic visual system. *Journal of the Optical Society of America, 51*, 747-754.

Kelly, D.H. (1969). Diffusion Model of linear flicker Responses. *Journal of the Optical Society of America, 59* (12), 5.

Kelly, D.H. (1971a). Theory of flicker and transient responses, I. Uniform fields. *Journal of the Optical Society of America, 61*, 537-546.

Kelly, D.H. (1971b). Theory of flicker and transient responses, II. Counterphase gratings. *Journal of the Optical Society of America, 61*, 632-640.

Kelly, D.H. (1972). Flicker. In: L. Hurvich, & D. Jameson (Eds.), *Handbook of sensory physiology*, VII (New York: Springer-Verlag.

Kelly, D.H. (1974). Spatio-temporal frequency characteristics of color-vision mechanisms. *Journal of the Optical Society of America, 64*, 983-990.

Kelly, D.H. (1976). Differences between red and green color-mechanism characteristics: Interaction or artifact? *Journal of the Optical Society of America, 66*, 1430-1435.

Kelly, D.H. (1981). Nonlinear visual responses to flickering sinusoidal grating. *Journal of the Optical Society of America, 71*, 1051-1055.

Kelly, D.H. (1983). Spatiotemporal variation of chromatic and achromatic contrast thresholds. *Journal of the Optical Society of America, 73*, 742-750.

Kelly, D.H., & van Norren, D. (1977). Two-band model of heterochromatic flicker. *Journal of the Optical Society of America, 67*, 1081-1091.

Kelly, D.H., & Wilson, H.R. (1978). Human flicker sensitivity: Two stages of retinal diffusion. *Science, 202*, 896-899.

King-Smith, P.E., & Carden, D. (1976). Luminance and opponent-color contributions to visual detection and adaptation and to temporal and spatial integration. *Journal of the Optical Society of America, 66*, 709-717.

Krauskopf, J., Williams, D.R., & Heeley, D.W. (1982). Cardinal directions of color space. *Vision Research, 22*, 1123-1131.

Krauskopf, J., Wu, H.J., & Farell, B. (1996). Coherence, cardinal directions and higher-order mechanisms. *Vision Research, 36*, 1235-1245.

Kremers, J., Scholl, H.P.N., Knau, H., Berendschot, T.T.J.M., & Sharpe, L.T. (2000). L/M -cone ratios in human trichromats assessed by psychophysics, electroretinography and retinal densitometry. *Journal of the Optical Society of America A, 17*, 517-526.

Kulikowski, J.J., & Tolhurst, D.J. (1973). Psychophysical evidence for sustained and transient mechanisms in human vision. *Journal of Physiology, 232*, 149-163.

Le Grand, Y. (1968). Light, colour and vision. (London: Chapman and Hall.

Lee, B.B., Kremers, J., & Yeh, T. (1998). Receptive fields of primate retinal ganglion cells studied with a novel technique. *Visual Neuroscience, 15*, 161-175.

Lee, B.B., Martin, P.R., & Valberg, A. (1988). The physiological basis of heterochromatic flicker photometry demonstrated in the ganglion cells of the macaque retina. *Journal of Physiology, 404*, 323-347.

Lee, B.B., Martin, P.R., & Valberg, A. (1989a). Amplitude and phase of responses of macaque retinal ganglion cells to flickering stimuli. *Journal of Physiology, 414*, 245-263.

Lee, B.B., Martin, P.R., & Valberg, A. (1989b). Nonlinear summation of M- and L-cone inputs to phasic retinal ganglion cells of the macaque. *Journal of Neuroscience, 9*, 1433-1442.

Lee, B.B., Martin, P.R., & Valberg, A. (1989c). Sensitivity of macaque retinal ganglion cells to chromatic and luminance flicker. *Journal of Physiology, 414*, 223-243.

Lee, B.B., Pokorny, J., Smith, V.C., & Kremers, J. (1994). Responses to pulses and sinusoids in macaque ganglion cells. *Vision Research, 34*, 3081-3096.

Lee, B.B., Pokorny, J., Smith, V.C., Martin, P.R., & Valberg, A. (1990). Luminance and chromatic modulation sensitivity of macaque ganglion cells and human observers. *Journal of the Optical Society of America A, 7*, 2223-2236.

Lee, J., & Stromeyer, C.F. (1989). Contribution of human short-wave cones to luminance and motion detection. *Journal of Physiology, 413*, 563-593.

Lennie, P. (1984). Recent developments in the physiology of color vision. *Trends in Neurosciences, 7,* 243-248.

Lennie, P., & D'Zmura, M. (1988). Mechanisms of color vision. *CRC Critical Reviews in Neurobiology, 3,* 333-400.

Lennie, P., Krauskopf, J., & Sclar, G. (1990). Chromatic mechanisms in striate cortex of macaque. *Journal of Neuroscience, 10,* 649-669.

Lennie, P., Pokorny, J., & Smith, V.C. (1993). Luminance. *Journal of the Optical Society of America A, 10,* 1283-1293.

Levinson, J. (1966). One-stage model for visual temporal integration. *J. Opt. Soc. Amer., 56*

Levinson, J.Z. (1968). Flicker fusion fenomena. *Science, 160,* 21–28.

Lindsey, D.T., Pokorny, J., & Smith, V.C. (1986). Phase-dependent sensitivity to heterochromatic flicker. *Journal of the Optical Society of America A, 3,* 921-927.

Livingstone, M.S., & Hubel, D.H. (1987). Psychophysical evidence for separate channels for the perception of form, colour, movement and depth. *Journal of Neuroscience, 7,* 3416-3468.

Luther, R. (1927). Aus dem Gebiet der Farbreizmetrik. *Zeitschrift für technische Physik, 8,* 540-558.

Lythgoe, R.J., & Tansley, K.A. (1929). The relation of the critical frequency of flicker to the adaptation of the eye. *Proc. R. Soc. London, Ser. B* (105), 60-92.

MacLeod, D.I.A., & He, S. (1993). Visible flicker from invisible patterns. *Nature, 361,* 256-258.

MacLeod, D.I.A., Stockman, A., Johnson, N.E., & Vivian, J.A. (1987). Isolating red- and green-sensitive cones with transient chromatic adaptation. *Investigative Ophthalmology and Visual Science (supplement), 28,* 91.

MacLeod, D.I.A., Williams, D.R., & Makous, W. (1992). A visual nonlinearity fed by single cones. *Vision Research, 32,* 347-363.

Mandler, M.B., & Makous, W. (1984). A three channel model of temporal frequency perception. *Vision Research, 24*, 1881-1887.

Martin, P.R., Lee, B.B., White, A.J., Solomon, S.G., & Rüttiger, L. (2001). Chromatic sensitivity of ganglion cells in the peripheral primate retina. *Nature, 410*, 933-936.

Martinez-Uriegas, E. (1985). A solution to the color-luminance ambiguity in the spatiotemporal signal of primate X cells. *Investigative Ophthalmology and Visual Science (supplement), 26*, 183.

Matin, L. (1968). Critical duration, the differential luminance threshold, critical flicker frequency, and visual adaptation: a theoretical treatment. *Journal of the Optical Society of America, 58*, 404-415.

Merigan, W.H., & Eskin, T.A. (1986). Spatio-temporal vision of macaques with severe loss of P beta retinal ganglion cells. *Vision Research, 26*, 1751-1761.

Mollon, J.D., & Bowmaker, J.K. (1992). The spatial arrangement of cones in the primate fovea. *Nature, 360* (6405), 677-679.

Mullen, K.T., & Kingdom, F.A.A. (1996). Losses in peripheral colour sensitivity predicted from "hit and miss" post-receptoral cone connections. *Vision Research, 36*, 1995-2000.

Müller, G.E. (1930). Über die Farbenempfindungen. *Zeitschrift für Psychologie und Physiologie der Sinnesorgane, Ergänzungsband, 17*, 1-430.

Nagy, A.L. (1979). Unique hues are not invariant with brief stimulus durations *Vision Research, 19*, 1427-1432.

Nagy, A.L. (1980). Short-flash Bezold-Brücke hue shifts. *Vision Research, 20* (4), 361-368.

Nelson, T.M., & Bartley, S.H. (1961). The role of PCF in temporal manipulations of color. *Journal of Psychology, 52*, 457-477.

Nilsson, T.H. (1972). Effects of pulse duration and pulse rate on hue of monochromatic stimuli. *Vision Research, 12*, 1907-1921.

Nilsson, T.H., & Nelson, T.M. (1971). Hue shifts produced by intermittent stimulation. *Vision Research, 11*, 697-712.

Packer, O.S., Williams, D.R., & Bensinger, D.G. (1996). Photopigment transmittance imaging of the primate photoreceptor mosaic. *J. Neuroscience, 16*, 2251–2260.

Peirce, C.S. (1877). Note on the sensation of color. *American Journal of Science and Arts, 13*, 247-251.

Petrova, D. (2010). Experimental study of the pre-nonlinearity, nonlinearity and post-nonlinearity stages at medium wavelengths. *Journal of Vision, 10* (7), 442.

Petrova, D., Henning, G.B., & Stockman, A. (2010a). Brightness and colour changes of amplitude-modulated flicker used to dissect visual pathways into early and late stages. *Perception, 39* (ECVP Abstract Supplement), 189.

Petrova, D., Henning, G.B., & Stockman, A. (2010b). The temporal characteristics of the early and late stages of the visual pathways signaling brightness and colour. *Journal of Vision, 10* (15), 9.

Piéron, H. (1929). Lois d'établissement du chroma des impressions lumineuses. *C. R. Ac. des Sciences, 189*, 194-197.

Plateau, J. (1835). Sur un principle de photométrie. *Bulletins de l'Académie royale des sciences et belles-lettres de Bruxelles, 2*, 52-59.

Pokorny, J., Moreland, J.D., & Smith, V.C. (1975). Photopigments in anomalous trichromacy. *Journal of the Optical Society of America, 65*, 1522-1524.

Pokorny, J., Smith, V.C., & Yamashita, Y. (1987). Hue of flickering lights: effect of heterochromatic phase. In: J.J. Kulikowski, C.M. Dickinson, & I.J. Murray (Eds.), *Seeing contour and colour* (pp. 269-273). Oxford: Pergamon.

Pridmore, R.W. (1999). Bezold-Brücke hue-shift as functions of luminance level, luminance ratio, interstimulus interval and adapting white for aperture and object colors. *Vision Research, 39* (23), 3873-3891.

Purdy, D.M. (1931). Spectral hue as a function of intensity. *American Journal of Psychology, 63*, 541-559.

Purpura, K., Tranchina, D., Kaplan, E., & Shapley, R.M. (1990). Light adaptation in the primate retina: Analysis of changes in gain and dynamics of monkey retinal ganglion cells. *Visual Neuroscience, 4*, 75-93.

Rabelo, G., & Grossner, O.J. (1961). Die Abhängigkeit der subjektieven Helligkeit intermittierender Lichtreize von der Flimmerfrequenz. Untersuchungen bei verschiedene Leuchtdichte und Feldgriisse. *Psychol. Forschung., 26* (12), 3.

Rashbass, C. (1976). Unification of two contrasting models of the visual increment threshold. *Vision Res., 16*, 1281-1283.

Rayleigh, L. (1881). Experiments on colour. *Nature, 25*, 64-66.

Reid, R.C., & Shapley, R.M. (1992). Spatial structure of cone inputs to the receptive fields in primate lateral geniculate nucleus. *Nature, 356*, 716-718.

Reid, R.C., & Shapley, R.M. (2002). Space and time maps of cone photoreceptor signals in macaque lateral geniculate nucleus. *Journal of Neuroscience, 22*, 6158-6175.

Roorda, A., Metha, A.B., Lennie, P., & Williams, D.R. (2001). Packing arrangement of the three cone classes in primate retina. *Vision Res., 41*, 1291–1306.

Roufs, J.A.J. (1972). Dynamic properties of vision-I. Experimental relationships between flicker and flash thresholds. *Vision Research, 12*, 261-278.

Roufs, J.A.J. (1974). Dynamic properties of vision-IV. Thresholds of decremental flashes, incremental flashes and doublets in relation to flicker fusion. *Vision Research, 14*, 831-851.

Rushton, W.A.H. (1972). Pigments and signals in colour vision. *Journal of Physiology, 220*, 1-31P.

Rushton, W.A.H., Powell, D.S., & White, K.D. (1973a). Exchange thresholds in dichromats. *Vision Research, 13*, 1993-2002.

Rushton, W.A.H., Powell, D.S., & White, K.D. (1973b). The spectral sensitivities of the "red" and "green" cones in the normal eye. *Vision Research, 13*, 2003-2015.

Savoie, R.E. (1973). Bezold-Brücke effect and visual nonlinearity. *J Opt. Soc.Amer., 63*, 1253-1261.

Schiller, P., Logothetis, N.K., & Charles, E.R. (1990). Functions of the colour-opponent and broad-band channels of the visual system. *Nature, 343*, 68-70.

Schnapf, J.L., Kraft, T.W., & Baylor, D.A. (1987). Spectral sensitivity of human cone photoreceptors. *Nature, 325*, 439-441.

Schneeweis, D.M., & Schnapf, J.L. (1999). The Photovoltage of Macaque Cone Photoreceptors: Adaptation, Noise, and Kinetics. *Journal of Neuroscience, 19* (4), 1203–1216.

Schrödinger, E. (1925). Über das Verhältnis der Vierfarben zur Dreifarbentheorie. *Sitzungberichte. Abt. 2a, Mathematik, Astronomie, Physik, Meteorologie und Mechanik. Akademie der Wissenschaften in Wien, Mathematisch-Naturwissenschaftliche Klasse, 134*, 471.

Sharpe, L.T., Stockman, A., Jägle, H., & Nathans, J. (1999). Opsin genes, cone photopigments, color vision and colorblindness. In: K. Gegenfurtner, & L.T. Sharpe (Eds.), *Color vision: From Genes to Perception* (pp. 3-51). Cambridge: Cambridge University Press.

Smith, C.V., Pokorny, J., Davis, M., & Yeh, T. (1995). Mechanisms subserving temporal modulation sensitivity in silent-cone substitution. *J Opt. Soc.Amer. A, 12* (2), 241-249.

Sperling, G., & Sondhi, M.M. (1968). Model for visual luminance discrimination and flicker detection. *Journal of the Optical Society of America, 58*, 1133-1145.

Sperling, H.G., & Lewis, W.G. (1959). Some Comparisons between Foveal Spectral Sensitivity Data Obtained at High Brightness and Absolute Threshold. *J. Opt. Soc. Am., 49* (10), 983-988.

Stewart, G.N. (1887). Is the law of Talbot true for very rapidly intermittent light? *Proceedings of the Royal Society of Edinburgh, 15*, 441-464.

Stockman, A. (1993). Changes in color produced by amplitude-modulated M- and L-cone detected flickering lights survive flicker photometric cancellation. *Investigative Ophthalmology and Visual Science (supplement), 34*, 912.

Stockman, A., & Brainard, D.H. (2009). Color vision mechanisms. In: J.M. Enoch, & V. Lakshminarayanan (Eds.), *Handbook of Optics, 3rd edition* (New York: McGraw Hill.

Stockman, A., Langendörfer, M., Smithson, H.E., & Sharpe, L.T. (2006). Human cone light adaptation: from behavioral measurements to molecular mechanisms. *Journal of Vision, 6*, 1194-1213.

Stockman, A., & MacLeod, D.I.A. (1986). Visible beats from invisible flickering lights: Evidence that blue-sensitive cones respond to rapid flicker. *Investigative Ophthalmology and Visual Science (supplement), 27*, 71.

Stockman, A., MacLeod, D.I.A., & DePriest, D.D. (1991). The temporal properties of the human short-wave photoreceptors and their associated pathways. *Vision Research, 31*, 189-208.

Stockman, A., MacLeod, D.I.A., & Lebrun, S. (1993). Faster than the eye can see: blue cones respond to rapid flicker. *Journal of the Optical Society of America A, 10*, 1396-1402.

Stockman, A., & Plummer, D.J. (1998). Color from invisible flicker: a failure of the Talbot-Plateau law caused by an early "hard" saturating nonlinearity used to partition the human short-wave cone pathway. *Vision Research, 38,* 3703-3728.

Stockman, A., & Plummer, D.J. (2005a). Long-wavelength adaptation reveals slow, spectrally-opponent inputs to the human luminance pathway. *Journal of Vision, 5,* 702-716.

Stockman, A., & Plummer, D.J. (2005b). Spectrally-opponent inputs to the human luminance pathway: slow +L and -M cone inputs revealed by low to moderate long-wavelength adaptation. *Journal of Physiology, 566,* 77-91.

Stockman, A., Plummer, D.J., & Montag, E.D. (2005). Spectrally-opponent inputs to the human luminance pathway: slow +M and -L cone inputs revealed by intense long-wavelength adaptation. *Journal of Physiology, 566,* 61-76.

Stockman, A., & Sharpe, L.T. (2000a). Spectral sensitivities of the middle- and long-wavelength sensitive cones derived from measurements in observers of known genotype. *Vision Research, 40,* 1711-1737.

Stockman, A., & Sharpe, L.T. (2000b). Tritanopic color matches and the middle- and long-wavelength-sensitive cone spectral sensitivities. *Vision Research, 40,* 1739-1750.

Stockman, A., Sharpe, L.T., Merbs, S., & Nathans, J. (2000). Spectral sensitivities of human cone visual pigments determined *in vivo* and *in vitro*. In: K. Palczewski (Ed.) *Vertebrate phototransduction and the visual cycle, Part B. Methods in Enzymology, Vol. 316,* 316 (pp. 626-650). New York: Academic Press.

Stockman, A., Williams, M.R., & Smithson, H.E. (2004). Flicker-clicker: cross modality matching experiments. *Journal of Vision, 4,* 86a.

Stromeyer, C.F., & Lee, J. (1987). Motion and short-wave cone signals: influx to luminance mechanisms. *Investigative Ophthalmology and Visual Science (supplement), 28,* 232.

Swanson, W.H., Pokorny, J., & Smith, V.C. (1987). Effects of temporal frequency on phase-dependent sensitivity to heterochromatic flicker. *Journal of the Optical Society of America A, 4*, 2266-2273.

Talbot, H.F. (1834). Experiments on light. *Philosophical Magazine Series 3, 5*, 321-334.

Tyler, C.W., & Hamer, R.D. (1990). Analysis of visual modulation sensitivity. IV. Validity of the Ferry-Porter law. *Journal of the Optical Society of America A, 7*, 743-758.

van der Horst, G.J.C., & Muis, W. (1969). Hue shift and brightness enhancement of flickering light. *Vision Research, 9*, 953-963.

Veringa, F. (1970). Diffusion Model of Linear Flicker Responses. *J. Opt. Soc. Am. , 60*, 285-286.

Virsu, V., & Lee, B.B. (1983). Light Adaptation in Cells of Macaque Lateral Geniculate Nucleus and Its Relation to Human Light Adaptation. *Journal of Neurophysiology, 50* (4), 864-878.

von Bezold, W. (1873). Über das Gesetz der Farbenmischung und die physiologischen Grundfarben. *Annalen der Physiologie und Chemie, 150*, 221-247.

Walls, G.L. (1955). A branched-pathway schema for the color-vision system and some of the evidence for it. *American Journal of Ophthalmology, 39*, 8-23.

Walraven, P.L. (1961). On the Bezold-Brücke phenomenon. *Journal of the Optical Society of America, 51*, 1113-1116.

Walraven, P.L. (1962). On the mechanisms of colour vision. 50 (The Netherlands: Institute for Perception RVO-TNO.

Walraven, P.L., van Hout, A.M.J., & Leebeek, H.J. (1966). Fundamental response curves of a normal and a deuteranomolous observer derived from chromatic adaptation. *Journal of the Optical Society of America, 56*, 125-127.

Walters, J.W., & Harwerth, R.S. (1978). The mechanism of brightness enhancement. *18*, 777-779.

Wasserman, G.S. (1966). Brightness enhancement and opponent-colors theory. *Vision Research, 6*, 689-699.

Wasserman, G.S., & Kong, K.L. (1974). Illusory correlation of brightness enhancement and transients in the nervous system. *Science, 184*, 911-913.

Watson, A.B. (1986). Temporal sensitivity. In: K. Boff, L. Kaufman, & J. Thomas (Eds.), *Handbook of Perception and Human Performance*, 1 (pp. 6-1-6-43). New York: Wiley.

Watson, A.B., & Robson, J.G. (1981). Discrimination at threshold: labelled detectors in human vision. *Vision Research, 21*, 1115-1122.

Werner, J.S., Bieber, M.L., & Schefrin, B.E. (2000). Senescence of foveal and parafoveal cone sensitivities and their relations to macular pigment density. *J Opt Soc Am A Opt Image Sci Vis, 17* (11), 1918–1932.

Wesner, M.F., Pokorny, J., Shevell, S.K., & Smith, V.C. (1991). Foveal cone detection statistics in color-normals and dichromats. *Vision Research, 31*, 1021-1037.

Westheimer, G. (1966). The Maxwellian view. *Vision Research, 6*, 669-682.

Wiesel, T.N., & Hubel, D. (1966). Spatial and chromatic interactions in the lateral geniculate body of the rhesus monkey. *Journal of Neurophysiology, 29*, 1115-1156.

Wildt, G.J., & Bouman, M.A. (1968). The dependence of Bezold-Brücke hue shift on spatial intensity distribution. *Vision Res., 8*, 303-313.

Williams, D.R. (1985). Aliasing in human foveal vision. *Vision Research, 25*, 195-205.

Wu, S., Burns, S.A., & Elsner, A.E. (1995). Effects of flicker adaptation and temporal gain control on the flicker ERG. *Vision Research, 35*, 2943-2953.

Wu, S., Burns, S.A., Reeves, A., & Elsner, A.E. (1996). Flicker brightness enhancements and nonlinearity. *Vision Research, 36*, 1573-1583.